

DISSERTATION

submitted to the
Combined Faculty of Natural Sciences and Mathematics
of the Ruperto Carola University Heidelberg, Germany
for the degree of
Doctor of Natural Sciences

Presented by
Vanessa Aphaia Fiona Schmidt, M.Sc.
Born in Wiesbaden, Germany

Oral examination: _____

**Polarization of a small GTPase at the plasma membrane
of the root hair initiation domain**

Referees:

Prof. Dr. Karin Schumacher

Dr. Guido Großmann

Für Michael

*When life gives you lemons, don't make lemonade!
Make life take the lemons back!*

- Cave Johnson from Portal 2 -

Acknowledgement

I am very grateful that I had the opportunity to conduct this exciting scientific work. Science is team work and I would not have been successful without the help of many people, to whom I would like to express my gratitude:

First and foremost, I would like to thank Dr. Guido Grossmann. Guido, thank you for believing in me, for always supporting me and for giving me this unique opportunity to follow my curiosity about cell polarization! I am very thankful for all the time filled with inspiring discussions, but also for your patience with me and my project. Thank you for this great and memorable time, which I will never forget! I am looking forward to continue this scientific journey together with you 😊

A special thanks goes to my TAC members Prof. Dr. Karin Schumacher and Prof. Dr. Britta Brügger for critical advises, helpful discussions and open ears throughout my PhD! Furthermore, I would also like to thank Prof. Dr. Thomas Greb for his willingness to be my forth examiner! Additionally, I would like to thank the Schmeil Foundation, who supported me and my work with the Schmeil Extension Award!

I am very thankful to Dr. Jan-Felix Evers who not only supported us with an essential microscope, but also kicked my a** when I needed it and introduced me to the beautiful phenomenon of fluorophore blinking! Thank you, Felix, for your moral, personal and scientific support!

Furthermore, I am very thankful to Dr. Ulrike Engel who made it possible to discover and visualize what we now call nanodomains. Additionally, she maintained and further developed the microscope I spent most of my time with. Thank you Ulrike for your precious input, advices and patience!

A special thanks goes to Dr. Philipp Denninger, who built the fundament of the work presented here. Nearly all practical lab skills I obtained, I learned from you! You were not only a teacher but also an inspiring colleague and friend with whom I discovered several times that it is possible to see the Strahlenburg from our bay...Incredible!

A very, very big “thank you” goes to my colleague Anna Denzler! Since you came to the lab many birthdays have been celebrated and many cakes have been eaten, a lot of rabbits appeared and the lab life became even more joyful! Anna, thank you not only for your scientific but especially for your moral support during my PhD!

I also would like to thank Dr. Linda Manhart (and her legs 😊) not only for the tiny ice box that I took more often than you know ^^, but also for travelling the whole journey together with me and for understanding how I felt! I wish you all the best for your (zoological) future.

A special thanks goes to Dr. Rik Brugman (mainly for sharing secret photos^^) who was a great, ticklish and bearded colleague! Dr. Milan Župunski (aka “M”) and Dr. Marjorie Guichard for being great colleagues! Thank you for your precious input in my project and analyses and for many inspiring discussions, patient explanations, new ideas and for bringing a great working atmosphere to the lab. Dr. Phil-Alan Gärtig, thank you for being patient about all my “Aloooooon”s, your support and your cake record 😊

One of the biggest “thank you”s goes to all my students: Rachel Röhrich, Friederike Korn, Clara Baader, Viktoria Frajs, Jasmin Onistschenko, Natascha Bartsch and Verena Kaul, for their helping hands, brains and precious input! Enric Betran Garcia de Olalla for being an inspiring, patient and really wunderbar HiWi – I wish you all the best for your future (not only!) in science. And of course I would also like to thank all other harvesting-HiWis like Janos Löffler, Laura Ruppert, Sophie-Luise Landua and Andrea Sarvari. To be honest, I think all the work from our lab would not have been proceeding that fast without those people that do the “dirty” work! And I really hope I did not forget anyone of you, in case I did: I’m Sorry!

Ein ganz großer Dank geht an die Besetzung des „Writing&Thinking“-Raums im 1ten Stock: Petra, Katja, Ruth, Sarah, Nancy und Angelika. Danke, dass ihr mich so nett aufgenommen habt! Danke auch für die ein oder andere Kannen Tee und Diskussionen zu diversen, nicht nur arbeitsbezogenen Themen.

Da Wissenschaft ja nicht alles im Leben ist, möchte ich mich ganz herzlich bei denen bedanken, die mich außerhalb des Labors unterstützt haben. Und da möchte ich mit meinen Eltern anfangen, ohne die das hier alles überhaupt nicht möglich gewesen wäre:

Liebe MaPas, danke, dass ihr mir diese Doktorarbeit ermöglicht habt und all die Jahre für mich da gewesen seid! Nicht nur, dass ihr mich bei all meinen (Irr-) Wegen unterstützt habt, sondern, dass ihr mich sogar ermutigt habt sie überhaupt zu gehen! Ihr habt nie aufgehört an mich zu glauben, auch wenn ich selbst am Zweifeln war. Ich bin sehr stolz, so tolle Eltern zu haben! Danke!

Ich möchte mich auch bei meinen Freunden bedanken, die in all den Jahren jeden Stimmungswandel mit mir durchgestanden haben! Danke Marlene, Nora, Flo, Anja, und Theresa für eure Unterstützung und vor allem dafür, dass ihr mir immer wieder gezeigt habt, dass es außerhalb des Labors noch ein Leben gibt. Danke für eure Wertschätzung meiner Person, die mir in vielen Momenten des Zweifelns Kraft gegeben hat weiter an mich und meinen Weg zu glauben. Ich möchte mich auch bei Paul bedanken, den ich zwar nicht persönlich kenne, der aber maßgeblich an dem motivierenden Ausdruck „einfach mal den Paul machen!“ beteiligt war 😊.

Und zum Schluss der Mensch, der mir nicht nur der wichtigste ist, sondern dem ich auch am meisten dankbar bin: Herr Fuchs! Ich kann mit Worten nicht ausdrücken, was du mir bedeutest und auch nicht wie dankbar ich dir bin, dass du diesen Weg zusammen mit mir gegangen bist! Du hast mich nicht nur wissenschaftlich, sondern auch auf persönlicher Ebene unterstützt und warst einfach immer für mich da! Du bist das Beste was mir passieren konnte und ich hoffe, dass wir diesen Weg noch ganz lange gemeinsam gehen werden! Ich liebe dich!

Table of Content

Acknowledgement	6
Table of Content	9
Summary	15
Zusammenfassung	16
General Introduction	17
1. Cell polarity and polar growth	17
2. Small GTPases	18
3. Initiation of polar growth	20
4. Arabidopsis root hairs: a model system for polar growth and polar growth initiation	20
4.1. ROP2 is a core component of the root hair growth machinery	23
4.2. Proteins involved in regulating ROP activity	24
4.3. Receptor-like kinases acting upstream of GEFs and ROPs	25
4.4. The role of the actin cytoskeleton in root hair growth	26
4.5. Root hair growth is controlled by $[Ca^{2+}]_{cyt}$ -ROS-ROP interplay	27
4.6. The role of membrane lipids during root hair growth	28
Chapter I	31
1. Introduction	33
1.1. ROP2 protein structure	33
1.2. Aim of Chapter I	35
2. Results	37
2.1. Are electrostatic interactions between anionic lipids in the PM of the RHID and ROP2 involved in ROP2 polarization?	39
2.2. How do the N- and the C-terminus of ROP2 affect its polarization at the RHID?	41
2.3. Is the polarization of ROP2 at the RHID influenced by its activity state?	44
2.4. Is GEF3 involved in ROP2 polarization by regulating ROP2 membrane association?	46
3. Discussion	49
3.1. Membrane association is a prerequisite for ROP2 polarization	49
3.2. Local activation of ROP2 at the RHID	52

Chapter II	55
1. Introduction	56
1.1. Spontaneous polarization in the absence of landmark proteins	56
1.2. Aim of Chapter II	57
2. Results	59
2.1. Does the activity state of ROP2 impact on its mobility?	59
2.1.1 Does GEF3 influence ROP2 mobility at the RHID?	60
2.2. How is the immobilization of ROP2 at the RHID achieved?	62
2.2.1 Blinking behavior of mCitrine allows super-resolution microscopy.	64
2.2.2 SRRF reveals the GEF3-dependent localization of ROP2 into nanoclusters.	67
2.3. Does protein mobility impact on protein polarization at the RHID?	70
2.3.1 ROP2 immobilization precedes its polarization.	70
2.3.2 ROP2 immobilization depends on reduced mobility of GEF3.	75
2.3.3 Do ROP2-nanoclusters depend on its activity state?	80
2.3.4 Does S-acylation influence ROP2 polarity and mobility?	83
2.4. Are other proteins of the tip growth machinery also recruited into nanoclusters at the RHID?	87
2.4.1 Can VAEM-SRRF be used to elucidate the function of ROP2 and GEF3 nanoclusters in the RHID by co-localization experiments?	88
2.4.2 Do other proteins of the tip growth machinery also localize into nanoclusters?	92
3. Discussion	97
3.1. Local activation causes ROP2 immobilization at the RHID	97
3.2. Nanoclusters as a site of protein immobilization	101
Chapter III	105
1. Introduction	107
1.1. Proximity labelling	108
1.2. Aim of Chapter III	110
2. Results	112
2.1. Trichoblast-specific, inducible promoters	112
2.2. A Is a TurboID-GEF3 fusion protein able to facilitate biotinylation in <i>N. benthamiana</i> ?	114
3. Discussion	117
3.1. Trichoblast-specific inducible promoters	117
3.2. Proximity labeling using TurboID	118

3.3. Future experimental plans to find GEF3-interactome at the RHID	120
---	-----

Materials and Methods 122

1. Molecular Biology	122
1.1. Molecular cloning	122
1.1.1 PCR and PCR fragment purification	122
1.2. Entry vector cloning	122
1.2.1 Removal of internal Bsal-sites	123
1.2.2 Destination vector assembly	123
1.3. Plasmid validation	123
1.3.1 Preparation of chemical competent <i>E. coli</i>	124
1.3.2 Transformation of chemically competent <i>E. coli</i>	124
1.3.3 Colony-PCR	125
1.3.4 Plasmid isolation from <i>E. coli</i>	125
1.3.5 Vector sequence validation	125
1.4. Agrobacterium transformation	125
1.4.1 Preparation of chemical competent <i>A. tumefaciens</i>	125
1.4.2 Transformation of chemically competent <i>A. tumefaciens</i>	126
1.5. Nucleic acid isolation and testing methods	126
1.5.1 Isolation of genomic DNA from <i>A. thaliana</i>	126
1.5.2 Genotyping PCR	127
1.6. Protein isolation and analysis for proximity labelling	127
1.6.1 Protein isolation from <i>N. benthamiana</i> leaves	127
1.6.2 Pull-down of biotinylated Proteins	128
1.6.3 Qualitative detection of proteins using Western blot	129
2. Plant handling	131
2.1. Seed sterilization	131
2.2. Growth conditions	131
2.2.1 Standard plant growth conditions	131
2.2.2 Root Chip experiments	131
2.3. Plant transformation and transfection	131
2.3.1 Transfection of <i>N. benthamiana</i> leaves by leaf infiltration	131
2.3.2 Transformation of <i>A. thaliana</i> via floral dipping	132
2.3.3 Identification of stable, transgenic <i>A. thaliana</i> lines	132
2.3.4 Estradiol induced gene expression	132
2.3.5 Induction of gene expression in <i>N. benthamiana</i>	133
2.3.6 Induction of <i>A. thaliana</i> on agar-plates	133

3. Imaging	133
3.1. Stereoscopic imaging	133
3.2. Spinning-disc confocal microscopy	133
3.3. Confocal laser scanning microscopy	134
3.3.1 FRAP	134
3.4. Variable angle epifluorescence microscopy	134
3.5. Plant stainings	135
3.5.1 Propidium iodide	135
3.6. Chemical treatment of plants	135
3.6.1 Pharmacological treatments	135
4. Data analysis	135
4.1.1 Chemical fixation	135
4.2. Image processing	136
4.3. Protein mobility analysis	136
4.3.1 FRAP analysis	136
4.3.2 Particle tracking	136
4.3.3 Quantification of Particle tracking data	136
4.4. Analysis of Protein localization	137
4.4.1 Polarity index measurements	137
4.4.2 Membrane association measurements	137
4.4.3 Cell-type specificity measurements	137
4.5. Nanodomain analysis	138
4.5.1 SRRF- analysis	138
4.5.2 Measurements of nanodomain dimensions	138
4.6. Scripts and Macros	138
4.6.1 ANOVA-Tukey test using R	138
4.6.2 Image Processing for Particle Tracking using Fiji	139
4.6.3 Polynomial fitting and two-way ANOVA using R	140
4.6.4 Counting and measuring of nanodomains after SRRF using Fiji	141
5. Material used in this thesis	143
5.1. Plant lines not generated in this thesis	143
5.2. Entry vectors cloned in the course of this thesis	143
5.3. List of destination vectors cloned in the course of this thesis	145
5.4. List of primers used in this thesis	149

Bibliography	155
---------------------	------------

Appendix	167
-----------------	------------

List of figures	167
-----------------	-----

List of tables	172
----------------	-----

List of abbreviations	173
-----------------------	-----

Summary

Functional specialization of single cells but also of whole tissues requires the division of labor and leads to the establishment of unequal distribution and polar organization. As a consequence, a diverse spectrum of cells with polar shapes has arisen in all kingdoms of life and conceptual similarities between these cells indicate the presence of a general unifying machinery. Even though we have a good understanding of the process of polar growth itself, we still know very little about the initial steps that lead to cellular asymmetry and polarity establishment.

The root hair system of *Arabidopsis thaliana* is an excellent model to study all aspects of polarity and especially its initiation. One of the first proteins to localize at the root hair initiation domain (RHID) in *Arabidopsis* is the small GTPase RHO-OF PLANTS 2 (ROP2), which is a central regulator of the root hair growth machinery. ROP2 is a molecular switch that shuffles between an active (GTP-bound) and an inactive (GDP-bound) state. It is obvious that the spatio-temporal control of ROP2 positioning and its activation is of critical importance for proper root hair development, however to date it remains unclear how ROP2 is recruited to the RHID, how ROP2 polarization is timed and how its polar accumulation is maintained.

In this thesis I could show that the poly-basic region close to the C-terminus of ROP2 is necessary, but not sufficient for its accumulation at the RHID. I could further demonstrate that polar accumulation of ROP2 depends on its N-terminus, which we have reported to be involved in the interaction with its putative activator and landmark protein GEF3. I found that the ability to shuffle between its active and inactive state is critical for ROP2 polarization and have presented evidence for an activation-dependent immobilization of ROP2 that involves the interaction with GEF3, activation of GDP-ROP2 and differential protein mobility.

Using single-molecule localization microscopy I was able to show that ROP2, GEF3 and other proteins of the root hair growth machinery localize into nanoclusters at the PM. To fully characterize the proteome of these nanoclusters, I established biotin-ligase based proximity labelling in *Arabidopsis* root hairs. This will allow us to elucidate whether the structuring of the PM (at the RHID) into nanoclusters plays a role in the establishment, maintenance and plasticity of cellular polarity.

Zusammenfassung

Die funktionelle Spezialisierung einzelner Zellen aber auch ganzer Gewebe erfordert Arbeitsteilung und führt zu Asymmetrie beziehungsweise polarer Organisation. Infolgedessen ist ein vielfältiges Spektrum polaren Zellformen entstanden und konzeptionelle Ähnlichkeiten zwischen diesen Zellen weisen auf das Vorhandensein einheitlicher Grundmechanismen hin. Obwohl wir den Prozess des polaren Wachstums an sich bereits gut verstehen, wissen wir immer noch sehr wenig über die ersten Schritte, die zur Ausbildung zellulärer Asymmetrie und Polarität führen.

Die Wurzelhaare der Modelnpflanze *Arabidopsis thaliana* sind ein hervorragendes System, um genau diese Aspekte zu untersuchen: Eines der ersten Proteine, das in der Wurzelhaar-Initiationsdomäne (RHID) von *Arabidopsis* akkumuliert ist die kleine GTPase RHO OF PLANTS 2 (ROP2), bei der es sich um einen zentralen Regulator der Wachstumsmaschinerie handelt. ROP2 ist ein molekularer Schalter, der zwischen einem aktiven (GTP-gebundenen) und einem inaktiven (GDP-gebundenen) Zustand wechselt. Welche Rolle genau der Aktivitätszustand des Proteins spielt und wie die positionsspezifische Rekrutierung von ROP2 reguliert wird, ist bislang noch unklar.

Im Verlauf dieser Arbeit konnte ich zeigen, dass die poly-basische Region nahe dem C-Terminus von ROP2 notwendig, aber nicht ausreichend für seine Akkumulierung ist. Ich konnte weiterhin zeigen, dass die polare Akkumulierung von ROP2 von seinem N-Terminus abhängt, der an der Wechselwirkung mit dem mutmaßlichen Aktivator und Pionierfaktor GEF3 beteiligt ist. Ich fand heraus, dass die Fähigkeit zwischen dem aktiven und inaktiven Zustand zu wechseln für die ROP2-Polarisierung entscheidend ist und lege Beweise für eine aktivierungsabhängige Immobilisierung von ROP2 vor, welche die Wechselwirkung mit GEF3, die Aktivierung von GDP-ROP2 und Änderungen der Proteinmobilität beinhaltet.

Mithilfe von Einzelmolekül-Lokalisationsmikroskopie konnte ich zeigen, dass ROP2, GEF3 und andere Proteine der Wachstumsmaschinerie an der Plasmamembran in Nanostrukturen zu finden sind. Zur weiteren Charakterisierung dieser Strukturen, habe ich eine Methode zur Markierung von Umgebungsproteinen in Wurzelhaaren von *Arabidopsis* etabliert. Wir werden somit in der Lage sein herauszufinden, ob die Strukturierung der Membran (an der RHID) eine Rolle bei der Etablierung, Aufrechterhaltung und Plastizität von Zellpolarität spielt.

General Introduction

1. Cell polarity and polar growth

The term “polarity” describes a state of order that is defined by unequal distribution and the maintenance of local differences in for example the concentration of molecules or electrical charges. In biology, polarity is the prerequisite for any functional specialization on a subcellular level, on the level of single cells, but also on the scale of whole tissues and organisms, which at this level results from the tissue wide coordination of individual cell polarities. Therefore, the establishment of polarity, sometimes also referred to as “symmetry breaking”, is arguably the most important event in the life of a cell.

While polarity within a cell can occur on a purely molecular level, it is often accompanied by the establishment of polar cell shapes that are critical for the specialized functions of these cells. Examples of highly polar cells can be found across all kingdoms of life and polarity has led to diverse cell types like neurons, fungal hyphae, pollen tubes and root hairs. The polar shape of these cell types is achieved by polar growth, which requires the orchestration of various cellular processes including the establishment of an intracellular force pushing outwards and a simultaneous relaxation of the surrounding extracellular matrix, enabling the cell to grow into the newly created space. Studies in diverse organismal groups such as nematodes, insects, mammals, fungi and plants have identified common concepts in the establishment of polar growth: First, external or internal cues initiate site selection for subsequent polarized growth. This information is then transmitted to the downstream growth machinery, leading to polarized re-organization of the cytoskeleton. Finally, targeted secretion and local deposition of (cellular) building material leads to locally restricted growth. Precise feedback regulation during all these steps ensures the proper initiation of cell polarity and its maintenance. While many different forms of cell polarity and polar growth have evolved, the conceptual similarities between phylogenetically distinct species suggest a general unifying machinery (Drubin and Nelson, 1996), potentially predating the advent of multicellularity. Small GTPases have been identified as an important component of this ancient machinery for polar growth.

2. Small GTPases

Small GUANOSINE TRIPHOSPHATASEs (GTPases), also known as small G-proteins or monomeric GTPases, of the rat sarcoma (Ras) superfamily, are evolutionary conserved key molecules for a plethora of cellular processes (Colicelli, 2004; Wennerberg et al., 2005; Goitre et al., 2013). The Ras-superfamily consists of 5 structural and functionally distinct members: Ras, Rho, Rab, Ran and Arf. While Ran-, Arf- and Rab-proteins control nuclear and vesicular trafficking processes, Ras- and Rho-proteins are both involved in gene expression, cell proliferation and cell differentiation. In addition, Ras-proteins act in cell survival and apoptosis and Rho-proteins play a role in actin reorganization, cell cycle progression, cell polarity and polar growth (Berken and Wittinghofer, 2008).

To control this multitude of complex cellular processes, small GTPases act as molecular switches, performing a simple biochemical reaction: By hydrolyzing GTP, they switch between an active, GTP-bound and an inactive, GDP-bound form (for example reviewed in Vetter and Wittinghofer, 2001; Etienne-Manneville and Hall, 2002) (Figure 1). The hydrolysis of GTP is inefficient, causing small GTPases to reside in the active state for an extended period of time. On the other hand, the low dissociation coefficient of GDP causes an inefficient release of GDP from the inactive state and requires enzymatic regulation to be able to switch back to the active state (Bourne et al., 1991; Vetter and Wittinghofer, 2001). Therefore, the activation cycle of small GTPases is tightly regulated by GDP-/GTP-exchanging GEFs (GUANINE NUCLEOTIDE EXCHANGE FACTORS) and GTP-hydrolysis enhancing GAPs (GTase-ACTIVATING PROTEINs) (for example reviewed in Schmidt and Hall, 2002; Etienne-Manneville and Hall, 2002; Jaffe and Hall, 2005; Berken et al., 2005) (Figure 1).

Small GTPases of the Ras-superfamily share a set of conserved sequence motifs at their N-terminus, the 5 G-boxes, which together with five alpha helices and six beta-strands form the G-domain that is responsible for GTP/GDP-binding and GTP-hydrolysis (for example reviewed in Wennerberg et al., 2005; Goitre et al., 2013). While the GTP-bound form (active state) and the GDP-bound form (inactive state) of GTPases are very similar in their overall protein conformation, there are very distinct differences when looking specifically at the switch domains: Upon GTP-binding, the switch I domain and the switch II domain undergo a conformational change, leading to an increased affinity for effector targets (Bishop and

Hall, 2000; Repasky et al., 2004). Another important regulatory feature of a number of small GTPases is the post-translational attachment of a lipid modification. Members of the Ras- and the Rho-family contain a C-terminal CaaX-motif (C = cysteine, a = aliphatic amino acid, X = any amino acid), which serves as a recognition sequence for farnesyltransferases and type I geranylgeranyltransferases. Rab-family members contain a different, cysteine containing C-terminal motif, which is recognized by type II geranylgeranyltransferases (Wennerberg et al., 2005; Goitre et al., 2013). These lipid modifications are involved in the association of the small GTPases with membranes and the correct targeting to different intracellular compartments and are therefore important for proper GTPase function.

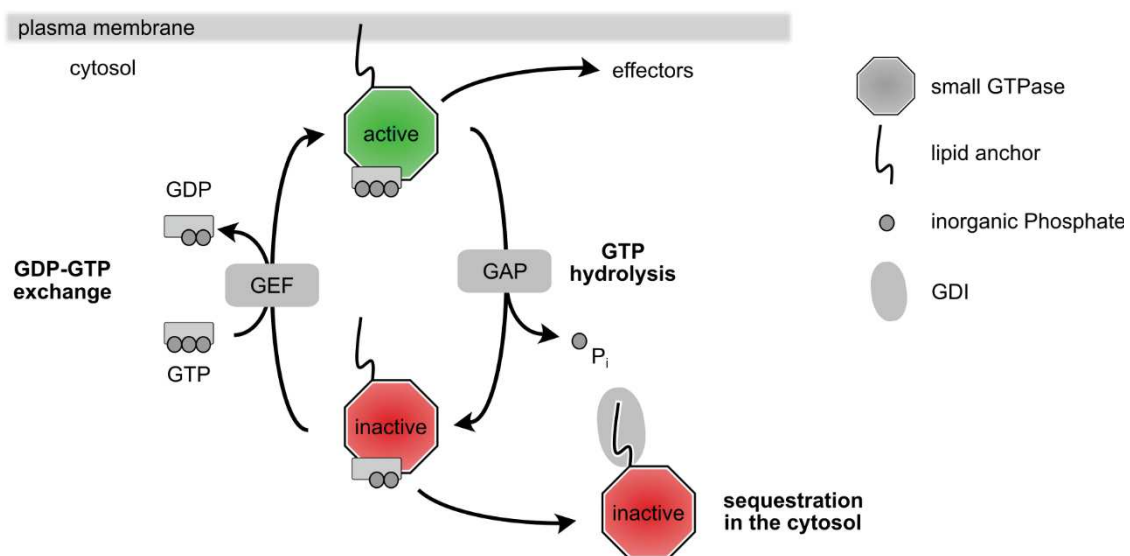


Figure 1: The activity cycle of small GTPases, at the example of a GTPase with a lipid anchor. In the active form, the GTPase is associated with the plasma membrane and binds GTP, which is hydrolyzed via a GTPase ACTIVATING PROTEIN (GAP). The GDP-bound GTPase in its inactive state is sequestered in the cytosol by GUANINE DISSOCIATION INHIBITORS (GDIs), that bind to the lipid anchor. GDP is replaced by GTP via GUANINE NUCLEOTIDE EXCHANGE FACTORS (GEFs), leading to the activation and association of the small GTPase with the plasma membrane.

For small GTPases that carry a lipid modification (farnesyl or geranylgeranyl) at their C-terminus (members of the Ras-, Rho- and Rab-families), the activation-cycle is accompanied by an intracellular shuffling between the intracellular membranes and the cytosol. This shuffling is mediated by GUANINE DISSOCIATION INHIBITORS (GDIs) which bind to the lipid moiety and solubilize the small GTPase in the cytosol (Ueda et al., 1990; Leonard et al., 1992; Dovas and Couchman, 2005; DerMardirossian and Bokoch, 2005; Cherfils et al., 2013) (Figure 1). The intracellular shuffling of the small GTPase is a means to transduce intra- and extracellular cues into spatially regulated cellular responses (Feiguelman et al., 2018).

3. Initiation of polar growth

Small GTPases have been shown to be important for the regulation and initiation of polar growth. Their role has been especially well studied in the budding yeast *Saccharomyces cerevisiae*, which exhibits polar growth during budding and mating (for example reviewed in Park and Bi, 2007; Bi and Park, 2012). During bud formation, the RAS-RELATED GTPase 1 (RSR1/BUD1) is recruited to the site of future bud emergence where it is activated by its GEF BUD SITE SELECTION 5 (BUD5) and is inactivated by its GAP BUD2 (Bender and Pringle, 1989; Chant et al., 1991; Park et al., 1993). RSR1 recruits and activates the CELL DIVISION CYCLE 24 (CDC24) protein (Park et al., 2002; Shimada et al., 2004), which in turn acts as a GEF for the Rho-like GTPase CDC42 (Hartwell et al., 1974; Adams et al., 1990; Johnson and Pringle, 1990; Zheng et al., 1994). CDC42 itself, is necessary for bud emergence and outgrowth (Hartwell et al., 1974).

Homologues of CDC42 were found in nearly all eukaryotes where they act as key players in polar growth (Etienne-Manneville, 2004). Even though the mechanism as well as the underlying machinery of polar growth are well conserved and have been extensively studied, the cues by which the site of polar growth is selected are far from fully understood. From studies on the bud emergence of *S. cerevisiae* we know that the landmark proteins AXIAL GROWTH 1 (AXL1) and AXL2 (Halme et al., 1996; Roemer et al., 1996), as well as BUD8 and BUD9 (Zahner et al., 1996; Harkins et al., 2001) are involved in recruiting BUD5 (the GEF for RSR1) to the site of future bud outgrowth (Kang et al., 2001; Lord et al., 2002). This recruitment is likely to happen via protein-protein interactions (Marston et al., 2001; Kang et al., 2004; Krappmann et al., 2007). But how these landmark proteins themselves get polarized in the first place remains elusive. Additionally, besides landmark proteins in yeast and fungi, we lack knowledge about landmark proteins for polar growth in other organisms.

4. Arabidopsis root hairs: a model system for polar growth and polar growth initiation

The establishment of root hairs in the model plant *Arabidopsis thaliana* has been widely used as a system to study the chronology of polar growth and polar growth initiation in plants (Schiefelbein and Somerville, 1990; Grierson et al., 2014). Root hairs are tubular

protrusions that grow out at a defined position of specialized epidermal root cells, so called trichoblasts. They greatly increase the rhizosphere volume and therefore play a central role in plant anchorage on the one hand and on the other hand allow the plant to explore a larger volume of soil, thus increasing nutrient accessibility. Root hair length and density depend on nutrient availability and are both highly dynamic in reaction to changing environments (Stanley et al., 2018) (Figure 2, B). Additionally, the kinetics of tip growth are influenced by the abundance of the molecular components of the underlying machinery (Xing et al., 2017).

Actively growing root hairs show a polarized organization, which exhibits some similarities to other tip growing structures like pollen tubes or moss protonema. At the apex, the cytoplasm of root hairs is densely packed with vesicles that deliver new cell material to the growing tip (Sherrier and VandenBosch, 1994; Galway et al., 1997; Ketelaar et al., 2008; Ketelaar, 2013). Since this region is free from larger organelles it is called the clear zone. In contrast, the cytoplasm of the sub-apical region contains organelles like mitochondria, endosomes, Golgi bodies, endoplasmic reticulum (ER), ribosomes, actin and microtubule cytoskeleton and in older hairs also the nucleus (Carol and Dolan, 2002; Grierson et al., 2014). Root hair growth is driven by turgor pressure which is generated by the vacuole located throughout the root hair tube (Lew, 2004; Volgger et al., 2010). This polar organization of the cytoplasm dissipates as soon as the root hair stops growing and expansion of the vacuole into the hair tip leaves only a thin layer of cytoplasm (Miller et al., 1999). Similar to pollen tubes, root hairs exhibit an oscillatory gradient of cytosolic calcium ($[Ca^{2+}]_{cyt}$) at the tip (Wymer et al., 1997; Bibikova and Gilroy, 2002; Monshausen et al., 2008).

Due to their location at the surface of the root, trichoblast are easily accessible to visualization techniques, as well as chemical and mechanical manipulations. Root hairs are not essential for plant viability under laboratory conditions and therefore allow the study of many different kinds of mutants, that alter root hair development, function or positioning (Grierson et al., 2014). Additionally, trichoblasts are organized in cell files, originating from the root apical meristem close to the root tip. With increasing distance from the meristem, trichoblasts progress in development accompanied by cell elongation and hair outgrowth. Consequently, all trichoblasts of one such cell file are part of a

continuous developmental timeline, which allows us to investigate the entire process of root hair development simultaneously within one plant.

Initial root hair positioning is very robust and happens approximately 10 μm away from the root-tip-ward end of the cell. Interestingly, this position is kept constant even though, the cell body elongates perpendicular to the growing protrusion. This robustness and predictability of positioning allows to investigate initial steps of root hair development, even before any morphological changes are visible, making the root hairs of *A. thaliana* an excellent model system to study the initiation of polar growth and especially the aspect of site selection.

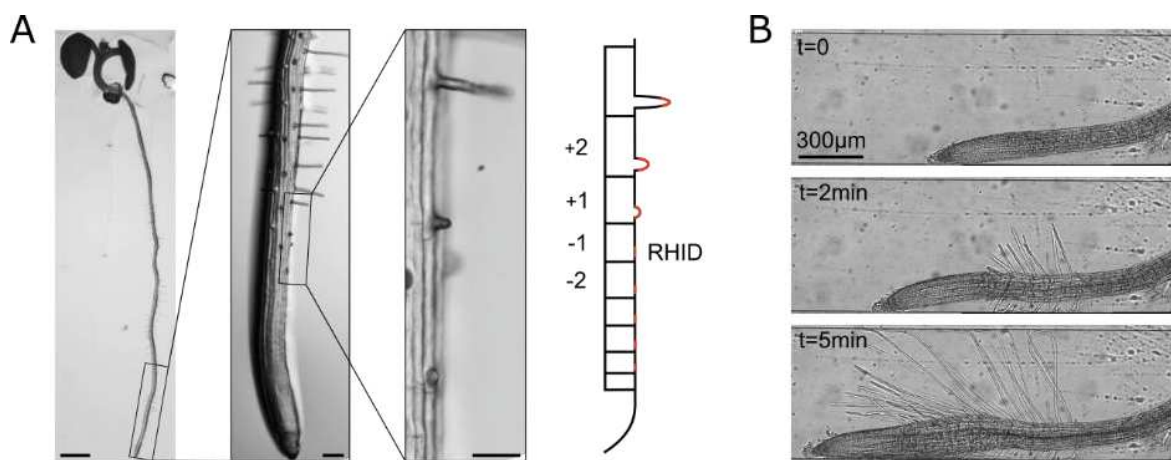


Figure 2: The Arabidopsis root hair system is a suitable model system to study the initiation of tip growth. (A) From left to right: Micrograph of an *Arabidopsis thaliana* seedling (scale bar = 1 mm), micrograph of the primary root tip of an Arabidopsis seedling (scale bar = 100 μm), magnified view of the previous micrograph depicting a trichoblast cell file including cell stages +1 to +3 (scale bar = 50 μm), schematic representation of a trichoblast cell file depicting the developmental time line and the nomenclature for cell stage determination: the first cell from the root tip that shows a bulge is named +1, younger cell are termed with increasing negative numbers. (B) Micrographs from a time lapse movie of a root grown in a microfluidic chamber showing the root hair growth response to the stop of flow (scale bar = 300 μm).

After selection of the position of the future root hair, proteins involved in polar tip growth are recruited to this root hair initiation domain (RHID), initiating, promoting and regulating hair outgrowth. Even though many studies on the regulation of root hair growth during later stages have been conducted, little is known about the initial steps during site selection. One of the first proteins known to localize to the RHID, already before hair outgrowth, is the small Rho-type GTPase RHO-OF-PLANTS 2 (ROP2) (Molendijk et al., 2001; Jones et al., 2002) – but the exact mechanism for RHID as well as for the site specific recruitment of ROP2 positioning is not yet fully understood.

4.1. ROP2 is a core component of the root hair growth machinery

In general, the Rho-family of small GTPases can be subdivided into three subfamilies according to their cellular function: RAC, CDC42 and RHO (Chant and Stowers, 1995; Hall, 1998). RHO-OF-PLANTS (ROPs), however, resemble a unique subfamily of Rho-type GTPases, as phylogenetic analysis have revealed that they are distinct from CDC42, RAC and RHO (Li et al., 1998; Zheng and Yang, 2000; Vernoud et al., 2003) and possess combined functions of RAC, CDC42 and RHO (Feiguelman et al., 2018). Furthermore, ROPs are regulated by plant specific ROPGEFs (Berken et al., 2005; Gu et al., 2006), ROPGAPs containing a CDC42-RAC-INTERACTING-BINDING (CRIB) (Wu et al., 2000) and RENGAPs (ROP1 ENHANCER GAPS) (Hwang et al., 2008).

The Arabidopsis genome encodes for 11 ROPs (Vernoud et al., 2003) which can be classified into two types, according to their posttranslational lipidations which in turn depends on their C-terminal sequence. Type I ROPs (ROP 1 to 8) contain a C-terminal CaaL-motif (C = cysteine, a = aliphatic amino acid, L = leucine), which is geranylgeranylated at the cysteine. This lipid moiety is added by PROTEIN GERANYLGERANYLTRANSFERASE 1 (PGGT1) and inserts into the membrane of the endoplasmic reticulum (ER) where the three last amino acids (“aaL”) of the ROP are proteolytically cleaved off (for example reviewed in Crowell, 2000; Crowell and Huizinga, 2009; Running, 2014; Wang and Casey, 2016). Proper lipidation is crucial for ROP2 function and thus root hair development, as mutations in the PGGT1 subunit PLURIPETALA (PLP) lead to loss of membrane attachment of ROP2 and shorter root hairs that are wider but grow less dense (Chai et al., 2016).

Type II ROPs (ROP 9 to 11) contain C-terminal GC-CG boxes (C = cysteine, G = glycine) in which the cysteine residues get S-acylated by PROTEIN S-ACYLTRANSFERASEs (PATs) (Lavy et al., 2002; Lavy and Yalovsky, 2006; Chamberlain and Shipston, 2015). Reversible S-acylation of type II ROPs also plays a role in root hair development, since loss of function mutants of PAT TIP GROWTH DEFECTIVE 1 (TIP1) show shorter root hairs that are wider than regular root hairs and also have a branching phenotype (Hemsley et al., 2005). This indicates redundancy of type I and type II ROPs in root hair development.

4.2. Proteins involved in regulating ROP activity

In Arabidopsis we find 14 ROPGEFs that all localize to the plasma membrane. They contain a catalytic PLANT-SPECIFIC ROP NUCLEOTIDE EXCHANGER (PRONE) domain that is only functional with ROPs but not with other Rho-type GTPases like CDC42, RhoA or RAS (Berken et al., 2005; Gu et al., 2006). In contrast to other GEFs, ROPGEFs are thought to act as dimers, since the PRONE domain was shown to homodimerize and bind to two ROP molecules (Thomas et al., 2007). The interaction between ROPs and ROPGEFs is believed to take place at the plasma membrane and may be regulated by phosphorylation of the GEF via RECEPTOR LIKE KINASES (RLKs) (Berken and Wittinghofer, 2008). In addition, the activity of the ROPGEF is regulated by the interaction of its C-terminus with the constitutively active PRONE domain (Berken et al., 2005; Gu et al., 2006).

Several ROPGEFs have been demonstrated to regulate ROP activity during tip growth in plant cells. ROPGEF1 and ROPGEF12 were shown to act in pollen development downstream of POLLEN RECEPTOR KINASE (PRK) signaling (Zhang and McCormick, 2007; Chang et al., 2013). ROPGEF4 and ROPGEF10 were found to act in regulating root hair elongation downstream of receptor-like kinase FERONIA (FER) signaling (Huang et al., 2013).

The Arabidopsis genome encodes for 6 ROPGAPS, which contain both a CDC42-RAC-INTERACTING-BINDING (CRIB)- and a GAP-domain (Wu et al., 2000). The CRIB-domain enhances the interaction between the GAP and the ROP and is therefore required for proper GAP activity (Wu et al., 2000; Schaefer et al., 2011), but also for its subcellular localization (Klahre and Kost, 2006). The GAP-domain of ROPGAP2 is crucial for GAP dimerization and the interaction with ROP molecules in a 2:2 ratio (Schaefer et al., 2011). ROPGAP1 is required for proper pollen tube growth by restricting the activity of ROP1 to the tip, accompanied by a tip focused organization of the actin cytoskeleton and directed tip growth (Fu et al., 2001; Hwang et al., 2010).

Another class of plant GAPs are the ROP1 ENHANCER GAPs (RENGAPs), which contain a pleckstrin homology (PH)-domain responsible for binding to phosphatidylinositols (PIPs) in addition to the GAP domain (Hwang et al., 2008). RENGAP1 (also called REN1) was shown to be involved in ROP1 polarity establishment, as the *ren1* mutant exhibited swollen pollen

tubes (Hwang et al., 2008). However, in root hair development no regulation of ROPs by GAPs has been described yet.

Unlike ROPGEFs and ROPGAPs, plant GUANINE DISSOCIATION INHIBITORS (GDIs) are very similar compared to mammalian RhoGDI homologues and contain a typical GDI domain (Bischoff et al., 2000). Structural analysis have revealed that the protein structure as well as the RhoGDI-Rho complex shows high similarities between plant and mammalian systems (summarized in for example Berken and Wittinghofer, 2008). The Arabidopsis genome encodes for 3 GDIs, amongst which RhoGDI1 / SUPERCENTIPIDE 1 (SCN1) was shown to be involved in root hair development: Loss of SCN1 results in the initiation of multiple hairs per trichoblast, an unpolar distribution of ROP2 and the isotropic production of reactive oxygen species (ROS) on the surface of hair cells (Carol et al., 2005).

The binding of RhoGDI and Rho-proteins under physiological conditions is dependent on a hydrophobic pocket in the RhoGDI and the C-terminal geranylgeranylation of the GTPase (Hoffman et al., 2000; DerMardirossian and Bokoch, 2005). This geranylgeranyl-anchor is also essential for the membrane association of type I ROPs. Since type II ROPs are not geranylgeranylated but their membrane association is facilitated by S-acylation, we may speculate that type II ROPs are also not regulated by RhoGDIs. Even though RhoGDI triple mutants are less fertile compared to wild type plants, they are still viable and able to produce seeds (Feng et al., 2016). This would indicate, that type I and type II ROPs act redundantly (Feiguelman et al., 2018).

4.3. Receptor-like kinases acting upstream of GEFs and ROPs

Translation of environmental stimuli into intracellular ROP signaling, requires the action of signaling peptides and their corresponding RECEPTOR-LIKE KINASEs (RLKs). For example, pollen tubes are guided to the ovules by LURE peptides (for example reviewed in Dresselhaus and Franklin-Tong, 2013; Higashiyama and Takeuchi, 2015), which in the case of AtLURE1 is sensed by several receptors, including the POLLEN-SPECIFIC RECEPTOR KINASE 6 (PRK6) (Takeuchi and Higashiyama, 2016; Wang et al., 2016). It was shown that PRK6 interacts with pollen specific ROPGEFs (ROPGEF 8, 9 and 12) and that the pollen tubes adjust their growth direction towards the LURE peptide (Takeuchi and Higashiyama, 2016), indicating the activation of downstream ROPs and the subsequent redirection of the

growth machinery. In root hairs, extracellular signals mediated by the peptide RAPID ALKALINIZATION FACTOR (RALF) were shown to be sensed by the RLK FER and translated into hair growth control by local protein synthesis of components of the tip growth machinery (amongst others also ROPs and ROPGEFs) (Zhu et al., 2020).

4.4. The role of the actin cytoskeleton in root hair growth

It was shown that the actin paralogue ACTIN 7 as well as the ACTIN INTERACTING PROTEIN 1-2 (AIP1-2) are involved in correct positioning of the ROP2 patch and with that in positioning of the root hair (Kiefer et al., 2015).

The actin network of the clear zone at the root hair apex is composed of a densely packed array of filamentous actin (termed F-actin) (Ketelaar et al., 2003), which consists of repeatedly branched actin filaments. To create and maintain such a mesh-like network, actin filaments constantly nucleate and depolymerize in a controlled manner. This modulation of F-actin mesh organization is facilitated by ROPs together with ROP-INTERACTIVE CRIB-CONTAINING PROTEINS (RICs) in response to growth signals (Wu et al., 2001). More specifically, it was shown in pollen tubes that ROP1 can interact with different RICs to differentially modulate the organization of the actin cytoskeleton (Gu et al., 2005).

F-actin nucleation is facilitated by the ACTIN RELATED PROTEIN (ARP) 2/3 complex, which adds actin to existing filaments in a fixed angle of 70° (Higgs and Pollard, 2001), consequently building up a branched actin mesh. In maize, ZmARP3 was found to localize to the plasma membrane of the root hair apex (Van Gestel et al., 2003). The ARP2/3 complex is activated by the SUPPRESSOR OF cAMP RECEPTOR (SCAR) / wiskott-aldrich syndrome protein family verprolin-homologous protein (WAVE) complex, which was shown to localize to membranes and to physically interact with ROP2 (Basu et al., 2004; Szymanski, 2005; Yanagisawa et al., 2013). Thus, ROP2 most likely has a direct impact on modulating the F-actin network at the root hair tip.

F-actin depolymerization on the other hand is controlled by ACTIN DEPOLYMERIZATION FACTORS (ADFs) or actin severing proteins like PLASMA MEMBRANE ASSOCIATED CALCIUM BINDING PROTEIN 2 (PCAP2) – also termed MICROTUBULE-ASSOCIATED PROTEIN 18 (MAP18) (Smertenko et al., 1998; Dong et al., 2001; Augustine et al., 2008; Kato et al., 2010; Zhu et al., 2013). The actin severing activity of ZmADF is enhanced by phosphorylation via

a CALCIUM-DEPENDENT PROTEIN KINASE (CDPK) (Smertenko et al., 1998; Allwood et al., 2001) and by ACTIN INTERACTING PROTEIN 1 (AIP1) (Staiger et al., 2010; Allwood et al., 2002) and is inhibited by the phosphoinositides phosphatidylinositol 4,5-bisphosphate (PIP2) and phosphatidylinositol 4-phosphate (PIP) (Gungabissoon et al., 1998). Therefore, actin depolymerization is sensitive to changing cytoplasmic $[Ca^{2+}]_{\text{cyt}}$ concentrations and changing lipid composition at the apical PM.

4.5. Root hair growth is controlled by $[Ca^{2+}]_{\text{cyt}}$ -ROS-ROP interplay

The growth of plant cells is driven by an internal pushing force from the vacuole, called turgor pressure, and is counterbalanced by physical restriction of the rigid cell wall. These two forces need to be under tight spatio-temporal control to enable directed growth of cells, like we find for example at the tip of a root hair. An essential component to regulate this interplay is the second messenger calcium ($[Ca^{2+}]_{\text{cyt}}$, cytosolic calcium ion) which together with ROPs acts in a feedback-loop controlling tip growth in general and root hair growth especially.

Active ROPs promote the increase of $[Ca^{2+}]_{\text{cyt}}$ (Kost et al., 1999; Li et al., 1999; Molendijk et al., 2001), which in turn inactivates ROPs by triggering their release from the PM, potentially via GDIs (Hwang et al., 2010; Wu et al., 2013; Himschoot et al., 2015). In pollen tubes, it was shown that this feedback loop leads to a periodic increase of $[Ca^{2+}]_{\text{cyt}}$ that follows on the oscillating activation of ROPs. In turn, this results in an equally oscillatory growth behavior of the pollen tubes (Hwang et al., 2005; Cárdenas et al., 2008). For root hairs, similar results could be reported, but direct evidence of oscillatory ROP activation is still lacking (Monshausen et al., 2008).

Besides its inhibitory effect on ROP activity, $[Ca^{2+}]_{\text{cyt}}$ activates nicotinamide adenine dinuclotide phosphate (NADPH) oxidases (in root hairs: ROOT HAIR DEFFECTIVE 2 (RHD2) – also called RESPIRATORY BURST OXIDASE HOMOLOG C (RBOHC)), which causes the production of reactive oxygen species (ROS) (Takeda et al., 2008; Kimura et al., 2012) as well as an alkalinization of the cell wall and simultaneous acidification of the cytosol (Monshausen et al., 2007, 2009). Apoplastic ROS and pH counteract each other: In regions with a low ROS concentration, the concentration of protons is high, resulting in a low pH, which is known to cause loosening of the cell wall. In regions with a high ROS concentration,

the concentration of protons is low, resulting in a high pH, which is known to cause stiffening of the cell wall. Interestingly, ROS accumulate in the shank region of the hair during root hair growth, but as soon as growth ceases, ROS accumulate at the hair apex (Monshausen et al., 2007). These results suggest that the cell wall is rigidified at the shank (ROS accumulation, high pH, low proton concentration) to prevent lateral expansion of the hair due to isotropic turgor pressure. Therefore, the internal pushing force is directed to the hair apex (little ROS, low pH, high proton concentration), where the cell wall is loosened (Monshausen et al., 2007, 2009; Haruta et al., 2015).

At the same time, in addition to stimulating ROS production which inhibits hair growth, $[Ca^{2+}]_{cyt}$ causes the depolymerization of F-actin via CDPK-dependent phosphorylation of ADF (Smertenko et al., 1998; Allwood et al., 2001), therefore further negatively impacting root hair growth. Additionally, ROS stimulates the influx of $[Ca^{2+}]$ from the apoplast, which in turn again inhibits ROPs and increases ROPGAP expression (Baxter-Burrell et al., 2002; Foreman et al., 2003). Inhibition of ROPs, however, leads to a decrease in $[Ca^{2+}]_{cyt}$ concentration, promoting the association of ROPs with the PM and the activation of downstream targets (Hwang et al., 2005; Monshausen et al., 2007). Taken together, $[Ca^{2+}]_{cyt}$, ROS and ROPs interact in multileveled feedback loops controlling F-actin organization and thus tip growth.

4.6. The role of membrane lipids during root hair growth

The tip of a growing root hair is a distinct microenvironment that differs from the rest of the cell – in terms of accumulation of specialized proteins as well as the composition of membrane lipids such as sterols and phosphoinositides (PIs). The former are thought to be important for hair growth as their sterical properties may lead to a curved membrane upon accumulation (Stanislas et al., 2015). The latter represent a group of regulatory lipids with low abundancy that are involved in cell polarity and general signaling in eukaryotic cells. PIs fulfill their regulatory function by either interacting with target proteins, by directly influencing membrane properties or by serving as precursors of signaling molecules (Heilmann, 2016). They contain an inositol ring that can be phosphorylated at different hydroxyl groups creating a set of different phosphatidylinositols (PtdIns). Different PtdIns have been shown to localize to membranes of distinct cellular compartments of plant cells

(Simon et al., 2014; Platre et al., 2018). At the PM of root hairs, phosphatidylinositol 4-phosphate (PI4P) and phosphatidylinositol 4,5-phosphate (PIP2) are most prominent.

Growing root hairs and pollen tubes show a tip-focused PIP2 gradient in the PM, which quickly dissipates as soon as growth stops (Kost et al., 1999; Dowd et al., 2006; Helling et al., 2006; Ischebeck et al., 2008, 2011; Zhao et al., 2010). PIP2 is locally synthesized by PHOSPHATIDYLINOSITOL 4-PHOSPHATE 5-KINASE 3 (PIP5K3), which polarizes at the root hair apex and phosphorylates PI4P to generate PIP2 (Kusano et al., 2008). PI4P in turn is locally brought into the membrane via a phosphatidylinositol transfer protein, CAN OF WORMS 1 (COW1) – also called SFH1, that binds to PIP2 (Böhme et al., 2004; Vincent et al., 2005). Local accumulation of PIP2 is required for proper root hair growth, as mutants of PIP5K3 and COW1/SFH1 have shorter hairs or hairs with disrupted morphology (Böhme et al., 2004; Kusano et al., 2008).

PIP2 acts as a second messenger in two ways: On one hand it serves as precursor of Phosphatidic acid (PA), diacylglycerol (DAG) and inositol 1, 4, 5-triphosphate (IP3), which have been reported to be involved in regulating $[Ca^{2+}]$ release from intracellular storages and actin polymerization (Cole and Fowler, 2006; Munnik and Nielsen, 2011; Heilmann et al., 2016). And on the other hand, PIP2 directly interacts with positively charged protein domains, like the polybasic region within ROPs (Cho and Stahelin, 2005; Do Heo et al., 2006; Zhao et al., 2010; Ischebeck et al., 2011) as well as the heterodimeric F-actin capping protein (CP), in that case influencing the organization of the actin cytoskeleton (Huang et al., 2006).

Taken together, ROPs integrate not only PIP2 signaling but also the organization of the actin cytoskeleton and $[Ca^{2+}]$ -signaling to locally promote and regulate polar cell growth. It follows that correct positional targeting is crucial, however little is known about the initial steps in site selection.

Chapter I

Polarization of the small Rho-type GTPase ROP2 at the root hair
initiation domain

What came first? The chicken or the egg?

1. Introduction

1.1. ROP2 protein structure

Even though ROP2 has been identified as a key player during tip growth, little is known about how the protein is recruited to the root hair initiation domain (RHID), how it is maintained there and how its activity is restricted to the future site of root hair growth. It remains unclear which intrinsic structural features of ROP2 are involved in these processes.

Like other members of the Ras-superfamily of small GTPases, ROPs consist of a C-terminal hypervariable region, which is involved in subcellular localization and an N-terminal catalytic G-domain through which interactions with nucleotides, regulators and effectors take place. Subcellular localization of ROPs is regulated by post-translational prenylation at their C-terminus and allows to classify them into two types (see General Introduction 4.1). Being a type I ROP, ROP2 is post-translationally prenylated by a geranylgeranyl residue at cysteine 192 (C192, Figure I- 1). This prenylation serves as a lipid-anchor and facilitates plasma membrane (PM) attachment, which is potentially further stabilized by an adjacent poly-basic region of 7 lysine residues and one arginine. This positively charged region within the protein is hypothesized to interact with the head groups of negatively charged lipids like phosphatidylserine (PS) or phosphatidylinositols (Won et al., 2006; Lavy and Yalovsky, 2006; Platre et al., 2019). Whether an interaction between negatively charged lipids and the positively charged polybasic region of ROP2 is involved in initiating or stabilizing the accumulation of ROP2 at the RHID is yet unclear and remains to be investigated.

Besides C192, ROP2 contains 3 additional cysteines (C8, C20, C157, Figure I- 1), that are hypothesized to be S-acylated (Feiguelman et al., 2018). For ROP6 (a type II ROP), it has been postulated that activation-dependent S-acylation stabilizes the interaction with the PM, is involved in recruitment of ROPs to membrane compartments and is required for proper GTPase function (Sorek et al., 2007, 2011). However, these studies have later been retracted due to figure manipulation and have been republished (Sorek et al., 2017). Whether the concept postulated holds true and whether transient S-acylation is involved in subcellular localization and polarization of ROP2 remains an open question in the field for now.

ROP2 binding of GTP/GDP and nucleotide hydrolysis is facilitated by amino acids of 5 conserved G-box motives (G1-G5) that are spread over the protein sequence (Figure I- 1) (Berken and Wittinghofer, 2008). Two mutations in G1 and G4 lock ROP2 in the active or inactive state, respectively: The mutation of a glycine (G14V) in G1 prevents GTP hydrolysis and locks ROP2 in the GTP-bound state, rendering the protein constitutively active (*rop2CA*, Figure I- 1). On the other hand, the mutation of an aspartic acid (D120A) in G4 locks ROP2 in the inactive, GDP-bound state. The block of GDP release causes a dominant negative effect, presumably by sequestering activating factors (Glotzer and Hyman, 1995; Berken and Wittinghofer, 2008) and ROP2 with the D120A mutation is termed dominant negative ROP2 (*rop2DN*, Figure I- 1). It has been shown, that *rop2CA* leads to an increased number of root hairs per trichoblast and that *rop2DN* has the opposite effect, namely a reduction in root hair initiation (Jones et al., 2002). These results indicate, that the recycling between the active and the inactive state is important for proper function of ROP2. Furthermore, it has been shown in yeast, that GDIs interact with GDP-bound Rho-type GTPases (Dovas and Couchman, 2005; Berken and Wittinghofer, 2008). Therefore, the activation cycle of Rho-type GTPases is accompanied by a cycling between the PM and the cytosol. Together, these findings suggest that ROP2 function in root hair development depends on the activity-based shuffling between the PM and the cytosol.

Close to G1 and G2, ROP2 contains two sequence motives called switch I and switch II (Figure I- 1). These are hypothesized to exhibit conformational changes, depending on whether GDP or GTP is bound, similar to what has been shown for the small GTPase from rice OsRAC1 (Kosami et al., 2014). These two switch domains are important for protein-protein interactions, as their conformational change fosters the interaction with effector proteins (Berken and Wittinghofer, 2008). Among those are ROP activity regulators like ROPGEFs, ROPGAPs and GDIs that interact with the N-terminus of ROPs (Figure I- 1).

Between G4 and G5, ROPs contain a Rho-specific sequence called Rho-insert domain (Figure I- 1). It forms a helical structure that is exposed at the surface of the protein and was shown to also change its conformation in an activity-dependent manner (Kosami et al., 2014). The Rho-insert domain is hypothesized to be involved in differential interaction with effector proteins (Feiguelman et al., 2018), like for example PRONE-GEFs (Thomas et al., 2007). However, its exact function is unknown and remains to be investigated.

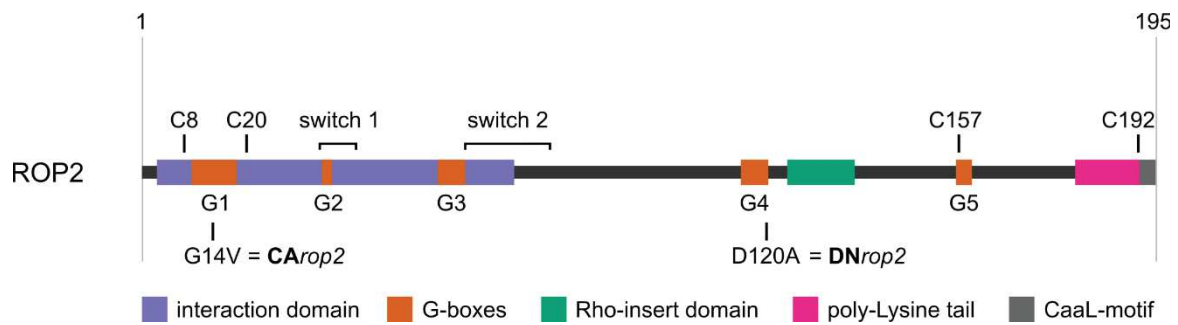


Figure I- 1: Schematic representation of the secondary protein structure of ROP2. ROP2 = full length ROP2, 195AA; G14V mutation leads to constitutively active ROP2 (*rop2CA*), D120A mutation leads to dominant negative ROP2 (*rop2DN*); amino acid abbreviations: G = glycine, V = valine, D = aspartic acid, A = alanine, C = cysteine.

1.2. Aim of Chapter I

ROP2 was described as one of the first proteins localizing at the RHID, early in root hair development even before morphological changes occur. The question how this small GTPase is polarized at the PM, maintains polar localization and how its activity is locally restricted is still not fully understood. Since ROP2 contains a positively charged poly-lysine tail at its C-terminus that is hypothesized to be involved in electrostatic interactions with negatively charged membrane lipids, I aimed to investigate the role of electrostatic interaction in ROP2 polarization at the RHID. Furthermore, I aimed to characterize additional protein domains within ROP2 with regard to their role in ROP2 polarization and function.

Molecular switches such as Rho-type GTPases need to be highly regulated to ensure their proper cellular function. Consequently, the spatial but also the temporal control of their activity cycle is of critical importance. For ROPs, it is postulated that the cycling between its active and its inactive state goes along with a re-localization of protein between the plasma membrane (PM) and the cytosol. It follows that the control of membrane association would be critical with regard to proper function and activation of down-stream factors. In addition, to ensure a locally restricted outgrowth at the RHID, the activity of ROP2 needs to be regulated locally as well. Therefore, I further aimed to investigate the role of ROP2 activity status on its polarization at the RHID, as well as on its association with the PM. During the course of this project, we were able to show that the guanine-nucleotide exchange factor GEF3 is necessary for ROP2 polarization via the ROP2 N-terminus. To better understand the underlying mechanism, I further investigated the effect of GEF3 on ROP2 membrane association and polarity.

2. Results

To characterize protein domains within ROP2 that are involved in protein polarization at the RHID and protein function, I analyzed fluorescently tagged ROP2 variants in regard to their subcellular localization in trichoblasts. As protein abundance is critical and can influence the localization of the fusion protein, it is critical to carefully control protein expression levels. To prevent pleiotropic effects due to overexpression of different modified ROP2 variants (Figure I- 2), their expression was controlled using an estradiol inducible promoter system. The results obtained were always compared to a plant line expressing the native ROP2-CDS under the control of the estradiol inducible promoter as well. Cells of the stages -1 and +1 (Note: the first cell from the root tip, that showed a bulge was termed +1; younger cells were named with increasing negative numbers; see also Figure 2, page 22) were investigated to assess the functional impact of structural features of ROP2 prior to and after bulging. To minimize the effect of abundant protein levels on subcellular protein localization, the induction time was kept as short as possible, but as long as necessary to measure fluorescent intensity.

In the following subchapters the polarity index and the membrane association for various ROP2 variants were determined by analyzing image stacks obtained by fluorescent microscopy. The method used is described in detail in the Material and Methods chapter. In brief, the mean fluorescent intensity in a small ROI at the plasma membrane (PM) of the RHID was divided by the mean fluorescent intensity of the PM outside the RHID to obtain the polarity index (Figure I- 3). Membrane association was determined by dividing the mean fluorescent intensity at the PM by the mean fluorescent intensity in a ROI placed directly underneath it and within the cytosol (Figure I- 3). It should be noted that, due to the optical resolution of the microscope used, the ROI for the PM includes not only the membrane, but also a cytosolic fraction.

Part of this work was published in Denninger et al. (2019), however, all data presented in this thesis has been newly acquired to ensure comparability to the respective controls.

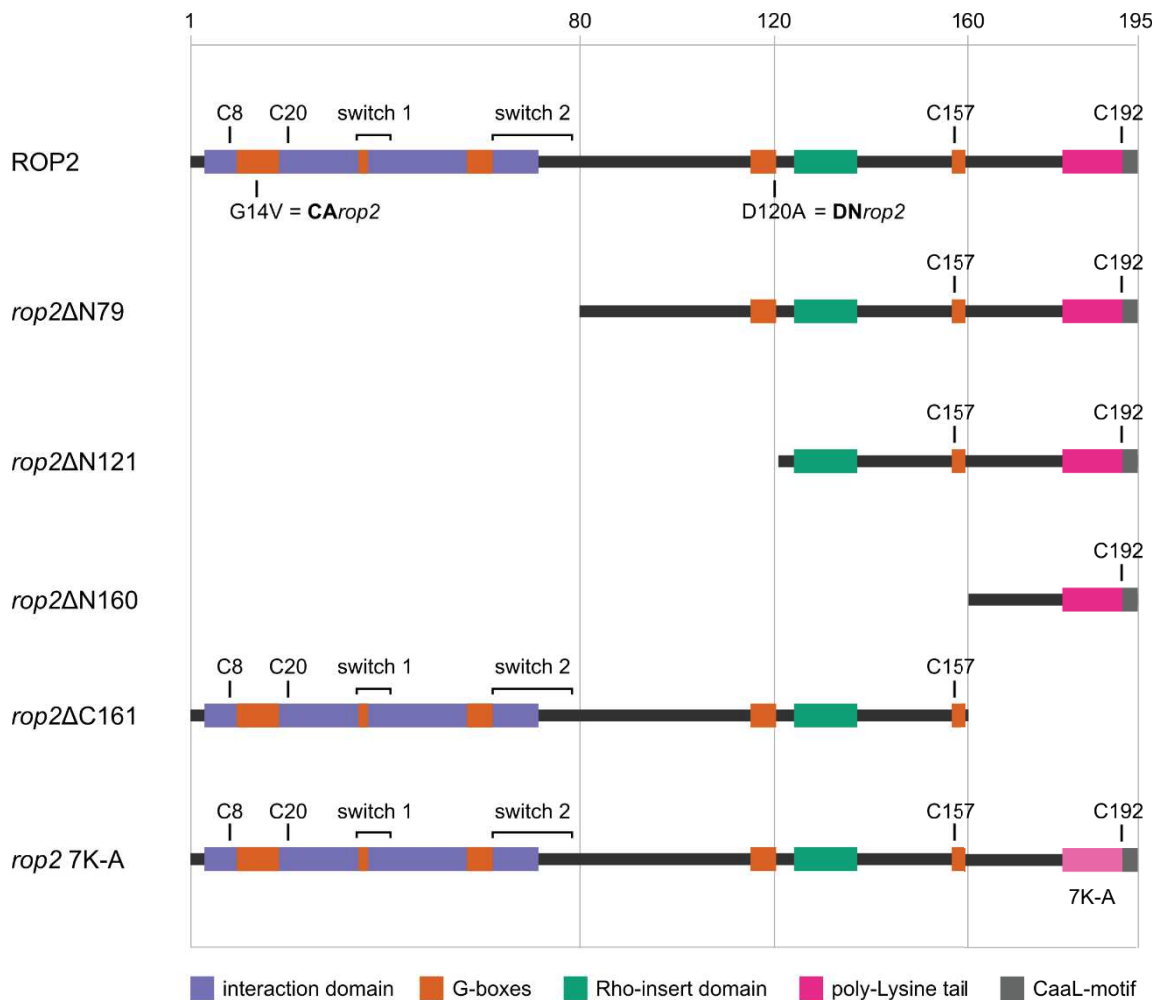


Figure I- 2: Schematic representation of the secondary protein structure of ROP2 and the ROP2 deletion variants investigated in this chapter. ROP2 = full length ROP2, G14V mutation leads to constitutively active (CA) ROP2, D120A mutation leads to dominant negative (DN) ROP2; *rop2ΔN79* = deletion of the first 79 AA of the N-terminus of ROP2; *rop2ΔN121* = deletion of the first 120 AA of the N-terminus of ROP2; *rop2ΔN160* = deletion of the first 160 AA of the N-terminus of ROP2; *rop2ΔC161* = deletion of the last 35 AA of the C-terminus of ROP2; *rop2 7K-A* = full length ROP2 in which the 7 lysines of the poly-lysine tail are substituted by alanines.

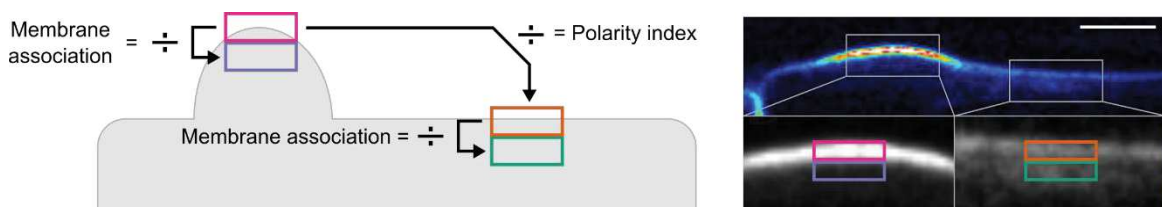


Figure I- 3: Schematic showing the calculations for the polarity index and membrane association. On the left side, a schematic trichoblast cell illustrates the relation of individual ROIs for each of which the mean fluorescent intensity was measured. On the right side an example image of a fluorescent marker line is shown: Close-up views of indicated regions including ROIs with the original scaling of 15x3 px. Scale bar represents 10 μm .

2.1. Are electrostatic interactions between anionic lipids in the PM of the RHID and ROP2 involved in ROP2 polarization?

It has been shown, that interactions between anionic (negatively charged) lipids and polybasic (positively charged) protein domains are involved in targeting proteins into distinct membrane domains. This raises the hypothesis that electrostatic interactions between anionic lipids and the poly-lysine tail of ROP2 might be involved in ROP2 polarization at the RHID. If this was true, I would expect to find an accumulation of anionic lipids at the RHID and I would further expect that a ROP2 variant, in which the poly-Lysine tail was mutated does no longer accumulate at the RHID.

To investigate the first expectation, if anionic lipids accumulate at the RHID prior to and after root hair bulging, I analyzed lipid reporter lines designed to indicate the localization of phosphatidylserine (PS) and phosphatidylinositol 4-phosphate (PI(4)P). These plant lines were kindly provided by Yvon Jaillais (ENS, Lyon). The PS reporter was observed to be unpolar at the cell stages -1 and +1 and in addition did not show a strong association with the PM inside the RHID (in comparison to ROP2) in either of the two developmental stages (Figure I- 4). This is in line with a report that PS shuffles between endosomes and the cytosolic leaflet of the PM (Platre et al., 2018). It is possible that the higher cytosolic signal, caused by endosomes might interfere with the analysis and may reduce the value of the membrane association inside the RHID to an extent, where it does not differ significantly from the cytosolic control mCitrine. In contrast, outside the RHID, the membrane association seemed to be higher, but the difference was not statistically significant. For the fluorescent reporter for PI(4)P I have observed a strong accumulation with the PM, but could not see polar accumulation in either of the two developmental stages. In a parallel PhD-thesis, Philipp Denninger could show, that the negatively charged lipid Phosphatidylinositol 4,5-bisphosphate (PIP2) polarizes at the RHID in cell stage +1 (Denninger et al., 2019).

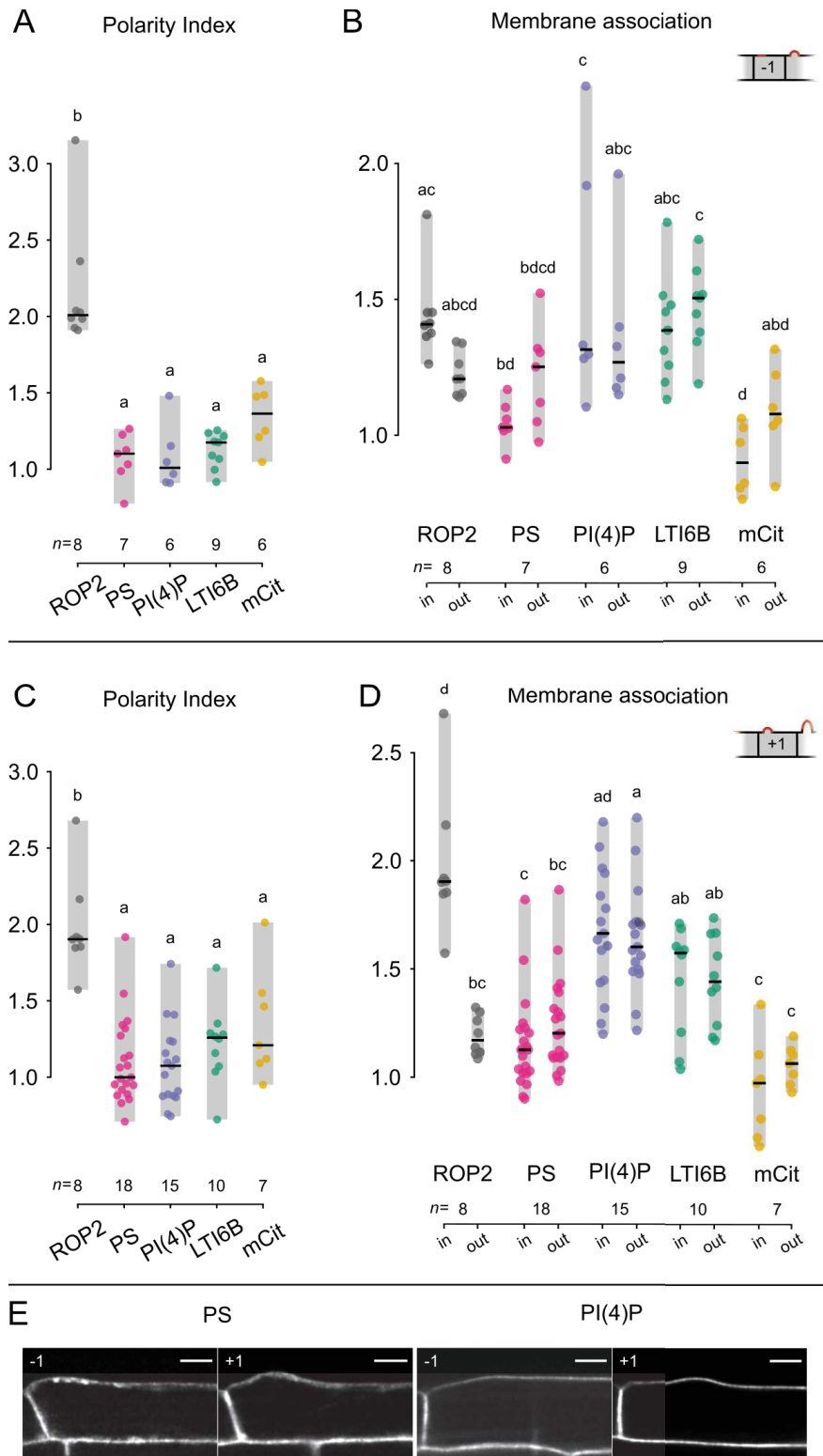


Figure I- 4: The anionic lipids PS and PI(4)P do not polarize at the RHID. Polarity index of ROP2, a sensor for phosphatidylserine (PS), a sensor for phosphatidylinositol 4-phosphate (PI(4)P), LTI6B and mCitrine (mCit) at cell stage -1 (A) and $+1$ (C). Membrane association of ROP2, PS, PI(4)P, LTI6B and mCit inside (in) and outside (out) of the RHID at cell stage -1 (B) and $+1$ (D). Cell stage is indicated by the cartoon. Center lines represent median values, gray boxes represent the data range, n indicates the number of cells measured and letters represent the result of an ANOVA-Tukey test (significance value = 0.01; same letters indicate no significant difference). (E) representative images of PS and PI(4)P at the indicated cell stages. The scale bar represents 10 μm , the root tip is located to the left side of the cells shown. Cartoons indicate the respective cell stage.

Taken together, the results presented here show no accumulation of the investigated lipids (PS and PI(4)P) at the RHID prior to or just after bulging. ROP2 polarization seemed to be independent of the anionic lipids PIP2 (Denninger et al., 2019), PS and PI(4)P. However, these results require further testing, as the fluorescent reporters can only bind to lipids, that are freely accessible. Accessibility however might be reduced or inhibited due to protein-lipid interactions (for example with ROP2) and therefore lipids might not be visible even though they would be present already earlier than described. To further investigate the hypothesis that electrostatic interactions are involved in ROP2 polarization at the RHID, plants without or with reduced levels of the respective lipids could be tested for ROP2 localization. However, since these plants often show pleiotropic phenotypes, I next analyzed a ROP2 variant with a mutated poly-lysine tail instead.

2.2. How do the N- and the C-terminus of ROP2 affect its polarization at the RHID?

At their C-terminus ROPs contain a CaaL-motif, which is post-translationally geranylgeranylated, and a polybasic region consisting of a poly-lysine tail. The geranylgeranyl-anchor is involved in regulating the membrane association of the small GTPase by facilitating the attachment to the PM and by binding to GDIs, which in turn keep the protein solubilized in the cytosol. The poly-lysine tail of ROPs are hypothesized to be involved in electrostatic interactions with anionic lipids. For ROP6, this was already shown to be important for proper ROP signaling (Platre et al., 2019).

To investigate to which extend the C-terminus of ROP2 is involved in ROP2 polarization, I analyzed ROP2 variants that either lacked the C-terminus (*rop2* Δ C161), only consist of the C-terminus (*rop2* Δ N160) or contain mutations within the C-terminal poly-lysine tail (*rop2* 7K-A, all 7 lysines are substituted by alanines). Furthermore, to investigate whether the polybasic tail alone is sufficient for polarization at the RHID, I analyzed plant lines expressing a peptide consisting of 8 lysine residues and a CaaX motif that is post-translationally farnesylated. Plant lines expressing this “8K-Farn” construct were kindly provided by Yvon Jaillais (ENS, Lyon) (Simon et al., 2016).

ROP2 variants either lacking the C-terminus (Δ C161) or with a substituted poly-lysine tail (7K-A) showed a reduced association with the PM and hence an unpolar distribution within

the cytosol (Figure I- 5). Besides the mutated poly-lysine tail, the *rop2* 7K-A variant still contains all domains required for protein function. To assess whether the *rop2* 7K-A protein was functional, I investigated its ability to rescue the reduced root hair density and delayed initiation phenotype of the *rop2-rop4* double mutant. Plants of this potential rescue line did not show an enhanced root hair growth 24 h after induction of the *rop2* 7K-A-construct, suggesting that the protein was not functional and that membrane association is a prerequisite for proper ROP2 function.

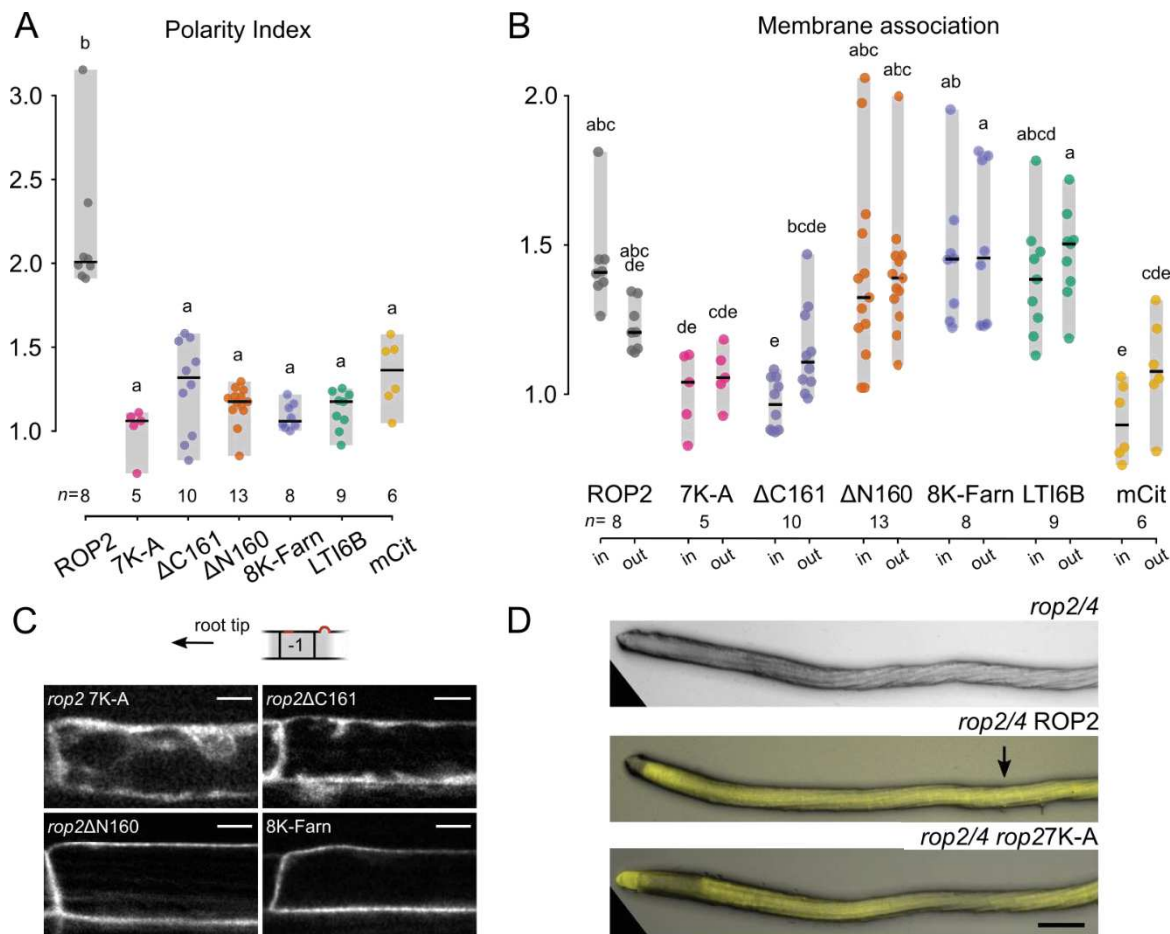


Figure I- 5: The C-terminus of ROP2 is required, but not sufficient for its polarization at the RHID. (A) Polarity index of ROP2, *rop2* 7K-A (7K-A), *rop2* Δ C161 (Δ C161), *rop2* Δ N160 (Δ N160), a Farnesyl-Anchor with 8 lysines (8K-Farn), LTI6B and mCitrine (mCit). **(B)** Membrane association of ROP2, 7K-A, Δ C161, Δ N160, 8K-Farn, LTI6B and mCit inside (in) and outside (out) of the RHID. Center lines represent median values, gray boxes represent the data range, n indicates the number of cells measured and letters represent the result of an ANOVA-Tukey test (significance value = 0.01; same letters indicate no significant difference). All measurements were performed in cells of the developmental stage -1. Measurements for ROP2, LTI6B and mCit are shown for comparability, but are the same as already presented in Figure I- 4. **(C)** Representative images of 7K-A, Δ C161, Δ N160 and 8K-Farn. The root tip is located to the left side of the cells shown. The scale bar represents 10 μ m. Cartoon indicates the respective cell stage and orientation **(D)** Micrographs of potential *rop2/4* rescue lines, either expressing full length ROP2 (middle panel) or the *rop2* 7K-A (lower panel). Arrows indicate the first detectable bulge. The scale bar represents 300 μ m.

ROP2 lacking the N-terminus ($\Delta N160$), as well as the “8K-Farn” did not show polar accumulation at the RHID, but strong association with the PM (Figure I- 5), indicating that membrane anchorage and a poly-lysine tail alone are not sufficient for protein recruitment to the RHID and that the N-terminus is involved in ROP2 polarization. Furthermore, these results indicate, that electrostatic interactions between the poly-lysine tail of ROP2 and anionic lipids in the PM of the RHID, are indirectly involved in ROP2 polarization by regulation its association with the PM. This leads to the hypothesis, that electrostatic interactions may be involved in stabilizing the ROP2 patch once it has been initiated and to facilitate downstream signaling.

To assess which part of the N-terminus is involved in protein polarization and membrane attachment, I analyzed variants of ROP2 containing subsequent N-terminal deletions with increasing length. Plant lines expressing these deletions have been generated by Philipp Denninger. All investigated N-terminal deletion variants of ROP2 lacked the interaction domain, known to be involved in interaction with up- and downstream factors (Feiguelman et al., 2018).

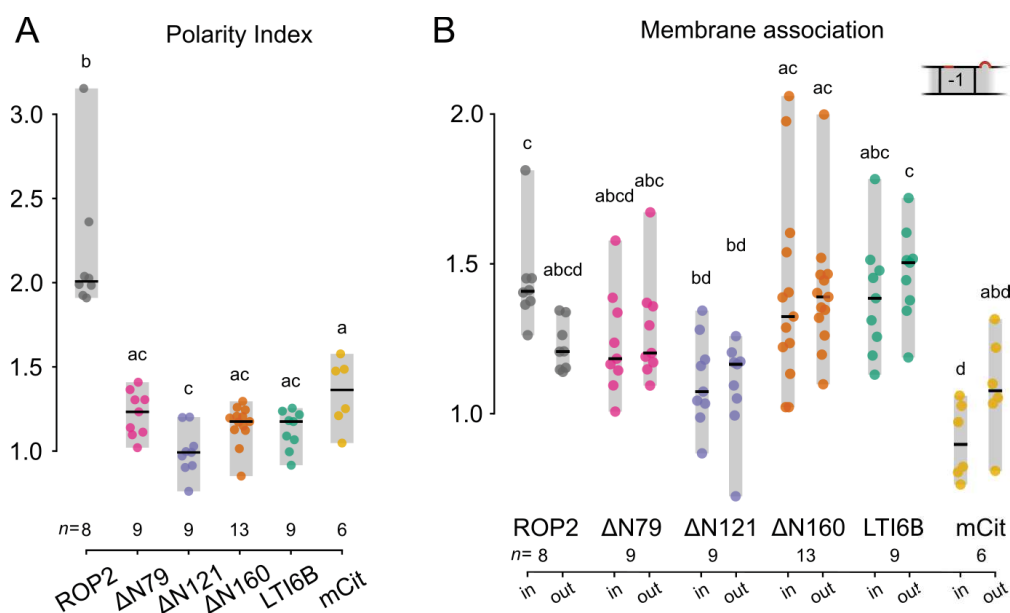


Figure I- 6: The N-terminus of ROP2 is involved in its polarization at the RHID. (A) Polarity index of ROP2, *rop2* $\Delta N79$ ($\Delta N79$), *rop2* $\Delta N121$ ($\Delta N121$), *rop2* $\Delta N160$ ($\Delta N160$), LTI6B and mCitrine (mCit). **(B)** Membrane association of ROP2, $\Delta N79$, $\Delta N121$, $\Delta N160$, LTI6B and mCit inside (in) and outside (out) of the RHID. Center lines represent median values, gray boxes represent the data range, n indicates the number of cells measured and letters represent the result of an ANOVA-Tukey test (significance value = 0.01; same letters indicate no significant difference). All measurements were performed in cells of the developmental stage -1. Cartoon indicates the respective cell stage. Measurements of ROP2, $\Delta N160$, LTI6B and mCit are shown for comparability, but are the same as already presented in Figure I- 4 and -5.

A loss of polar accumulation at the RHID was observed for all N-terminal deletion variants, however they differed in the degree of association with the plasma membrane (Figure I-6). As previously mentioned, *rop2* Δ N160 showed a strong accumulation with the PM. In comparison, *rop2* Δ N121 showed a significant reduction in membrane association while for *ROP* Δ N79, PM association was in between the values observed for the two other deletion constructs and did not differ significantly from either of them. Even though differences between these deletion constructs were subtle, the results point towards a tendency for the two longer constructs (Δ N79 and Δ N121) to be more cytosolic than the shorter construct (Δ N160), giving rise to the hypothesis, that the region between amino acid 80 and 160 might negatively impact on membrane association.

Taken together, the data presented here shows, that the C-terminus of ROP2 is necessary, but not sufficient for polarization at the RHID. Furthermore, it can be concluded that the association with the PM is a prerequisite for protein function and polarization. Additionally, we can say that the N-terminus of ROP2 is involved in its polar recruitment to the RHID and that association with the PM might be differentially influenced by a protein sequence between amino acids 80 and 160.

2.3. Is the polarization of ROP2 at the RHID influenced by its activity state?

I have previously shown that association with the PM is a prerequisite for ROP2 polarization. Since the activity cycle of ROPs is postulated to be accompanied by a shuttling between the PM and the cytosol, I have investigated, whether the activity status of ROP2 has an influence on its localization at the RHID. To this end I analyzed constitutively active (CA) and dominant negative (DN) variants of ROP2 with regard to their accumulation at the RHID and their association with the plasma membrane inside and outside of the RHID (Figure I-7). The plant lines either expressing full-length ROP2, *rop2*CA or the *rop2*DN construct have been generated by Philipp Denninger.

Full-length ROP2 protein exhibited a polar accumulation at the RHID (Figure I-7 A) and its association with the PM outside the RHID was lower than inside the RHID (Figure I-7 C), pointing towards a mechanism in which differential membrane association might be involved in protein polarization. Compared to ROP2 at the RHID, *rop2*DN showed a reduced

association with the PM inside, as well as outside the RHID. In comparison to ROP2 outside the RHID however, the PM association of *rop2DN* was not significantly different. Besides the reduced association with the PM, *rop2DN* was distributed evenly and lacked polar accumulation at the RHID. Only after excessive induction (for longer than 10 h) fluorescent signal for the mCitrine-*rop2DN* could be detected and the plants showed a reduction in bulges and a delay in root hair initiation.

For *rop2CA*, the opposite result was obtained: Here, the protein mainly associated with the PM (which was similar to the behavior of ROP2 inside the RHID but different from ROP2 outside the RHID; Figure I- 7 C) and in addition, did not show any polar accumulation (Figure I- 7 A). The expression of *rop2CA* led to strong phenotypes already 3 to 4 h after induction, such as shifted bulges or wider bulges, sometimes spanning the whole cell surface.

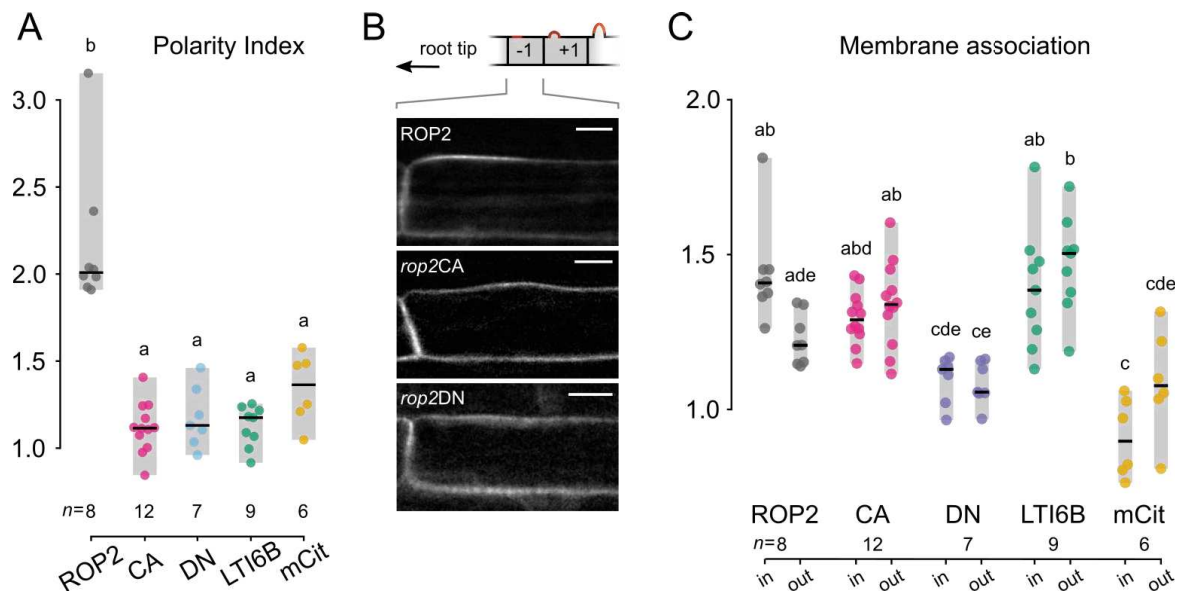


Figure I- 7: The activity status of ROP2 influences its polarization and association with the plasma membrane. (A) Polarity index of ROP2, constitutively active *rop2* (CA), dominant negative *rop2* (DN), LTI6B and mCitrine (mCit). (B) Representative images of ROP2, *rop2CA* and *rop2DN*. The root tip is located to the left side of the cells shown. Cartoon indicates the respective cell stage. The scale bar represents 10 μ m. (C) Membrane association of ROP2, CA, DN, LTI6B and mCit inside (in) and outside (out) of the RHID. Center lines represent median values, gray boxes represent the data range, n indicates the number of cells measured and letters represent the result of an ANOVA-Tukey test (significance value = 0.01; same letters indicate no significant difference). All measurements were performed in cells of the developmental stage -1. Measurements of ROP2, LTI6B and mCit are shown for comparability, but are the same as already presented in Figure I- 4.

Taken together, these results show that the activity status of ROP2 is important for its association with the PM and that proper activity regulation is required to ensure local outgrowth at the RHID. Furthermore, the differential association with the PM in- and outside the RHID points towards a local activation of ROP2.

2.4. Is GEF3 involved in ROP2 polarization by regulating ROP2 membrane association?

As we have recently shown that the GUANINE NUCLEOTIDE EXCHANGE FACTOR 3 (GEF3) is necessary and sufficient for ROP2 polarization at the RHID and in ectopic RHID-like membrane domains (Denninger et al., 2019), I wanted to further investigate the underlying mechanism. Therefore, I determined the polarity index, as well as the association with the PM for ROP2 in the *gef3-1* mutant background. This plant line was generated by Philipp Denninger and harbors a ROP2-CDS mCitrine fusion construct under the control of the endogenous ROP2 promoter. The measurements presented in this thesis were performed in the fourth and fifth filial generation (F4 and F5), whereas earlier measurements by Philipp Denninger were performed in the F3. Homozygosity for the T-DNA insertion disrupting the *GEF3* gene was verified by genotyping PCR in the F4.

Prior to bulging, at cell stage -1, ROP2 showed a statistically significant loss of polarity at the RHID, which was comparable to the result described for *rop2ΔN79* and is in line with previously published results (Figure I- 8 A). The membrane association of ROP2 in the *gef3-1* mutant background was not statistically different from ROP2 inside the RHID and the protein can be considered as PM associated (Figure I- 8 B). Furthermore, the difference in association with the PM for ROP2 in the *gef3-1* mutant background, inside and outside the RHID, was statistically not significant, but showed a tendency towards a lower association outside of the RHID. Additionally, the measurements for outside of the RHID showed no significant difference compared to the cytosolic control mCitrine, which is in contrast to the measurements for inside the RHID.

In bulged cells of the stage +1, ROP2 in the *gef3-1* mutant background showed a reduction in polarity, which however was not statistically significant compared to ROP2 in the wild type background (Figure I- 8 C). This finding is contradicted by the previously published results from our lab (Denninger et al., 2019).

Besides the reduced polarity, ROP2 in the *gef3-1* mutant background showed a reduced association with the membrane inside the RHID, in comparison to ROP2 in wild type background (Figure I- 8 D). Outside the RHID however, the membrane association of ROP2 in the *gef3-1* mutant background was not significantly different from ROP2 in the wild type

background. Additionally, a comparison to the PM control LTI6B, also did not show a statistically significant difference, pointing to a reduced but not complete abolished association with the PM.

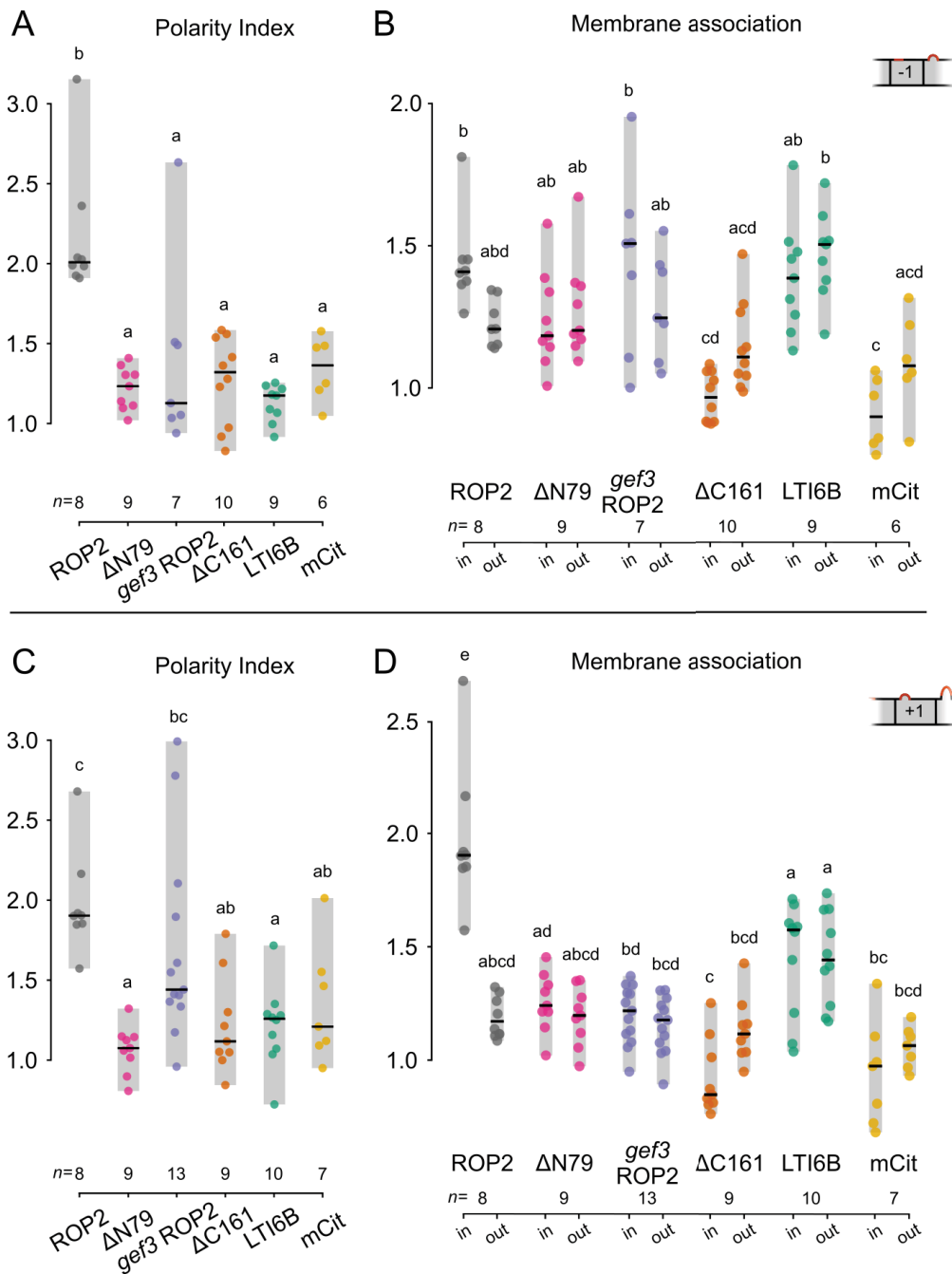


Figure I- 8: The N-terminal interaction domain is involved in GEF3-dependent ROP2 polarization at the RHID. Polarity index of ROP2, *rop2* $\Delta N79$ ($\Delta N79$), ROP2 in the *gef3-1* mutant background (*gef3-1* ROP2), *rop2* $\Delta C161$ ($\Delta C161$), LTI6B and mCitrine (mCit) at cell stage - 1 (A) and + 1 (C). Membrane association of ROP2, $\Delta N79$, *gef3-1* ROP2, $\Delta C161$, LTI6B and mCit inside (in) and outside (out) of the RHID at cell stage - 1 (B) and + 1 (D). Center lines represent median values, gray boxes represent the data range, n indicates the number of cells measured and letters represent the result of an ANOVA-Tukey test (significance value = 0.01; same letters indicate no significant difference). Cartoons indicate the respective cell stages. Measurements of ROP2, $\Delta N79$, $\Delta C161$, LTI6B and mCit are shown for comparability, but are the same as already presented in Figure I- 4, -5 and -6.

Taken together, the results shown indicate that the loss of ROP2 polarity prior to bulging does not go along with a loss of membrane association. It can therefore be concluded, that the association of ROP2 with the PM is independent of GEF3 and that GEF3-dependent polarization is either mediated by differential sorting in the PM or by local recruitment from a cytoplasmic pool. After bulging however, ROP2 could partially restore its polar accumulation at the RHID and showed a reduced association with the PM. This result may point towards an additional GEF3-independent polarization mechanism.

3. Discussion

ROP2 is a central player in root hair development and was shown to polarize at the root hair initiation domain (RHID) prior to root hair outgrowth (Jones et al., 2002). It regulates downstream factors including the actin cytoskeleton, the microtubule network, vesicle trafficking or the production of reactive oxygen species (Feiguelman et al., 2018). As a member of the Ras super-family of small G-proteins, ROP2 functions as a molecular switch: It undergoes conformational changes upon GTP-binding and -hydrolysis, leading to differential interactions with effectors and regulators. To ensure the locally restricted outgrowth of a root hair, ROP2 function and its interaction with downstream factors needs to be locally restricted as well and needs to be carefully controlled.

Even though a lot of studies have been conducted to understand the function of ROP2 in regulating root hair growth, little is known about the initial steps of RHID site selection. In this thesis, I aimed to gain further knowledge on the mechanism of ROP2 polarization at the RHID. I have investigated the role of the activity status of ROP2, ROP2 intrinsic protein domains and the role of electrostatic interaction between ROP2 and lipids of the plasma membrane at the RHID.

3.1. Membrane association is a prerequisite for ROP2 polarization

Close to its C-terminus ROPs contain a polybasic tail consisting of 7 lysine and 1 arginine residue. Other proteins with such a negatively charged region within the protein have been shown to interact with anionic (negatively charged) lipids. Such electrostatic interactions were further shown to be involved in recruiting proteins with polybasic regions into membrane domains (Cho and Stahelin, 2005; Do Heo et al., 2006; Zhao et al., 2010; Ischebeck et al., 2011). For ROPs specifically, it has been shown that electrostatic interactions between the GTPase and membrane lipids are not only involved in the regulation of protein function, but also in correct subcellular targeting (Platre et al., 2019). Therefore, I investigated the hypothesis that electrostatic interactions between the poly-lysine tail of ROP2 and negatively charged lipids in the plasma membrane (PM) may be involved in recruitment of ROP2 to the RHID. To this end, I first analyzed whether fluorescent reporters for the anionic lipids phosphatidylserine (PS) and phosphatidylinositol 4-phosphate (PI(4)P) show a polar pattern at the RHID prior to bulging

of the root hair. In a second approach I analyzed a ROP2 variant in which the lysine residues were substituted by alanines (*rop2* 7K-A, Figure I- 2), abolishing the potential of the protein to undergo electrostatic interactions.

Both lipids sensors did not show polar accumulation at the RHID prior to or after bulging (Figure I- 4). Our lab has been able to show that another anionic lipid, phosphatidylinositol (4,5)-bisphosphate (PIP2), accumulates at the RHID prior to bulging, however only one developmental cell stage later than ROP2 (Denninger et al., 2019). These results led to the conclusion, that electrostatic interactions between PS, PI(4)P, PIP2 and ROP2 are unlikely to be involved in initial ROP2 recruitment. It needs to be mentioned however, that since the lipid reporters indicate the presence of the respective lipid by binding to it, we can only detect freely available and thus unbound lipids. It could be, that the lipids accumulate in much earlier developmental stages and could not be detected at cell stages -1 and +1 since they are not freely available but are already bound by proteins (for example by ROP2).

Another approach would be to substitute the polybasic tail of ROP2 by uncharged amino acids (*rop2* 7K-A). Using this approach, I could show, that the *rop2* 7K-A protein did not associate with the PM and that it also did not accumulate at the RHID (Figure I- 5), indicating that the polybasic tail of ROP2 is involved in proper association with the PM. In addition, I could demonstrate that *rop2* 7K-A was not able to complement the delayed hair initiation phenotype of the *rop2/4* double mutant (Figure I- 5, D). I could further show, that ROP2 without its C-terminus, and thus without a membrane anchor, does not polarize at the RHID (Figure I- 5, A). Furthermore, I could show that a farnesylated polybasic tail (8K-Farn) or the C-terminus of ROP2 (*rop2*ΔN160) alone are not sufficient for polarization at the RHID (Figure I- 5, A). Taken together, these results led to the conclusion that the polybasic tail of ROP2 as well as its association with the PM are necessary, but not sufficient for ROP2 polarization and function. These findings are supported by previous reports from yeast, where it was shown that the polybasic region of the small GTPase CDC42 is not sufficient for polarization, but is required for membrane attachment (Richman et al., 2002, 2004).

Even though, we were not able to detect PIP2, PS or PI(4)P at the RHID prior to ROP2 polarization, all data regarding the polybasic tail of ROP2 point towards an involvement of electrostatic interactions between ROP2 and anionic lipids at the RHID in root hair development. Whether these electrostatic interactions are involved in ROP2 recruitment

or whether they are involved in stabilizing ROP2 at the root hair apex remains unanswered. In an attempt to more closely investigate the role of PIP2 (which polarizes at the RHID) on ROP2 recruitment I aimed to investigate plants with reduced PIP2 levels. Since genetic manipulation, but also chemical treatments lead to a plethora of side effects, I decided to use an inducible promoter driving a PIP2 specific phosphatase *in planta*. For this, I chose SUPPRESSOR OF ACTIN 9 (SAC9) from *Arabidopsis thaliana* (Williams et al., 2005) and attempted to generate plant expression vectors, which however was ultimately not successful. In the meantime, the groups of Yvon Jaillais and Marie-Cécile Caillaud were able to create a similar system in *Arabidopsis* by using the phosphatase domain of the *Drosophila melanogaster* protein DmOCRL (iDePP; Doumane et al., 2020). With this tool in hand, it would be interesting to investigate to which extent ROP2 recruitment to the RHID is influenced by the presence of PIP2. Additionally, this system would allow to investigate whether the ROP2 domain at the RHID is stabilized by electrostatic interactions with PIP2. Since membrane association of ROP2 is critical for its function as a key regulator in root hair development, I further investigated protein domains within ROP2 in regard to their role in polarization and association with the PM at the RHID. I found that the N-terminus of ROP2 is necessary for its accumulation at the RHID, potentially by mediating the interaction with effectors – which will be discussed to some extent later in this chapter. By comparing ROP2 variants with deletions of variable length within the N-terminus, I found a tendency for the longer constructs to be more cytosolic than the shorter constructs ($\Delta N79$ and $\Delta N121$ compared to $\Delta N160$: see Figure I- 6, B). This result raised the hypothesis that the region between amino acids 80 and 160 might be involved in regulating PM association. Like all proteins of the Rho-family, ROP2 contains a Rho-insert domain between amino acids 124 and 137 (Figure I- 1). Even though the presence of an insert domain is conserved among ROPs, its sequence and length differs, giving rise to the hypothesis that the insert domain might mediate effector specificity (Berken and Wittinghofer, 2008). For AtROP4 it was shown that the insert domain is involved in binding to the PRONE domain of ROPGEFs (Thomas et al., 2007). Additionally it has been shown, that the conformation of the insert domain changes depending on which nucleotide is bound (Kosami et al., 2014). As we have shown, that ROP2 polarization is dependent on the presence of GEF3 and that interaction of the two occurs via the ROP2 N-terminus (Denninger et al., 2019), it would be interesting

to test if the subtle differences in membrane association that I have observed for truncated ROP2 variants, might reflect a role of the insert domain in regulating ROP2 membrane association. Therefore, I have started cloning further truncation constructs of ROP2, where either the whole insert domain or parts of it were deleted. Together with linker-substitutions of the insert domain, these constructs may serve as a basis for future studies that will help to elucidate the role of the insert domain.

3.2. Local activation of ROP2 at the RHID

Spatio-temporal control of ROP2 activity is a prerequisite for positioning of the root hair growth machinery and thus proper root hair growth. Being molecular switches, small GTPases such as ROPs undergo a constant cycle of activation and inactivation, which is accompanied by a shuffling between the PM and the cytosol. With the data presented in this thesis, I could further confirm that the GDP-bound form of ROP2 (represented by *rop2DN*) is predominantly cytosolic, whereas GTP-ROP2 (represented by *rop2CA*) is strongly associated with the PM (Figure I- 7, B). However, both activity variants did not show a polar association with the RHID (Figure I- 7, A). Full length, unmutated transgenic ROP2, which is a mix of GTP-bound ROP2 and GDP-bound ROP2 has a higher membrane association inside the RHID compared to outside the RHID (Figure I- 5, A), from which we can conclude that the pool of ROP2 at the RHID contains more GTP-ROP2 compared to outside. It follows that the association of ROP2 with the PM is influenced by its activation state (namely, the type of the bound nucleotide). Furthermore, it can be concluded that not the nucleotide-state itself, but rather the ability to shuttle between the two states causes a polarization of ROP2. These findings are in line with data from previous work from yeast, where it could be shown that the cycling between GTP- and GDP-bound CDC42 was crucial for its polarization (Irazoqui et al., 2003).

For local enrichment of GTP-ROP2 (activated ROP2), two mechanisms seem plausible: local activation of ROP2 or local immobilization of already activated ROP2. The latter would require differential diffusion rates of GDP-ROP2 and GTP-ROP2. The former however would require the local presence of an activating factor, like for example a ROPGEF. We could show recently that the polarization of ROP2 at the RHID is dependent on the presence of the ROPGEF GEF3 and that GEF3 is able to recruit ROP2 into ectopic RHID-like patches

(Denninger et al., 2019). During my PhD-thesis I could confirm this finding for trichoblast of the cell stage -1 (Figure I- 8, A). Furthermore, I could show that ROP2 is still associated with the PM in the *gef3* mutant background. However, for cells of the developmental stage +1 my results showed reduced but not completely abolished polarity of ROP2 in the *gef3-1* mutant, accompanied by a reduction in membrane association (Figure I- 8, C and D). These results suggest that at cell stage -1 the association of ROP2 with the PM is independent of GEF3, while at cell stage +1 it is dependent on GEF3.

I have observed that cytosolic proteins like *rop2ΔC161* or mCitrine showed a slightly increased polarity index compared to the unpolar, membrane bound control LTI6B (Figure I- 8, D). Most likely, this is a general effect for cytosolic proteins due to the accumulation of cytosol in the bulge. Therefore, it could be hypothesized that the reduction in PM association that can be observed for ROP2 in the *gef3-1* mutant similarly leads to a perceived polarity. However, statistical analysis revealed that ROP2 polarity was not statistically different between wild type and the mutant background and the median of polarity indices measured for ROP2_{*gef3-1*} was above the median of the unpolar controls. The range of polarity indices for ROP2 in the *gef3-1* mutant background was relatively broad: While in some plants ROP2 was highly polar, others showed unpolar behavior of fluorescently tagged, transgenic ROP2. This heterogeneity in ROP2 polarity indices did not result from heterozygosity of the *gef3* mutant background, as genotyping revealed a homozygous mutant population.

It needs to be kept in mind that the cell stage was determined by the position of the first root hair and that by definition every +1 cell has been able to grow out a hair and consequently has been able to accumulate enough ROPs at the RHID to activate the tip growth machinery. The ROPs that have accumulated and have led to hair growth may include fluorescently tagged ROP2, which I can detect and then measure polar accumulation. Additionally, however, the pool of ROPs also includes the endogenous untagged ROP2, which of course can contribute to tip growth but whose polarity cannot be determined. Furthermore, other ROPs can also contribute to tip growth as is evident by the lack of a root hair phenotype in *rop2-1* mutant plants (Denninger et al., 2019). In this case, the wide range of polarity indices would be explained by the differential contribution of different ROPs to tip growth, of which only one can be measured.

In general, the *gef3-1* mutant plants are still able to grow out root hairs but do so with a delay in development, shown by an increased distance between the root tip and the first hair, as well as a reduction in root hair density (Denninger et al., 2019). This indicates, that in the absence of GEF3-dependent ROP2 polarization, the root hair growth machinery is polarized by a GEF3-independent mechanism working with a lower efficiency. Such a mechanism could involve spontaneous polarization (which will be discussed in detail in Chapter II) and could be less specific for ROP2 but facilitate the polarization of other ROPs (like for example ROP4). The results presented led to the hypothesis that GEF3 could act as an accelerator of ROP2 polarization, raising the question of how GEF3 is facilitating this.

Since ROP2 and GEF3 have been shown to interact with each other in heterologous systems (Denninger et al., 2019), it seems plausible that GEF3 either acts as an activator of ROP2 or that it recruits ROP2 into the RHID by lateral sorting. My result regarding membrane association of ROP2 in the *gef3-1* mutant background in trichoblast of the cell stage -1 (not significantly different compared to wild type) seems to hint towards a lateral sorting mechanism. On the other hand, I could also indirectly show evidence for an enrichment of GTP-ROP2 at the RHID, which would argue in favor of local activation. The fact that ROP2 can polarize even in absence of GEF3 additionally points towards a second mechanism which could involve self-polarization of ROP2. Indeed, the phenomenon of spontaneous polarization has already been described for small GTPases and was linked to differential diffusion rates depending on the activity state of the GTPase (Wedlich-Soldner and Li, 2003; Johnson et al., 2011). Since I could already show evidence for an enrichment of GTP-ROP2 at the RHID and to test if the same process is involved in ROP2 polarization, I have performed mobility measurements of ROP2, *rop2CA* and ROP2 in the *gef3-1* mutant background, which will be presented and discussed in Chapter II.

Taken together, I could show that association with the PM is a prerequisite for ROP2 polarization. Furthermore, I could present evidence for a self-polarization potential of ROP2 and also for an enrichment of GTP-ROP2 at the RHID, which however still lacks direct evidence. Since very recent progress in the field has led to the establishment of fluorescent sensors for ROP activity (Platre et al., 2019) it would be interesting to directly analyze the distribution of active ROP2 in trichoblast cells and test if the evidence derived from my data holds true.

Chapter II

Local immobilization of ROP2 in membrane nanodomains by GEF3

Sometime small things can make the difference

1. Introduction

1.1. Spontaneous polarization in the absence of landmark proteins

Back in 1952 the mathematician, theoretical biologist and logician Alan Turing proposed a model for pattern formation and morphogenesis. This model suggested, that spatial patterns can spontaneously arise via the amplification of stochastic fluctuations within a homogeneously distributed population of diffusible molecules interacting with each other (Turing, 1952). A prerequisite for this hypothesized reaction-diffusion-model is that physical interactions of molecules lead to changes in their diffusion rate. These differences in mobility, depending on the reactional state of the components, create local concentration maxima and concentration minima causing patterns different from homogenous distribution and therefore a break in symmetry. In this model no previous landmark proteins are necessary for the establishment of polarity.

It has been reported that in the budding yeast *S. cerevisiae* cell polarization can indeed occur spontaneously independently from known landmark proteins. Usually, BUD8/9 and AXL1 serve as landmark proteins for the targeted activation of CDC42 via the small GTPase RSR1, leading to directed polarization (described in General Introduction 3). However, in the absence of RSR1 and BUD8, CDC42 spontaneously polarizes at random locations (Wedlich-Soldner et al., 2003; Irazoqui et al., 2003), indicating an intrinsic property of the small GTPase to polarize without the prerequisite for landmark proteins (for example reviewed in Wedlich-Soldner and Li, 2003; Johnson et al., 2011).

Instead the spontaneous polarization of CDC42 was reported to be dependent on the scaffold protein BUD EMERGENCE 1 (BEM1) and the CDC42 effector protein p21-ACTIVATED KINASE (PAK) (Irazoqui et al., 2003; Kozubowski et al., 2008). BEM1 and PAK form a complex with CDC24, which is the GEF for CDC42 (Kozubowski et al., 2008). The authors postulate a model in which the BEM1-PAK-CDC24 complex is then recruited to the plasma membrane (PM) via the interaction with GTP-CDC42. At the membrane, CDC24 can interact with and activate GDP-CDC42, thereby further increasing the number of GTP-CDC42 molecules. This growing patch in turn recruits more BEM1-PAK-CDC24 complex, which further adds to the growth of the patch. Recent studies have linked this self-

amplifying mechanism to differential lipid composition at the bud site (Slaughter et al., 2013; Meca et al., 2019).

Differential diffusion rates for the GTP-bound and the GDP-bound state of CDC42 have been measured and confirmed (Bendezú et al., 2015). A similar Turing-like mechanism has been suggested for ROP2, which would suggest that differential diffusion rates of GTP-ROP and GDP-ROP together with a cellular auxin gradient determine the position of the RHID, in a cell-length-dependent manner (Payne and Grierson, 2009). However, to date this model still requires further experimental evidence.

1.2. Aim of Chapter II

During the course of this project, we were able to show that GEF3 acts as a landmark protein for ROP2 during root hair initiation (Denninger et al., 2019). In addition, however, data presented in this thesis shows that even in the *gef3-1* mutant background ROP2 is still able to occasionally polarize and initiate root hairs (Chapter II 2.4). Therefore, we can hypothesize that there is a (primary) GEF3-dependent mechanism for ROP2 polarization and another (secondary) GEF3-independent mechanism for ROP2 accumulation, which for example could involve spontaneous ROP2 polarization at the RHID.

It has also been postulated, that ROP2 polarization is driven by a reaction diffusion (Turing-like) model, where diffusion rates are influenced by the nucleotide/activity state of ROPs (Payne and Grierson, 2009). This model further suggests that the diffusion rate for GTP-ROP2 would be lower than the diffusion rate for GDP-ROP2. The formation of the ROP2-domain would involve the immobilization of ROP2 at the RHID via its activation, which would cause the accumulation of more and more active ROP2 protein. Since RHID formation was shown to be influenced by the presence of GEF3, and since I could present evidence for an enrichment of GTP-bound ROP2 at the RHID, it can be hypothesized that GEF3 acts as an activator of ROP2 in the reaction diffusion model, causing the immobilization of ROP2 and thereby accelerating its polarization and supporting a controlled initiation of root hairs.

Therefore, I aimed to determine the activity-dependent protein mobility for ROP2 in wild type in the *gef3-1* mutant background by using Fluorescence Recovery After Photobleaching (FRAP). Based on the obtained results, I then further investigated protein

dynamics at a higher spatio-temporal resolution using Variable Angle Epifluorescence Microscopy (VAEM). For this, I used fusion proteins with mCitrine and mRuby2 and took advantage of the characteristic of these fluorophores to undergo fluorophore blinking, to perform single molecule localization microscopy.

2. Results

To investigate protein mobility at the plasmamembrane and its impact on polarization at the RHID I have used plant lines either expressing GEF3, ROP2 or activity mutants of ROP2 (described in Chapter I) fused to mCitrine. GEF3 and ROP2 fusion proteins were expressed under the control of the respective endogenous promoter, while the activity mutants were expressed from the estradiol inducible *ubiquitin10* promoter. The line expressing ROP2 in the *gef3-1* mutant background was a line in the F2 generation. All transgenic plant lines used in this chapter have originally been generated by Phillip Denninger.

2.1. Does the activity state of ROP2 impact on its mobility?

To determine the mobility of ROP2 and of the activity mutants of ROP2 (constitutively active ROP2 = *rop2CA*; dominant negative ROP2 = *rop2DN*), I performed Fluorescence Recovery After Photobleaching (FRAP) measurements.

For ROP2, fluorescence recovery (FR) was slower inside compared to outside the RHID (Figure II- 1, A-C). The median of the half time recovery ($t^{1/2}$) inside the RHID was observed at 40.27 sec, whereas the median of $t^{1/2}$ outside the RHID was at 5.75 sec. This result was very much in accordance to my previous observation that the membrane association of ROP2 was higher inside the RHID than outside the RHID (see Chapter I, Figure I- 7, page 45). Furthermore, I observed that ROP2 outside the RHID could recover to 100% of its pre-bleach fluorescence, defined as the mobile fraction of the protein, whereas ROP2 inside the RHID only recovered to 89.2%, consequently having an immobile fraction of 10.8%. Values for the mobile fractions were calculated from fitting to the mean data curve.

For *rop2CA* the FR inside the RHID (median $t^{1/2}$ 59.38 sec) was slower than for ROP2 (median $t^{1/2}$ 40.27 sec) and slower than for *rop2DN* (median $t^{1/2}$ 24.63 sec) (Figure II- 1, D-F). The mean mobile fraction for *rop2CA* was observed to be 55.8% and 51.6% for *rop2DN*. This was surprising since the membrane association of *rop2DN* was lower in comparison to ROP2 and *rop2CA* (see Chapter I, Figure I- 7, page 45) and it seems reasonable to assume that a more cytosolic protein should have a higher mobile fraction as the bleached protein can easily be replenished via cytoplasmic diffusion. Outside the RHID, *rop2CA* showed a

median $t^{1/2}$ of 62.96 sec and a mean mobile fraction of 70%, whereas *rop2DN* had a median half time recovery of 38.32 sec and a mean mobile fraction of 84.29%.

Interestingly, $t^{1/2}$ for *rop2CA* inside the RHID is higher than for ROP2. This result is in line with my previous observation, that the membrane association for *rop2CA* inside the RHID was also higher in comparison to ROP2 (Figure I- 7).

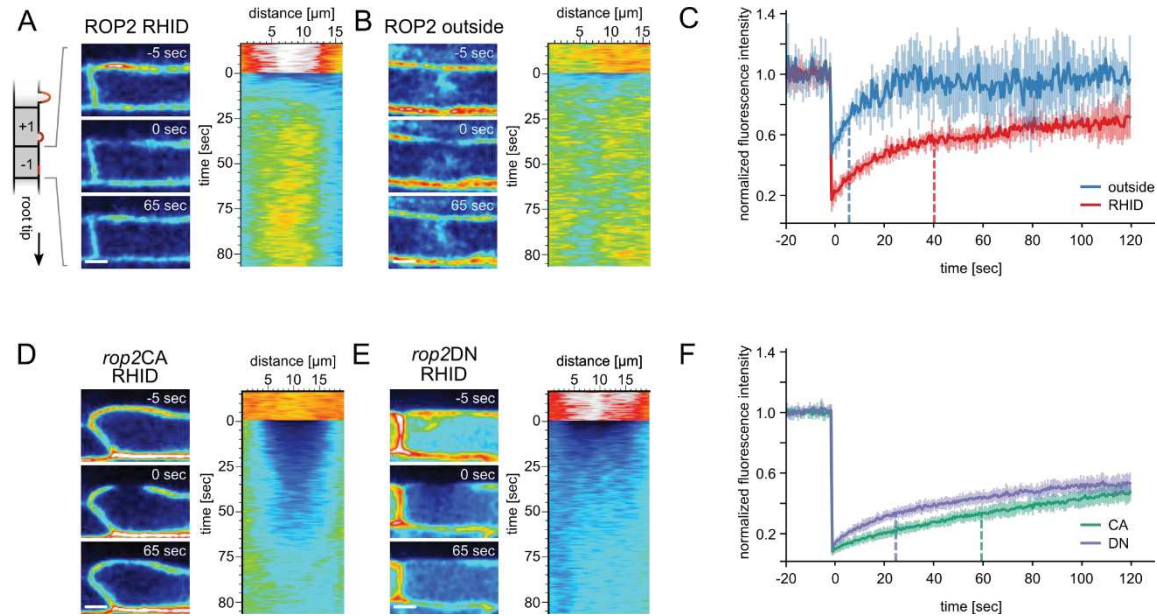


Figure II- 1: ROP2 activation caused protein immobilization at the RHID. Fluorescent Recovery After Photobleaching (FRAP) measurements of ROP2 inside (A) and outside the RHID (B) and the corresponding mean recovery-curves (C). FRAP measurements for ROP2CA (D) and *rop2DN* (E) inside the RHID and the corresponding mean recovery-curves (F). Images of single time points before bleaching (-5 sec), directly after bleaching (0 sec) and at the middle of the recorded time (65 sec) are shown for each protein as well as kymographs drawn along a line spanning the bleached region. All measurements were performed at cell stage -1. Scale bars represent 10 μm .

2.1.1 Does GEF3 influence ROP2 mobility at the RHID?

To determine the impact of GEF3 on the mobility of ROP2, I performed additional FRAP measurements for GEF3 as well as for ROP2 in the *gef3-1* mutant background (Figure II- 2). For the latter, I observed FR with a median $t^{1/2}$ value of 8.81 sec inside the RHID and of 11.98 sec outside the RHID. Interestingly, that means that in the *gef3-1* mutant background, the mobility of ROP2 inside the RHID as well as outside the RHID was reduced to the same level as ROP2 outside the RHID in a wild type background (see Figure II- 2, D). The mean mobile fraction for ROP2 in the *gef3-1* mutant was 88.83% inside the RHID and 97% outside the RHID. This is in line with my previous result showing that the membrane association for ROP2 in the *gef3-1* mutant background was not significantly different in comparison to ROP2 wild type background (see Chapter I, Figure I- 8).

In contrast to both, ROP2 and ROP2 in *gef3-1*, FRAP measurements for GEF3 showed that its fluorescence recovery was significantly slower (median $t^{1/2}$ 104.84 sec), with a mean mobile fraction of 73.5%. Taken together, I have observed that GEF3 was less mobile than ROP2, which in turn became even more mobile in the absence of GEF3. This strongly suggests a mechanism, in which GEF3 negatively impacts on ROP2 mobility, thereby causing its polarization.

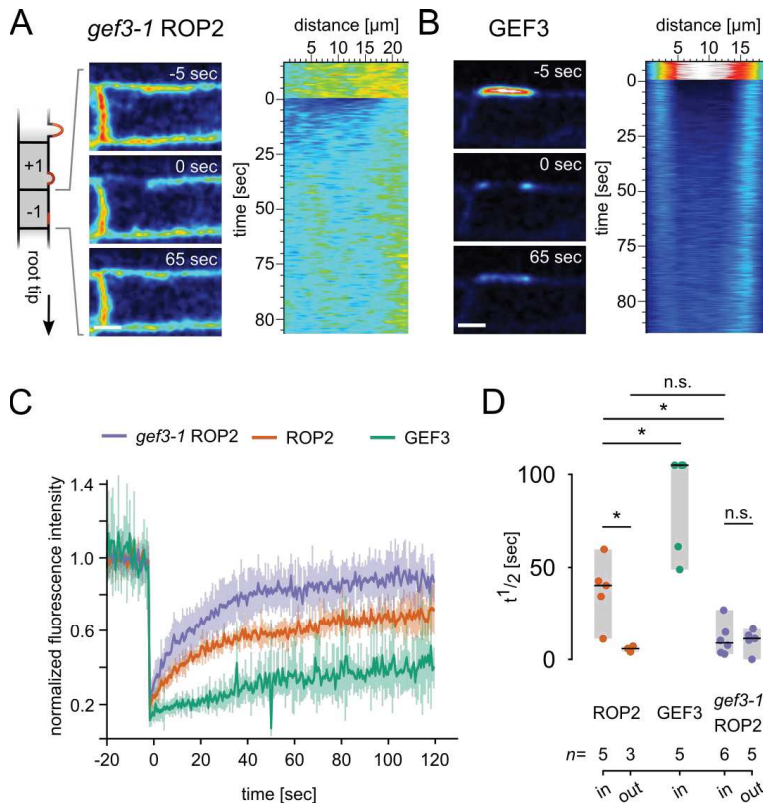


Figure II- 2: GEF3 caused ROP2 immobilization at the RHID. (A, B) FRAP measurements for ROP2 in the *gef3-1* mutant background (A) and GEF3 (B), both inside the RHID. All measurements were performed at cell stage -1. Images for single time points before bleaching (-5 sec), directly after bleaching (0 sec) and at the middle of the recorded recovery time (65 sec) are shown for each protein, as well as a kymograph drawn along a line spanning the bleached region. Scale bars represent 10 μm . (C) Corresponding mean recovery-curves for ROP2 in the *gef3-1* mutant background and GEF3. For comparison, the recovery-curve of ROP2 from Figure II- 1 is shown again. (D) Half time of recovery ($t^{1/2}$) for ROP2, GEF3 and ROP2 in the *gef3-1* mutant background inside (in) and outside (out) the RHID. Center lines represent median values, gray boxes show the data range, n indicates the number of measured cells. Asterisk indicate statistically significant difference; p-value determined by Student's t-test: n.s. = p-value >0.05; * = p-value < 0.05.

Table II- 1: Half time recovery ($t^{1/2}$) and mobile fraction calculated for ROP2, *rop2CA*, *rop2DN*, GEF3 and ROP2 in *gef3-1*, both at the inside of the RHID (RHID) or outside (out) of the RHID.

		median $t^{1/2}$ [sec]	mean mobile fraction
ROP2	RHID	40.27	89.20%
	out	5.75	100.00%
<i>rop2CA</i>	RHID	59.38	55.80%
	out	62.97	70.00%
<i>rop2DN</i>	RHID	24.63	51.60%
	out	38.32	84.29%
GEF3	RHID	104.87	73.50%
ROP2 in <i>gef3-1</i>	RHID	8.81	88.83%
	out	11.98	97.00%

Taken together, the results presented here point towards an activation-dependent immobilization of ROP2 at the RHID (p-value of 0.033 for the comparison of the mobile fraction of ROP2 and *rop2CA* inside the RHID). Additionally, the results show that the mobile fraction of ROP2 is independent of GEF3 (p-value of 0.976 for the comparison of ROP2 and ROP2 in *gef3-1* inside the RHID; p-value of 0.215 outside the RHID), whereas the kinetics of recovery however are GEF3-dependent (Figure II- 2, D). Furthermore, it can be hypothesized that GEF3 acts as a catalyzer, depleting more mobile (“unbound”) ROP2. In general, GEF3 showed a low mobility which led me to the hypothesis that GEF3 may act as an anchor, activating and thus immobilizing ROP2 at the RHID.

2.2. How is the immobilization of ROP2 at the RHID achieved?

To more closely investigate the differences measured in protein mobility, I performed Variable Angle Epifluorescence Microscopy (VAEM) measurements (Figure II- 3). This microscopy technique allows for imaging of plant membrane proteins with an increased spatio-temporal resolution compared to confocal microscopy techniques. The main technical difference between VAEM and confocal microscopy is that VAEM lacks a pinhole and instead uses an angulated excitation laser, which excites only a small sheet of the sample close to the surface and reduces the amount of cytosolic background signal (Konopka and Bednarek, 2008) (Figure II- 3). Since VAEM therefore allows only imaging of

regions within the sample that are close to the cover slip, I imaged trichoblast in a top view. The first cell from the root tip, that showed a bulge (indicated by a widening and loss of its rectangular shape) was always determined to be cell +1. Subsequently, younger trichoblasts were counted backwards with negative numbers, as described previously (Figure 2, page 22).

By using a minimal exposure time of 60 ms, I was able to visualize ROP2 and GEF3 in diffraction limited puncta (Figure II- 3). These puncta showed a dynamic behavior with frequent appearance and disappearance but only little lateral movement. Interestingly, the puncta were easier to identify in time-lapse movies in contrast to single time point slices, further underlining their dynamic nature. In addition, the overall fluorescence intensity showed an initial, fast decrease followed by a long and stable phase (Figure II- 3, B). To visualize this dynamic behavior, I generated kymographs over the cell surface, including the RHID but also the PM outside of the RHID. It became clear, that GEF3 localized into stable clusters within the RHID, as indicated by the presence of discontinuous stripes within the kymograph (Figure II- 3, C). While these clusters were indeed stable with regard to their position, they dynamically appeared and disappeared in varying time intervals. ROP2 was less mobile than GEF3 in general, however, it still formed stable clusters within the RHID, but not outside the RHID (Figure II- 3, D). In the *gef3-1* mutant the stable ROP2 clusters within the RHID were lost and the protein showed a behavior similar to ROP2 outside the RHID in wild type plants (Figure II- 3, E).

Taken together, the analysis of VAEM time lapse movies strongly suggested that the RHID is sub-compartmentalized and includes regions where ROP2 and GEF3 show a reduced lateral mobility and an increased positional stability. Furthermore, the association of ROP2 with these stable structures was lost in the *gef3-1* mutant, suggesting an important role of GEF3 in the stabilization of ROP2 in these clusters.

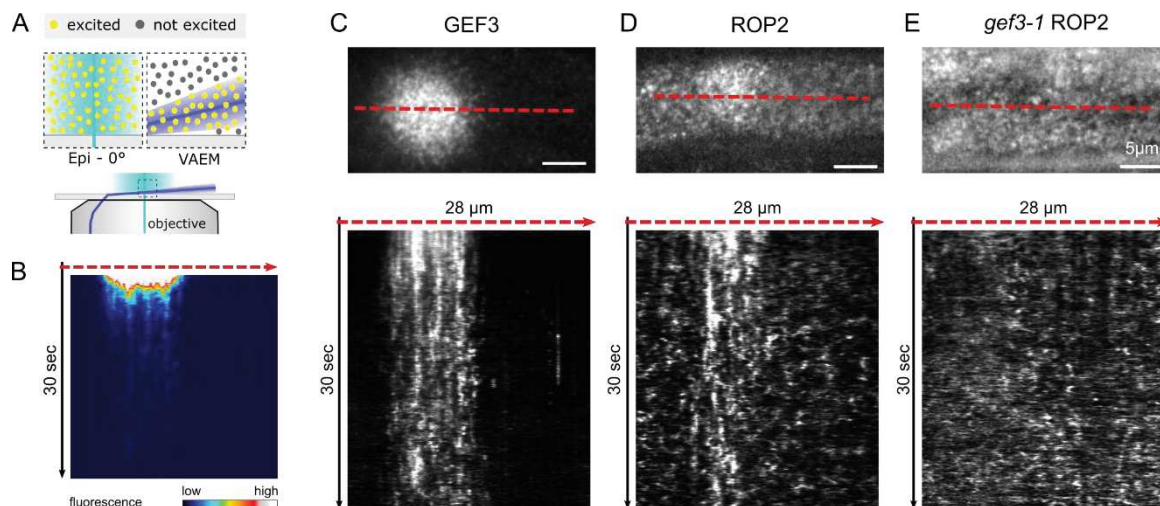


Figure II- 3: VAEM reveals that ROP2 and GEF3 localize in diffraction limited, mobile puncta in the PM of trichoblasts of cell stage -1. (A) Schematic representation of the excitation illumination in Variable Angle Epifluorescence Microscopy (VAEM) compared to epifluorescence (Epi). (B) kymograph of a mCitrine-GEF3 VAME time-lapse movie, drawn along the red line of the VAEM micrographs represented in (C, upper panel). VAEM micrographs of GEF3 (C), ROP2 (D) and ROP2 in the *gef3-1* mutant background (E). Single slices of time lapse stacks (upper panel) and kymographs drawn along the red, dashed line (lower panel). Note that the kymographs in (C-E) were created from time lapse stacks with enhanced contrast. The kymographs in (B) and (C, lower panel) are derived from the same time-lapse. Scale bars represent 5 μm.

2.2.1 Blinking behavior of mCitrine allows super-resolution microscopy.

In general, the visibility of the puncta in the VAEM time lapse movies was enhanced after a few seconds of recording: An initial, fast decrease of overall fluorescence intensity was followed by a long and stable phase, where distinct puncta showed a blinking behavior. To test if this phenomenon was due to intrinsic properties of the tagged proteins or of the fluorophore used as a tag, I transiently expressed the actin probe LifeAct tagged with different fluorescent proteins in tobacco leaves. I found that LifeAct tagged with either GFP, Citrine or mCitrine showed the same initial, fast decrease in fluorescence, followed by a long and steady blinking phase (Figure II- 4). Interestingly, this behavior was in direct positive correlation with the energy output of the excitation laser (laser intensity indicated by %). At high laser power LifeAct labeled actin filaments did no longer appear as “thick cables”, but more closely resembled “pearls on a string”. In a sum projection of the corresponding time lapse movie, those “pearls” added up and again led to the visualization of the whole actin filaments. In contrast, LifeAct tagged with mNeonGreen neither showed the characteristic fast decrease nor a blinking behavior (Figure II- 4). These results supported the assumption, that the fluorophore was responsible for the blinking appearance of LifeAct, ROP2 and GEF3 fusion proteins and would explain why stable structures appeared as discontinuous stripes in the kymographs.

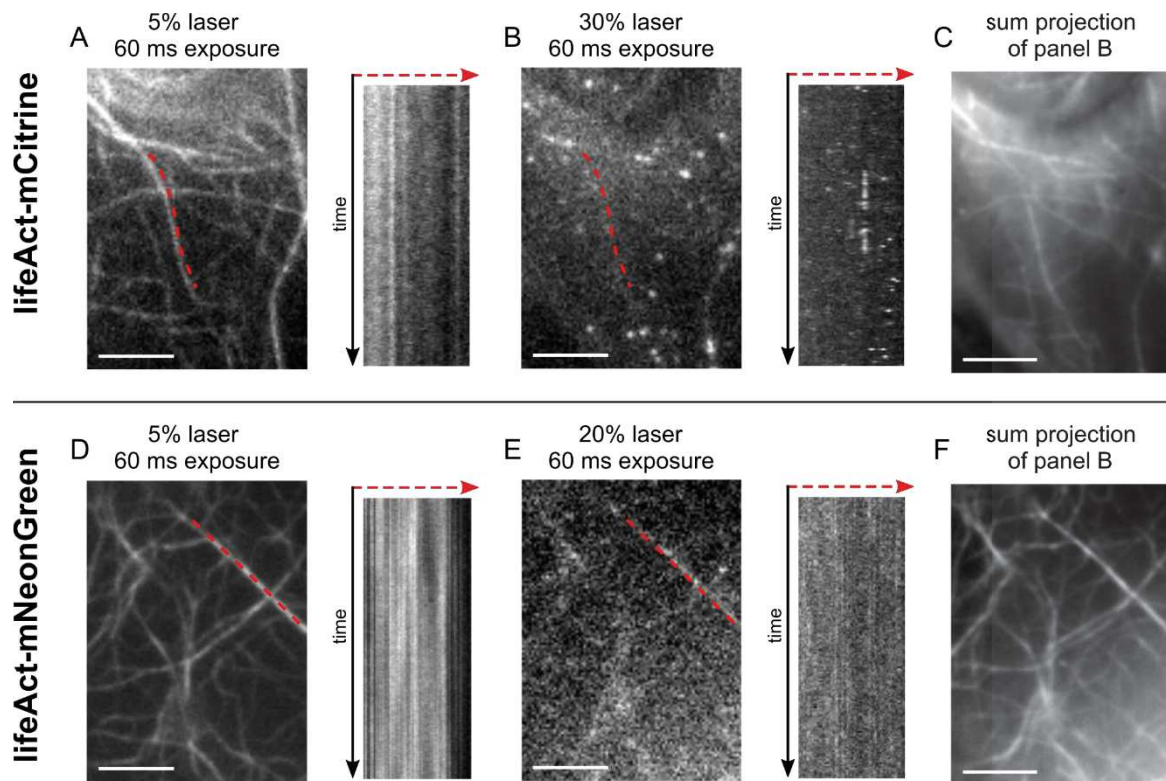


Figure II- 4: mCitrine, but not mNeonGreen shows fluorophore blinking behavior in tobacco leaves. VAEM-micrographs of the actin probe LifeAct tagged with mCitrine (A-C) and mNeonGreen (D-F). Single images from a time lapse stack acquired with the indicated imaging settings are shown (laser power in % and exposure time in ms). Kymographs drawn along the red, dashed lines are depicted next to the corresponding image. Panel (C) and (F) show sum projections of the time lapse stacks of (B) and (E), respectively. Scale bars represent 5 μm .

GFP and its derivatives, including mCitrine, have already been described to have a photochromic behavior (Dickson et al., 1997; Fölling et al., 2008). Fluorescence intermittency (also called fluorophore blinking or photochromic behavior) is based on a stochastic process, in which electrons of a fluorophore transition into the “dark state” (a non-excitable and non-emitting energy state). The more energy is transferred to the fluorophore, the higher are the chances that electrons undergo this transition, leading to a reduced percentage of excitable fluorophores. This concept is used in ground state depletion microscopy (Hell and Kroug, 1995; Fölling et al., 2008). With reduced numbers of excitable fluorophores at any given time, the fluorophore density is decreased and therefore the likelihood to detect single fluorophores increases. The integration of the position of a multitude of different single fluorophores over time then allows for the computation of super-resolved images (Bierwagen et al., 2010) (Figure II- 5, A).

For the integration of blinking events over time, I used the Super Resolved Radial Fluctuation (SRRF) algorithm (Gustafsson et al., 2016). The SRRF algorithm does not only

allow for the computation of a super-resolved image, but also color-codes the structures according to their stability, meaning the re-occurrence of blinking events. The more often a blink event occurred at a certain pixel, the brighter this pixel appears in the reconstructed image. It is important to keep in mind that the fluorophore concentration positively correlates with the frequency of blinking events: The higher the fluorophore density (local concentration), the more likely it is that at least one fluorophore is currently emitting photons. As the SRRF algorithm additionally performs intensity weighing, the brightness of SRRF images can be interpreted as a measure for relative stability correlating with fluorophore concentration. Furthermore, the SRRF algorithm assumes for its analysis that the image consists of point sources and that the actual signal is convolved with point spread functions of a higher degree of local symmetry than point spread functions of the background (Gustafsson et al., 2016). This assumption of radial symmetry is used to perform sub-pixel localization, further increasing the resolution compared to the initial image.

The increase in resolution can be readily appreciated by comparing a SRRF reconstruction of LifeAct-mCitrine to a sum intensity projection of the same initial VAEM time-lapse movie (Figure II- 5, B). In the reconstructed image using the SRRF algorithm, actin filaments are more easily distinguishable and the signal to background ratio is drastically increased.

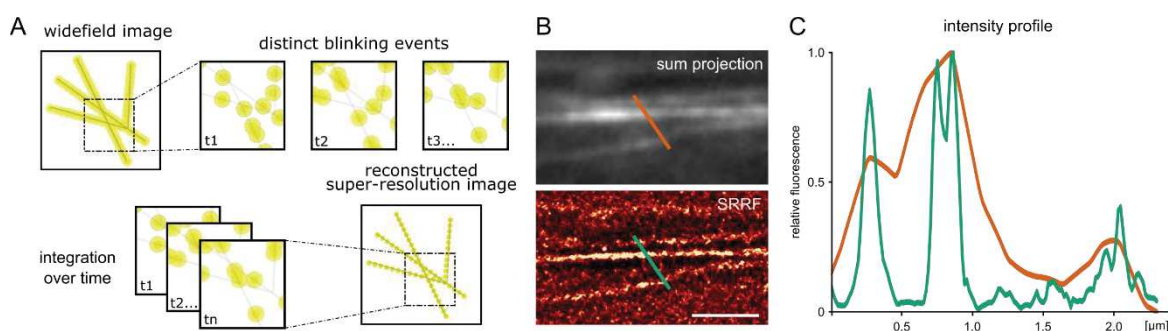


Figure II- 5: SRRF reconstruction can increase image resolution and signal to background ratio (A) Schematic representation of the reconstruction of a super resolved image by integrating distinct blinking events **(B)** Sum intensity projection (upper panel) and a SRRF reconstruction (lower panel) of a time-lapse VAEM movie of an *Arabidopsis* trichoblast stably expressing LifeAct-mCitrine under the control of the *Ubiquitin10* promoter. The scale bar represents 5 μm ; colored lines within the micrographs represent the lines, along which the relative intensity profiles **(C)** were measured.

2.2.2 SRRF reveals the GEF3-dependent localization of ROP2 into nanoclusters.

In contrast to other single molecule localization (SML) algorithms, SRRF is suitable for high fluorophore densities and low signal-to-noise ratios. In addition, it is more tolerant towards movement within the sample, since sub-pixel localization is performed prior to time integration (Gustafsson et al., 2016). Therefore, the SRRF algorithm seemed ideal to perform SML for ROP2, GEF3 and ROP2 in the *gef3-1* mutant background at the RHID of living *Arabidopsis* roots.

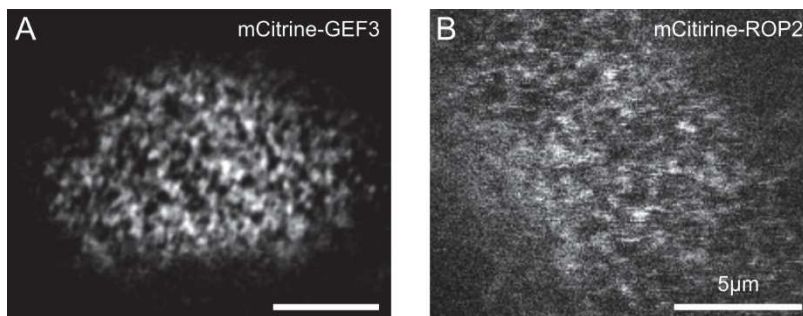


Figure II- 6: Sub-compartmentation of the RHID visualized by live-cell, laser scanning confocal microscopy. Micrographs of GEF3 (A) and ROP2 (B) in trichoblasts of cell stage -1. Scale bar represents 5 μm .

SRRF reconstructions revealed the sub-compartmentalization of the RHID into distinct mCitrine-ROP2 and mCitrine-GEF3 clusters, with an area of approximately 70-170 nm (Figure II- 7), which could also be confirmed by laser scanning microscopy (Figure II- 6). At cell stage -4, mCitrine-GEF3 nanoclusters showed a certain tendency to localize at the root-tip-ward end of the cell, but could also be found over the whole cell surface (Figure II- 7, A). One cell stage later, at cell stage -3, the nanoclusters could already be observed to localize very specifically at the RHID and this localization persisted in subsequent developmental stages (Figure II- 7, A). At the same time, the contrast between the nanoclusters and the background in the SRRF images increased steadily over the course of development indicating an increase in protein amount and relative, positional stability. The density of nanoclusters was determined by dividing the number of nanoclusters by the total area of the mCitrine-GEF3 patch, which was determined from the epi-fluorescent image that was acquired after the time-lapse stack. It appears as if the area for the GEF3 patch increased over the course of root hair development, while the density of nanoclusters

remained stable and did not show any statistically significant changes from cell stage -4 to cell stage +1 (Figure II- 7, D).

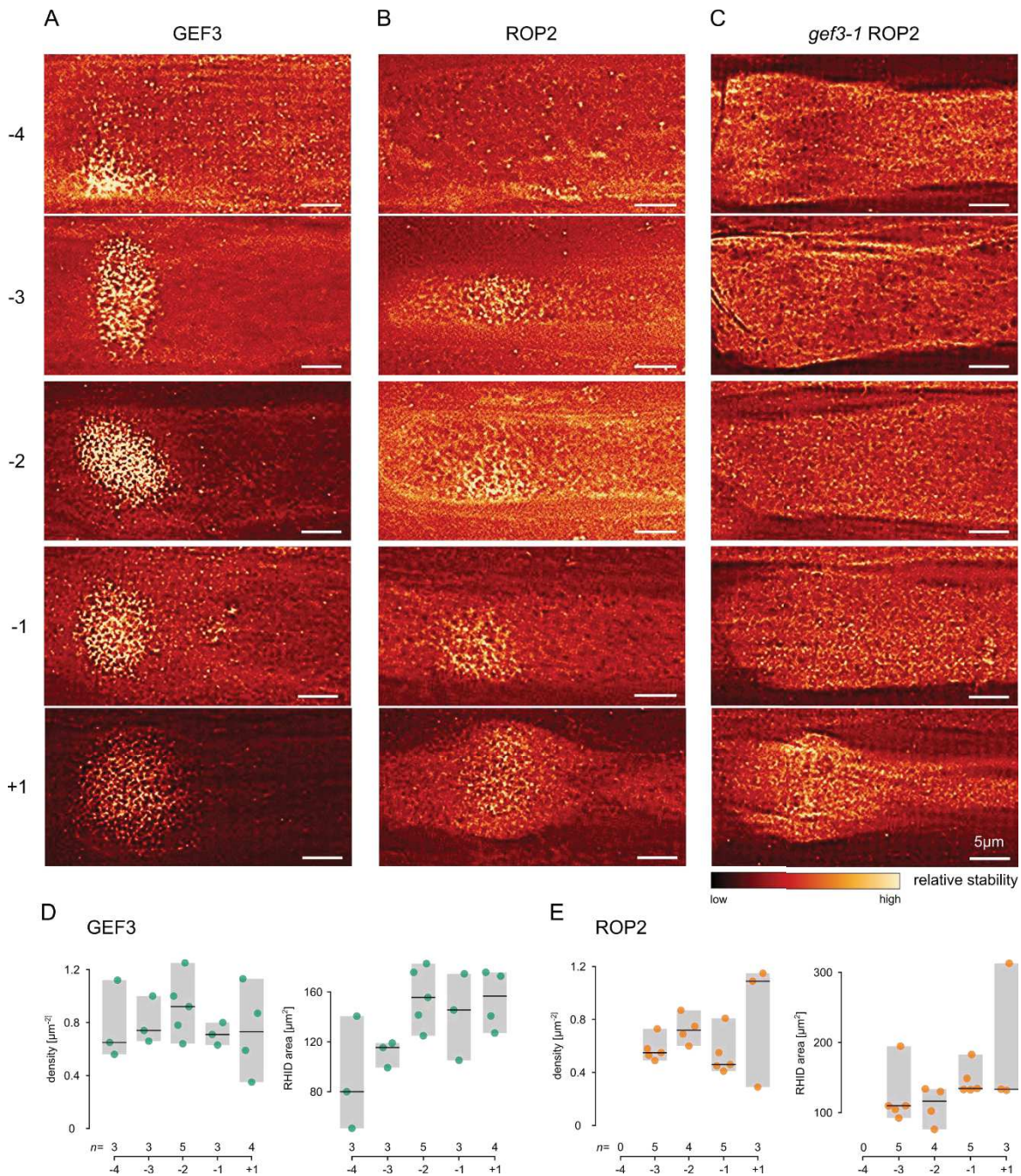


Figure II- 7: ROP2 is recruited into stable nanoclusters in the RHID in a GEF3-dependent manner. (A-C) Super Resolution Radial Fluctuation (SRRF) reconstructions of VAEM micrographs of GEF3 (A), ROP2 (B) and ROP2 in the *gef3-1* mutant background (C) in different developmental cell stages (-4 to +1). For each protein, the images were taken from different trichoblast cell stages but from the same root (exception: GEF3 +1 is derived from a different root than the other GEF3 cell stages). The root tip is always located to the left side of the cells. Stability of the structures is false-colored as indicated; scale bars represent 5 μm. (D, E) Quantification of the nanocluster density and area of the RHID for GEF3 (D) and ROP2 (E) over the course of root hair development. Center lines represent median values; gray boxes show the data range; n indicates the number of cells measured; note that for each graph an ANOVA-Tukey test (significance value = 0.01; same letters indicate no significant difference) revealed no significant difference between data for each developmental stage.

It needs to be kept in mind however, that the number of biological replicates in this experiment varied between only 3 and 5, consequently making any statistical analysis prone to fluctuations due to natural variation and thus difficult to interpret. Therefore, I can merely state that there is a tendency for an increase in the area of the GEF3-patch, accompanied by a seemingly unchanged density of nanoclusters, however both observations require further testing and an increased numbers of replicates. If these observations can be verified it would suggest that once the mCitrine-GEF3 nanoclusters are established, they accumulate more GEF3, but that the density of mCitrine-GEF3 nanoclusters is limited and that the spacing between the nanoclusters might be controlled. mCitrine-ROP2 was distributed in few nanoclusters over the whole cell surface at cell stage -4 and unlike GEF3 did not show any tendency for the accumulation of nanoclusters at the RHID at this stage (Figure II- 7, B). In the next developmental stage, in cell stage -3, mCitrine-ROP2 nanoclusters accumulated at the RHID and showed an increase in contrast between nanoclusters and background compared to cell -4. The localization of nanoclusters at the RHID persisted in subsequent development and the contrast between nanoclusters and background increased, suggesting a further increase in protein concentration. The density of mCitrine-ROP2 nanoclusters remained unchanged over the course of root hair development, as well as the area of the mCitrine-ROP2 patch (Figure II- 7, E). It needs to be noted that for this analysis the same statistical limitations apply as have been described for the analysis of GEF3 nanoclusters. Consequently, these results require further testing and can only indicate a tendency, which however suggests that once the mCitrine-ROP2 nanoclusters are established, more protein is recruited and accumulates in these stable structures.

Interestingly, mCitrine-ROP2 in the *gef3-1* mutant background did not show any polar accumulation of nanoclusters prior to bulging, that is before cell stage +1 (Figure II- 7, C). This observation was in line with my previous polarity index measurements (Chapter I, Figure I- 8) that had shown polar accumulation of ROP2 in the *gef3-1* mutant background at the RHID only at cell stage +1. Compared to ROP2 in the wild type background however, the nanoclusters that were observed to localize at the RHID eventually showed a lower contrast, indicating a lower amount of protein and a lower positional stability.

Taken together, protein fusions with mCitrine enabled me to perform SML and the integration of localization events over time allowed for the reconstruction of the sub-compartmentalization of the RHID into GEF3 and ROP2 nanoclusters, which to some extent had also already been visible in laser scanning confocal microscopy. The nanoclusters seemed to be established at the onset of root hair development. Furthermore, I could show that the polarization of mCitrine-GEF3 nanoclusters not only preceded but were necessary for the polar accumulation of ROP2 nanoclusters prior to bulging. After bulging however, ROP2 was able to form stable nanoclusters at the RHID even in the *gef3-1* mutant background and therefore independently of GEF3.

2.3. Does protein mobility impact on protein polarization at the RHID?

2.3.1 ROP2 immobilization precedes its polarization.

As I have mentioned before, developmental stages of trichoblast cells were classified by identifying the youngest cell in a cell file that showed morphological changes typical for the outgrowth of a root hair, eg. widening of the cell and loss of its rectangular shape. This cell was named +1 cell and younger cells, that is cells towards the root tip, were named subsequently with decreasing, negative numbers. In VAEM, due to the limitations in optical depth, trichoblast cells were imaged from a top view perspective and the root was pressed against the cover slip. Therefore, it is possible that young bulges that normally would not have qualified a cell to be identified as a +1 cell, already led to a clear deformation of the cell corpus and its classification as +1. As a result, labelling of the whole cell file in VAEM might be shifted in comparison to spinning disc confocal imaging. To investigate this possibility, I aimed to determine the timing of protein polarization using VAEM and compared it to the timing of protein polarization as it has been previously determined using spinning disc confocal imaging. To this end, I measured the density of blinking events (which positively correlates with protein concentration) inside and outside the RHID using VAEM over the course of root hair development. For this, a protein was considered to be polarized when the density of blinking events in the RHID was significantly higher than outside the RHID (Figure II- 8).

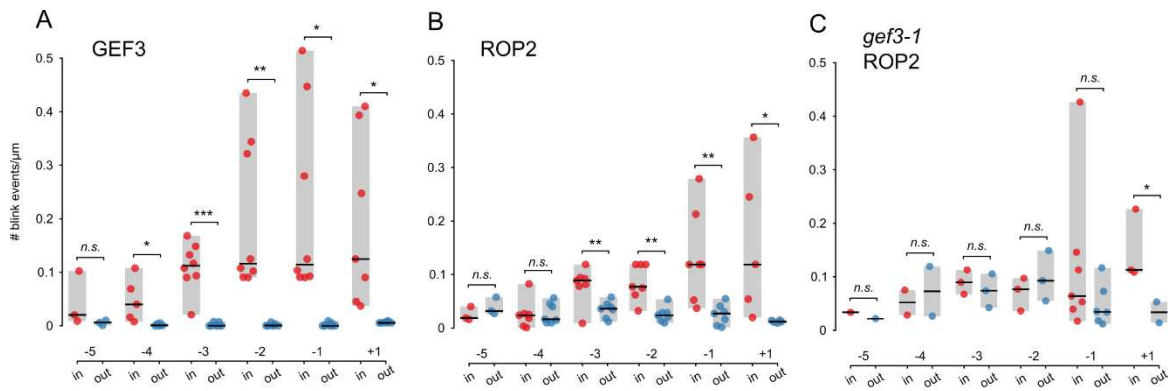


Figure II- 8: ROP2 polarization depends on and follows GEF3 polarization. Spot density determined by particle tracking inside (in) and outside (out) the RHID for GEF3 (A), ROP2 (B) and ROP2 in the *gef3-1* mutant background (C). Center lines represent median values; gray boxes show the data range. Asterisks indicate statistically significant differences; p-value determined by Student's t-test: n.s. = p-value > 0.05; * = p-value < 0.05; ** = p-value < 0.01; *** = p-value < 0.001.

The youngest cell stage where the density of mCitrine-GEF3 blink events was significantly higher inside the RHID in comparison to outside the RHID, indicating polar localization at the RHID, was cell stage -4. The median blink-density at the RHID further increased in cell stage -3 and then stayed constant until stage +1, even though a tendency towards a further increase in density seemed visible (Figure II- 8, A). Outside the RHID, almost no blink events could be detected after cell stage -5.

For mCitrine-ROP2, polarization was first detectable in cell stage -3, that means one stage later than GEF3, and the blink-density did not show further statistically significant increase over the course of root hair development (Figure II- 8, B), even though, similar to mCitrine-GEF3, a tendency towards a step-wise increase in blinking density seemed visible. In the *gef3-1* mutant background, mCitrine-ROP2 did not polarize at the RHID prior to bulging, but polarization could only be observed at cell stage +1 (Figure II- 8, C).

These results were partially in line with previous findings from our lab: GEF3 polarization precedes ROP2 polarization by one developmental stage and ROP2 polarization is dependent on GEF3. However, the polarization of GEF3 and ROP2 has previously been reported to occur at stage -5 and -4, respectively (Denninger et al., 2019). This discrepancy confirmed my previous suspicion with regard to cell staging and suggests, that determination of cell stage during VAEM was generally shifted by one cell, meaning that the cell stage +1 (determined by VAEM) corresponds to cell stage -1 in sideways imaging using spinning disc confocal microscopy. In addition, polarization of ROP2 in *gef3-1* was detected at cell stage +1 using VAEM, which corresponds to cell stage -1 in side view

imaging using regular confocal microscopy. At first glance this finding seems to conflict with the data presented in Chapter I, where polarization of ROP2 in *gef3-1* (using confocal microscopy) was observed in cell stage +1. This discrepancy however, might be explained by increased sensitivity due to an increased signal-to-background ratio of VAEM.

To test the hypothesis that ROP2 polarization is caused by local immobilization, I aimed to determine the mobility of mCitrine-ROP2 and mCitrine-GEF3 puncta using particle tracking over time. It has to be noted that the overall fluorophore density in my setup was higher compared to SML microscopy techniques that use photoactivatable fluorophores, like for example sptPALM (single-particle tracking photoactivated localization microscopy; Manley et al., 2008), where only a small number of fluorophores is activated. In general, the ability to track a single molecule directly correlates with the density of fluorophores: The lower the density of visible fluorophores is, the easier it is to identify and follow individual proteins. Therefore, the quality of particle tracking is highly dependent on the fluorophore density and a low fluorophore density can be advantageous. Due to the stochastic nature of the photochromic behavior of mCitrine and due to the initial fast decrease in fluorescence, in my setup the fluorophore density is variable over the course of the time-lapse stack, as well as between different samples, which consequently adds another layer of variability that needs to be considered when assessing tracking quality and results. In addition, fusion proteins can only be tracked when the fluorophore is in the “on”-state (excitable and emitting state). Since the switching of fluorophores between the “off”- and “on”-state is a stochastic process, it is conceivable that in between frames one proteins turns “off” and another one which is very close turns “on”. In such a case two distinct proteins would be falsely allocated to the same track, further compromising the tracking results. To minimize this potential bias in my tracking analysis, I decided to not allow a frame gap for gap closing and to set the maximal linking distance between two dots to a value slightly bigger than half the diameter of the initial dot ($d = 0.5 \mu\text{m}$, max linking distance $0.3 \mu\text{m}$). While this reduced the risk of falsely allocating two spatially distinct dots to the same track, it also leads to an artificial upper limit of velocities, since puncta that moved further than $0.3 \mu\text{m}$ in 60 ms (which is the time between two images of the time lapse movie) would not be linked in the tracking analysis. For all these reasons, particle tracking of fluorophores exhibiting fluorophore blinking has its limitations in tracking the

mobility of individual proteins, however, I would argue that the track velocity measured may still serve as a qualitative indicator of the mobility of the overall population of proteins.

Despite these limitations, I used particle tracking to analyze the dynamic behavior of mCitrine-ROP2 and mCitrine-GEF3 puncta. To this end, a histogram of all track velocities measured within a cell at a certain location (in- or outside the RHID) was generated and normalized to the track velocity that occurred with the highest frequency. Data from different cells of the same developmental stage and from the same location were integrated by applying polynomial fitting (6th degree) to the combination of all histograms. The local maximum of the fitted curve then indicated the velocity representing the majority of tracks, which in turn served as a measure for the overall mobility of the population of proteins.

The distribution of track velocities for mCitrine-ROP2 in cell -5 showed no significant difference between inside and outside the RHID (Figure II- 9), with a peak around 2 $\mu\text{m}/\text{sec}$ (2.01 $\mu\text{m}/\text{sec}$ outside and 2.15 $\mu\text{m}/\text{sec}$ inside) and a second peak at 4.39 $\mu\text{m}/\text{sec}$ and 4.35 $\mu\text{m}/\text{sec}$, respectively. Those two peaks can be interpreted as a fast (high track velocity) and a slow (low track velocity) subpopulation of tracked puncta. Likewise, in cell -4 the distribution of track velocities was also not significantly different between in- and outside according to statistical analysis (p -value = 0.88, Figure II- 9). However, the peak for the slow population as well as the peak for the fast population measured inside the RHID showed a shift towards a lower track velocity (peak at 1.67 $\mu\text{m}/\text{sec}$ and 4.28 $\mu\text{m}/\text{sec}$). Even though this subtle shift of track velocities did not represent a significant change from outside the RHID, a tendency towards a reduction of overall track velocity and therefore of ROP2 mobility can already be appreciated and is further backed by the relatively low p -value of 0.147 (Table II- 3) for comparing the distribution of track velocities in the RHID of cell -5 to -4. One cell stage later, at -3 (the cell stage in which ROP2 was determined to polarize at the RHID; Figure II- 8), the track velocities measured showed a distribution that was significantly different between inside and outside the RHID (p -value $3.2 \cdot 10^{-16}$, Figure II- 9). Additionally, the second peak at around 4.28 $\mu\text{m}/\text{sec}$, representing a subpopulation of fast tracks, disappeared inside the RHID, but not outside the RHID where a peak at 4.39 $\mu\text{m}/\text{sec}$ remained.

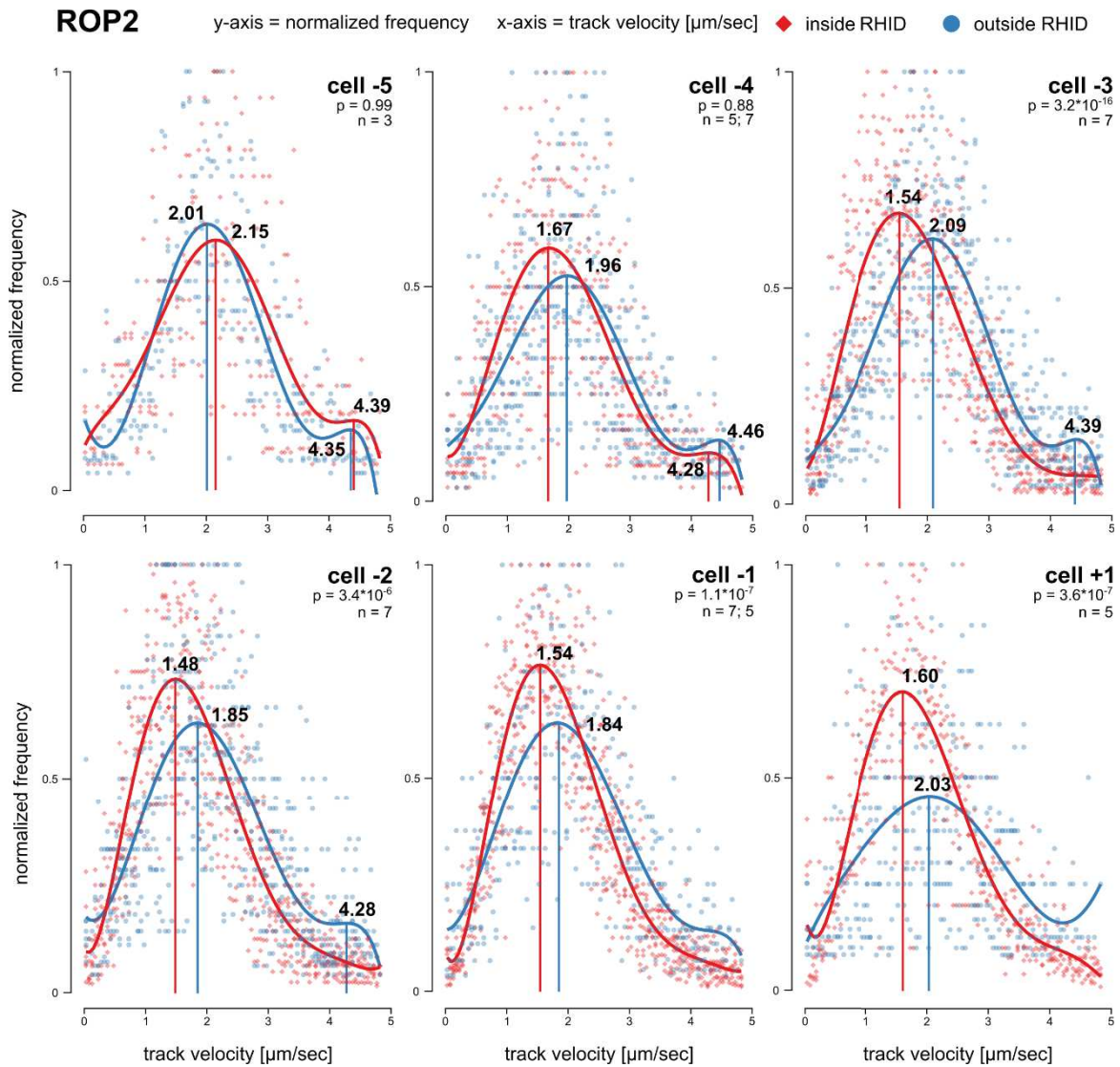


Figure II- 9: ROP2 shows a subtle reduction in mobility at the RHID prior to its polarization. Normalized distribution of track velocities for mCitrine-ROP2 puncta inside and outside the RHID over the course of root hair development. P-values indicate the statistical difference between the distribution of velocities inside and outside the RHID and were determined by two-way ANOVA. Curves represent polynomial fits (6th degree) of the data set, vertical lines indicate local maxima of the fitted curves. R² values for the fits can be found in Table II- 2. The y-axis shows the normalized frequency; the x-axis shows the track velocity; n (in; out) indicates the number of cells measured.

Table II- 2: R² values for the polynomial fitted curves for ROP2 inside and outside the RHID (see Figure II- 9).

ROP2	-5	-4	-3	-2	-1	+1
inside	0.4211	0.5452	0.7138	0.7663	0.8374	0.7614
outside	0.6255	0.4128	0.5928	0.4875	0.5266	0.1992

Table II- 3: p-values for the velocity distributions of ROP2, tested by two way ANOVA.

p-values	-5 vs -4	-4 vs -3	-3 vs -2	-2 vs -1	-1 vs +1
RHID vs RHID	0.1470	0.3265	0.9999	0.9484	0.5576
out vs out	0.9977	0.9786	0.4292	0.6846	0.9871

During subsequent development, the distribution of the track velocities showed a statistically significant difference between inside and outside the RHID. The second peak representing a subpopulation of fast tracks was still detectable outside the RHID in cell - 2, but disappeared in cell -1, as well as +1. Additionally, the track velocities outside the RHID, compared to cell -3, showed a shift towards lower velocity in cells -2 and -1, followed by a subtle shift towards velocity mobility in cell +1. Inside the RHID, the distribution of track velocities remained similar in cells -3, -2 and -1, but was slightly shifted towards higher velocities in cell +1.

Together, the results presented here indicate that the polar accumulation of ROP2 at the RHID is accompanied by a reduction in protein mobility as was evident from the reduction in the velocity of tracked puncta. Furthermore, a subtle reduction in mobility could be observed to precede polarization, potentially suggesting a functional role of immobilization in its polarization.

2.3.2 ROP2 immobilization depends on reduced mobility of GEF3.

To investigate whether the local immobilization of ROP2 could be caused by GEF3, I performed mobility analysis for mCitrine-GEF3 in wild type, as well as for mCitrine-ROP2 in the *gef3- 1* mutant background.

For mCitrine-GEF3, the number of traceable puncta outside the RHID was very low. In addition, the distribution of track velocities, exemplarily shown for cell stages -5 and -4 (Figure II- 10) could not be reliably represented using polynomial fitting (Table II- 4). Inside the RHID the distribution of track velocities peaked at 0.67 $\mu\text{m}/\text{sec}$ and 2.99 $\mu\text{m}/\text{sec}$ in cell -5 (Figure II- 10). Over the course of root hair development, the distribution of track velocities for GEF3 inside the RHID did not change significantly between cell stages and showed peaks at around 1 $\mu\text{m}/\text{sec}$ to 1.18 $\mu\text{m}/\text{sec}$ and approximately 3.6 $\mu\text{m}/\text{sec}$, with the exception of cell -4 that was lacking the second peak.

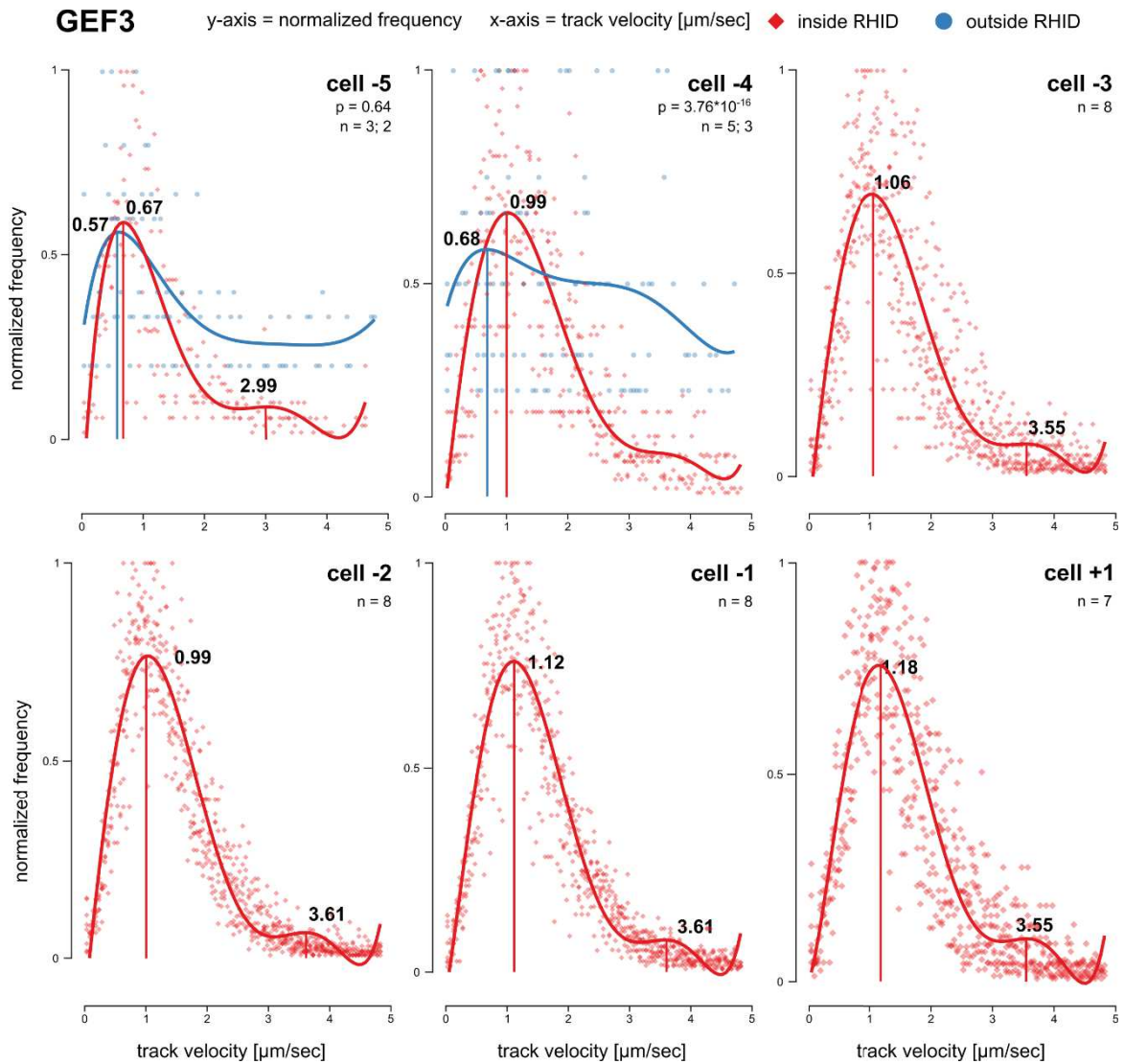


Figure II- 10: GEF3 mobility is not altered during RHID establishment. Normalized distribution of track velocities for mCitrine-GEF3 puncta inside and outside the RHID over the course of root hair development. p-values indicate the statistical difference between the distribution of velocities inside and outside the RHID and were determined by two-way ANOVA. Curves represent polynomial fits (6th degree) of the data set, vertical lines indicate local maxima of the fitted curves. R^2 values for the fits can be found in Table II- 4. The y-axis shows the normalized frequency; the x-axis shows the track velocity; n (in; out) indicates the number of cells measured.

Table II- 4: R^2 values for the polynomial fitted curves for GEF3 inside and outside the RHID (see Figure II- 10).

GEF3	-5	-4	-3	-2	-1	+1
inside	0.6247	0.6763	0.7641	0.8949	0.8844	0.8071
outside	0.2526	0.0095				

In general, GEF3 tracks showed a lower velocity compared to ROP2 tracks. Furthermore, upon ROP2 polarization (cell -3), a second, fast population of GEF3 tracks appeared. Interestingly, GEF3 tracks showed a tendency towards an increase in velocity upon ROP2 polarization while ROP2 tracks showed a reduction in velocity, which then led to its polarization in the following cell stage. This observation suggests that the two proteins mutually influence their mobility, most likely by protein-protein interactions. This hypothesis however requires further investigation, by for example measuring the mobility of GEF3 puncta in the *rop2rop4* double mutant background.

Table II- 5: p-values for the mobility distributions of GEF3, tested by two way ANOVA.

p-values	-6 vs -5	-5 vs -4	-4 vs -3	-3 vs -2	-2 vs -1	-1 vs +1
RHID vs RHID	0.9978	0.2327	0.7591	0.9903	0.9651	1

In comparison, mCitrine-ROP2 puncta in the *gef3-1* mutant background generally showed distributions of track velocities that were shifted towards higher velocities (Figure II- 11). The velocity distribution inside and outside the RHID did not differ significantly, except at cell stage +1 (p-value $5.59 \cdot 10^{-7}$), while the position of velocity peaks inside and outside the RHID appeared to not differ from each other at all over the course of root hair development. The position of velocity peaks between cell stages fluctuated slightly, however, no tendencies became obvious and no significant differences could be observed either inside or outside the RHID (Table II- 6).

Table II- 6: p-values for the velocity distributions of ROP2 in *gef3-1*, tested by two-way ANOVA.

ROP2 in <i>gef3-1</i>	-5 vs -4	-4 vs -3	-3 vs -2	-2 vs -1	-1 vs +1
RHID vs RHID	0.9952	0.9920	0.9999	0.9999	0.9404
out vs out	0.9998	0.8933	0.8098	0.8098	0.9914

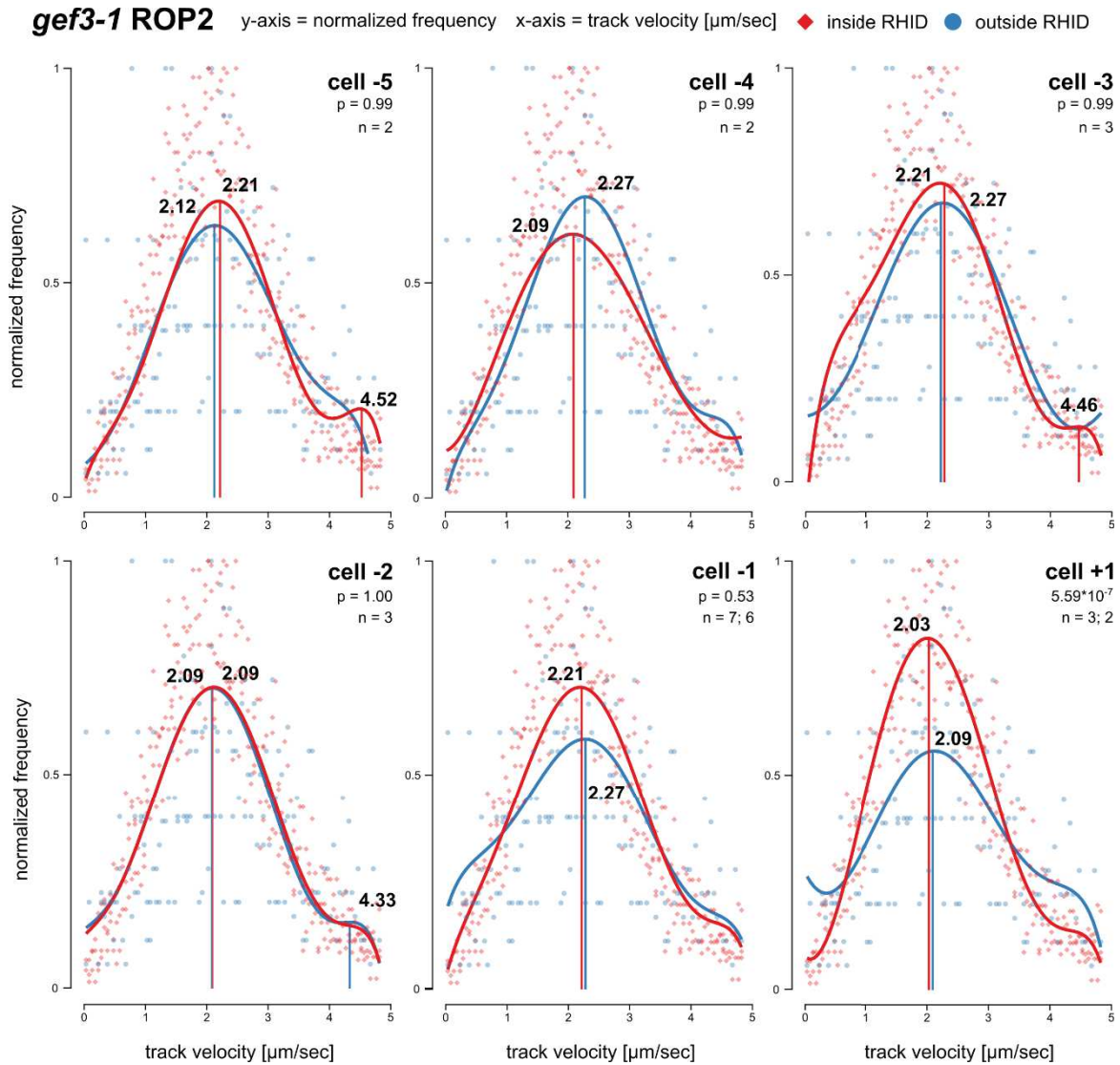


Figure II- 11: ROP2 immobilization during root hair development depends on GEF3. Normalized distribution of track velocities for mCitrine-ROP2 puncta in the *gef3-1* mutant background, inside and outside the RHID over the course of root hair development. p-values indicate the statistical difference between the distribution of velocities inside and outside the RHID and were determined by two-way ANOVA. Curves represent polynomial fits (6th degree) of the data set, vertical lines indicate local maxima of the fitted curves. R² values for the fits can be found in Table II- 7. The y-axis shows the normalized frequency; the x-axis shows the track velocity; n (in; out) indicates the number of cells measured.

Table II- 7: R² values for the polynomial fitted curves for *gef3-1* ROP2 inside and outside the RHID (see Figure II- 11).

<i>gef3-1</i> ROP2	-5	-4	-3	-2	-1	+1
inside	0.6356	0.5661	0.6098	0.7594	0.5939	0.8833
outside	0.5813	0.6220	0.5873	0.7519	0.3701	0.2842

In line with the distribution of track velocity that I have previously reported, at cell stage - 1 the median displacement (that is the distance a track has moved) for GEF3 puncta was significantly lower compared to ROP2 puncta (Figure II- 12, A). No significant difference between inside and outside the RHID could be measured for ROP2 tracks, either in wild type or in the *gef3-1* mutant background. However, I observed a tendency towards an increased displacement for ROP2 in *gef3-1*. Interestingly, the median displacement for the constitutively active ROP2 (*rop2CA*) was significantly lower than for ROP2 outside the RHID and ROP2 in *gef3-1*, both in- and outside the RHID (Figure II- 12, A). No significant difference for the displacement of *rop2CA* tracks could be determined in comparison to GEF3. Additionally, the ROP2 variant lacking the first 79 aa (*rop2 Δ N79*), rendering it unable to physically interact with GEF3, did not show an accumulation in nanoclusters (Figure II- 12), suggesting that the nanoclusters could be the sites where ROP2 is immobilized by the interaction with GEF3.

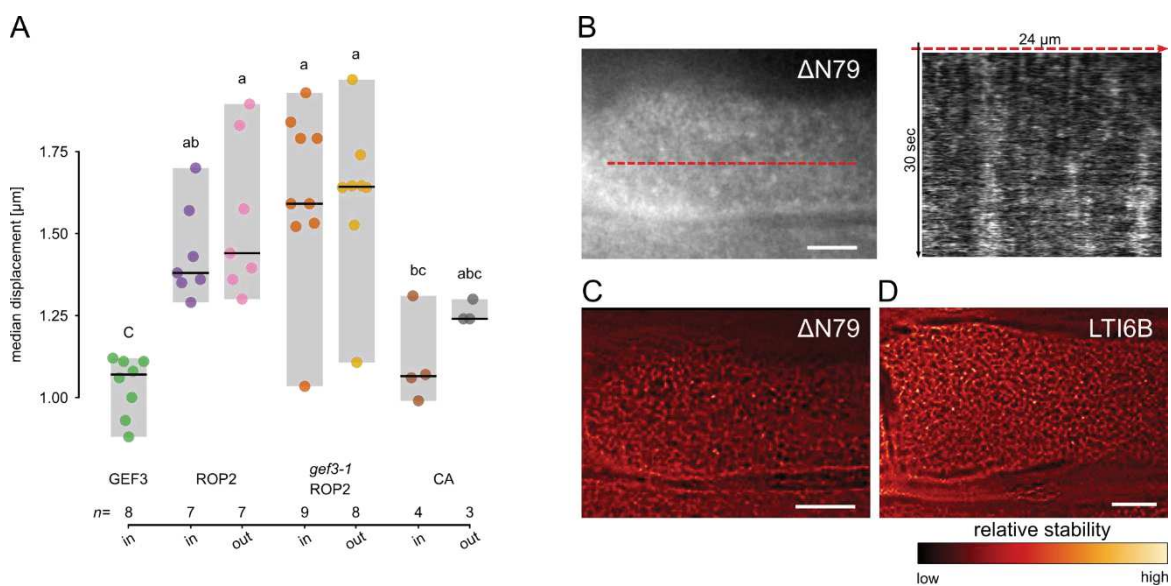


Figure II- 12: The displacement of ROP2 is influenced by its activation as well as by GEF3. (A) Median displacement of mCitrine tagged GEF3, ROP2 and *rop2CA* dots inside (in) and outside (out) of the RHID. Center lines represent median values; gray boxes represent the data range; n indicates the number of cells measured and letters represent the result of an ANOVA-Tukey test (significance value = 0.01; same letters indicate no significant difference). All measurements were performed in cells of the developmental stage -1. (B) Single slice of a VAEM time-lapse movie of ROP2 Δ N79 and a kymograph drawn along the indicated line. (C) SRRF reconstruction of the same VAEM time-lapse movie shown in panel (B). (D) SRRF reconstruction of a VAEM time-lapse movie of a trichoblast from a plant stably expressing LTI6B-GFP under the control of the 35S promoter. The scale bar represents 5 μ m.

Taken together, the data presented in this chapter show that the reduced mobility for ROP2 at the RHID is dependent on the presence of GEF3 which is accompanied by a GEF3-dependent reduction in displacement. Furthermore, the localization of ROP2 into nanoclusters in the RHID is dependent on its N-terminus, which has previously been shown to be involved in protein-protein interactions with GEF3.

2.3.3 Do ROP2-nanoclusters depend on its activity state?

Since *rop2CA* tracks showed a reduced displacement (Figure II- 12) and since the FRAP measurements for *rop2CA* showed a lower recovery rate compared to ROP2 (Figure II- 1), it seems plausible to hypothesize that the reduced mobility of ROP2 at the RHID is caused by a local activation. To further investigate the effect of the activity status of ROP2 on its mobility, I performed tracking analysis for mCitrine-*rop2CA*. The main peak in the distribution of track velocity for *rop2CA* puncta showed a shift towards lower mobility (Figure II- 13, A), compared to ROP2 tracks at the same cell stage (Figure II- 9). This shift was statistically significant (Table II- 8).

rop2CA puncta were visually indistinguishable from ROP2 puncta in that they appeared as position stable discontinuous stripes in VAEM time lapse kymographs, as well as nanoclusters in SRRF reconstructions (Figure II- 13, B and C). In contrast to ROP2 puncta however, these clusters were evenly distributed over the whole cell surface, which was in line with the loss of polar accumulation of *rop2CA* at the RHID (Chapter I, Figure I- 7), and no statistically significant difference between the distribution of track velocities inside compared to outside the RHID in cell -1 and +1 could be observed (Figure II- 13, A).

Table II- 8: p-values for the velocity distributions of *rop2CA* in comparison to ROP2 at the RHID of the cell stages -1 and +1, tested by two-way ANOVA.

p-value	-1	+1
RHID (<i>rop2CA</i>) vs RHID(ROP2)	5.18*10 ⁻⁵	0.4168

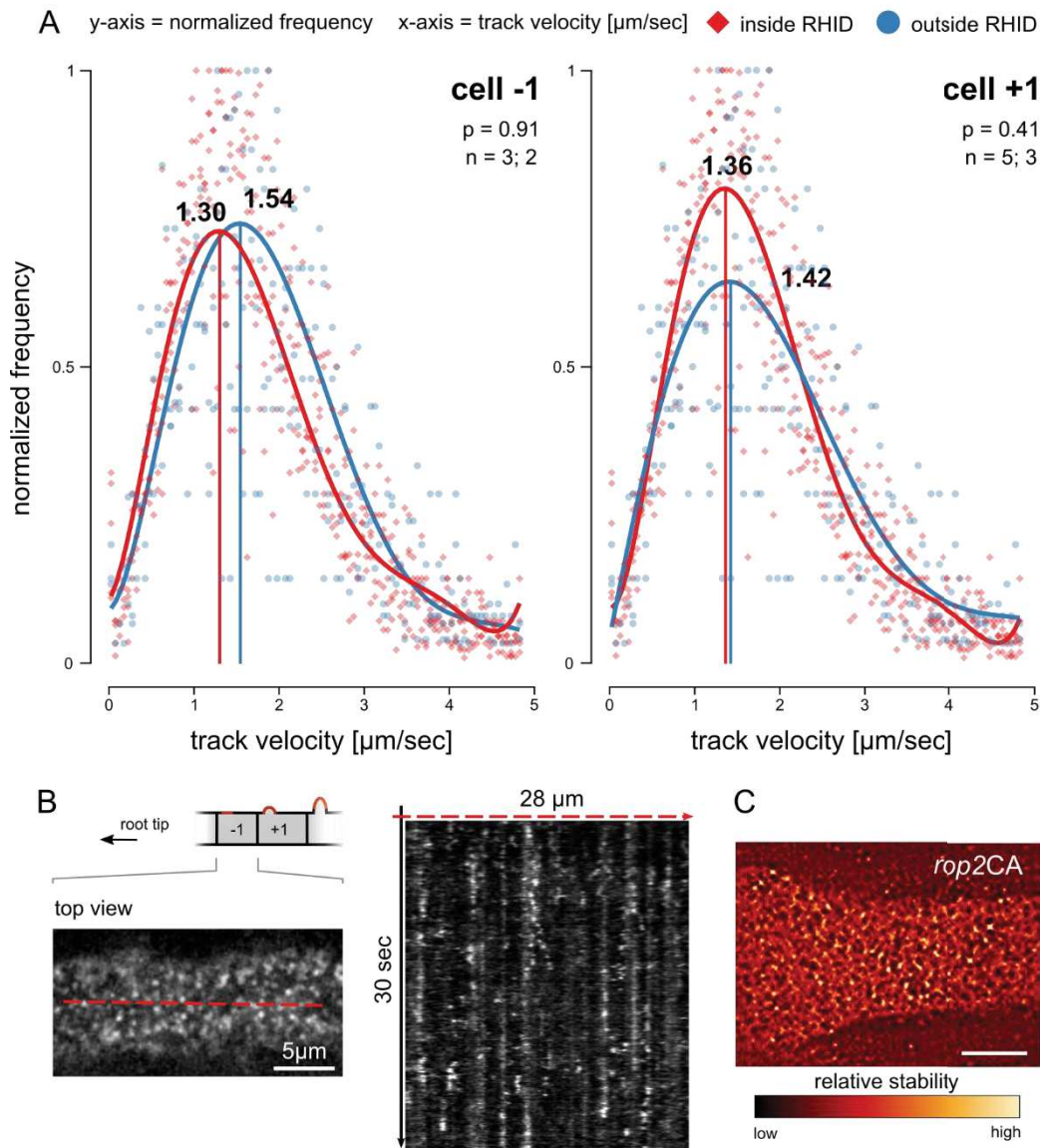
rop2CA

Figure II- 13: Activation of ROP2 caused a reduction in protein mobility as well as its accumulation in nanoclusters. (A) Normalized distribution of track velocities for mCitrine- *rop2CA* puncta, inside and outside of the RHID in trichoblast cells of stage -1 and stage +1. P-values indicate the statistical difference between the distribution of velocities inside and outside the RHID and were determined by two-way ANOVA. Curves represent polynomial fits (6th degree) of the data set; vertical lines indicate local maxima of the fitted curves. R² values for the fits can be found in Table II- 9. The y-axis shows the normalized frequency; the x-axis shows the track velocity; n (in; out) indicates the number of cells measured. **(B)** Single slices of a VAEM time lapse stacks (left panel) and a kymograph (right panel) drawn along the red, dashed line. Note that the kymograph was created from a time lapse stack with enhanced contrast. **(C)** SRRF reconstruction of a trichoblast cell expressing *rop2CA*. The scale bar represents 10 μm in (C) and 5 μm in (B).

Table II- 9: R² values for the polynomial fitted curves for *rop2CA* inside and outside the RHID (see Figure II- 13).

<i>rop2CA</i>	-1	+1
inside	0.7413	0.8485
outside	0.8416	0.6107

To complete our understanding of the role of the ROP2 activity status on ROP2 polarization and to investigate the hypothesis that the mobility of GDP-ROP2 should be lower than the mobility of GTP-ROP2, I next aimed to measure the distribution of track velocities for the second ROP2 activity mutant: *rop2DN*. I was able to observe mobile *rop2DN* using VAEM, despite the membrane association of *rop2DN* being relatively low (Chapter I, Figure I- 7). The distribution of velocities peaked at 0.69 $\mu\text{m}/\text{sec}$ inside the RHID and at 0.75 $\mu\text{m}/\text{sec}$ outside the RHID in cell stage -1 (Figure II- 14). This result was in line with the previously shown FRAP measurements, where the mobile fraction for *rop2DN* was lower than for ROP2 and *rop2CA* (Table II- 1). Since the signal intensity of induced *rop2DN* was very low, even after prolonged induction, it is possible that these results may be influenced by autofluorescence (caused by, for example, components of the cell wall).

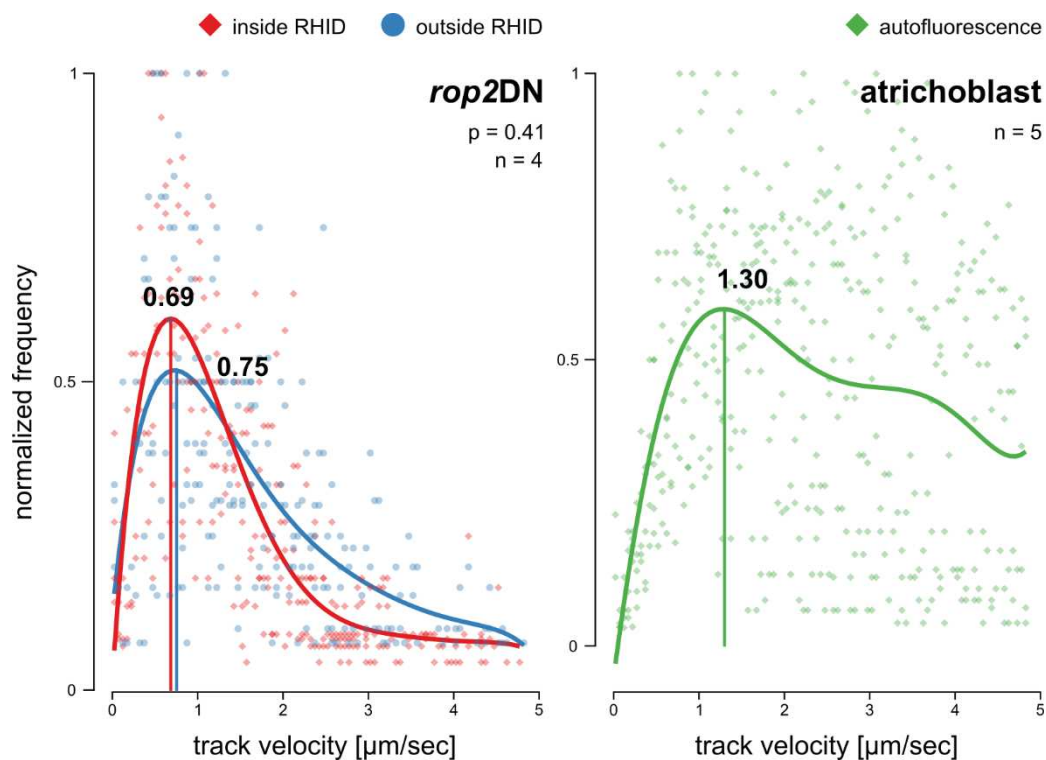


Figure II- 14: GDP-locked ROP2 showed a reduced mobility in the plasmamembrane of root hair cells. (A) Normalized distribution of track velocities for mCitrine- *rop2DN* puncta, inside and outside of the RHID in trichoblast cells of stage -1. P-values indicate the statistical difference between the velocity distribution inside and outside the RHID and were determined by two-way ANOVA. (B) Normalized distribution of track velocities for autofluorescent puncta in atrichoblasts of wild type plants. Curves represent polynomial fits (6th degree) of the data set; vertical lines indicate local maxima of the fitted curves. R^2 values for the fits can be found in Table II- 10. The y-axis shows the normalized frequency; the x-axis shows the track velocity; n indicates the number of cells measured.

Table II- 10: R² values for the polynomial fitted curves for *rop2DN* inside and outside the RHID, as well as for autofluorescent particles of atrichoblasts from wild type plants (see Figure II- 14).

	RHID(<i>rop2DN</i>)	outside(<i>rop2DN</i>)	autofluorescence
R ² values	0.6132	0.3640	0.1724

In a parallel experiment, I had gathered preliminary data on autofluorescence in wild type root epidermis cells. The results of a tracking analysis of autofluorescent puncta could not be described with polynomial fitting very well, potentially due to a more uniform distribution of track velocities. However, the fitted distribution of track velocities showed a peak at 1.3 $\mu\text{m}/\text{sec}$ with an R² value of 0.1724 (Table II- 10) - which was different from the velocity peak observed for *rop2DN* (Figure II- 14). It has to be noted though, that both these experiments have been performed independently from each other and that the mobility of autofluorescent puncta measured in atrichoblasts cannot serve as a direct control experiment for the low expressing *rop2DN* plants. For instance, autofluorescence may differ between trichoblast and atrichoblast cells, very likely reflecting differences in the composition of the cell wall between these cells (see also Chapter III), and the mobility of autofluorescent puncta in trichoblasts remains to be determined. These preliminary results however, do not support the suspicion that the tracking analysis in the *rop2DN* plants may just be the analysis of autofluorescence.

Together with the result obtained in FRAP measurements (Figure II- 1), the tracking analysis of *rop2DN* puncta, further indicates that the protein behaves relatively immobile. The mobility data regarding *rop2CA* is in line with the measurements of its displacement as well as the FRAP measurements and allows for the conclusion that the immobilization that I could show for ROP2 at the RHID is due to a locally increased concentration of GTP-ROP2.

2.3.4 Does S-acylation influence ROP2 polarity and mobility?

It has been shown that ROP6 is transiently S-acylated upon GTP binding and gets partitioned into detergent-resistant membranes (Sorek et al., 2017). From this, the authors hypothesized a general mechanism in which the association between ROPs and stable PM domains is regulated by activation-dependent S-acylation, which in turn causes polarization of ROP proteins. Since I could show that ROP2 localized into nanoclusters at the RHID in a GEF3-dependent and most likely also activity-dependent manner, I aimed to investigate

whether the postulated idea of activation-dependent, transient S-acylation could be a plausible mechanism for ROP2 polarization.

In addition to the C-terminal cysteine within the CaaL motive, ROP2 contains 3 additional internal cysteines which could potentially be S-acylated (Figure I- 2). To determine whether S-acylation is involved in ROP2 mobility, polarization or function, I investigated a plant line, expressing a ROP2 variant where the relevant cysteine residues (C8, C20 and C157; compare Figure I- 2) have been substituted by alanine residues (named *rop2ΔC* from now on). This plant line, expressing the *rop2ΔC* protein under the control of the estradiol inducible *Ubiquitin10* promoter has been generated by Philipp Denninger, who also has performed a preliminary analysis (Denninger, 2018).

I used VAEM and particle tracking analysis to determine the velocity distribution of mCitrine-*rop2ΔC* puncta in the PM of *Arabidopsis* trichoblasts. The time lapse movies of *rop2ΔC* were imaged with a frequency of 6.67 fps (instead of 16.67 fps, as had been done in all previous VAEM experiments). In order to better compare these data to the previous data, I processed existing ROP2 time lapse stacks and reduced their temporal resolution to 8.3 fps by deleting every second frame. This allowed for a more consistent comparison of *rop2ΔC* data to ROP2 data, even though it is clear that this can only serve as a first approximation.

Table II- 11: R² values for the polynomial fitted curves for ROP2 and *rop2ΔC* inside and outside the RHID (see Figure II-15).

cell stage -1	ROP2	<i>rop2ΔC</i>
Inside	0.4376	0.5623
outside	0.2861	0.4559

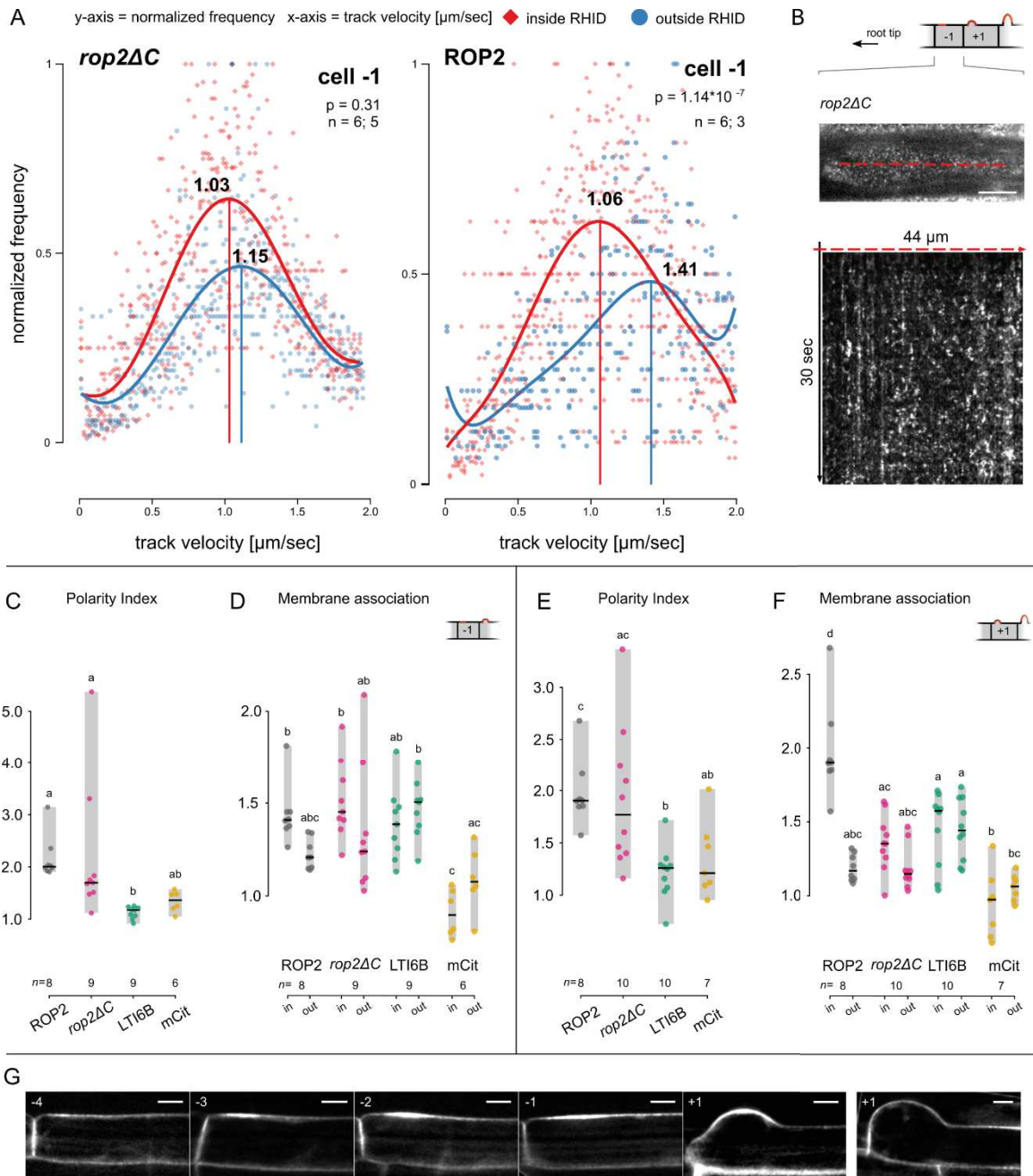


Figure II- 15: S-acylation of ROP2 does not reduce protein mobility, polarization or membrane association. (A) Normalized distribution of track velocities for mCitrine-*rop2 ΔC* puncta (left panel) and mCitrine-ROP2 puncta (right panel), inside and outside the RHID at cell stages -1. p -values indicate the statistical difference between the velocity distribution inside and outside the RHID and were determined by two-way ANOVA. Curves represent polynomial fits (6th degree) of the data set, vertical lines indicate local maxima of the fitted curves. R^2 values for the fits can be found in Table II- 11. The y-axis shows the normalized frequency; the x-axis shows the track velocity; n (in; out) indicates the number of cells measured. **(B)** Single slices of a *rop2^{C8,20,157A}* VAEM time lapse stack and a kymograph drawn along the red, dashed line. Note that the kymograph was created from a time lapse stack with enhanced contrast. **(C-F)** Polarity index of ROP2, *rop2^{C8,20,157A}*, LTI6B and mCitrine (mCit) at cell stage -1 **(C)** and +1 **(E)**. Membrane association of ROP2, *rop2^{C8,20,157A}*, LTI6B and mCit inside (in) and outside (out) of the RHID at cell stage -1 **(D)** and +1 **(F)**. Center lines represent median values; gray boxes represent the data range; n indicates the number of cells measured and letters represent the result of an ANOVA-Tukey test (significance value = 0.01; same letters indicate no significant difference). Measurements of ROP2, LTI6B and mCit are shown for comparability, but are the same as already presented in Figure I- 3. **(G)** Representative images of *rop2^{C8,20,157A}* at the indicated cell stages; the rightmost image shows a trichoblast exhibiting a ROP2-overexpression phenotype. The scale bars represent 10 μm .

In cell stage -1, the distribution of track velocities of *rop2ΔC* did not show a significant difference between inside and outside the RHID (p-value = 0.31; Figure II- 15). Comparing *rop2ΔC* with ROP2, track velocity distributions outside the RHID showed a significant difference from each other (p-value = 1.3×10^{-9}), but not inside the RHID (p-value = 0.2699). Similarly, when looking at the transition of cell stage -1 to cell stage +1, inside the RHID both proteins showed no differences between the two cell stages (*rop2ΔC*: p-value = 0.787; ROP2: p-value = 0.999). Similar to ROP2, *rop2ΔC* puncta were positional stable at the RHID. However, unlike for ROP2 such clusters were also detectable outside of the RHID (Figure II- 15, B).

With regard to polarization at the RHID, *rop2ΔC* behaved indistinguishable from ROP2: *rop2ΔC* polarized as early as cell stage -4 (Figure II- 15, G) and its polarity index was not significantly different from ROP2 at cell stage -1 as well as at cell stage +1 (Figure II- 15, C and E). The same was true for the membrane association of both proteins with the PM in stage -1, while at cell stage +1 the membrane association of *rop2ΔC*, both inside and outside the RHID, was reduced to the same level as ROP2 outside the RHID (Figure II- 15, D and F). Already 4 h after induction *rop2ΔC* plants started to show phenotypes reminiscent of ROP2 overexpression phenotypes such as an increase of cytosolic signal due to a surplus of protein as well the formation of wider bulges, which were shifted towards the root tip end of the cell (Figure II- 15, G), further supporting that there was no functional difference between *rop2ΔC* and wild type ROP2. The reduction in mobility of *rop2ΔC* outside the RHID that was measured at cell stage -1 can be explained by the overexpression phenotype since this region would bulge out in the next cell stage, forming a widened bulge. To conform this assumption, it would be necessary to perform particle tracking on ROP2 puncta in ROP2 overexpression plants.

Taken together, my results showed that despite its inability to be S-acylated *rop2ΔC* behaved like regular wild type ROP2: Polarization, timing of polarization and association with the PM at the RHID were not affected and the protein induced the same overexpression phenotypes as ROP2. Likewise, the distribution of track velocities inside the RHID remained unchanged (unlike *rop2CA*, where the track velocities inside the RHID were shifted towards lower velocities) and the reduction in *rop2ΔC* mobility outside the RHID can be attributed to the effect of the overexpression phenotype. Therefore, it can be

concluded, that the internal cysteines that are hypothesized to be S-acylated in an activation-dependent manner, are not involved in ROP2 polarization, ROP2 function in site selection or protein mobility at the RHID.

2.4. Are other proteins of the tip growth machinery also recruited into nanoclusters at the RHID?

So far, I have been able to show that ROP2 and GEF3 both localize in nanoclusters at the RHID. However, it remains unclear whether these are actually the same structures and whether they play a functional role in root hair development. Over the past years, several studies have indicated the presence of nanodomains for a variety of proteins in plants (recent examples: Martiniere et al., 2019; Pan et al., 2019; Platre et al., 2019; Smokvarska et al., 2020; Gronnier et al., 2020). To understand whether there is a functional relevance to nanoclusters and to fully understand the function of such nanodomains, it is necessary to understand the protein composition within them. One approach to shed light on the proteome of the nanoclusters we have observed, assuming that they indeed have a functional relevance, would be to test known components of the tip growth machinery for their ability to co-localize in such structures.

In order to investigate the nanocluster-proteome, it was necessary to obtain another fluorophore that showed a similar photochromic behavior like mCitrine and could therefore be used in co-localization experiments. Many proteins have been described to show photochromic properties under certain conditions, however, since fluorescence intermittency is influenced by factors such as pH and electronegativity of the surrounding medium, which may differ between different organisms and cellular environments, it is essential to always confirm photochromic behavior specifically. In my case, I aimed to find a fluorophore that showed fluorescence intermittency in the cellular environment at the PM close to the plant cell wall, as well as sufficiently bright emission at a wavelength that can be clearly distinguished from cell wall autofluorescence caused by aromatic and electron rich components. This is especially important in VAEM where the cell wall, and therefore consequently also its autofluorescence, is overrepresented due to the angulated laser and the resulting small imaging depth.

I investigated 6 different fluorescent proteins, representing different positions along the spectrum of wavelengths, for their applicability in VAEM: GFP (originally from *A. Victoria*), its yellow derivatives Citrine and mCitrine and its blue derivative mTurquoise2 as well as mNeonGreen derived from *B. lanceolatum* and mRuby2 from *E. quadricolor*. GFP, Citrine and mCitrine all showed fluorescence intermittency and their emission spectra did not conflict with cell wall autofluorescence. In contrast, I could not observe fluorophore blinking for mNeonGreen, while mTurquoise2 emission was not sufficiently different from autofluorescent signal. mRuby2 on the other hand, showed fluorophore blinking as well as a good signal to background ratio and therefore seemed well suited for VAEM measurements together with GFP, Citrine or mCitrine.

2.4.1 Can VAEM-SRRF be used to elucidate the function of ROP2 and GEF3 nanoclusters in the RHID by co-localization experiments?

To test whether mRuby2 could be used in co-localization experiments with mCitrine, I aimed to co-localize ROP2 fusion proteins tagged with either of the fluorophores. To this end, I used plants expressing mRuby2-ROP2 and mCitrine-ROP2, both under the endogenous *ROP2* promoter, in wild type background.

In VAEM, mRuby2-ROP2 behaved similar to what I have observed for mCitrine-ROP2: The fusion protein appeared in diffraction limited dots, with frequent appearance and disappearance and little lateral mobility. In line with my previous findings for mCitrine-ROP2, within the RHID mRuby2-ROP2 dots were more position stable compared to outside the RHID (Figure II- 16, D), where in general, mRuby2-ROP2 dots were rarely visible. To further test if the fluorophore used for fluorescent tagging would impact negatively on ROP2 protein mobility or on measurability of puncta behavior, I performed particle tracking and analyzed the distribution of track velocities. In comparison to mCitrine-ROP2 puncta, mRuby2-ROP2 puncta were not significantly different in the distribution of track velocities inside the RHID of cell stage - 1 (p-value = 0.9995). Outside the RHID at the same cell stage however, the velocity distributions of mCitrine-ROP2 puncta showed a significant difference from mRuby2-ROP2 puncta (p-value = 0.007). It needs to be noted though, that the number of biological replicates for mRuby-ROP2 outside the RHID was only two and

that the number of traceable dots was relatively low due to the fact that after sample preparation one of the two the specimen was not positioned perfectly parallel to the cover

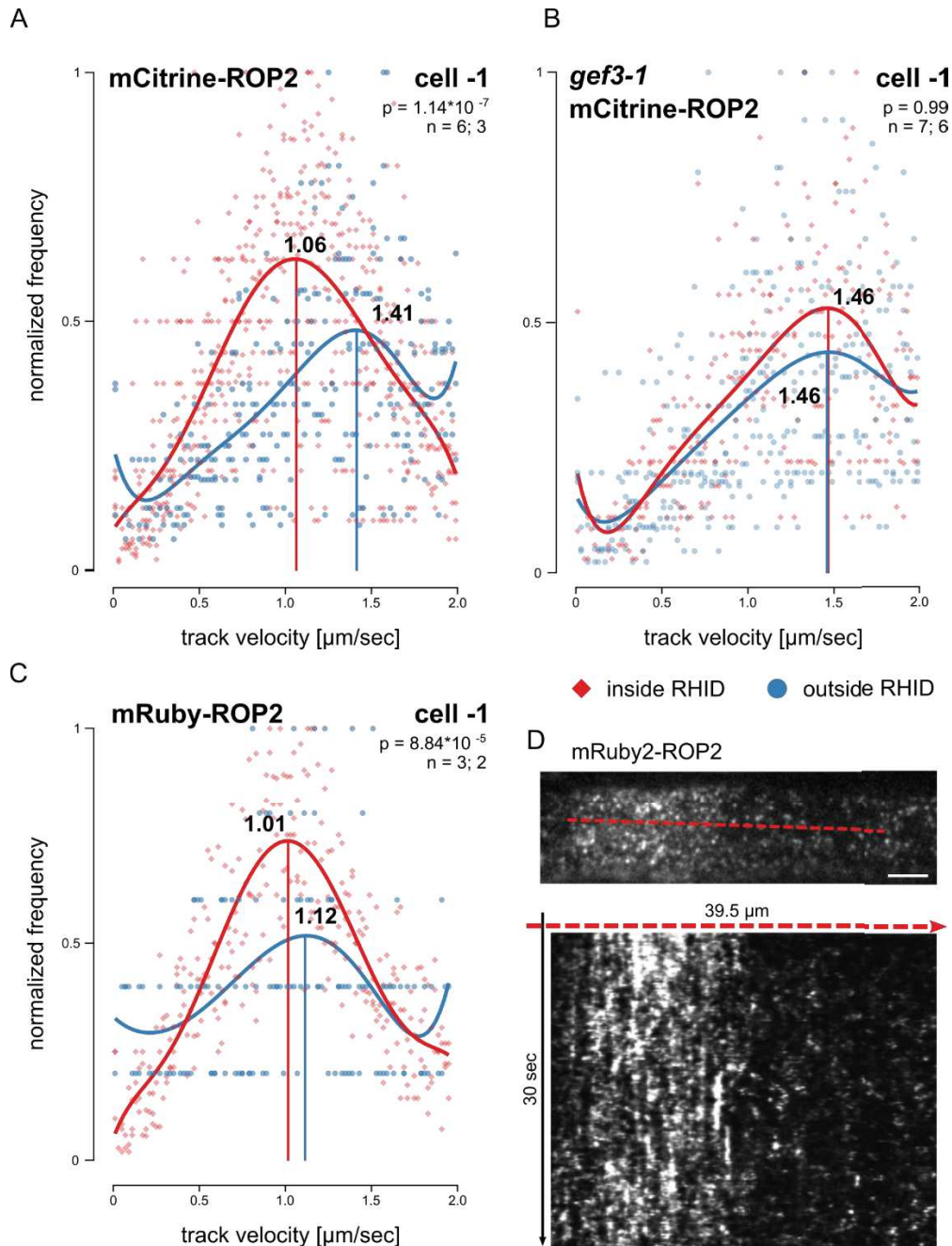


Figure II- 16: The mobility of ROP2 proteins was independent of the fluorophore-tag. (A-C) Normalized track velocities for mCitrine-ROP2 puncta in wild type plants (A) and in the *gef3-1* mutant background (B) and normalized track velocities for mRuby2-ROP2 puncta in wild type plants (C), inside and outside the RHID in cell stage -1. Curves represent polynomial fits (6th degree) of the data set; vertical lines indicate local maxima of the fitted curves. P-values indicate the statistical difference between the velocity distribution inside and outside the RHID and were determined by two-way ANOVA; n (in; out) indicates the number of cells measured. R² values for the fits can be found in Table II- 12. The y-axis shows the normalized frequency; the x-axis shows the track velocity; n indicates the number of cells measured. Measurements for mCitrine-ROP2 in wild type background as well as the *gef3-1* mutant background are shown for comparability, but are the same as presented previously in Figure II- 15 and -Table II- 11. (D) Single slices of a mRuby2-ROP2 VAEM time lapse stack and a kymograph drawn along the red, dashed line. Note that the kymograph was created from a time lapse stack with enhanced contrast. The scale bar represents 10 μm .

slip, but was slightly tilted. Therefore, it seems plausible to assume that the statistically significant difference between mCitrine-ROP2 puncta and mRuby2-ROP2 puncta was rather caused by insufficient fitting of the data (R^2 of 0.1014, Table II- 12) and the low number of puncta. Overall however, my data suggested that mRuby2 and mCitrine were both equally suited for co-localization experiments using VAEM.

Table II- 12: R^2 values for the polynomial fitted curves for mCitrine-ROP2 in the *gef3* mutant background and mRuby2-ROP2 in the wild type background inside and outside the RHID (see Figure II- 16). R^2 values for mCitrine-ROP2 fitting can be found in Table II- 11.

cell stage -1	mCitrine-ROP2 in <i>gef3-1</i>	mRuby2-ROP2
inside	0.4078	0.7007
outside	0.2757	0.1014

In a proof-of-principle experiment using VAEM and SRRF, I tested for co-localization of mCitrine-ROP2 with mRuby2-ROP2 in wild type plants. In a first attempt, I imaged unfixed trichoblast cells, acquired time lapse movies using sequential scanning of both fluorophores and performed SRRF reconstruction (Figure II- 17). Both fusion proteins showed a similar, mesh-like sub-compartmentalization of the RHID into nanoclusters that overlapped with a correlation coefficient of 0.171 (Figure II- 17, upper panel). Since deconvolution algorithms like the SRRF algorithm amplify local differences in signal intensities, they are prone to create imaging artefacts that at first glance can be mistaken as biological structures. Therefore, I determined the correlation efficiency of structures outside the specimen which logically must be derived from background noise. Since noise is occurring stochastically, it should be distributed randomly and should therefore lead to random structures in SRRF reconstructions. The correlation coefficient of such random structures can then serve as a measure for random co-localization. Indeed, the background signal outside the specimen showed a structured appearance in SRRF reconstructions, which however differed from the ROP2 structures in regard to density and cluster size. The correlation coefficient of the reconstructed noise was determined to be 0.451 (Figure II- 17, lower panel), which was a higher value than the correlation coefficient for mCitrine-ROP2 and mRuby2-ROP2. This result indicated that mCitrine-ROP2 did not co-localize with mRuby2-ROP2.

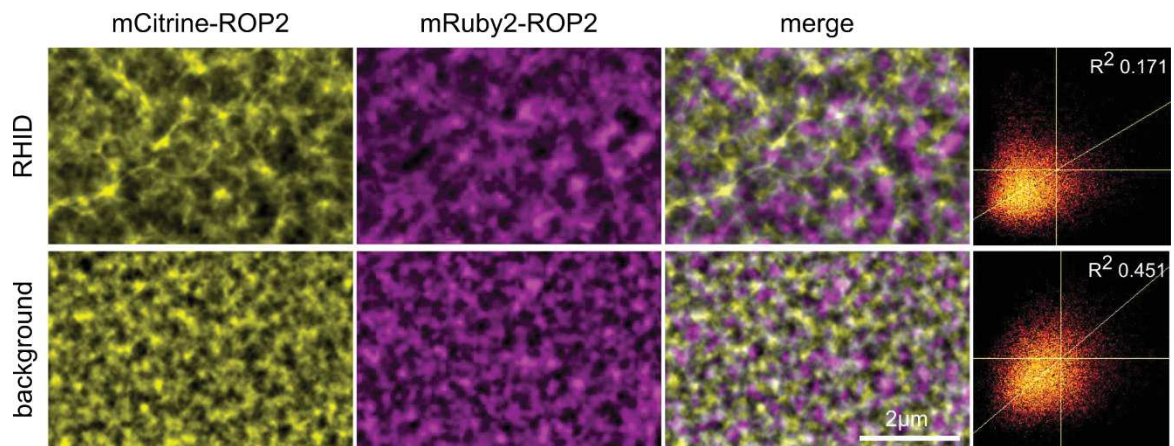


Figure II- 17: Test for co-localization of mCitrine-ROP2 and mRuby2-ROP2 in SRRF reconstructions. Single channel SRRF images of mCitrine-ROP2 (left), mRuby2-ROP2 (middle) and their merge (right), in a region within the RHID (upper panel) and in the background outside the sample (lower panel). The scale bar represents 2 μm . Correlation maps of the images from the respective panel including the correlation coefficient R^2 . Images were taken at a root hair of cell stage +1 from an unfixed *Arabidopsis* root stably co-expressing mRuby2-ROP2 and mCitrine-ROP2, both under the control of the endogenous *ROP2* promoter in wild type background.

To test if this lack of co-localization was due to protein mobility, I performed chemical fixation. Unfortunately, VAEM micrographs of fixed samples revealed, that the blinking behavior of the fluorophores was affected, which was either due to the chemical fixation process itself or due to the fact that the cells were dead. Vacuole rupture during cell death might have caused a change in the electrochemical properties of the cell, reducing the potential of the fluorophore to undergo fluorophore blinking. Additionally, vacuole fragmentation and plasmolysis may have led to an increase in autofluorescence and may have hampered with the detection of single dots. Similar to unfixed images, SRRF reconstructions did not show co-localization of ROP2 nanoclusters (with a correlation coefficient R^2 of 0.106, data not shown).

It is important to keep in mind, that while the decrease in (emitting) fluorophore density due to fluorophore blinking makes the visualization of these nanoclusters possible, at the same time it complicates co-localization, since only a fraction of all fluorophores present is visible over the course of time-lapse recording. Therefore, the chance to localize two fusion proteins into one spot, especially with a high-resolution method, is rather low.

As a result, I have to conclude, that with the methods currently available in our lab, it is not possible to co-localize mCitrine-ROP2 with mRuby2-ROP2. Lacking a proof-of-principle for this essential positive control for co-localization studies, I did not attempt to further test co-localization of ROP2 with other proteins of the tip growth machinery.

2.4.2 Do other proteins of the tip growth machinery also localize into nanoclusters?

In order to investigate the functionality of nanoclusters in the RHID, I aimed to analyze whether other proteins that are part of the tip growth machinery also localize in nanoclusters. A first candidate to check was BRK1, a member of the SCAR/WAVE complex, which is involved in regulating the ARP2/3 complex and therefore actin nucleation. It has been shown that ROP2 interacts with the SCAR/WAVE complex and that BRK1 localizes into distinct clusters at the PM of Arabidopsis trichomes (Basu et al., 2004; Szymanski, 2005; Yanagisawa et al., 2013), raising the hypothesis that BRK1 might localize in nanoclusters in Arabidopsis trichoblasts as well.

BRK1 protein showed a polar accumulation within trichoblasts in the wild type background, starting as early as cell stage -3, and was exclusively localized to the RHID from cell stage -1 (Figure II- 18, A, C). This polar accumulation was lost in *gef3-1* mutant plants prior to bulging at cell stage -1, but polar accumulation at the RHID could still be observed at cell stage +1 (Figure II- 18, B-C). Using VAEM and SRRF reconstruction, I could observe the localization of BRK1 into nanoclusters, that polarized at the RHID (Figure II- 18, D). In the wild type background, at cell stage -1, BRK1 nanoclusters were distributed over the whole RHID, whereas in cell stage +1 BRK1 nanoclusters could only be found at a confined region at the tip of the bulge. In the *gef3-1* mutant background BRK1 was still able to associate with nanoclusters, however their localization was not restricted to the RHID. At cell stage +1, BRK1 nanoclusters were also restricted to the RHID, but still covered a broader area and were clearly not as confined and as densely packed as in the wild type background (Figure II- 18, D). These data led me to the conclusion, that similar to ROP2, GEF3 was, directly or indirectly, necessary for the polarization of BRK1 at the RHID prior to bulging. However, after bulging (at cell stage +1), BRK1 was still able to polarize, but to a lesser extent. The association of BRK1 with nanoclusters seemed to be independent of GEF3, whereas the restriction of these clusters to a confined region within the RHID seemed to depend on the presence of GEF3.

Since the restriction of BRK1 accumulation to the RHID was GEF3-dependent, I next investigated whether GEF3 was sufficient for BRK1 recruitment into ectopic patches upon GEF3 overexpression. Therefore, I co-expressed BRK1-mTurquoise2 (under the

endogenous *BRK1* promoter) and mCitrine-GEF3 (controlled by the inducible *Ubiquitin10* promoter). After inducing for an extended time, GEF3 localized into ectopic patches in trichoblast and atrichoblasts (Figure II- 18, E). In the RHID and at the tip of young root hairs, I observed the co-localization of BRK1 and GEF3. However, no signal for BRK1 could be detected within ectopic GEF3 patches. This led to the conclusion, that GEF3 is involved in polarization of BRK1, but is not sufficient and again suggested the existence of a GEF3 independent mechanism for the polarization of proteins of the tip growth machinery to the RHID. Whether the loss of BRK1 polarity in the *gef3-1* mutant resulted from the loss of ROP2 polarity or whether GEF3 can directly influence BRK1 polarization remains to be tested. To this end it would be interesting to investigate BRK1 polarity in the *rop2/rop4* double mutant. Plant lines for this experiment have been generated in this thesis, but remain to be analyzed.

So far, I have been able to show that three proteins of the root hair growth machinery localized into nanoclusters at the RHID. This raises the question, whether other PM associated proteins would show a similar behavior and whether the association with nanoclusters might even be a common mechanism.

First, I investigated ROP4, another trichoblast specific ROP, which I found to also localize into nanoclusters at the RHID and whose sub-compartmentalization at the RHID was indistinguishable from ROP2 (Figure II- 19). GEF4, which is another GEF involved in root hair outgrowth and growth regulation and which has been shown to polarize at the RHID just prior to bulging (at cell stage -1) (Denninger et al., 2019), was associated with nanoclusters in the PM of the RHID at cell stage +1 (Figure II- 19) (VAEM images: cell stage +1 corresponds to cell stage -1 in confocal microscopy). In younger trichoblast cells, GEF4 mainly localized in the cytoplasm and consequently no association with nanoclusters could be detected.

The POLLEN RECEPTOR LIKE KINASE 7 (PRK7) is expressed in roots and accumulates at the RHID at cell stage +1 (Denninger et al., 2019) and previous data from our lab has shown, that PRK7 is involved in the regulation of root hair growth and density (Shrivastava, 2018). In addition to its association with intracellular vesicles, VAEM and SRRF reconstructions showed that PRK7 associated with nanoclusters at the RHID at cell stage -1 (Figure II- 19) (which corresponds to cell stage -2 in confocal imaging). Therefore, we can assume that

PRK7 associates with the PM of the RHID already prior to root hair outgrowth and can therefore hypothesize a role of PRK7 in root hair development much earlier than previously thought.

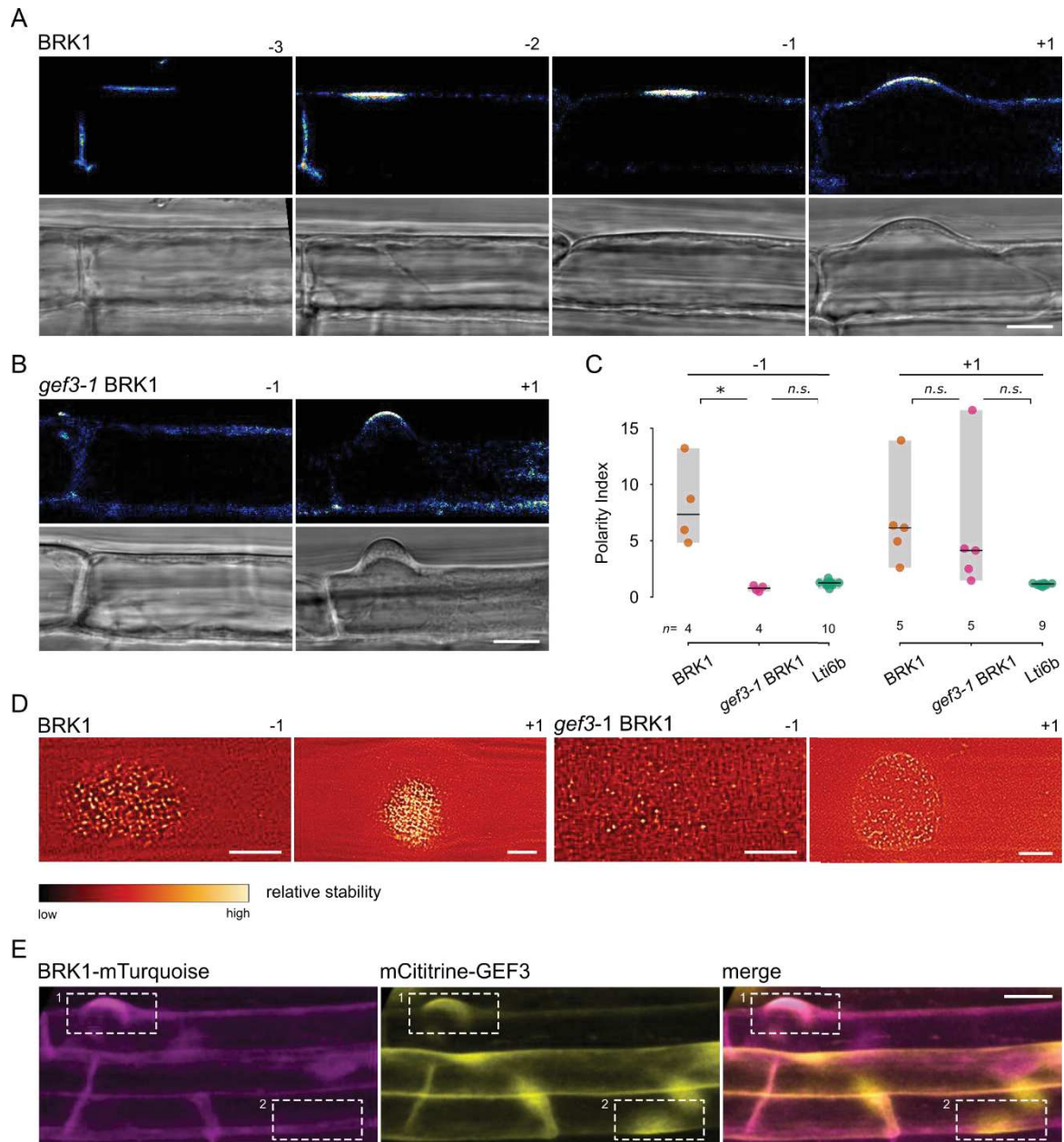


Figure II- 18: GEF3 is necessary but not sufficient to polarize Brk1 into nanoclusters at the RHID. (A-B) Representative confocal images of BRK1-YFP (BRK1) in wild type (A) and the *gef3* mutant (B) background over the course of root hair development. (C) Polarity index of BRK1, *gef3-1*BRK1 and LTI6B at cell stages -1 and +1. Measurements for LTI6B are shown for comparability, but are the same as already presented in Figure I- 3. Asterisks indicate statistically significant difference (p-value determined by Student's t-test: n.s. = p-value >0.05; * = p-value < 0.05); n represents the number of cells measured. (D) SRRF reconstructions of a VAEM time-lapse stack of BRK1-YFP in the wild type (left side) and in the *gef3-1-1* mutant background (right side) in trichoblasts of the cell stage -1 and +1. (E) Maximum intensity projection of an *Arabidopsis* root expressing BRK1-mTurquoise2 under its native promoter and mCitrine-GEF3 under the control of the estradiol inducible *Ubiquitin10* promoter. Box1 shows a trichoblast cell with co-localization; box2 shows an atrichoblast cell with no co-localization. The scale bars represent 10 μ m in (A) and (B), 5 μ m in (D) and 20 μ m in (E).

The PM localized receptor like kinase FERONIA (FER) has been shown to positively regulate root hair growth via GEF4 and GEF10 (Huang et al., 2013) and using confocal imaging has been shown to polarize at the RHID at cell stage +2 (Denninger et al., 2019). VAEM and SRRF reconstructions of FER-GFP (at the corresponding cell stage in VAEM: cell stage +1) revealed its association with nanoclusters all over the cell surface, but interestingly showed no preferential accumulation at the RHID (Figure II- 19).

The PI4P-5 kinase PIP5K3 is involved in root hair growth by synthesizing PI(4,5)P₂, which is an important structural and signaling lipid. PIP5K3 was shown to polarize at cell stage -2, whereas PI(4,5)P₂ accumulates at the RHID at cell stage +1 (Denninger et al., 2019). VAEM and SRRF reconstructions of PIP5K3 showed its association with nanoclusters at the RHID, however, the density of nanoclusters appeared to be lower compared to the other proteins investigated so far (Figure II- 19).

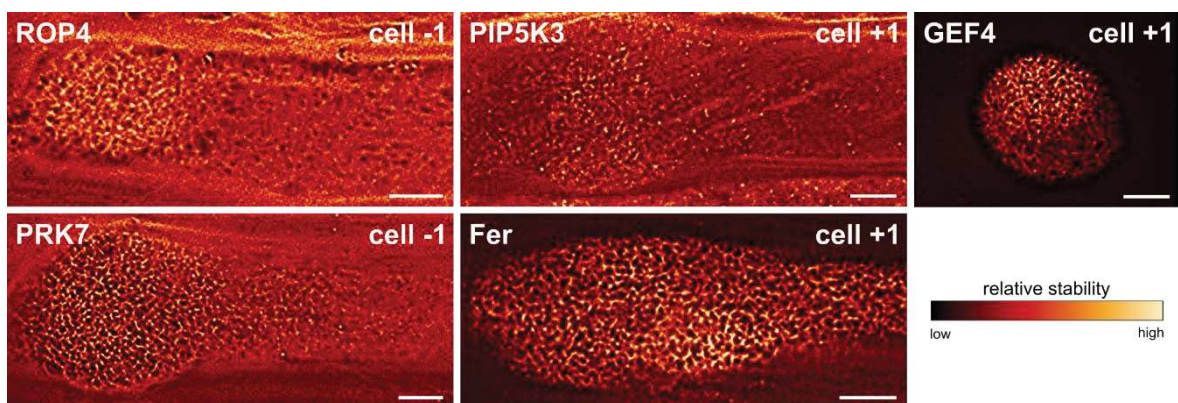


Figure II- 19: Other proteins of the tip growth machinery also localize into nanoclusters within the RHID. SRRF reconstructions of: mCitrine-ROP4 at cell stage -1; PIP5K3-mCitrine at cell stage +1; mCitrine-GEF4 at cell stage +1; PRK7-mCitrine at cell stage -1; Fer-GFP at cell stage +1;. The scale bars represent 5 μ m.

Taken together, I could show that other PM-localized proteins involved in root hair growth also associated in nanoclusters at the PM of trichoblasts. Proteins that showed no distinct polarization at the RHID (e.g. FER), still localized into nanoclusters, however these nanoclusters were distributed over the whole cell surface. This result indicates, that the organization into nanoclusters may be a general phenomenon for PM-associated proteins of the tip growth machinery. For BRK1 I could show that its association with nanoclusters was in part dependent on GEF3. However, the fact that we still see polarization and association of BRK1 with nanoclusters in the *gef3-1* mutant background, suggests that the

association of BRK1 with nanoclusters is independent of GEF3, whereas the confinement to the apex of the bulge depends on GEF3. It would be interesting to see whether this is caused by interdependencies of the proteins involved in tip growth or by spontaneous accumulation and local concentration after (GEF3-dependent) protein immobilization. Furthermore, it would greatly add to our understanding of the role of nanoclusters and their function, if we could shed light on their protein composition. Which proteins share nanoclusters and is this functionally relevant for root hair growth?

3. Discussion

The polarization of the small GTPase ROP2 at the site of root hair initiation, is a critical step in root hair development and requires precise control to ensure the spatio-temporally restricted outgrowth of a root hair. Recently, we could show that the guanine nucleotide exchange factor GEF3 acts as a landmark protein for ROP2 and is necessary to correctly target ROP2 to the RHID (Denninger et al., 2019). In this thesis I have already shown that ROP2 additionally has the potential to self-polarize in the absence of GEF3, albeit with a lower efficiency (see Chapter I). Additionally, I have presented evidence for an enrichment of GTP-ROP2, that is activated ROP2, at the root hair initiation domain (see Chapter I).

Historically, a self-polarizing mechanism based on differential diffusion rates for GTP-bound and GDP-bound (inactive) ROP2 has been postulated to be involved in ROP2 polarization and RHID positioning (Payne and Grierson, 2009). Similar mechanisms have indeed been described for other small GTPases, for an example in fission yeast (Bendezú et al., 2015).

In this thesis I aimed to gain further knowledge on the mechanisms of GEF3-dependent as well as GEF3-independent ROP2 polarization at the RHID. To this end, I closely investigated the mobile behavior of ROP2, representing a mixed pool of active and inactive protein, in wild type and in the *gef3-1* mutant background. Additionally, I have analyzed the mobility of ROP2 activity mutants, which can be imagined as the artificially nucleotide-locked extremes of a natural ROP2 population.

3.1. Local activation causes ROP2 immobilization at the RHID

From the data presented in this thesis, it can be hypothesized that GEF3 acts as an accelerator of ROP2 polarization by facilitating local activation or immobilization of GTP-ROP2 specifically at the RHID (Chapter I 2.3 and 3.2). Therefore, I analyzed the mobility of ROP2 in dependence of its activity status as well as the presence of absence of GEF3. To this end I performed fluorescence recovery after photobleaching (FRAP) measurements, as well as a combination of variable angle epifluorescence microscopy (VAEM) followed by a particle tracking analysis to determine the overall mobility of the respective protein population at the plasma membrane (PM) (see Chapter II 2.3.1 for a detailed description of

the method). From now on the latter method will be referred to as “VAEM mobility measurements”.

FRAP as well as VAEM mobility measurements revealed a reduction in mobility for ROP2 inside the RHID compared to outside the RHID (Figure II- 1 and Figure II- 9). VAEM mobility measurements further showed that the ROP2 population within the RHID, consisting of a mix of both nucleotide variants of ROP2, exhibits a subtle shift towards lower mobility already one cell stage prior to bulging. This strongly suggests that local immobilization of ROP2 is involved in or even causative for ROP2 polarization at the RHID. Along the same lines, I could show that the displacement of ROP2 puncta was lower inside the RHID compared to outside the RHID in cell stage -1 (Figure II- 12), which in turn was in line with the increased association of ROP2 with the PM at the RHID (Figure I- 7).

I have previously reported that constitutively active ROP2 (*rop2CA*) showed an increased association with the PM (Figure I- 7) and I have discussed the hypothesis that GTP-ROP2 may be enriched at the RHID and might impact on the immobilization of ROP2. Interestingly, mobility measurements using FRAP and VAEM showed a reduction in mobility of *rop2CA* at the RHID that was even stronger than for ROP2 (Figure II- 1 and Figure II- 13). Additionally, the displacement of *rop2CA* puncta was also lower than for ROP2 puncta (Figure II- 12). These findings appear plausible considering that ROP2 represents a mixed pool of GTP-bound as well as GDP-bound protein, while *rop2CA* is a pure population of GTP-locked protein. From this we can also already conclude that active and inactive ROP2 will have different properties with regard to their mobility at the RHID.

Interestingly, even though the other activity mutant, dominant negative ROP2 (*rop2DN*), exhibited a mostly cytoplasmic localization (Figure I- 7) and consequently had a low association with the PM, FRAP and VAEM measurements revealed a relatively low mobile fraction and low protein mobility (Figure II- 1 and Figure II- 14). At the same time however its recovery time was shorter compared to both ROP2 and *rop2CA* at the RHID, but higher than the recovery time of ROP2 outside the RHID (Figure II- 1). This result was in line with the result that in fission yeast the small GTPase CDC42 exhibited a faster recovery in FRAP measurements in its GDP-bound state, compared to its GTP-bound state (Bendezú et al., 2015). It is noteworthy, that the fluorescent signal of the *rop2DN* fusion protein during FRAP experiments showed a higher potential to recover inside the cytosol, compared to

the region directly at the PM (Figure II- 1, E). It is possible that *rop2DN* might exist in two subcellular populations: one subpopulation inside the cytosol that caused the fast recovery rate and another less mobile subpopulation at the PM that caused the detection of a low mobile fraction. The fact that I was able to visualize trackable *rop2DN* puncta in VAEM supports the assumption that while *rop2DN* was predominantly cytosolic, it also has the potential to reside at the PM. *rop2DN*, which has been named for the dominant negative effect of the protein caused by the block of GDP release, has been hypothesized to sequester one or multiple activating factors (Glotzer and Hyman, 1995; Berken and Wittinghofer, 2008). It is conceivable, that such an activating factor resides at the PM, binds to GDP-ROP2 and causes its activation by exchanging the GDP for a GTP. However, since *rop2DN* is mutated in a manner that prevents the replacement of GDP by GTP, it stays bound to its activator and cannot relocate to the cytosol. This hypothesis would readily explain the reduced mobility of *rop2DN* that I have observed at the PM of trichoblast cells.

A potential activating factor of ROP2 is GEF3, which is necessary for ROP2 polarization at the RHID and has been shown to physically interact with ROP2 regardless of its activity state (Denninger et al., 2019). FRAP and VAEM mobility measurements showed reduced mobility of GEF3 compared to ROP2 inside the RHID and also compared to *rop2CA* (Figure II- 2, Figure II- 10 and Figure II- 13). Furthermore, in the *gef3-1* mutant background ROP2 was more mobile at the RHID than it was in the wild type background and actually had a similar mobility as ROP2 outside the RHID in the wild type background (Figure II- 2 and Figure II- 11). These results led to the conclusion that GEF3 causes ROP2 polarization at the RHID by local immobilization.

Interestingly, even though I could measure ROP2 polarization in the *gef3-1* mutant at the RHID using VAEM at cell stage +1 (Figure II- 8), this polarization was not accompanied by a measurable decrease of protein mobility at the RHID specifically (Figure II- 11). At a first glance this seems to contradict the finding that protein immobilization precedes visible polarization. The observed discrepancy in polarization timing, can be explained when considering the increase of spatial resolution in VAEM due the relatively specific excitation of the PM and the reduction of excited fluorophores within the cytoplasm. In contrast, if a bulging hair is imaged from a side view perspective, as it is done in confocal microscopy, the excitable fusion proteins at the PM can hardly be distinguished from excitable fusion

proteins within the cytoplasm close to the PM. The increased spatial resolution in VAEM impacts on cell staging and leads to a cell stage shift by one cell, meaning that a +1 cell in VAEM resembles a -1 cell in confocal imaging.

As I have already discussed in Chapter I, *gef3-1* plants maintain the ability to grow out root hairs, however with a much lower efficiency, and it seems plausible that redundantly acting ROPs may dilute the amount of fluorescently tagged ROP2 that can be detected in imaging. Therefore, it is possible, that the slower polarization of ROPs at the RHID is accompanied by a slower reduction in mobility (which will be discussed in more detail later in this chapter) which may not be measurable. In addition, it has to be noted, that in this particular experiment the number of biological replicates was rather low (with three replicates inside the RHID and two replicates outside the RHID).

GEF3 overexpressing plants exhibit a similar phenotype (initiation of multiple, multi-branched root hairs) as plants lacking the GDI supercentipede 1 (*scn1*), which has led to the suggestion that GEF3 acts as an activating factor of ROP2 (Carol et al., 2005; Denninger et al., 2019). This suggestion was further supported by the observation that GEF3 is able to interact with *rop2DN* (Denninger et al., 2019). Therefore, the reduced mobility of *rop2DN* at the PM is likely to be caused by protein-protein interaction with GEF3. Along the same lines, it seems noteworthy that the distribution of track velocities for *rop2DN* showed similarities to the distribution of track velocities of GEF3 in cell stage -5, that is prior to ROP2 polarization (Figure II- 10 and Figure II- 14). This leads me to the hypothesis that it may be GDP-ROP2 that is bound by GEF3 and thus immobilized. In wild type ROP2 this interaction would then lead to an exchange of the GDP for a GTP and subsequent ROP2 activation. Since *rop2DN* is not able to release its bound GDP however, it is trapped at the PM and exhibits a mobility similar to GEF3. This hypothesis does require further testing as it is yet unclear whether GDP-ROP2 mobility in *rop2DN* plants is solely influenced by binding to GEF3. Therefore, it would be interesting to perform particle tracking of *rop2DN* puncta in the *gef3-1* mutant background.

Another interesting observation I made was that the mobility of *rop2CA* determined by VAEM on the one hand was lower than ROP2 at the RHID, but on the other hand was faster than GEF3. Furthermore, from cell stage -5 to -4 GEF3 showed a slight increase in mobility, followed by a further increase at cell stage -3, which is the cell stage where ROP2 was

determined to polarize) (Figure II- 10). These results would indicate that GEF3 and ROP2 mutually slow down each other. This suggestion is backed by the observation that in the *rop2/rop4* double mutant background GEF3 was still able to polarize at the RHID, but lost its polar accumulation in later root hair development, indicating a mutual stabilization of the two at the apex of growing root hairs (Denninger et al., 2019). To further confirm this mutual influence of both proteins on their mobility, very likely through direct protein-protein interactions, it would be interesting to investigate the mobile behavior of GEF3 in the *rop2/rop4* mutant background.

Taken together, the data on the mobility of protein populations at the RHID presented in this thesis strongly suggests that GEF3 causes ROP2 polarization at the RHID by local activation and immobilization. However, the reduction of ROP2 mobility prior to bulging was rather subtle and could not be shown to be statistically significant with the methods available in our lab. By integrating the mobility data, it would be interesting to test if such a subtle reduction in protein mobility could already be sufficient to drive protein polarization - maybe even in absence of GEF3.

3.2. Nanoclusters as a site of protein immobilization

The phenomenon of fluorophore blinking rarely needs to be considered in live-cell imaging as it occurs at high energy densities that in confocal microscopy would require very high laser power, resulting in fluorophore bleaching and phototoxicity. Using VAEM, however, the energy of the exciting laser is distributed only in a small sheet of the sample and only molecules at the surface can be excited. Therefore, high energy densities can be reached at relatively low laser power and trigger photochromic behavior of fluorophores. Fluorophore blinking has the advantage in that a reduction of the number of emitting (visible) fluorophores allows for a more precise determination of their position and consequently the localization of proteins with a higher x-y-resolution. The integration of single molecule localization events over time allows to compute super-resolved images with a resolution below the diffraction limit (down to only ~30 nm) (Hell and Kroug, 1995; Fölling et al., 2008). A disadvantage of commonly used algorithms for the computation of single molecule localization microscopy (SMLM) images is, that they can hardly account for movement of the fluorophores and therefore are not useful for motile structures as we

find in live-cell imaging. The SRRF algorithm has been developed to be more tolerant towards movement within the sample and in addition is suitable for high fluorophore densities and low signal-to-noise ratios (Gustafsson et al., 2016). These qualities make the SRRF algorithm attractive to perform SMLM in living cells. An additional feature of SRRF is that it visualizes differences in the mobility of molecules, since positionally stable structures appear brighter in the reconstruction than more mobile structures. Consequently, color-coded signal intensities within single SRRF images serve as a read-out for local protein mobility.

I could demonstrate that mCitrine shows fluorescent intermittency in plant cells (Figure II- 4) allowing to perform SMLM. I have used the SRRF algorithm to integrate the positions of mCitrine-GEF3 and mCitrine-ROP2 molecules over time on the surface of trichoblast cells (Figure II- 7). Interestingly, in SRRF reconstructions both proteins localized in structured clusters at the RHID and the presence of ROP2-nanoclusters was largely dependent on GEF3. A certain sub-compartmentalization of the RHID could be confirmed by laser scanning confocal microscopy (Figure II- 6), suggesting that these nanoclusters are unlikely to be imaging artefacts or artefacts introduced by the SRRF algorithm. The contrast between the nanoclusters and the surrounding area varied over the course of development as well as between the two proteins, indicating differential degrees of cluster stability. It has to be noted that stability in this case is defined by the re-occurrence of blink events at a certain position, meaning that the respective protein has resided at this position for a prolonged time. The activity mutant *rop2CA* similarly appeared in structured clusters, which however covered the whole surface of the cell. These clusters had a high contrast, indicating a high degree of positional stability and very little mobility (Figure II- 13). Together with the mobility analysis, showing the GEF3-dependent immobilization specifically at the RHID, and together with the fact that *rop2CA* had a reduced mobility compared to ROP2, this observation may suggest that these nanoclusters are functional domains in which the activation-dependent immobilization of ROP2 occurs. To test this theory, it would be important to know whether ROP2 and GEF3 localize into shared nanodomains or whether they populate distinct nanoclusters. Unfortunately, due to the nature of the fluorophore blinking, more specifically due to the fact that only a portion of the whole protein population is visible, it was not possible to perform co-localization

experiments between ROP2 and GEF3. An alternative method that would even benefit from a low fluorophore density would be fluorescence cross-correlation spectroscopy (FCCS) (Schwillle et al., 1997). With this technique it should be possible to answer the question whether ROP2 and GEF3 move together in the PM by correlating their diffusion behavior. Additionally, it would be interesting to perform FCCS measurements of the activity mutants *rop2CA* and *rop2DN* and compare their mobility to GEF3 as well as ROP2 which after all is a mixed population of GTP-bound and GDP-bound ROP2. Comparing FCCS measurements for all four proteins in the *gef3-1* mutant background as well as the wild type background would potentially be a good starting point to decipher the exact composition of these nanoclusters in the PM.

Activation-dependent recruitment of ROPs into nanoclusters in the PM has recently been reported (Platre et al., 2019). Furthermore, the authors could show that the formation of such nanoclusters was dependent on the presence of phosphatidylserine (PS). It would be interesting to investigate whether GEF3 nanoclusters, ROP2 nanoclusters or both are also dependent on the presence of PS or another anionic lipid.

Another question that arises from the observation of nanoclusters at the RHID is with regard to the potential function of these sub-compartments. In my understanding, the principle of functional nanodomains is that they represent sites where certain proteins and lipids accumulate to concentrations above a threshold necessary to make specific protein-protein interactions more likely and therefore locally facilitate a specific function. It seems plausible to hypothesize that the ROP2- and GEF3-nanoclusters that I observed might fulfill the function of such nanodomains. Therefore, it would be interesting to identify other proteins localizing in such clusters together with ROP2, GEF3 or even both. In a first attempt, I investigated several other proteins known to be involved in the tip growth machinery of root hairs with regard to their ability to localize into nanoclusters using VAEM and SRRF (Figure II- 18 and Figure II- 19). Interestingly, all candidate proteins showed a structured appearance, either at the RHID specifically (ROP4, GEF4, PIP5K3 and PRK7) or over the whole cell surface (FER). The organization of membrane proteins into a multitude of partially overlapping protein-nanoclusters, in a self-organizing manner, has been observed in yeast and has formed the basis for the “patchwork membrane” model (Spira et al., 2012). This model integrates interactions between proteins, proteins and lipids, the

cell wall and the membrane as well as the membrane and the cytoskeleton into the highly dynamic, but also highly structured organization of the PM. External and internal signals can be integrated into a cellular response by dynamically altering these interactions. This enables the cell to quickly react and adapt to changing conditions. For root hairs the rapid adaptation of growth in response to external cues, presumably even without changes in gene expression, has been reported (Stanley et al., 2018). Therefore, it seems plausible to hypothesize that the nanoclusters that I have observed could be involved in such a patchwork-organization of the PM of the RHID.

Taken together, I hypothesize that the organization into nanoclusters indicates the presence of functional nanodomains and that these play a role in root hair development. However, the question of the protein composition of such nanodomain remains unanswered. For a targeted approach one could perform FCCS measurements, as described above, with different proteins and thereby answer the question if these selected proteins occur within the same nanodomain. An untargeted approach to identify the nanodomain interactome could involve proximity labeling (for example reviewed in Han et al., 2018). During this thesis I have started a project that aimed to establish proximity labeling as a method to determine unknown interaction partners of GEF3 as well as the general proteome of nanodomains in trichoblasts. These experiments are further described in Chapter III.

Chapter III

Establishment of proximity labeling to aid the identification of
protein-protein interactions in trichoblasts

Knowing the unknown is the basis of understanding

1. Introduction

I was able to show that ROP2, GEF3 and other proteins of the root hair growth machinery each localize into nanoclusters in the plasma membrane (PM) of *Arabidopsis* trichoblasts. To understand the functional role of these nanoclusters it is necessary to understand their protein composition. Therefore, it seems reasonable to investigate protein-protein interactions (PPIs) between known nanocluster proteins and unknown interaction partners in an untargeted approach.

A classical untargeted approach to find unknown PPIs is affinity purification (AP) coupled to the subsequent identification of proteins via mass spectrometry (MS) (for example reviewed in Miernyk and Thelen, 2008). AP-MS requires the expression of the protein of interest (POI) fused to an epitope tag. Cells are then lysed and a pull-down against the tag is performed on the lysate, resulting in the purification of the POI and all proteins that remain bound to it. Consequently, AP-MS has a bias towards high affinity PPIs since these are more likely to persist during the harsh conditions of cell lysis. Furthermore, as the pull-down is performed after cell lysis, which includes the break-down of all intracellular compartments, proteins that would not have been in the same cellular compartment under native conditions might appear as false positive PPIs. For the same reason, all information on the spatial as well as the temporal characteristics of PPIs is lost.

To overcome these problems and to gain spatio-temporal information on PPIs, *in vivo* labeling of interaction partners has been developed. To this end, an enzyme that can introduce stable modifications to other proteins is fused to the POI. These modifications occur on all proteins that enter the vicinity of the modifying enzyme (including proteins that form weak and transient PPIs) and can later be used in a pull-down experiment. Since this results in labeling of all proteins proximal to the POI and the modifying enzyme, the method has been called proximity labeling (recently reviewed in for example Han et al., 2018; Gingras et al., 2019).

In general, it is important to state, that there is no method equally suited to investigate all PPIs and that any PPI that has been identified using one method should always be confirmed by using another to exclude false positive results. Therefore, a combination of untargeted approaches followed by targeted approaches is a powerful tool to identify

novel PPIs. Classical targeted approaches, which unlike untargeted approaches require previous knowledge about likely interaction partners, include for example yeast-2-hybrid (Y2H) (Fields and Song, 1989), (ratiometric) bi-molecular fluorescence complementation ((r)BiFC) (Hu et al., 2002; Grefen and Blatt, 2012), Förster resonance energy transfer combined with fluorescence lifetime imaging (FRET-FLIM) (for example reviewed in Bhat et al., 2006; Xing et al., 2016) as well as fluorescence (cross-)correlation spectroscopy (F(c)CS) (for example reviewed in Lalonde et al., 2008).

1.1. Proximity labelling

Based on the catalyzing enzyme, there are two categories of proximity labeling (PL): peroxidase-based and biotin-ligase based proximity labeling (Han et al., 2018). Whereas peroxidase based PL relies on the expression of either engineered ascorbate peroxidases (APEX or APEX2) (Martell et al., 2012; Rhee et al., 2013; Lam et al., 2014) or horseradish peroxidases (HRP) (Kotani et al., 2008; Honke and Kotani, 2011; Loh et al., 2016) in the tissue of interest, biotin-ligase based PL requires the expression of a promiscuous biotin-ligase (Figure III- 1) (Roux et al., 2012; Kim et al., 2016; Branon et al., 2018).

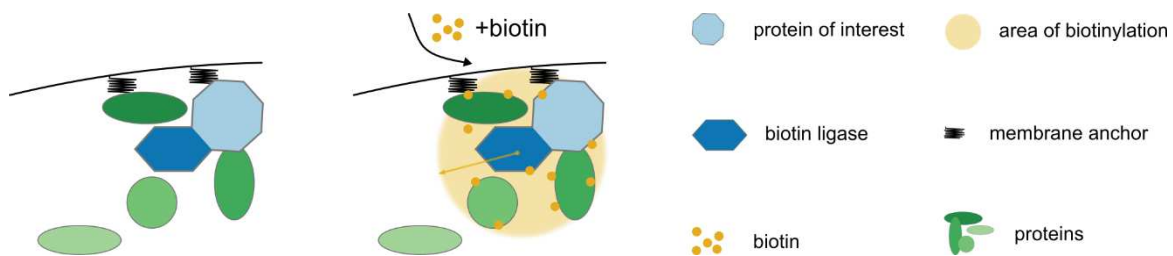


Figure III- 1: Schematic overview of proximity labelling using a biotin ligase based system: All transient and stable interaction partners of the biotin ligase-fusion protein are marked by covalent attachment of a biotin residue.

To facilitate labeling using peroxidase based PL, the addition of a substrate like biotin-phenol (BP) or its derivatives BxxP, alkyne-phenol or desthiobiotin phenol (Rhee et al., 2013; Loh et al., 2016; Lee et al., 2017) as well as the toxic co-substrate H_2O_2 is required. The substrate is oxidized by the peroxidase, generating a phenoxy radical that can react with electronically rich side chains of proximal proteins. Since the half-life of the phenoxy radical is less than 1 ms (Mortensen and Skibsted, 1997), the labeling efficiency is reduced with increasing distance to the active site of the peroxidase. This allows for the discrimination of differential proximity, for example in large protein complexes, by quantitative proteomics. The rapid kinetics (less than 1 min labelling time) and the small

size of APEX and APEX2 of 28 kDa allow for the identification of dynamic protein interaction networks (Han et al., 2018). Another advantage of APEX facilitated PL is the ability of APEXs to be functional even after sample fixation and preparation for electron microscopy (EM). By oxidative polymerization of 3,3'-diaminobenzidine, APEX is able to generate contrast in EM samples after OsO₄ treatment and allows for the investigation of subcellular localization of APEX-fusion proteins in addition to interactome analysis (Martell et al., 2012).

The main difference between APEX/APEX2 and HRP is that HRP requires the formation of intrinsic disulfide bonds for proper peroxidase function and can therefore only be active in the secretory pathway and extracellular matrix (shown in mammalian cells) (Martell et al., 2012).

Biotin-ligase based PL is based on the *E. coli* derived biotin ligase BirA, which relies on ATP to catalyze the reaction of biotin into biotiny-5'-AMP (bioAMP) and is able to covalently attach bioAMP to lysine residues of bacterial carboxylases. A mutation of BirA at arginine 118 to glycine (R118G) renders BirA promiscuous, consequently reducing its substrate specificity (Choi-Rhee et al., 2008) and allows for usage of BirA in PL (then named BioID) (Roux et al., 2012). Even though the half-life of bioAMP in water is in the range of minutes (Xu and Beckett, 1994), it was shown that BioID has a labeling radius of approximately only 10 nm (Kim et al., 2014; Firat-Karalar and Stearns, 2015), suggesting a reduction of bioAMP half-life in a cellular environment (Han et al., 2018).

In comparison to APEX/APEX2, BioID features slower kinetics (of 18-24 h or even longer (Uezu et al., 2016)), which reduces its usability for studying highly dynamic interaction networks. Furthermore, BioID has a higher molecular weight of 35 kDa (compared to 28 kDa for APEX/APEX2), which may cause problems in targeting BioID-fusion proteins to their subcellular destination (Liu et al., 2013). To overcome potential miss-targeting effects of BioID, a smaller version of the biotin ligase was engineered (BioID2; 27 kDa) that is also suitable for proximity labeling and in addition requires a lower amount of exogenously added biotin (Kim et al., 2016).

Besides its application in mammalian cells (Roux et al., 2012; Kim et al., 2014; Gupta et al., 2015; Bagci et al., 2020), yeast (Opitz et al., 2017), mouse (Uezu et al., 2016) or *Dictyostelium* (Batsios et al., 2016; Meyer et al., 2017), BioID has been successfully used in plants (Lin et al., 2017; Khan et al., 2018; Conlan et al., 2018; Das et al., 2019). In general

however, the usage of BioID in plant science is hampered by the fact that the temperature optimum of BioID is at 37°C (Kim and Roux, 2016), while the optimal growth temperature for commonly used model plants is much lower, resulting in greatly reduced biotinylation efficiency. Consequently, the application of BioID so far was limited to examples with either transient overexpression of genes in heterologous systems or to genes with high endogenous expression levels and in any case resulted only in poor labeling efficiencies.

In order to create an enzyme that combines the simple and non-toxic applicability of BioID/BioID2 with the high catalytic activity of APEX/APEX2, Branon and colleagues used yeast display-based directed evolution on BioID/BioID2 (Branon et al., 2018). The resulting promiscuous biotin-ligases TurboID (35 kDa) and miniTurboID (28 kDa) have the advantage of a reduced labeling time of 10 min, lower temperature requirements as well as a greater labeling efficiency. The authors showed that these advantages allow for the application of PL in additional model systems like *Drosophila melanogaster* or *Caenorhabditis elegans* where the use of BioID was not possible before (Branon et al., 2018). Since then, TurboID and miniTurboID have additionally been used to analyze protein-protein interactions in plant systems such as *Nicotiana benthamiana* (Zhang et al., 2019) as well as *Arabidopsis thaliana* (Mair et al., 2019).

1.2. Aim of Chapter III

I could show that ROP2, GEF3 and other proteins involved in root hair growth localize into nanoclusters within the PM of root hair cells. However, the biological function of these nanoclusters remains unclear. In addition, we still lack mechanistic understanding of how GEF3 is polarized at the RHID. Current hypotheses suggest, that this might be achieved via interaction with other proteins, by sensing developmental cues or by anchoring GEF3 to the plasma membrane. Proximity labeling methods allow the identification of unknown and transient interaction partners of a protein of interest, not only in its native environment but importantly in a small interaction radius around the protein of interest. Therefore, I set out to adapt a proximity labeling method *in planta*, to study the GEF3-interactome in root hairs and in nanoclusters in the RHID.

For proximity labelling experiments, biotin ligases have been modified to reduce their specificity and to promiscuously label every protein that enters their vicinity. This however

can also be disadvantageous, since unspecific biotinylation increases with increasing expression time of the ligase. This is especially problematic in plants, which naturally synthesize biotin, easily reaching a cytosolic biotin concentration of up to 11 μM (Alban et al., 2000). Consequently, the biotin ligase is not limited by substrate availability and the total amount of biotin cannot be controlled by external application. To reduce unspecific labelling due to excessive availability of endogenous biotin and to increase the signal to background ratio, for example in mass spectrometry analyses, we need to reduce the time period during which the biotin ligase gets expressed to a minimum.

To exclude unspecific results from atrichoblasts and other cells, I aimed to express the biotin ligase in a cell type specific manner. Therefore, I needed to find a promoter that is specific to the trichoblast lineage and ideally is already active in cells of stage -5 or younger (the cell stage in which GEF3 expression was detected the earliest). To this end, I aimed to characterize selected promoters with regards to their trichoblast-specificity in the estradiol inducible system.

At the beginning of this project I aimed to newly establish a biotin ligase system, since no reports on proximity labelling *in planta* had been published by then. As the research field developed over the course of this project, more and more scientific reports of proximity labeling were published. From these reports I deduced that TurboID appeared to be the most efficient biotin ligase available *in planta* (Branon et al., 2018; Mair et al., 2019). Therefore, I decided to use this variant to establish proximity labeling in our research group and aimed to assess the suitability of TurboID in the context of nanoclusters at the RHID using GEF3.

2. Results

2.1. Trichoblast-specific, inducible promoters

To generate trichoblast-specific, inducible promoters, I used the estradiol inducible promoter system based on the chimeric transcription factor XVE. It consists of the DNA-binding domain of the bacterial repressor LexA, the VP16 trans-activating domain and the regulatory region of the human estrogen receptor (Zuo et al., 2000). The estradiol inducible expression system has been adapted for use in our lab (Denninger et al., 2019). It consists of two expression cassettes that have been ligated in reverse orientation into one entry vector. One cassette consists of a promoter controlling the expression of XVE and a terminator. The other cassette harbors 8 copies of the LexA operator and a minimal 35S promoter (oLexA). This promoter module can be used in Green Gate cloning (Lampropoulos et al., 2013) to drive the expression of a gene of interest inducibly and in a cell type-specific manner, if the XVE is controlled by a suitable promoter (Figure III- 2).

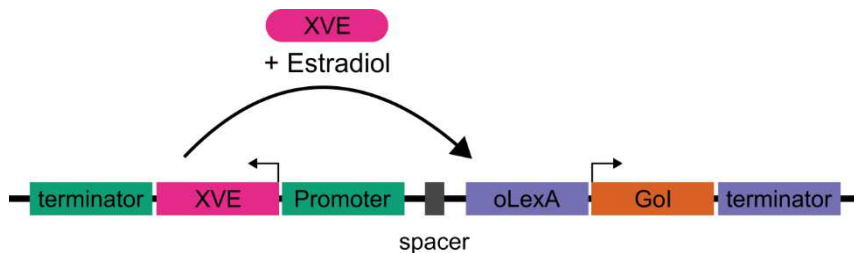


Figure III- 2: Schematic overview of the estradiol inducible promoter system. A promoter of choice is driving the expression of the chimeric transcription factor XVE. XVE binds to the oLexA-minimal 35S promoter only in the presence of estradiol and activates the transcription of the gene of interest (GoI).

Based on this, I cloned entry vectors with trichoblast-specific promoters controlling the expression of XVE: I used the promoters of GEF3, GEF14, EXPA7, Cobl9 and GEF4, as they have been described to be root hair cell-specific (Cho and Cosgrove, 2002; Jones et al., 2006; Denninger et al., 2019) and the ROP2 promoter, which is reported to not be trichoblast-specific. Cell type-specificity of those promoters was checked by creating transcriptional reporters using the fluorophore mCitrine in *Arabidopsis* plants.

For *pCobl9*, *pGEF4* and *pGEF14*, the transformation efficiency was very low and I obtained few transgenic plants. In the second transgenic generation (T2), the induction efficiency was very low and the expression of mCitrine was sometimes patchy. Therefore, these lines were not analyzed further.

For *pROP2*, *pGEF3* and *pExpA7* I obtained several T2-lines, for which estradiol induction led to sufficient expression of mCitrine. For *ROP2* and *GEF3*, however, induction efficiency was lower than I have observed for the ubiquitin-promoter controlled XVE constructs used previously in this study, as only extended induction for more than 24 h led to a detectable amount of fluorescent signal. In contrast, the induction time for *ExpA7* was comparable to the ubiquitin promoter construct (between 4-8 h).

To quantify cell-type-specificity of the inducible promoter constructs, the distribution of mCitrine signal was compared to the fluorescent signal of the cell wall staining agent propidium iodide (PI) in optical cross-sections of the epidermis of transgenic roots. Trichoblast identity was determined by the relative position of the epidermal cells to the underlying cortex cells (Figure III- 3 A-C, see asterisks). As expected, the inducible *ROP2* construct did not show trichoblast-specific expression of mCitrine (Figure III- 3, A and E). In contrast, the inducible *GEF3* and *ExpA7* constructs showed a brighter mCitrine signal in trichoblasts compared to atrichoblasts (Figure III- 3, B-C and E). The atrichoblast signal for the *GEF3* promoter construct, was higher compared to the *ExpA7* construct, however, not significantly different with regard to the cell-type-specificity index (Figure III- 3, E). For both constructs, the youngest cells that reliably showed mCitrine fluorescence were cells of the stage -2 and in rare cases cells of stage -3 (an example for *ExpA7* is shown in Figure III- 3, D).

Another interesting observation was, that propidium iodide (PI) seemed to show a slightly higher signal in trichoblasts compared to atrichoblasts (Figure III- 3), suggesting a higher accumulation of the dye. Since propidium iodide binds to pectin (Rounds et al., 2011), it is tempting to assume a differential composition of different pectin variants in trichoblast and atrichoblast cell walls. Further analysis of this phenomenon however was not part of this thesis.

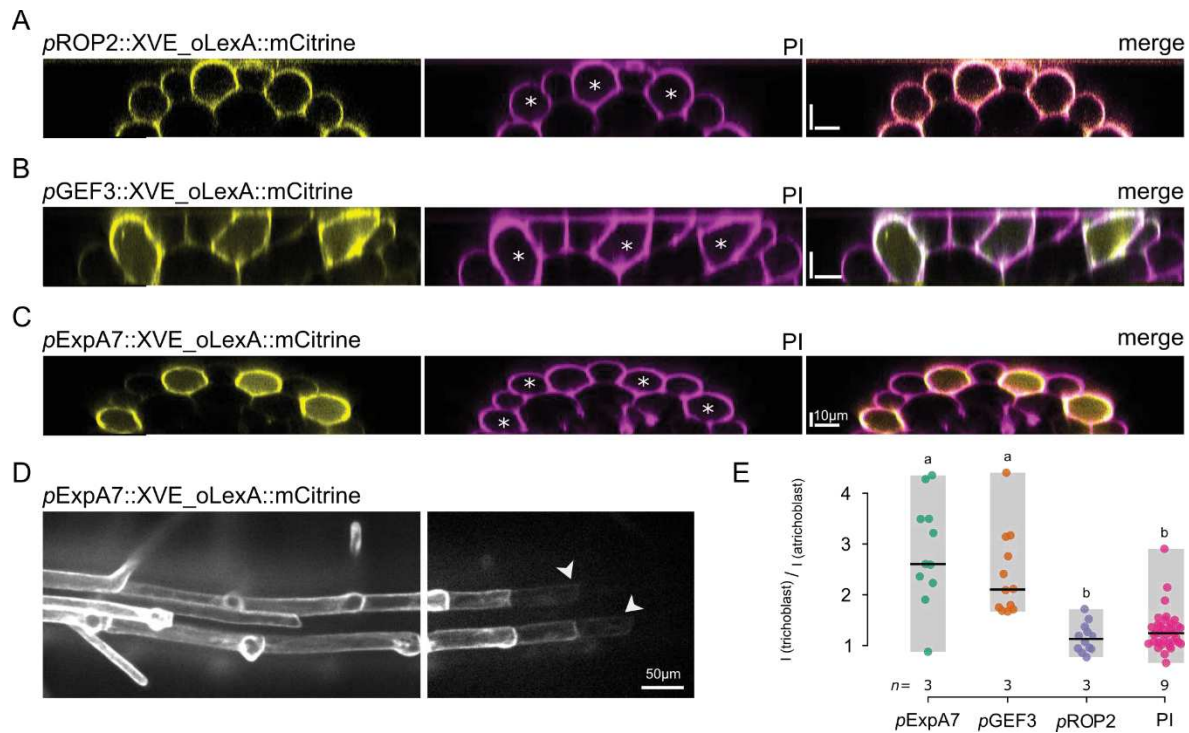


Figure III- 3: Characterization of estradiol inducible, root hair-specific promoters. Cross-sections (A, B, C) and a maximum intensity projection (D) of the estradiol-inducible ROP2 (A), GEF3 (B) and ExpA7 (C and D) promoters driving mCitrine expression. Fluorescent images of mCitrine expression (left panel), propidium iodide (PI) staining (middle panel) and merge (right panel) are shown for each promoter. Asterisks indicate trichoblasts. Scale bars represent 10 μm for A-C and 50 μm for D. The arrows indicates the youngest cell in which signal for mCitrine was visible. Note that the two images belong to the same root, but their brightness was scaled differently. (E) Quantification of trichoblast-specificity of the fluorescent signal. Center lines represent median values, gray boxes represent the data range, n indicates the number of roots measured and letters represent the result of an ANOVA-Tukey test (significance value = 0.01, same letters indicate no significant difference). To obtain these values, 4 cross-sections per root were measured.

2.2. A Is a TurboID-GEF3 fusion protein able to facilitate biotinylation in *N. benthamiana*?

At the beginning of this project, all biotin ligases that were available had not yet been shown to be applicable for proximity labelling in plants. To test whether the *E. coli* derived biotin ligase BioID or the *Arabidopsis* derived biotin ligase HCS1 (in collaboration with the lab of Thomas Ott, Freiburg) could be used for proximity labelling and therefore to investigate the interactome of the RHID in the framework of this project, I tested their biotinylation capacity in *N. benthamiana* leaves. The entry vector for BioID had been created previously by Philipp Denninger, while the subsequent cloning into expression vectors was performed by me. The plant expression vector carrying the construct pUbi10::HCS1:GFP was kindly provided by Nikolaj Abel (lab of Thomas Ott, Uni Freiburg).

Both biotin ligases were expressed in *N. benthamiana* leaves and their biotinylation profile was tested via western blot. Unfortunately, for both biotin ligases, the results remained

inconclusive on whether or not they were able to biotinylate proteins in *N. benthamiana* leaves. A mCitrine-BioID-ROP2 fusion construct expressed in *Arabidopsis* roots however revealed that the polar accumulation of the fusion protein was comparable to mCitrine-ROP2 (data obtained during the student internship of Clara Baader under my supervision). However, as it was not possible to detect biotinylation of proteins in *N. benthamiana*, it was decided to not proceed with these biotin ligases.

In the meantime, a publication on the novel biotin ligase TurboID, which had been generated by targeted evolution of BioID, became available (Branon et al., 2017, 2018). The authors reported an increased catalytic efficiency of the protein and the applicability of this biotin ligase for proximity labelling in plants was subsequently shown by Mair et al. (2019). Therefore, I aimed to test whether TurboID can be used in a GEF3 fusion protein, which would eventually allow the identification of unknown interaction partners of GEF3 in general and in nanoclusters specifically.

Expression of a TurboID-HA-GEF3 construct under the control of the *pUbi10*-estradiol inducible promoter in *N. benthamiana* leaves showed that the fusion protein, as well as its break-down product, TurboID-HA, were biotinylated (Figure III- 4) upon estradiol induction. Furthermore, the result showed that biotinylation already occurred without any addition of exogenous biotin. Even though the same amount of total protein was loaded onto the gel, the sample with additional biotin (+bio.) showed a reduced intensity for the TurboID-HA-GEF3-band.

In a recent study we could show that ROP2 and GEF3 interact with each other in heterologous systems (split-ubiquitin and ratiometric bi-molecular fluorescent complementation (Denninger et al., 2019)). In order to test for *trans*-biotinylation (biotinylation of nearby proteins, in contrast to *cis*-biotinylation: biotinylation of the biotin ligase itself) I transiently co-expressed the inducible TurboID-HA-GEF3 construct together with mCitrine-ROP2 under the control of the *ubiquitin10* promoter in *N. benthamiana* leaves. I then performed a biotin pull-down to check whether mCitrine-ROP2 could be detected by Western Blot. However, even though I confirmed the expression of both transgenic proteins, mCitrine-ROP2 was not detectable in the pull-down fraction.

Taken together, I was able to show that the GEF3-TurboID fusion construct was able to *cis*-biotinylate itself *in planta*, strongly suggesting that the TurboID can be used in our

approach to find interaction partners of GEF3. *Trans*-biotinylation of ROP2 however, could not be shown in this pioneer experiment and requires further testing.

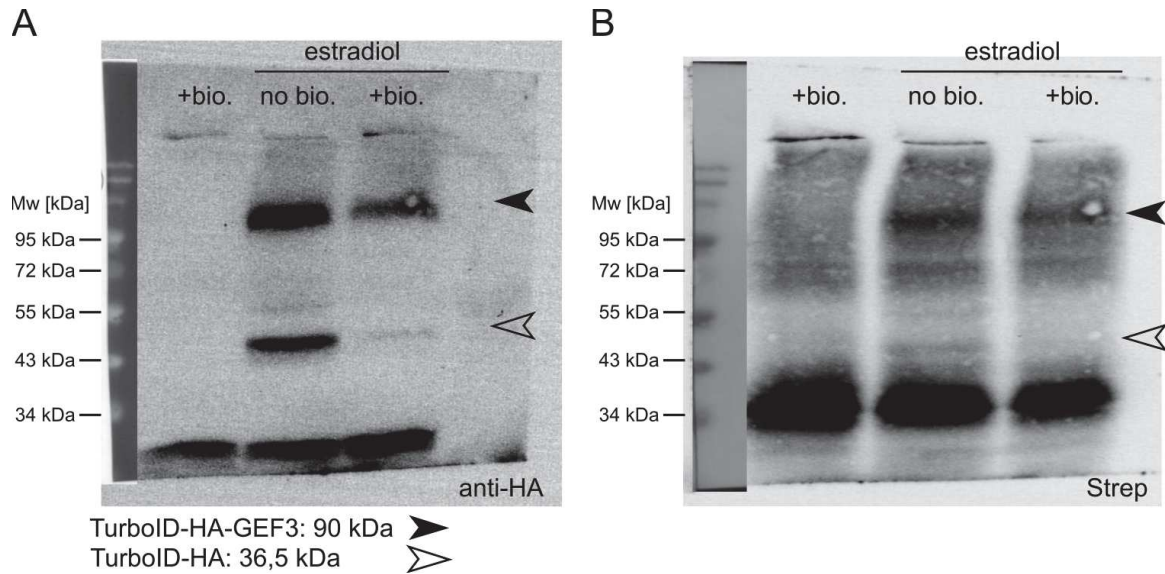


Figure III- 4: Proof-of-concept: Auto-biotinylation of TurboID in *N. benthamiana* leaves. Western Blots of protein extract from *N. benthamiana*, transiently expressing the GEF3-TurboID-HA construct under the control of an estradiol inducible promoter. **(A)** Western Blot membrane showing signal for the anti-HA antibody. **(B)** Western Blot membrane showing signal for Streptavidin, which binds to biotin. Asterisks indicates GEF3-TurboID-HA, dots indicate the break-down product TurboID-HA. The most left lane was loaded with proteins from not induced *N. benthamiana* leaves, but supplied with 100 μ M biotin; the middle lane was loaded with proteins from induced *N. benthamiana* leaves, not supplemented with biotin; rightmost lane was loaded with induced *N. benthamiana* leaves supplemented with 100 μ M biotin. As molecular weight standard, the protein ladder #p7719 from NEB was used.

3. Discussion

To shed light on the mechanism of how GEF3 might be polarized at the RHID, we need to analyze the interactome of GEF3 in trichoblasts in general and more specifically, the functional role of GEF3 nanoclusters in the RHID throughout root hair development. Therefore, I characterized trichoblast-specific promoters in the estradiol inducible system to be used in proximity labeling. Furthermore, I tested the applicability of the TurboID proximity labeling system that will allow us to identify unknown and transient interaction partners of GEF3 via an untargeted approach.

3.1. Trichoblast-specific inducible promoters

Biotin ligases that are used for proximity labeling have been engineered to promiscuously label proteins that enter their vicinity. Especially in plants however, this can be disadvantageous, as biotin is naturally synthesized, reaching cytosolic concentrations of up to 11 μM (Alban et al., 2000). As the biotin ligase is therefore not limited by substrate availability, it is necessary to control the time window in which it is expressed to reduce unspecific labeling. In addition, a cell type specific expression is required to exclude unspecific results from other cell types. To comply with these two requirements, I characterized a set of promoters in regard to their trichoblast specificity as well as their suitability for use in an estradiol inducible expression system.

I found that the *GEF3* promoter and the *ExpA7* promoter were both suitable for trichoblast-specific expression of cytosolic mCitrine. However, the *ExpA7* promoter seemed to be slightly more specific and required a drastically shorter induction time for sufficient expression in comparison to *pGEF3*. It is conceivable that the reduced specificity of the *GEF3* promoter is a result of the long induction time, since cytosolic mCitrine is able to freely diffuse through plasmodesmata and might be able to enter neighboring atrichoblasts. This could be clarified by not using free mCitrine, but mCitrine trapped in any intracellular compartment not spanning the plasmodesmata (e.g. the nucleus) or by increasing its size to a level above the size exclusion limit of plasmodesmata (e.g. using 3 x mCitrine).

For both promoters the first cell reliably showing fluorescent signal usually was -2 and in rare cases cell stage -3. This is interesting since *GEF3* was reported to be expressed already very early in root hair development (as early as cell stage -6) (Denninger et al., 2019). This discrepancy can be explained however by taking a closer look at the estradiol inducible promoter system that was used in this study (Figure III- 3): First, the artificial transcription factor XVE is expressed under the control of the promoter of choice, needs to be folded, needs to bind estradiol, can only then bind to the engineered *oLexA* promoter and in the following induces the expression of the reporter gene. Second, the reporter gene itself needs to be expressed, folded and needs to accumulate to a detectable level. Consequently, the use of the estradiol inducible promoter system for expressing a reporter gene will always introduce a time delay compared to direct expression. This leads to a temporal bias that needs to be considered, when choosing the promoter for any experiment utilizing this system. For example, if the research question relates to cell stage -3, it would be important to choose a promoter that is already active earlier in development. In our case, a good candidate could be the promoter of the transcription factor ROOT HAIR DEFFECTIVE 6 (RHD6), which is a prerequisite for trichoblast identity (Masucci and Schiefelbein, 1994).

In general, it also needs to be considered, that the *oLexA* promoter has been engineered to provide strong expression and therefore induction potentially leads to an amplification of expression in comparison an endogenous promoter without induction. In case of a transcriptional reporter this can be an advantage due to enhanced visibility. However, in case of a functional fusion protein this might lead to overexpression phenotypes. To avoid undesired overexpression resulting from prolonged induction, the induction time needs to be optimized and kept to a minimum. Therefore, it seems advisable to perform an individual time course of induction for every construct, to account for differential promoter strength and differential maturation times of fusion proteins.

3.2. Proximity labeling using TurboID

One of the first enzymes that was used for biotin-ligase based proximity labeling was the *E.coli* derived BirA (Roux et al., 2012). Even though BirA was successfully applied in plants (Lin et al., 2017; Khan et al., 2018; Conlan et al., 2018; Das et al., 2019), its temperature

optimum is at 37°C (Kim and Roux, 2016), which is far above the growth optimum of *Arabidopsis thaliana*. Using directed-evolution of BioID, a mutated variant of BirA, the biotin ligases TurboID was generated (Branon et al., 2018), which allowed the application of biotin-based proximity labeling *in planta* under more physiological conditions (Mair et al., 2019). In an attempt to use biotin-ligase based proximity labeling to identify unknown interaction partners of GEF3 and to decipher the interactome within GEF3 nanoclusters in the RHID, I tested TurboID for its suitability in regard to our research questions.

First, I tested whether a fusion protein of TurboID and GEF3 was able to perform *cis*-biotinylation in *N. benthamiana*, which I could observe with and without the addition of exogenous biotin (Figure III- 4). Interestingly, the amount of TurboID-GEF3 fusion protein in the sample with the addition of exogenous biotin was lower than in the sample without additional biotin. This might be due to mechanical damage of the cells caused by the biotin infiltration procedure, leading to a reduced amount of transgene expression and therefore a reduced concentration of fusion protein in the total protein extract. However, this problem can be neglected as we are interested in finding unknown interaction partners of GEF3 in trichoblasts and final experiments should rather be performed in hydroponic culture, where no mechanical infiltration of biotin into the root tissue is required. Hydroponic growth conditions furthermore allow for a convenient and uniform application of exogenous compounds, such as biotin or estradiol, as the tissue is fully submerged in the solution.

To also test for the ability of TurboID-GEF3 to facilitate *trans*-biotinylation, I performed a co-expression experiment with the known interaction partner ROP2 fused to mCitrine in *N. benthamiana*, followed by a subsequent streptavidin pull-down. However, even though induction and co-expression were successful, as confirmed by Western blot, no mCitrine-ROP2 fusion protein could be detected after the pull down. It is evident that the pull-down will require further optimization: For instance, given the high levels of endogenous biotin, it seems advisable to perform a removal of free biotin prior to pull-down (as described in Mair et al., 2019), thereby reducing the competition between free biotin and biotinylated proteins for streptavidin molecules on the surface of the beads. It also has to be considered, that ROP2 and GEF3 are membrane associated proteins which in general are more difficult to solubilize compared to cytosolic proteins and therefore might require harsher conditions

during cell lysis. Implementation of the suggested optimizations however, will have to be done by Marjorie Guichard, who has taken over this project in the meantime.

3.3. Future experimental plans to find GEF3-interactome at the RHID

The preliminary experiments discussed above, provide a basic toolkit for the further identification of unknown interaction partners of GEF3 in trichoblasts. Due to the cell type-specific, inducible promoters described here the system currently seems best suited to find downstream factors of GEF3 that are present shortly before bulging.

To this end, the applicability of the proximity labeling system in roots first needs to be confirmed by using a suitable positive control. For a potential positive control we could use ROP2, as it has been shown previously to interact with GEF3 in heterologous systems (split-ubiquitin system and ratiometric bi-molecular fluorescent complementation) (Denninger et al., 2019). GEF3-ROP2 protein-protein interaction in *Arabidopsis* roots however remains to be confirmed and is a prerequisite for the use of ROP2 as a positive control.

In order to reduce results that may arise from the fact that we currently cannot distinguish between different developmental stages and also have no subcellular resolution, it is necessary to perform the experiment with a set of different controls and to compare their interactomes. The interactome of the fusion protein TurboID-GEF3 will include direct and indirect as well as transient and more stable interaction partners of GEF3 in trichoblasts. It will however also include unspecific cytosolic or membrane associated proteins that have entered the vicinity of the fusion protein just by chance as well as endogenously biotinylated proteins that may have originated from the whole root tissue. To enrich GEF3 specific interactions and exclude unspecific biotinylation, we need to compare the interactome of TurboID-GEF3 to the interactome of TurboID fused to a membrane anchor as well as the interactome of cytosolic TurboID. Similarly, we can compare the interactome of TurboID-GEF3 expressed from a trichoblast-specific promoter to the interactome of ubiquitously expressed TurboID-GEF3, to enrich for interactions that are functionally relevant in trichoblasts and exclude non cell type-specific interactions. In addition, recent advances in single cell sequencing of whole root tissue (Ryu et al., 2019; Denyer et al., 2019) and cell type-specific transcriptomics will allow for a qualitative evaluation of the obtained interactomes. This will help to narrow down the number of potential candidates that need

to be tested for direct or indirect interaction with GEF3 in targeted approaches as well as for their functional relevance in trichoblast development.

I have previously shown that GEF3 immobilizes ROP2 in nanoclusters and that the mobility of ROP2 is influenced by its activity status. We can hypothesize that the GEF3-dependent immobilization of ROP2 may be caused by direct protein-protein interaction, potentially depending on the activity status of ROP2. Therefore, it would be interesting to analyze the interactome of the constitutive active, as well as the dominant negative variant of ROP2 in general, but also in regard to GEF3. Future work along these lines will be performed by Marjorie Guichard.

Materials and Methods

1. Molecular Biology

1.1. Molecular cloning

All plasmids created in this dissertation were created using the “GreenGate” cloning system (Lampropoulos et al., 2013). For enzymatic reactions Bsal-HF[®] v2 and T4 ligase from NEB[®] were used.

1.1.1 PCR and PCR fragment purification

PCRs for cloning were performed according to the protocol in Table 1. Using DNA-polymerase Q5[®] HF from NEB.

Table 1: Master-Mix and PCR program for cloning PCRs.

Master-Mix	μL	component	PCR program:	Time	Temp.	
	2	Template (100 ng/μL)		2 min	95°C	
	10	Buffer (10x)		20 sec	95°C	30X
	2	Primer_fwd (10 μM)		20 sec	T _m	
	2	Primer_rev (10 μM)		30 sec/kb	72°C	
	0.5	dNTPs (10 mM)		2 min	72°C	
	0.5	Q5 [®] HF		∞	8°C	
	33	H ₂ O				
	50	volume/reaction				

Bands were checked for correct size and purified via gel purification with the NucleoSpin[®] Gel and PCR Clean-up kit from Machery-Nagel. For elution 20 μL VE water were used. In case that several PCR fragments were used in one entry vector cloning, the gel pieces were pooled for the purification.

1.2. Entry vector cloning

20 μL gel extract were mixed with 100 ng of empty entry vector, 2 μL 10xCutSmart[®] Buffer (NEB) and 0.5 μL Bsal-HF[®] v2 and incubated at 37°C for 1h. This digest was purified using the NucleoSpin[®] Gel and PCR Clean-up kit from Machery-Nagel. Digested DNA was eluted with 20 μL VE water.

In some cases, additional oligo-annealing was performed to facilitate the insertion of another small linker or tag into the entry vector. Therefore, the primer pair was designed in a way that they overlap except for 4 bases at the 5' end. Those primers were mixed in a 1:1 ratio (10 μL of 100 ng/μL each). To ensure the annealing of the oligos, the DNA was heated to 95°C for 5 min and then cooled down to 25°C in 1°C steps, each temperature was kept stable for 1 min.

Ligation of PCR fragments, annealed oligos and the entry vector backbone was performed according to Table 2. The whole volume of the ligation mix was used for subsequent transformation into chemically competent *E. coli*.

Table 2: Ligation protocol for entry vectors.

Regular ligation:		Ligation with annealed oligos:	
μL	component	μL	component
20	purified reaction	20	purified reaction
2	T4 DNA Ligase Buffer, NEB(10x)	9	annealed oligos
0.5	T4 Ligase	3	T4 DNA Ligase Buffer, NEB(10x)
1h at room temperature		2	T4 Ligase
10 min at 70°C		1h at room temperature	

1.2.1 Removal of internal BsaI-sites

In some cases, the DNA fragment that should be ligated into an entry vector contained a BsaI recognition site. To remove this, two separate PCRs were performed that split the desired fragment into two fragments at the BsaI site. The reverse primer of the first PCR was designed to cover the recognition site and to introduced a point mutation. To facilitate the assembly of the two PCR fragments a BsaI recognition site was introduced at the 5' ends of the reverse primer of the first PCR and at the forward primer of the second PCR in a way that the BsaI site would be cut off, leaving the fragments with complementary, sticky ends.

1.2.2 Destination vector assembly

Inserts from entry vector modules were assembled into the pGGZ003 expression vector, according to the GreenGate protocol (Lampropoulos et al., 2013). The protocol was used as described in Table 3.

Table 3: Protocol for GreenGate assembly.

Master-Mix		PCR program:		
μL	component	Time	Temp.	
1.5	of each plasmid (A-F +Z module)	30 sec	37°C	30X
1.5	10xCutSmart® Buffer (NEB)	1 min	37°C	
1.5	ATP (10 mM)	1 min	16°C	
1	BsaI-HF® v2	5 min	50°C	
1	T4 Ligase	5 min	80°C	
15.5	V per reaction	∞	8°C	

The complete volume of the reaction was transformed into chemical competent *E. coli*.

1.3. Plasmid validation

DH5 α or XL1blueMR *Escherichia coli* (*E. coli*) cells were used as standard strains. For retransformations of empty entry vectors, which contain the ccdB gene, the ccdB resistant *E. coli* strain DB3.1 was used. Preparation of competent cells and transformation of all *E. coli* strains was done following the protocol mentioned below.

1.3.1 Preparation of chemical competent *E. coli*

4 mL LB medium without antibiotics were inoculated from a glycerol stock of *E. coli* originating from a single colony and incubated at 37°C over night. The next day, the overnight culture was transferred into 500 mL SOB-Medium without antibiotics and incubated at 20°C till an OD₆₀₀ of 0.55-0.6 was reached. The culture was chilled on ice for 10 min. Cells were harvested at 2500 rcf, 4°C for 15 min. The pellet was gently resuspended in 80 mL of ice cold TB buffer and kept on ice for 10 min. After centrifugation at 2500 rcf and 4°C for 15 min, the cell pellet was resuspended in 18.6 mL of ice cold TB buffer. 1.4 mL DMSO were added carefully. The cell suspension was aliquoted (100 µL), frozen in liquid nitrogen and stored at -80°C until usage.

Table 4: TB-buffer for chemical competent *E. coli*.

chemical	concentration	mass for 500mL
Pipes	10 mM	1.512 g
CaCl ₂ x 2 H ₂ O	15 mM	1.103 g
KCl	250 mM	9.32 g
Adjust pH to 6.7 with KOH		
Fill up to end volume		
Now add: MnCl ₂ xH ₂ O	55 mM	5.422 g
Filter sterilize; store at -20°C		

Table 5: SOB medium for chemical competent *E. coli*.

chemical	concentration	mass for 1 L
bacto tryptone	2% (w/v)	20 g
yeast extract	0.5% (w/v)	5 g
NaCl	10 mM	0.584 g
KCL	2.5 mM	0.186 g
MgCl ₂	10 mM	2.032 g
MgSO ₄	10 mM	2.464 g
Adjust to pH 6.7-7.0		
autoclave		

1.3.2 Transformation of chemically competent *E. coli*

An aliquot of chemically competent *E. coli* was thawed on ice. Depending on the purpose of the transformation, the following volumes of DNA-solution were added: 15 µL GreenGate reaction, 1 µL of a 1 ng/µL Plasmid solution (for retransformation) or 10 µL of a freshly ligated entry module. After DNA addition, cells were incubated on ice for 30 min. A heat shock was performed at 42°C for 30-50 sec. After 2 min on ice, 1 mL of LB medium was added and the cells were incubated at 37°C for up to 1h. Afterwards the cells were harvested at 4000 rcf for 5 min and plated on selective LB plates. Plates were then incubated at 37° over night. For *E. coli* selection the following concentrations of antibiotics were used: ampicillin 100 µg/mL, kanamycin 50 µg/mL, streptomycin 50 µg/mL.

1.3.3 Colony-PCR

Transformed colonies were tested for the presence of the correct insert via Colony PCR. Therefore, several colonies of one transformation reaction were picked with a toothpick, dipped onto a selective replica-plate, and then dipped into a PCR-tube already containing the PCR-Mix. The replica-plate served as a back-up and as the starting material for a liquid culture and was incubated at 37°C over night.

Table 6: Master-Mix and PCR program for Colony-PCR.

Master-Mix	μL	component	PCR program:	Time	Temp.	
	2.5	Buffer (10x)		2 min	95°C	
	0.25	Primer_fwd (10 μM)		20 sec	95°C	
	0.25	Primer_rev (10 μM)		20 sec	T _m	30X
	0.2	dNTPs (10 mM)		60 sec/kb	68°C	
	0.1	Taq Polymerase (NEB®)		∞	8°C	
	21.7	H ₂ O				
	25	V per reaction				

1.3.4 Plasmid isolation from *E. coli*

Plasmids were isolated from a 4 mL over night culture using the NucleoSpin® Plasmid kit from Macherey-Nagel™. To elute the plasmid DNA from the silica membrane 50 μL VE H₂O were used. Afterwards the DNA concentration was determined via NanoDrop™ measurements and adjusted to 100 ng/μL.

1.3.5 Vector sequence validation

For each entry vector, the correct sequence of the insert was validated by Sanger sequencing (performed by Eurofins Genomics). The presence and correct order of modules in GreenGate assembled destination vectors were validated by sequencing with up to 3 primers.

1.4. Agrobacterium transformation

For all experiments the *Agrobacterium tumefaciens* (*A. tumefaciens*) strain GV3101-pMP90RK-pSoup (Rif^r, Kan^r and Tet^r) was used (Koncz and Schell, 1986; Hellens et al., 2000).

1.4.1 Preparation of chemical competent *A. tumefaciens*

10 mL of selective LB medium were inoculated with a single colony of *A. tumefaciens* and incubated in a shaking incubator at 28°C over night. The next day, the over night culture was transferred into 500 mL fresh selective LB medium and incubated at 28°C until an OD₆₀₀ of 0.5 was reached. Cells were harvested at 2500 rcf for 15 min and resuspended in 100 mL of a sterile 150 mM NaCl-solution. Cells were harvested at 2500 rcf for 15 min, kept on ice and resuspended in 20 mL of an ice cold, sterile 20 mM CaCl₂ solution containing 10% glycerol. Afterwards the cell suspension was distributed in 200 μL aliquots, frozen in liquid nitrogen and stored at -80°C until needed.

1.4.2 Transformation of chemically competent *A. tumefaciens*

An aliquot of chemically competent *A. tumefaciens* was thawed on ice. 500 ng of plasmid DNA were added and the bacteria suspension was incubated on ice for 5 min followed by incubation for 5 min in liquid nitrogen. Heat shock was performed at 37°C for 5 min. 1 mL of LB medium was added and the suspension was incubated at 28°C for 4h. The cells were harvested at 4000 rcf for 5 min, plated on selective LB plates and incubated at 28°C for 3 days. Antibiotics were used in the following concentrations: rifampicin 10 µg/mL, gentamycin 50 µg/mL, tetracycline 10 µg/mL, spectinomycin 100 µg/mL.

1.5. Nucleic acid isolation and testing methods

1.5.1 Isolation of genomic DNA from *A. thaliana*

One big or 2 small rosette leaves of approximately 3 weeks old *A. thaliana* were frozen in liquid nitrogen and grinded in 1.5 mL reaction tubes using a precooled pistil. Samples were kept on ice and 750 µL extraction buffer (EB) were added and mixed with the leaf powder. After 10 min at 65°C, 200 µL 5 M potassium acetate were added and gently mixed by inverting the tubes. The samples were kept on ice for 20 min, followed by centrifugation at 16000 rcf for 10 min. The supernatant was carefully transferred into a new, 2 mL reaction tube and mixed with an equal volume of 2-propanol. The DNA pellet was collected by centrifugation at 16000 rcf for 2 min and washed with 500 µL 70% ethanol. After another centrifugation at 16000 rcf for 2 min, the pellet was dried and the DNA concentration was determined using a NanoDrop™.

Table 7: Extraction buffer (EB) for DNA isolation from *A. thaliana* leaves.

chemical	concentration
Tris	200 mM
NaCl	100 mM
EDTA	10 mM
SDS	1% w/v
β-Mercaptoethanol	10 mM

Adjust pH to 8.0 with HCl

1.5.2 Genotyping PCR

To test the presence of a T-DNA insertion into a gene, mutant plant lines were analyzed using 3 primers: two gene specific primers flanking the T-DNA and one primer specific to the T-DNA. In contrast, to test the presence of a transgene regardless of its localization in the genome, only two primers were used.

Table 8: Master-Mix and PCR program for genotyping PCR.

Master-Mix:	μL	component	PCR program:	Time	Temp.	
	1	gDNA (50-100 ng/ μL)		2 min	95°C	30X
	2.5	Buffer (10x)		20 sec	95°C	
	1	Primer_1 (10 μM)		20 sec	Tm	
	1	Primer_2 (10 μM)		60 sec/kb	68°C	
	1	Primer_3 (10 μM)		∞	8°C	
	0.2	dNTPs (10 mM)				
	0.1	Taq				
	18.2	H ₂ O				
	25	V per reaction				

1.6. Protein isolation and analysis for proximity labelling

1.6.1 Protein isolation from *N. benthamiana* leaves

This protocol was adapted from (Carnesecchi et al., 2020). For testing proximity labelling *in planta*, *N. benthamiana* leaves were infiltrated with Agrobacteria as described in Chapter 2.3.1, page 131. Estradiol induction (as described in Chapter 2.3.5, page 133) was performed 8h or 24h prior to harvesting of plant material. Infiltration of a 75 μM biotin solution was performed prior to induction.

Two days after infiltration, *N. benthamiana* leaves were cut from the plants, frozen in liquid nitrogen and grinded. 200 μL of extraction buffer (Table 9) were added per 100 mg of fresh weight. After an incubation for 10 min rotating at 4°C, the cell debris was pelleted by centrifugation at 20.000 rcf and 4°C for 30 min.

Table 9: Protein extraction buffer.

chemical	concentration
Tris (pH8)	50 mM
NaCl	150 mM
sodium deoxycholate	0.5% v/v
SDS	1% w/v
NP40	1%
protease inhibitor	

The protein containing supernatant was used to quantify protein concentration using the Pierce™ BCA™ Protein-Assay kit (Thermo Scientific™).

1.6.2 Pull-down of biotinylated Proteins

This protocol was adapted from (Carnesecci et al., 2020). Streptavidin magnetic beads (NEB-S1420, NEB) were equilibrated by washing two times in PBS, followed by resuspension in RIPA buffer. Washing consist of 3 times on the vortex for 1 sec, followed by a short centrifugation and 2 min on a magnet rack. Protein solutions (c = 1 mg/mL), were incubated with 20 µL of beads rotating over night at 4°C. Beads were washed two times with SDS-buffer, two times with ice cold RIPA buffer followed by resuspension in 50 µL of protein loading dye and boiling for 10 min at 95°C.

Table 10: Phosphate Buffer Saline (PBS) buffer for protein pull-down.

chemical	concentration
NaCl	137 mM
KCl	2.7 mM
Na ₂ HPO ₄	10 mM
KH ₂ PO ₄	1.8 mM

Table 11: RIPA buffer for protein pull-down.

chemical	concentration
Tris (pH8)	50 mM
NaCl	150 mM
sodium deoxycholate	0.5% v/v
NP40	1%

Table 12: SDS buffer for protein pull-down.

chemical	concentration
Tris HCl	10 mM
EDTA	1 mM
SDS	1% w/v
NaCl	200 mM

Table 13: Protein loading dye (6x concentrated).

chemical	concentration
Tris (pH 6,8)	350 mM
glycerol	30% v/v
SDS	10% v/v
bromphenol blue	0.012% w/v
DTT	600 mM

1.6.3 Qualitative detection of proteins using Western blot

For Western blot analysis of protein samples, gels were prepared according to the recipe in Table 14. Proteins were separated by electrophoresis at 120 V for 60 min using the running buffer described in

Table 15.

Table 14: Recipe for 2 1.5 mm thick, 10% Acrylamide gels for SDS-PAGE.

chemical	stacking gel (4%)	separating gel (10%)
water	6.4 mL	7.6 mL
Rotiphorese® NF-Acrylamide/Bis-Solution 40%	1 mL	4 mL
0.5 M Tris-HCl (pH 6.8)	2.5 mL	
1.5 M Tris-HCl (pH 8.8)		4 mL
10% SDS	100 µL	160 µL
10% APS	100 µL	160 µL
TEMED	10 µL	16 µL

Table 15: 10x running buffer for SDS-PAGE.

chemical	concentration
Glycine	2 M
Tris	250 mM
SDS	1% (w/v)

After separation, the proteins were either stained with Coomassie G-250, or specific antibodies. Coomassie staining was performed according to the microwave procedure of the SimplyBlue™ SafeStain (ThermoFischer). In brief, the gel was heated 3 times in VE water in the microwave, whereat careful attention was payed to not let the water boil. Afterwards, the gel was placed in Coomassie G-250 solution and heated in the microwave, followed by a 10 min incubation in the hot solution. Destaining was performed in VE water over night.

Table 16: Coomassie G-250 solution for staining proteins in acrylamide gels.

chemical	weight
Coomassie Brilliant Blue G-250	60-80 mg
VE water	up to 1 L
Shake until the powder is completely dissolved	
37% HCl	3 mL

To detect proteins with specific antibodies, the proteins were transferred on a PVDF membrane by wet blotting at 100 V in the 4°C cold room for 90 min using 1x transfer buffer with 20% ethanol. The membrane was activated by placing it for 15 seconds in 100% methanol followed by 1 min in 100% ethanol. After transfer, the membrane was blocked for 30-60 min using 5% BSA in 1x TBST (1x dilution of TBS buffer supplemented with 0.1% Tween 20).

Table 17: Transfer buffer for SDS-PAGE.

chemical	Final concentration
10x Transfer buffer	
glycine	2 M
Tris	250 mM

Table 18: 10x TBS buffer for western blot.

chemical	concentration
Tris base	200 mM
NaCl	1.5 M
pH 7.6 with 37% HCl	

After blocking, the protein containing membrane was incubated with the primary antibody shaking at 4°C over night. The next day, the membrane was washed 3 times with 1x TBST for 5 min, followed by incubation in the secondary antibody at room temperature for 2h. After washing 3 times with 1x TBST for 5 min, the signal of secondary antibody (conjugated to horseradish peroxidase (HRP)), was detected by using the enhanced chemiluminescence (ECL) solutions A and B (Table 19) in a ratio of 1:1.

Table 19: ECL solution A and B for chemiluminescent detection of the HRP conjugated to the secondary antibody used for western blotting.

ECL solution A		
Component	Stock	Volume
Luminol	250 mM in DMSO	20 µL
p-Coumaric Acid	90 mM in DMSO	88 µL
Tris-HCL pH8	1 M	2,5 mL
VE water		ad 20 mL
ECL solution B		
Component	Stock	Volume
hydrogen peroxide	30%	12 µL
Tris-HCL pH8	1 M	2 mL
VE water		ad 20 mL

Table 20: Antibodies and probes used in this study.

antigen	information	dilution
anti-GFP	Anti-GFP antiserum kindly provided by the lab of Prof. Dr. Karin Schumacher (COS Heidelberg) As reference see Roth et al. (2018)	1:10.000 in TBST with 0.02% NaN ₃
anti-HA	Polyclonal HA-antibody (from rabbit) Agrisera AS12 2220	1:10.000 in TBST with 0.02% NaN ₃
anti-rabbit	secondary antibody, HRP conjugate, Promega W401B	1:5.000 in TBST
Strep.-HRP	streptavidin conjugated with HRP GE Healthcare (Lot: 9739693)	1:100 in TBST

2. Plant handling

2.1. Seed sterilization

A. thaliana seeds were surface-sterilized using chlorine gas in a 2 mL reaction tube. The open tubes were placed in a sealable jar in which a beaker filled with 50 mL 10% sodium hypochlorite was placed. The addition of 2 mL 37% HCl started the production of chlorine gas and the jar was sealed immediately. After 2h, the tubes were transferred to the sterile bench where they were left open for at least 15 min to let leftover chlorine gas escape.

2.2. Growth conditions

2.2.1 Standard plant growth conditions

In general, *A. thaliana* was grown under long day (LD) conditions (16h light/ 8h dark) at 21°C. If grown on soil, plants were kept in a LD growth chamber with 65% relative humidity. For growth on plates, sterilized seeds were plated on ½ MS-plates (Murashige and Skoog Minimal Organic Powder Medium(Serva), 0.1% MES, pH adjusted to 5.7 with KOH, 0.8% plant agar (Duchefa)) and kept in a LD growth chamber. *N. benthamiana* plants were grown under long day conditions in the green house.

2.2.2 Root Chip experiments

Root Chip experiments were performed using the RootChip-8S (Denninger et al., 2019). Media perfusion was controlled by a syringe pump (World Precision Instruments). For regular root hair growth, a flow rate of 5 µL/min was used in each channel. To induce root hair growth, the flow rate was lowered to 2.5 µL/min.

2.3. Plant transformation and transfection

2.3.1 Transfection of *N. benthamiana* leaves by leaf infiltration

A single colony of transformed *A. tumefaciens* was inoculated in 4 mL of selective LB medium and incubated in a shaking incubator over night at 28°C. The next day 1 mL of this culture was transferred into 4 mL of fresh selective medium and incubated at 28°C for another 4-5h. The cells were harvested via centrifugation at 4000 rcf at 4°C for 5 min and resuspended in 2 mL ice cold AS medium. The OD₆₀₀ was measured in a 1:10 dilution. Afterwards the bacterial suspension was diluted with ice cold AS medium to 0.2 (Note: for double infiltrations, the final concentration is 0.2, meaning 0.1 per construct) and incubated on ice for 1h.

The bacterial suspension was injected into the lower side of *N. benthamiana* leaves using a 1 mL syringe. To make the leaves more accessible, the plants were sprayed with water and kept under a wet hood for 4-5h before infiltration. During the infiltration, the plants were kept outside their humid environment as short as possible to prevent closure of the stomata. Plants were kept in the LD growth chamber and transfected leaves was analyzed 2-3 days after infiltration.

Table 21: AS medium for transfection of *N. benthamiana* leaves.

final concentration	compound	V/m for 50 mL
5% (w/v)	sucrose	2.5 g
0.01% (v/v)	Silwet L77	5 μ L
spattle tip	MgSO ₄	spattle tip
spattle tip	glucose	spattle tip
450 μ M	acetosyringone (stored at -20°C)	112,5 μ L of 200 mM

2.3.2 Transformation of *A. thaliana* via floral dipping

Stable transformation of *A. thaliana* was performed using a modified version of the floral dip protocol (Clough and Bent, 1998). Therefore 2 times 4 mL of selective LB medium were inoculated with single, transformed *A. tumefaciens* colonies and incubated in a shaking incubator at 28°C, over night. The next day, these two cultures were transferred into 100 mL selective LB medium and incubated at 28°C until they reached an OD₆₀₀ of 0.6-0.8. Bacteria were harvested via centrifugation at 4000 rcf for 10 min and resuspended in 200 mL transformation medium (5% sucrose, 0.05% Silwet L77). Plant inflorescences were dipped in the suspension for 3-5 min. Afterwards the plants were kept in a plastic bag until the next morning to facilitate a humid environment. Those plants were grown until completely dried. Seeds were collected and transformants were selected subsequently as described below.

2.3.3 Identification of stable, transgenic *A. thaliana* lines

In general in our lab, constructs containing a fluorescent protein of the same color range have the same resistance cassette: CFP – kanamycin; YFP – glufosinate-ammonium; RFP – hygromycin (Denninger, 2018). T1 seeds were selected in different ways, depending on the T-DNA mediated resistance cassette. Most of the plant lines generated in this thesis contain the glufosinate-ammonium resistance and were therefore selected on soil by spraying 1 week old seedlings with a Basta®-Solution, Bayer (200 μ g/mL glufosinate-ammonium and 0.05% Tween20). The treatment was performed at least 3 times in intervals of 3-4 days. Hygromycin selection was performed on ½ MS-plates containing 20 μ g/mL hygromycin. Since hygromycin affects root elongation, plants were scored for root length with transformed plants showing no impairment of root length. Kanamycin selection was performed on ½ MS-plates containing 50 μ g/mL kanamycin. Since kanamycin affects the production of chlorophyll, plants were scored for bleaching phenotypes with transformed plants showing normal production of chlorophyll.

2.3.4 Estradiol induced gene expression

Several constructs used and created in this thesis, used an adapted version of the estradiol inducible system described by Zuo et al., 2000. The general design of the adapted pGGA promoter module was done by Philipp Denninger (Denninger, 2018). Based on this, several promoters of proteins involved in root hair development were cloned into this pGGA module, controlling the expression of the XVE. This resulted in a set of inducible promoters that facilitate a root hair specific expression.

Estradiol was purchased from Merck and the stock solution (20 mM in absolute ethanol) was stored at -20°C. Dilutions were prepared freshly for each experiment.

2.3.5 Induction of gene expression in *N. benthamiana*

To induce the expression of estradiol inducible constructs in *N. benthamiana* leaves, a solution containing 20 μ M estradiol (dilution (with water) from a 20 mM stock) and 0.01% Silwet L77 was brushed onto the lower side of the leaves using a paintbrush. Induction was performed 6-8h prior to sample preparation.

2.3.6 Induction of *A. thaliana* on agar-plates

For phenotypic analysis, *A. thaliana* seeds were sown onto ½ MS-plates containing 20 μ M estradiol and grown under standard growth conditions. For the investigation of subcellular protein localization, a solution containing 20 μ M estradiol (dilution from stock in ½ MS liquid medium) and 0.01% Silwet L77 was used. This solution was either sprayed onto the seedlings (24h and 6h prior to sample preparation) or applied with soaked cellulose tissue (between 3h and 24h prior to sample preparation and for a duration of 30 min).

3. Imaging

3.1. Stereoscopic imaging

Phenotypic analysis of *rop2/rop4* mutants and potential rescue lines was performed on a Nikon SMZ18 stereoscope, equipped with an Orca Flash 4.0 sCEMOS camera (Hamamatsu, Japan) and SHR Plan Apo 0.5x (NA 0.075) and 2x (NA 0.3) objectives (Nikon). Overview images were acquired with a 3.75x (0.5x objective; 0.75x zoom) magnification whereas close-up images were taken at 40x (0.5x objective 8.0x zoom) magnification. Exposure time was kept at 100 ms for brightfield and 1 sec for fluorescent images. Light intensity was adjusted for each image individually.

3.2. Spinning-disc confocal microscopy

For live-cell, fluorescence imaging a custom-built spinning-disc confocal microscope was used. It was built based on a Nikon Ti-E stand equipped with a motorized stage (Applied Scientific Instrumentation, USA), a spinning disc with 70 μ m hole diameter (CREST Optics, Italy), a motorized filter wheel Optospin IV (Cairn Research, UK), a laser launch box (Omicron, Germany), two dichroic mirrors (Chroma triple band 440/514/561 and Chroma quad band 405/488/561/640) and an EMCCD camera (Photometrics, USA). Furthermore, a 10x air (NA 0.3), 20x multi-immersion (NA 0.75) and a 60x water immersion (NA 1.2) objectives (all from Nikon) were equipped. Image acquisition was controlled via the NIS Elements software (Nikon). The imaging settings used can be found in Table 22.

Table 22: Imaging settings for different fluorescent proteins.

excitation wavelength [nm]	bandpass filter (brand)	fluorescent protein
445	480/40 (Chroma)	mTurquoise2
488	525/45 (Semrock)	GFP
515	542/27 (Semrock)	mCitrine, YFP
561	605/70 (Semrock)	mRuby2

Depending on the brightness of the sample, the intensity of the excitation laser as well as the exposure time were adjusted. Therefore, signal intensities between different images are not necessary comparable. If not specifically stated different, confocal images were acquired using the 70 μm pinhole disc.

3.3. Confocal laser scanning microscopy

Confocal laser scanning microscopy was performed on a Leica SP5II system. This system contained an argon laser, which is capable of emitting with 458, 476, 488, 496 and 514 nm, a diod pump solid state laser of 561 nm emission and a diod with 470 nm pulsed emission (pulse length of 50 ps).

Imaging was performed using a 63x water immersion objective (N.A. 1.2; Leica). For mCitrine detection excitation at 514 nm and an emission window of 520 - 550 nm was used. For mTurquoise detection, excitation at 458 nm and an emission window of 465-505 nm was used. For propidium iodide, excitation was set at 561 nm and an emission window of 570 - 650 nm was chosen.

Detection of fluorescent signal was performed using one or two Hybrid-Detectors (with the gain adjusted individually between 150 and 230%). Image acquisition was performed using the Leica Application Suit software.

3.3.1 FRAP

For measuring fluorescent recovery after photobleaching (FRAP), the built-in FRAP-Wizard of the Leica Application Suit was used. For the bleaching method, the "Zoom-In"-Modus was chosen, with 30 frames pre-bleach, 20 frames bleach and 200 frames post-bleach, each at 0.265 sec per frame. 100% relative laser power was applied in a 10x30 μm ROI during the bleach phase.

For imaging, the 63x water immersion objective, a 3x Zoom, a pinhole diameter of 2.5 AU, 1000 Hz bidirectional scan speed, a 2x line average and a 256x256 px scan field were used. The microscope settings were kept constant between and within experiments, except for the excitation power, which was adjusted as needed.

3.4. Variable angle epifluorescence microscopy

For imaging of proteins at the cell surface, a variable angle epifluorescence microscope (VAEM) was used. This system was provided by the Nikon Imaging facility (Heidelberg) and was build out of a Nikon eclipse Ti2 stand, equipped with an oil immersion 100x DIC N2 Plan Apo objective for TIRF measurements (NA 1.45; Nikon) and an EMCCD camera (Andor iXON Ultra).

Table 23: Imaging settings used for VAEM

excitation [nm]	excitation filter	emission filter	fluorescent protein
515		542/27	mCitrine
561	triple clean-up for 440, 515, 561 nm	triple-emission filter 468/40, 553/30, 641/75	mRuby2
488	525/50 HC	525/50 HC	GFP
561, 515	triple clean-up for 440, 515, 561 nm	triple-emission filter 468/40, 553/30, 641/75	mCitrine, mRuby2 simultaneously

To determine the appropriate angle of the laser, the focus was adjusted to the cover slip with the help of Alexa Fluor™ 647 conjugated dextran (Invitrogen™, D22914). Adjustment of the angle was performed until the highest contrast of the observed structures was reached. During and between measurements, this angle was kept constant to ensure comparability.

To enable fluorophore blinking, the laser power of was set to 60% for 561 nm and 40% for 515 nm.

3.5. Plant stainings

3.5.1 Propidium iodide

Propidium iodide (PI) was used in a final concentration of 1 µg/mL in water. Staining was performed by placing seedlings in the PI solution for 5 min followed by a short washing step in water and subsequent preparation for imaging using water instead of medium.

3.6. Chemical treatment of plants

3.6.1 Pharmacological treatments

Treatment with the plant hormone auxin (Indole-3-acetic acid (IAA)) was performed using a 1:1000 dilution in ½ MS medium, resulting in a final concentration of 100 µM. The stock solution was prepared using 99,8% ethanol as a solvating agent and was stored at -20°C. Staining of seedlings was done for 10 min, followed by a short washing step and subsequent preparation for imaging using ½ MS medium.

To test the protein mobility in response to an inhibited auxin efflux, seedlings were placed in a solution containing 20 µM 2,3,5-triiodobenzoic acid (TiBA) for 30 min. A 10 mM stock solution of TiBA in DMSO was kept at -20°C and freshly diluted in ½ MS medium, when needed. The treatment was followed by a short washing step and subsequent preparation for imaging using ½ MS medium.

4. Data analysis

If not stated otherwise, data analysis was performed using MS Excel. Boxplots were generated using the web-tool “BoxPlotR” created by the Rappsilber and Tyers labs (<http://shiny.chemgrid.org/boxplotr/>). Jitter plots were generated by the web application “PlotsOfData” (Postma and Goedhart, 2019). Visual appearance of the plots was refined using Inkscape without modifying the information content of the data.

4.1.1 Chemical fixation

Chemical fixation of seedlings was performed using 2% paraformaldehyde (PFA) in 1x PBS. An aqueous stock solution of 20% PFA was used for dilutions and was stored at -20°C. Seedlings were placed in the fixative for 5 min, followed by a short washing step in water and subsequent preparation for imaging using ½ MS medium.

4.2. Image processing

Representative images were processed by applying a rolling ball background subtraction with a ball radius of 50 px, followed by three subsequent applications of a Gaussian blur filter, each with a radius of 0.5 px. The processed image was multiplied with the original, unprocessed image. Image processing was performed using Fiji (Schindelin et al., 2012). If not stated explicitly different, image analysis was performed on the unprocessed, raw images.

4.3. Protein mobility analysis

4.3.1 FRAP analysis

To determine the fluorescence recovery rate, the signal intensity in three ROIs was measured over the course of the time-laps stack: at the bleached region, at a region outside the biological sample and in another region within the plasma membrane of the cell was measured over the course of the time-laps stack. The half-time recovery and the mobile fraction were calculated using the web-based application “EasyFRAPweb” (<https://easyfrap.vynet.upatras.gr>) as described in Koulouras et al., 2018. For normalizing the data, the “double” method was used. The curve fitting was chosen according to the highest R^2 value, which was the single exponential curve fitting for the majority of the data.

4.3.2 Particle tracking

For measuring protein mobility with a high spatiotemporal resolution, time laps movies acquired by variable angle epifluorescence microscopy (see chapter 3.4 page 134) were processed, according to the following procedure:

With the image stack a rolling ball background subtraction (radius = 5 px) was done, followed by three subsequent applications of a gaussian blur filter (sigma = 0.5). The resulting 32-bit image was divided by its maximum intensity value and multiplied with the original image stack. The brightness and contrast was set to a range from 0 to 65535 gray values and converted into a 16-bit image, that was used for subsequent analysis with TrackMate (Tinevez et al., 2017). A macro to automatize this process can be found in chapter 4.6.2, page 139.

For particle tracking with TrackMate, a ROI covering the RHID was selected. The particles – which reflect the single fluorophores – were detected with the Laplacian of Gaussian (LoG) detector, using an estimated blob diameter of 0.5 μm and an individually determined intensity threshold. Sub-pixel localization was allowed. To increase the quality of detection, no filter was applied. To prevent the splitting or merging of tracks, the simple linear assignment problem (LAP) tracker was used. A maximum linking, as well as a maximum gap-closing distance of 0.3 μm was allowed. To prevent that two distinct blink events are linked within one track, a frame gap for gap-closing was not allowed.

The resulting data was analyzed in MS Excel, in the Axon™pCLAMP™10 Clampfit (version 10.7.0) software or in R-Studios (version: 1.2.5033; R Core Team, 2019).

4.3.3 Quantification of Particle tracking data

The velocity of ROP2-proteins was determined via particle tracking (as described in Chapter 4.3.2, page 136). The maximum velocity was divided in 100 equal velocity-bins, which were used to create

a histogram of the measured velocities using the Axon™pCLAMP™10 Clampfit (version 10.7.0) software. This histogram data was fitted in R Studios (R Core Team, 2019) using a polynomial fitting model. The number of polynomials was increased until the correlation coefficient R^2 did not further increase significantly (significance was tested by one-way ANOVA). Assessment of whether the distribution of velocities was significantly different in- and outside of the RHID was done using a two-way ANOVA in R (for details and information about applied R packages see the script in chapter 4.6.3, on page 140).

4.4. Analysis of Protein localization

Statistical analysis of the data was performed in R-Studios using the script for ANOVA-Tukey test (see chapter 4.6.1, page 138).

4.4.1 Polarity index measurements

To determine how polar a protein is distributed within a trichoblast, the mean fluorescence intensity in the unprocessed image stack was measured in three 15 pixel wide and 3 pixel high ROIs: within the RHID, outside of the RHID, as well as outside of the biological sample. The value outside of the biological sample was considered as background and was subtracted from the values within and outside the RHID. The polarity index is calculated by dividing the background normalized value for inside the RHID by the value from outside of the RHID.

4.4.2 Membrane association measurements

To determine how well a protein within a trichoblast is associated with the plasma membrane (PM), the mean fluorescence intensity in the unprocessed image stack was measured in a 15x3 px ROI at the PM. A background value measured outside the biological sample is subtracted from this measurement and the resulting value is considered the PM value. Next, the ROI is moved 3 pixels away from the PM-ROI into the cytosol, resulting in a second ROI, that is directly located underneath. The same background value is subtracted again and the resulting value is considered the cytosol value. Membrane association is calculated by dividing the PM-value by the cytosol-value. This analysis was done for inside the RHID as well as for outside the RHID.

4.4.3 Cell-type specificity measurements

To determine trichoblast-specific of the expression of a fluorophore under the control of estradiol inducible versions of the GEF3, ROP2 or ExpA7 promoter, the plants were stained with propidium iodide (PI) 24 h after induction with estradiol. The fluorescence signal for mCitrine as well as PI was recorded with the Leica SP5 point scanning microscope, as described above. The obtained image stacks were rotated 90 degrees along the x-axis by using the “TransformJ: Turn” Plugin (developed by E.H.W. Meijering) of Fiji, resulting in a stack of cross-sections. ROIs for trichoblasts and atrichoblasts were assigned in the PI channel and were used to measure the fluorescence intensity in the mCitrine channel. Trichoblasts were identified according to their relative position to the underlying cortex cells. The ratio between the fluorescence intensity in trichoblasts and atrichoblasts was calculated and the mean value of ratios per cross-section was determined. Per root, 3 cross-sections were analyzed.

4.5. Nanodomain analysis

4.5.1 SRRF- analysis

To perform single-molecule localization over the course of time, the acquired VAEM time-laps stacks were used to perform SRRF-analysis (super-resolution radial fluctuation (Gustafsson et al., 2016)). Prior to SRRF, the drift was estimated using the built in “Estimate Drift”-tool and a time averaging of 100. The resulting drift table was used for drift correction during SRRF.

For SRRF-analysis, the following settings were applied: ring radius of 0.5, radial magnification of 5, axis ring of 8, 100 frames per time-point and temporal radiality average (TRA). Furthermore, intensity weighing was enabled.

4.5.2 Measurements of nanodomain dimensions

To determine the size and density of the nanodomains visualized by the SRRF algorithm, the threshold in a region of interest (for example the RHID) in the original SRRF image was set using the presetting “Moments” in the Fiji threshold menu and used to create a mask. This mask was turned into a binary image by dividing the gray value of each pixel by 255. This binary mask was multiplied with the original SRRF image to clear everything but the nanodomains; the resulting image was called “image1”. The individual nanodomains were found by using the “Find Maxima” function implemented in Fiji. “Segmented particles” was chosen as the output type and the noise tolerance was adjusted individually by checking the selection in the original image. The resulting image was converted into a binary mask by dividing each pixel value by 255. This binary mask was multiplied with “image1”, leading to a separation of the individual nanodomains. In the resulting image the threshold was set using the presetting “Moments” and used for the “analyze particles” function, which creates a table containing spatial information of the nanodomains. A macro to automatize this process can be found in Chapter 4.6.4 on page 141.

The resulting tables were further managed using MS excel. Statistical analysis and graphical representation of the data was performed as described previously (Chapter 4: Data analysis, page 135).

4.6. Scripts and Macros

4.6.1 ANOVA-Tukey test using R

This script is adapted from Yan Holtz’ “Tukey Test and boxplot in R” on www.r-graph-gallery.com. For this, the “multcomView” package (Graves et al., 2019) was used.

```
library(multcompView)

#load a tab delimited file that contains the data
DataDir <- choose.files()
data <- read.csv(DataDir,header=TRUE, stringsAsFactors = FALSE, sep = "\t")

model=lm( data$value ~ data$line )
ANOVA=aov(model)
TUKEY <-TukeyHSD(x=ANOVA, 'data$line', conf.level=0.99)
plot(TUKEY , las=1 , col="brown" )

#grouping the treatments that are not different to each other.
generate_label_df <- function(TUKEY, variable){
```

```

#extract labels and factor levels from Tukey post-hoc
Tukey.levels <- TUKEY[[variable]][,4]
Tukey.labels<- data.frame(multcompLetters(Tukey.levels) ['Letters'])

#the labels are put in the same order as the data in the boxplot
Tukey.labels$line=rownames(Tukey.labels)
Tukey.labels=Tukey.labels[order(Tukey.labels$line) , ]
return(Tukey.labels)}

#the "labels" function is applied to the data set
LABELS <- generate_label_df(TUKEY , "data$line")
str(LABELS)
head(LABELS)
capture.output(LABELS,file="#insert you file name here# .csv")

```

4.6.2 Image Processing for Particle Tracking using Fiji

This Fiji macro was written to automatize the image processing of VAEM time-laps images prior to particle tracking with the Fiji Plugin TrackMate (Tinevez et al., 2017). A detailed description of the underlying procedure can be found in Chapter 4.3.2, page 136.

```

//Copyright of this Macro: Vanessa Schmidt 2019
//open each file in a folder
directory = getDirectory("Images to be analyzed");
list = getFileList(directory);
dirSave = getDirectory("Where to save results");
//creat a folder for saving the processed stacks
File.makeDirectory(dirSave + "Processed");
separator = File.separator;
File.makeDirectory(dirSave + "EnhancedContrast");
for(i = 0; i < list.length; i++) {
  imageName = list[i];
  //define a variable that contains the path for saving the Transformation Matrices
  dirProcessed = dirSave + "Processed" + separator;
  dirRawEnhanced = dirSave + "EnhancedContrast" + separator;
  open(directory + imageName );
  current = getTitle();
  //duplicate image
  selectWindow(current);
  run("Duplicate...", "duplicate");
  duplicate = getTitle();
  //enhance contrast and save as Tiff and avi
  run("Duplicate...", "duplicate");
  rename("enhanced");
  selectWindow("enhanced");
  run("Enhance Contrast...", "saturated=0.1 process_all");
  saveAs("Tiff", dirRawEnhanced + current + "_enhanced.tiff");
  run("Close");
  //subtract Background and 3x Gaussian Blur
  selectWindow(duplicate);
  run("Subtract Background...", "rolling=5 stack");
  run("Gaussian Blur...", "sigma=0.5 stack");
  run("Gaussian Blur...", "sigma=0.50 stack");
  run("Gaussian Blur...", "sigma=0.50 stack");
  //convert image into 32-bit
  run("32-bit");
  //max Int projection
  run("Z Project...", "projection=[Max Intensity]");
  maxZ=getTitle();
  //measure max int value
  getStatistics(area, mean, min, max, std, histogram);
  //divide the processed image by the max int value
  selectWindow(duplicate);
  run("Divide...", "value=max stack");
  //multiply the 32bit processed image with the original image -> create a new
  32bit image
  imageCalculator("Multiply create 32-bit stack", current, duplicate);
  //scale the image from 0 to 65.535
  setMinAndMax(0, 65535);
  //convert into 16bit image
  run("16-bit");
  // save processed images as tiff

```

```

saveAs("Tiff", dirProcessed + current + "_processed.tiff");
//close all open images
close();
close(current);
close(duplicate);
close(maxZ);
}
run("Close All");

```

4.6.3 Polynomial fitting and two-way ANOVA using R

This script was adapted from a script kindly provided by Dr. Milan Župunski (University of Novi Sad, Faculty of Sciences; guest scientist in 2019 and 2020 at COS Heidelberg, AG Grossmann). For this, the “car” (Fox and Weisberg, 2019), the “ggplot2” (Wickham, 2016) and the “ggthemes” (Arnold, 2019) packages were used.

```

library(car)
library(ggplot2)
library(ggthemes)

#choose the file where the data is saved.
DataDir <- choose.files()

#create a dataframe
mydata <- read.delim(file= file.path(DataDir), header=TRUE, stringsAsFactors = FALSE, sep =
"\t")

#define variables as objects
vel <- mydata$velocity.bin

rhid1 <- mydata$RHID_1
out1 <- mydata$outside_1

#polynomial fit with seventh degree
fitrhid1 <- lm(rhid1~poly(vel,7,raw=TRUE))
fitout1 <- lm(out1~poly(vel,7,raw=TRUE))

#capture the Fitting Summary in the default folder, which in my case is the documents folder
capture.output(summary(fitrhid1),file="FitSummary_ROP2_+1_RHID.csv")
capture.output(summary(fitout1),file="FitSummary_ROP2_+1_out.csv")
#####ANOVA#####
#cell stage +1
AnovaDir <- choose.files()
anvel <- read.delim(file = file.path(AnovaDir), header = TRUE, stringsAsFactors = FALSE, sep =
"\t")
str(anvel)
anvel$velocity.bin <- as.factor(anvel$velocity.bin)
anvel$loc <- as.factor(anvel$loc)

anova.test <- Anova(lm(freq~velocity.bin*loc, data= anvel), type = "III")

#export it to a csv file
capture.output(anova.test,file="ResultANOVA_ROP2_+1.csv")
#####PLOTTING#####
#plot the 1st layer
p <- ggplot(mydata)+
  ylab(label = "Frequency")+ #y-axis name
  xlab("Velocity")+ #x-axis name+
  labs(title="ROP2 cell+1")
  theme_tufte()+ #choose your theme - type theme_ and choose from the list
  theme(text = element_text(size=18)) #change the size of the axis text
p

#make the 2nd layer
p1 <- p + stat_smooth(method = "lm",
  aes(x=vel, y=rhid1), colour="#fd8d3c",
  formula = y ~ poly(x,6,raw=TRUE), se=FALSE, size = 1)+
  stat_smooth(method = "lm",
  aes(x=vel, y=out1), colour="#88419d",
  formula = y ~ poly(x,6,raw=TRUE), se=FALSE, size = 1)+

```

Materials and Methods

```
      theme(axis.text.x = element_text(colour = "black", size = 14), #the color and size
of x-ax text
      axis.text.y = element_text(colour = "black", size = 14))+ #the color and size
of y-ax text
      scale_x_continuous(breaks = seq(0, 5, 0.5))+
      scale_y_continuous(breaks = seq(0, 1, 0.2))
p1

#third layer - x-axis maximum
gb <- ggplot_build(p1)

exact_x_value_of_the_curve_maximum1 <-
gb$data[[1]]$x[which(diff(sign(diff(gb$data[[1]]$y)))== -2)+1]
exact_x_value_of_the_curve_maximum2 <-
gb$data[[2]]$x[which(diff(sign(diff(gb$data[[2]]$y)))== -2)+1]

p2 <- p1 + geom_vline(xintercept=exact_x_value_of_the_curve_maximum1)+
      geom_vline(xintercept=exact_x_value_of_the_curve_maximum2)
p2

#get the maxima value
exact_x_value_of_the_curve_maximum1
exact_x_value_of_the_curve_maximum2

#the 4th, final layer with data points
p2 + geom_point(aes(x=vel, y=rhid1, color="1"), #plotting the 1st variable
      colour= "#fd8d3c", pch= 18, size = 3, alpha = 0.6)+ #colors
http://colorbrewer2.org/
      geom_point(aes(x=vel, y=out1, color="2"),
      colour= "#88419d",pch=16, size = 3, alpha = 0.6) #plotting the 2nd variable
```

4.6.4 Counting and measuring of nanodomains after SRRF using Fiji

This Fiji macro was written to automatize the size determination and counting of Nanodomains in SRRF-images. A detailed description of the underlying procedure can be found in Chapter 4.5.2 , page 138.

```
//Copyright of this Macro: Vanessa Schmidt 2019
//there needs to be one SRRF image open
//a ROI for the RHID needs to be depicted on the image
//add that ROI to the ROI-Manager - the macro will save this ROI automatically
//set scale to 31.25px/µm
run("Set Scale...", "distance=31.25 known=1 unit=µm");
title = getTitle();
Dir = getDirectory("Choose Where to save the results")
separator = File.separator;
dotIndex = indexOf(title, ".tif");
imageNameClean = substring(title, 0, dotIndex);
File.makeDirectory(Dir + imageNameClean );
saveDir = Dir + imageNameClean + separator;
//create a text-file for the documentation
run("Text Window...", "name=" + imageNameClean + "_Documentation width=80 height=24 menu");
//add ROI, save ROI
run("Select All");
roiManager("Save", saveDir + imageNameClean + "_RHID-ROI.zip");
//measure the ROI and save Results and clear results
run("Measure");
selectWindow("Results");
saveAs("Results", saveDir + imageNameClean + "_RHID-result.csv");
run("Clear Results");
//start with the image processing
roiManager("Select", 0);
run("Duplicate...", "title=duplicate");
//Clear outside of the ROI
setBackground(0, 0, 0);
run("Clear Outside");
//clear ROI manager and results
run("Select All");
roiManager("Deselect");
roiManager("Delete");
//Thresholding with Method: Moments - creat mask - rename in mask1
waitForUser("Press "+" \"OK\" "+" when you are done with thresholding");
```

Materials and Methods

```
//setAutoThreshold("Moments dark");
//run("Threshold...");
//setOption("BlackBackground", true);
  run("Convert to Mask");
  rename("mask1");
  run("Divide...", "value=255.000");
//Multiply the original image with mask1
imageCalculator("Multiply create", title, "mask1");
selectWindow("Result of " + title);
rename("image1");
run("Tile");
//Find Maxima. The Macro will automatically wait for the user to select a prominence value
//Note: You also have to check the following boxes in the Find Maxima window: Strict,
exclude edge maxima, above lower threshold
//Furthermore select as output type: "Segmented Particles"
selectWindow("image1");
setAutoThreshold("Moments dark");
//run("Threshold...");
  run("Find Maxima...");
//pause the macro to let the user performe documentation
waitForUser("Press "+ "\OK" +" when you are done with the documentation");
saveAs("Text", saveDir + imageNameClean + "_Documentation.txt");
run("Close");
//create mask2 by dividing the segmented image by 255
selectWindow("image1 Segmented");
run("Divide...", "value=255.000");
rename("mask2");
//Multiply the original image with mask2
imageCalculator("Multiply create", title, "mask2");
selectWindow("Result of " + title);
rename("image2");
//thresholding and analysis of particles
setAutoThreshold("Moments dark");
run("Analyze Particles...");
//save results and ROIs
selectWindow("Results");
saveAs("Results", saveDir + imageNameClean + "_results.csv");
run("Select All");
roiManager("Save", saveDir + imageNameClean + "_ROIs.zip");
//closing everything for the next round
run("Select All");
roiManager("Deselect");
roiManager("Delete");
selectWindow("image1");
close();
selectWindow("image2");
close();
selectWindow("mask1");
close();
selectWindow("mask2");
close();
run("Clear Results");
selectWindow(title);
close();
```

5. Material used in this thesis

5.1. Plant lines not generated in this thesis

Description	Name	origin
8K-Farn		Yvon Jaillais, ENS Lyon (Simon et al., 2016)
EstInd::mCitrine:GEF4	pPD202	Philipp Denninger, Grossmann lab
EstInd::mCitrine:ROP2	pPD184	Philipp Denninger, Grossmann lab
EstInd::mCitrine:ROP2-7K-A	pPD251	Philipp Denninger, Grossmann lab
EstInd::mCitrine:ROP2-CA	pPD191	Philipp Denninger, Grossmann lab
EstInd::mCitrine:ROP2-DN	pPD192	Philipp Denninger, Grossmann lab
EstInd::mCitrine:ROP2ΔC161	pPD198	Philipp Denninger, Grossmann lab
EstInd::mCitrine:ROP2ΔN160	pPD197	Philipp Denninger, Grossmann lab
EstInd::mCitrine:ROP2ΔN79	pPD195	Philipp Denninger, Grossmann lab
EstInd::mCitrine:ROP4	pPD200	Philipp Denninger, Grossmann lab
EstInd::PIP5K3:mCitrine	pPD213	Philipp Denninger, Grossmann lab
EstInd::PRK7:mCitrine	pPD220	Philipp Denninger, Grossmann lab
<i>gef3</i> pROP2::mCitrine:ROP2	pPD240m3x <i>gef3-1</i>	Philipp Denninger, Grossmann lab
p35S::Lti6b-GFP		Cutler et al., 2000
pBrk1::BRK1-mTurquoise2	pPD279	Philipp Denninger, Grossmann lab
pBrk1::BRK1-YFP		Djakovic et al., 2006
pFER::Fer-GFP		Nana Keinath, Schumacher lab (Denninger et al., 2019)
PI(4)P-reporter		Yvon Jaillais, ENS Lyon (Simon et al., 2014)
PS-reporter		Yvon Jaillais, ENS Lyon (Simon et al., 2016)
Ubi10::mCitrine	pPD267	Philipp Denninger, Grossmann lab

5.2. Entry vectors cloned in the course of this thesis

Table 24: List of entry vectors cloned in this thesis

Insert	Plasmid	Backbone	description
pGEF3::XVE_OlexTATA	pVS0133	pGGA	inducible expression under the control of the GEF3 promoter
pROP2::XVE_OlexTATA	pVS0134	pGGA	inducible expression under the control of the ROP2 promoter
pGEF4::XVE_OlexTATA	pVS0135	pGGA	inducible expression under the control of the GEF4 promoter
pGEF14::XVE_OlexTATA	pVS0136	pGGA	inducible expression under the control of the GEF14 promoter
mCit:HA:BirA* in B module	pVS0050	pGGB	mCit-BirA* for N-terminal tagging
HA:BirA* in B module	pVS0051	pGGB	BirA* for N-terminal tagging

Materials and Methods

mCit:HA:APEX2 in B module	pVS0056	pGGB	mCit-APEX2 for N-terminal tagging
HA:APEX2 in B module	pVS0057	pGGB	APEX2 for N-terminal tagging
mtFlot2-Head with GAGA linker in B module	pVS0073	pGGB	mtFlot2 as N tag in B module
mScarleti in B module	pVS0094	pGGB	mScarleti in B module
mScarlet in B module	pVS0095	pGGB	mScarlet in B module
S-YFP2 in B module	pVS0097	pGGB	S-YFP2 in B module
mCit:TurboID in B module	pVS0141	pGGB	mCitrine TurboID in B module
TurboID in B module	pVS0142	pGGB	TurboID in B module
mCit:miniTurbo in B module	pVS0145	pGGB	mCitrine-miniTurboID in B module
miniTurbo in B module	pVS0146	pGGB	miniTurboID in B module
AtSAC9 in C module	pVS0070	pGGC	At SAC9 without BSA sites in C module
ROP2 1-20 in C module	pVS0084	pGGC	ROP2 1-20 with STOP in c-module
ROP2 1-43 in C module	pVS0085	pGGC	ROP2 1-43 with STOP in c-module
ROP2 1-80 in C module	pVS0086	pGGC	ROP2 1-80 with STOP in c-module
GEF3-ORF without STOP in C module	pVS0111	pGGC	GEF3-ORF without STOP in C module
ROP2 d81-160 with STOP in C module	pVS0118	pGGC	ROP2 d81-160 with STOP in C module
ROP2 d81-120 with STOP in C module	pVS0119	pGGC	ROP2 d81-120 with STOP in C module
ROP2 d121-160 with STOP in C module	pVS0120	pGGC	ROP2 d121-160 with STOP in C module
ROP2 d124-137 with STOP in C module	pVS0121	pGGC	ROP2 d124-137 with STOP in C module
ROP2 d124-148 with STOP in C module	pVS0122	pGGC	ROP2 d124-148 with STOP in C module
BirA*:HA in D module	pVS0052	pGGD	BirA* for C-terminal tagging
BirA*:HA:mCit in D module	pVS0053	pGGD	mCit-BirA* for C-terminal tagging
APEX2:HA in D module	pVS0054	pGGD	APEX2 for C-terminal tagging
APEX2:HA:mCit in D module	pVS0055	pGGD	APEX2-mCit for C-terminal tagging
ROP2 mini in D module	pVS0071	pGGD	ROP2 C-terminus as C tag in D module
Lti6b in D module	pVS0072	pGGD	Lti6b as C tag in D module
mScarlet in D module	pVS0093	pGGD	mScarlet in D module
mScarleti in D module	pVS0096	pGGD	mScarleti in D module
S-YFP2 in D module	pVS0098	pGGD	S-YFP2 in D module
mCit:BirA* in D module	pVS0107	pGGD	mCit:BirA* in D module
BirA* in D module	pVS0108	pGGD	BirA* in D module
mCit-HCS1 in D module	pVS0109	pGGD	mCit-HCS1 in D module
HCS1 in D module	pVS0110	pGGD	HCS1 in D module
mCit:TurboID in D module	pVS0139	pGGD	mCitrine TurboID in D module
TurboID in D module	pVS0140	pGGD	TurboID in D module
mCit:miniTurbo in D module	pVS0143	pGGD	mCitrine-miniTurboID in D module
miniTurbo in D module	pVS0144	pGGD	miniTurboID in D module

5.3. List of destination vectors cloned in the course of this thesis

Table 25: Plant expression vectors cloned in this thesis.

Insert	Plasmid	Backbone	Description
pRHD4::mCit:RHD4	pVS0001	pGGZ003	RHD4 specific expression
pMRH3:MRH3:mCit	pVS0002	pGGZ003	MRH3 specific expression
Ubi10::BirA(R118G):HA:c- Decoy:C-Decoy:HSP18T	pVS0003	pGGZ003	ubiquitous expression of BirA(R118G)
Ubi10::BirA(R118G):HA-mCit:c- Decoy:C-Decoy:HSP18T	pVS0004	pGGZ003	ubiquitous expression of BirA(R118G) with mCit
pCobl9::BirA(R118G):HA:c- Decoy:C-Decoy:HSP18T	pVS0005	pGGZ003	trichoblast specific expression of BirA(R118G)
pCobl9::BirA(R118G):HA-mCit:c- Decoy:C-Decoy:HSP18T	pVS0006	pGGZ003	trichoblast specific expression of BirA(R118G) with mCit
pROP2::BirA(R118G):HA:c- Decoy:C-Decoy:HSP18T	pVS0007	pGGZ003	pROP2 driven expression of BirA(R118G)
pROP2::BirA(R118G):HA-mCit:c- Decoy:C-Decoy:HSP18T	pVS0008	pGGZ003	pROP2 driven expression of BirA(R118G) with mCit
pROP2::BirA(R118G):HA- mCit:ROP2-CDS:C-Decoy:HSP18T	pVS0009	pGGZ003	pROP2 driven expression of BirA(R118G)-ROP2 with mCit
pCobl9::BirA(R118G):HA- mCit:ROP2-CDS:C-Decoy:HSP18T	pVS0010	pGGZ003	trichoblast specific expression of BirA(R118G)-ROP2 with mCit
Ubi10::BirA(R118G):HA:ROP2- CDS:C-Decoy:HSP18T	pVS0011	pGGZ003	ubiquitous expression of BirA(R118G) fused to ROP2
Ubi10::BirA(R118G):HA- mCit:ROP2-CDS:C-Decoy:HSP18T	pVS0012	pGGZ003	ubiquitous expression of BirA(R118G) fused to mCit and ROP2
Ubi10::mCit:ROP2-CDS:C- Decoy:HSP18T	pVS0013	pGGZ003	ubiquitous expression of mCit fused to ROP2
UBI10::N-Decoy:PRK7- CDS:BirA(R118G)- HA:HSP18T:Basta	pVS0014	pGGZ003	ubiquitous expression of PRK7 fused to BirA(R118G)
UBI10::N-Decoy:PRK7- CDS:BirA(R118G)-HA- mCit:HSP18T:Basta	pVS0015	pGGZ003	ubiquitous expression of PRK7 fused to BirA(R118G)-mCit
pCOBL9::N-Decoy:PRK7- CDS:BirA(R118G)- HA:HSP18T:Basta	pVS0016	pGGZ003	trichoblast specific expression of PRK7 fused to BirA(R118G)
pCOBL9::N-Decoy:PRK7- CDS:BirA(R118G)-HA- mCit:HSP18T:Basta	pVS0017	pGGZ003	trichoblast specific expression of PRK7 fused to BirA(R118G)-mCit
pPRK7::N-Decoy:PRK7- CDS:BirA(R118G)- HA:HSP18T:Basta	pVS0018	pGGZ003	pPRK7 driven expression of PRK7 fused to BirA(R118G)
pPRK7::N-Decoy:PRK7- CDS:BirA(R118G)-HA- mCit:HSP18T:Basta	pVS0019	pGGZ003	pPRK7 driven expression of PRK7 fused to BirA(R118G)-mCit
pROP2::BirA(R118G):HA:ROP2- CDS:C-Decoy:HSP18T:Basta	pVS0020	pGGZ003	pROP2 driven expression of BirA(R118G)-ROP2

Materials and Methods

pCOBL9::BirA(R118G):HA:ROP2-CDS:C-Decoy:HSP18T:Basta	pVS0021	pGGZ003	trichoblast specific expression of BirA(R118G)-ROP2
Est-ind::BirA(R118G):HA:ROP2:C-Decoy:HSPT18:Basta	pVS0022	pGGZ003	Estradiol inducible expression of BirA(R118G)-ROP2
Est-ind::mCit: BirA(R118G):HA:ROP2:C-Decoy:HSPT18:Basta	pVS0023	pGGZ003	Estradiol inducible expression of mCit-BirA(R118G)-ROP2
Est-ind::N-Decoy:PRK7:HA: BirA(R118G):HSP T18:Basta	pVS0024	pGGZ003	Estradiol inducible expression of PRK7-BirA(R118G)
Est-ind::N-Decoy:PRK7:HA: BirA(R118G):mCit :HSPT18:Basta	pVS0025	pGGZ003	Estradiol inducible expression of PRK7-BirA(R118G)-mCit
EstInd::BirA(R118G):HA:C-Decoy:C-Decoy:HSPT18:Basta	pVS0026	pGGZ003	Estradiol inducible expression of BirA
EstInd::mCit: BirA(R118G):HA:C-Decoy:C-Decoy:HSPT18:Basta	pVS0027	pGGZ003	Estradiol inducible expression of mCit-BirA
UBI10::N-Decoy:PRK7-CDS:mCit:HSP18T:Basta	pVS0028	pGGZ003	ubiquitous expression of PRK7-mCitrine
Ubi10::BirA(R118G)*:HA:C-Decoy:C-Decoy:HSP18T	pVS0029	pGGZ003	ubiquitous expression of BirA(R118G)*
Ubi10::mCit: BirA(R118G)*:HA:C-Decoy:C-Decoy:HSP18T	pVS0030	pGGZ003	ubiquitous expression of mCit-BirA(R118G)*
Ubi10::BirA(R118G)*:HA:ROP2-CDS:C-Decoy:HSP18T	pVS0031	pGGZ003	ubiquitous expression of BirA(R118G)* fused to ROP2
Ubi10::mCit: BirA(R118G)*:HA:ROP2-CDS:C-Decoy:HSP18T	pVS0032	pGGZ003	ubiquitous expression of mCit-BirA(R118G)* fused to ROP2
Ubi10::APEX2:HA:C-Decoy:C-Decoy:HSP18T	pVS0033	pGGZ003	ubiquitous expression of APEX2
Ubi10::mCit: APEX2:HA:C-Decoy:C-Decoy:HSP18T	pVS0034	pGGZ003	ubiquitous expression of mCit-APEX2
Ubi10::APEX2:HA:ROP2-CDS:C-Decoy:HSP18T	pVS0035	pGGZ003	ubiquitous expression of APEX2 fused to ROP2
Ubi10::mCit: APEX2:HA:ROP2-CDS:C-Decoy:HSP18T	pVS0036	pGGZ003	ubiquitous expression of mCit-APEX2 fused to ROP2
pCOBL9-XVE_OlexTATA in A module	pVS0037	pGGZ003	Promoter construct for estradiol inducible, root hair specific expression
EstIndCobl9::mCit:Decoy:Decoy:HspT:BastaR	pVS0038	pGGZ003	Estradiol inducible, root hair specific expression of mCitrine
EstIndCobl9::mCit:ROP2:Decoy:HspT:BastaR	pVS0039	pGGZ003	Estradiol inducible, root hair specific expression of mCitrine fused to ROP2
EstIndCobl9::mCit:Lti6b:Decoy:HspT:BastaR	pVS0040	pGGZ003	Estradiol inducible, root hair specific expression of mCitrine fused to Lti6b
EstInd::mCit:SAC9:Lti6b:HspT:BastaR	pVS0041	pGGZ003	Estradiol inducible expression of mCit-SAC9 tagged with Lti6b
EstInd::mCit:SAC9:ROP2mini:HspT:BastaR	pVS0042	pGGZ003	Estradiol inducible expression of mCit-SAC9 tagged with ROP2 mini

Materials and Methods

EstInd::mtFlot2-Head:Sac9:mCit:HspT:BastaR	pVS0043	pGGZ003	Estradiol inducible expression of mCit-SAC9 tagged with mtFlot2
pEXP7A-XVE_OlexTATA in A module	pVS0044	pGGZ003	Promoter construct for estradiol inducible, root hair specific expression
pEXP7A-XVE_OlexTATA-mCit	pVS0045	pGGZ003	Estradiol inducible, root hair specific expression of mCitrine
pEXP7A-XVE_OlexTATA-mCit-Lti6b	pVS0046	pGGZ003	Estradiol inducible, root hair specific expression of mCitrine fused to ROP2
pEXP7A-XVE_OlexTATA-mCit-ROP2	pVS0047	pGGZ003	Estradiol inducible, root hair specific expression of mCitrine fused to Lti6b
pGEF3::mTurq2:GEF3ORF:HspT:KanR	pVS0048	pGGZ003	mTurq2-GEF3 ORF driven by the GEF3 promoter
Ubi::mCit:SAC9:Lti6b:HspT:BastaR	pVS0049	pGGZ003	ubiquitous expression of mCit-SAC9-Lti6b
Ubi::mCit:SAC9:Rop2mini:HspT:BastaR	pVS0058	pGGZ003	ubiquitous expression of mCit-SAC9-ROP2 mini
EstInd::mCit:ROP2 1-20:Cdecoy:HSPT:Basta	pVS0059	pGGZ003	Estradiol inducible expression of mCit-ROP2 1-20
EstInd::mCit:ROP2 1-43:Cdecoy:HSPT:Basta	pVS0060	pGGZ003	Estradiol inducible expression of mCit-ROP2 1-43
EstInd::mCit:ROP2 1-80:Cdecoy:HSPT:Basta	pVS0061	pGGZ003	Estradiol inducible expression of mCit-ROP2 1-80
Cobl9::mCit:ROP2 1-20:Cdecoy:HSPT:Basta	pVS0062	pGGZ003	Root hair specific expression of mCit-ROP2 1-20
Cobl9::mCit:ROP2 1-43:Cdecoy:HSPT:Basta	pVS0063	pGGZ003	Root hair specific expression of mCit-ROP2 1-43
Cobl9::mCit:ROP2 1-80:Cdecoy:HSPT:Basta	pVS0064	pGGZ003	Root hair specific expression of mCit-ROP2 1-80
Ubi::mScarlet:Cdecoy:Cdecoy:HSPT:Hyg	pVS0065	pGGZ003	ubiquitous expression of cytoplasmic mScarlet
Ubi::mScarlet-i:Cdecoy:Cdecoy:HSPT:Hyg	pVS0066	pGGZ003	ubiquitous expression of cytoplasmic mScarlet-i
Ubi::S-YFP2:Cdecoy:Cdecoy:HSPT:Basta	pVS0067	pGGZ003	ubiquitous expression of cytoplasmic S-YFP2
Ubi::Ndecoy:lifeAct:mScarlet:HSPT:Hyg	pVS0068	pGGZ003	ubiquitous expression of lifeact-mScarlet
Ubi::Ndecoy:lifeAct:mScarlet-i:HSPT:Hyg	pVS0069	pGGZ003	ubiquitous expression of lifeact-mScarlet-i
Ubi::Ndeoy:lifeAct:S-YFP2:HSPT:Basta	pVS0074	pGGZ003	ubiquitous expression of lifeact-S-YFP2
EstInd::Pdlp1a:mCit	pVS0075	pGGZ003	inducible expression of Pdlp1a-mCitrine
EstInd::Pdlp1a:mScarlet	pVS0076	pGGZ003	inducible expression of Pdlp1a-mScarlet
EstInd::mCit:ROP2d81-160:Cdecoy:HSPT:Basta	pVS0077	pGGZ003	estradiol inducible expression of ROP2 d81-160
EstInd::mCit:ROP2d81-120:Cdecoy:HSPT:Basta	pVS0078	pGGZ003	estradiol inducible expression of ROP2 d81-120

Materials and Methods

EstInd::mCit:ROP2d121-160:Cdecoy:HSPT:Basta	pVS0079	pGGZ003	estradiol inducible expression of ROP2 d121-160
EstInd::mCit:ROP2d124-137:Cdecoy:HSPT:Basta	pVS0080	pGGZ003	estradiol inducible expression of ROP2 d124-137
EstInd::mCit:ROP2d124-148:Cdecoy:HSPT:Basta	pVS0081	pGGZ003	estradiol inducible expression of ROP2 d124-148
Cobl9::mCit:ROP2d81-160:Cdecoy:HSPT:Basta	pVS0082	pGGZ003	pCobl9 driven expression of ROP2 d81-160
Cobl9::mCit:ROP2d81-120:Cdecoy:HSPT:Basta	pVS0083	pGGZ003	pCobl9 driven expression of ROP2 d81-120
Cobl9::mCit:ROP2d121-160:Cdecoy:HSPT:Basta	pVS0087	pGGZ003	pCobl9 driven expression of ROP2 d121-160
Cobl9::mCit:ROP2d124-137:Cdecoy:HSPT:Basta	pVS0088	pGGZ003	pCobl9 driven expression of ROP2 d124-137
Cobl9::mCit:ROP2d124-148:Cdecoy:HSPT:Basta	pVS0089	pGGZ003	pCobl9 driven expression of ROP2 d124-148
Ubi::N-Decoy:TUA6:Citrine:HSPT:Basta	pVS0090	pGGZ003	ubiquitous expression of TUA6-Citrine
Ubi::N-Decoy:TUA6:mCitrine:HSPT:Basta	pVS0091	pGGZ003	ubiquitous expression of TUA6-mCitrine
EstInd::PRK7:mCit-HA-TurboID	pVS0092	pGGZ003	inducible expression of PRK7 fused to mCitrine-TurboID
pGEF3::XVE_OlexTATA::mCitrine	pVS0099	pGGZ003	inducible expression under the control of the GEF3 promoter of mCitrine
pROP2::XVE_OlexTATA::mCitrine	pVS0100	pGGZ003	inducible expression under the control of the ROP2 promoter of mCitrine
pGEF4::XVE_OlexTATA::mCitrine	pVS0101	pGGZ003	inducible expression under the control of the GEF4 promoter of mCitrine
pGEF14::XVE_OlexTATA::mCitrine	pVS0102	pGGZ003	inducible expression under the control of the GEF14 promoter of mCitrine
Ubi::HA-TurboID	pVS0103	pGGZ003	ubiquitous expression of TurboID
Ubi::mCitrine-HA-TurboID	pVS0104	pGGZ003	ubiquitous expression of mCitrine-TurboID
EstInd::HA-TurboID	pVS0105	pGGZ003	estradiol induced expression of TurboID
EstInd::mCitrine-HA-TurboID	pVS0106	pGGZ003	estradiol induced expression of mCitrine-TurboID
EstInd::TurboID-HA:ROP2	pVS0112	pGGZ003	estradiol induced expression of TurboID fused to ROP2
EstInd::miniTurboID-HA:ROP2	pVS0113	pGGZ003	estradiol induced expression of miniTurboID fused to ROP2
pBrk1::Brk1CDS:mRuby2:HspT:Hyg	pVS0114	pGGZ003	Brk1-mRuby expression under the endogenous promoter
pGEF3::mRuby2:GEF3ORF:HspT:Hyg	pVS0115	pGGZ003	GEF3-mRuby expression under the endogenous promoter
Ubi::HA-miniTurboID	pVS0116	pGGZ003	ubiquitous expression of miniTurboID

Ubi::mCitrine-HA-miniTurboID	pVS0117	pGGZ003	ubiquitous expression of miniTurboID-mCitrine
EstInd::HA-miniTurboID	pVS0123	pGGZ003	estradiol inducible expression of miniTurboID
EstInd::mCitrine-HA-miniTurboID	pVS0124	pGGZ003	estradiol inducible expression of miniTurboID-mCitrine
pGEF3::XVE_OlexTATA::TurboID: GEF3orf	pVS0125	pGGZ003	GEF3 fused to TurboID under the control of an inducible GEF3 promoter
pGEF3::XVE_OlexTATA::miniTurboID:GEF3orf	pVS0126	pGGZ003	GEF3 fused to miniTurboID under the control of an inducible GEF3 promoter
EstInd::TurboID:GEF3orf	pVS0127	pGGZ003	estradiol inducible expression of GEF3 fused to TurboID
EstInd::miniTurboID:GEF3orf	pVS0128	pGGZ003	estradiol inducible expression of GEF3 fused to miniTurboID
EstInd::TurboID:GEF3cds	pVS0129	pGGZ003	estradiol inducible expression of GEF3 fused to TurboID
EstInd::miniTurboID:GEF3cds	pVS0130	pGGZ003	estradiol inducible expression of GEF3 fused to miniTurboID

5.4. List of primers used in this thesis

Table 26: List of primers used in this thesis.

description	Name	sequence
HA-tag-D overhang	oVS0001_rev	aacaGGTCTCaCTGAtgcGTAATCCGGTACATCGT
BirA-star for N terminal tagging-C-overhang	oVS0002_rev	aacaGGTCTCaaGCCGccttctcagcactcctcaatga
HA-tag-B-overhang	oVS0003_fwd	aaaaGGTCTCaAACAatgTACCCTTACGATGTACCGG ATTACGCAatgaaggataaacaccgtgcc
BirA-star_D overhang	oVS0004_fwd	aaaaGGTCTCaTCAGcaatgaaggataaacaccgtgcc
BirA-star-HA-tag STOP_E overhang	oVS0004_rev	aacaGGTCTCaGCAGctaTGCgTAATCCGGTACATC GTAAGGGTAggCcttctcagcactcctcaatga
HA tag with C overhang	oVS0005_fwd	aacaGGTCTCaGGCTgcaTACCCTTACGATGTACCG GA
APEX2-Bsa site mutation	oVS0006_fwd	aaaaGGTCTCgGTGAgAAGGAAGGACTCCTTCAG
APEX2-Bsa site mutation	oVS0006_rev	aacaGGTCTCcTCACcACTCAACAACCTCCGTGA
APEX2 for C terminal tagging_D overhang	oVS0007_fwd	aaaaGGTCTCaTCAGgaATGGGAAAGTCTTACCCAA CTGT
APEX2 for C terminal tagging_HA tag STOP_E overhang	oVS0007_rev	aacaGGTCTCaGCAGctatgcGTAATCCGGTACATCG TAAGGGTAggcATCAGCAAACCCAAGC
APEX_C overhang	oVS0008_rev	aacaGGTCTCaAGCCgcGGCATCAGCAAACCCAAGC
APEX for N terminal tagging_HA tag_B overhang	oVS0009_fwd	aaaaGGTCTCaAACAatgTACCCTTACGATGTACCGG ATTACGCAgaATGGGAAAGTCTTACCCAAGT

Materials and Methods

XVE with C overhang	oVS0010_rev	aacaGGTCTCaGGCTgtATTcAGTCGACTggtaccaac a
pCOBL9 with rev C overhang	oVS0011_fwd	aacaGGTCTCaAGCctgtgtcttttccagagaaagttaag
pCOBL9 with rev E overhang	oVS0011_rev	aaaaGGTCTCtGCAGggtcttttagtttaggagacgataatgg
OlexTata-mini 35S with E overhang	oVS0012_fwd	aaaaGGTCTCtCTGCagTCATTCCAGGTCCACGC
ROP2mini with D overhang	oVS0013_fwd	aaaaGGTCTCaTCAGcaACACAGCAGAACGTGAAG GC
ROP2mini with E overhang	oVS0013_rev	aacaGGTCTCtGCAGtcaCAAGAACGCGCAACG
SAC9 BSA mutation	oVS0014_fwd	aaaaGGTCTCtAGAGACTGAGAGgCCAATGGAGAA
SAC9 BSA mutation	oVS0014_rev	aacaGGTCTCtCTAATGGTATCAGGAATCTATT
SAC9 with C overhang	oVS0015_fwd	aaaaGGTCTCaGGCTatgGATCTGCATCCACCAGG
SAC9 with D overhang	oVS0015_rev	aacaGGTCTCtCTGAtccGACACTTCAAAGGCTAGT
SAC9 sequencing_772-793	oVS0016a_fwd	AGTGTGAGCAGCTTGTATGGA
SAC9 sequencing_772-793	oVS0016a_rev	TCCATACAAGCTGCTCACACT
SAC9 sequencing_1768-1789	oVS0016b_fwd	CGAAAGCTATGCACAGCCAAA
SAC9 sequencing_2742-2763	oVS0016c_rev	TTGTGGGAAGGGGTCAGAAGA
SAC9 sequencing_3758-3778	oVS0016d_fwd	TGCGACTGATTCAGCACCAT
SAC9 sequencing_3758-3778	oVS0016d_rev	ATGGTGCTGAATCAGTCGCA
Lti6b with GAGA linker and D overhang	oVS0017_fwd	aaaaGGTCTCaTCAGcaGGAGCAGGAGCGGGGGCT gtgAGTACAGCCACTTTTCGT
Lti6b with E overhang	oVS0017_rev	aacaGGTCTCtGCAGTCACTTGGTGATGATATAAAG AGCG
mtFlot2-head with B overhang	oVS0018_fwd	aaaaGGTCTCaAACAatgAAAATTTACCGGGTCGCG
mtFlot2-head with GAGA linker and C overhang	oVS0018_rev	aacaGGTCTCtAGCCgcGGCACCCGCCCTGCTCcG GGCACATCCACCAATTGC
pEXP7A with rev C overhang	oVS0019_fwd	aacaGGTCTCtAGCcttagcctcttttctttattcttaggg
pEXP7A with rev E overhang	oVS0019_rev	aacaGGTCTCaGCAGgagagcgccccggttggat
ROP2 1-20 with STOP D overhang	oVS0020_rev	aacaGGTCTCaCTGACTAGCAAGTTTTTCCGACGGC
ROP2 1-43 with STOP D overhang	oVS0021_rev	aacaGGTCTCaCTGACTACTAACTGAAGTTGTGCGAA AACAGTTGG
ROP2 1-80 with STOP D overhang	oVS0022_rev	aacaGGTCTCaCTGACTAGAAAACATCAGCACCCACG GT
BirA* as N-tag with C overhang	oVS0023_fwd	aaaaGGTCTCaGGCTATGAAAGATAATACAGTTCTT TTAAAATTGATTGC
BirA* as N-tag with E overhang	oVS0023_rev	aacaGGTCTCaGCAGctaCCTTTTTTCAGCACTTCTCA AACTAATT

Materials and Methods

BirA* as N-tag with D overhang	OVS0024_fwd	aaaaGGTCTCaTCAGatgTACCCTTACGATGTACCGG ATTACGCAaaaGATAATACAGTTCTTTAAAATTGA TTGC
HCS1 as N-tag with C overhang	oVS0025_fwd	aaaaGGTCTCaGGCTatgGAAGCAGTTCGTTCAACA ACAA
HCS1 as N-tag with E overhang	oVS0025_rev	aacaGGTCTCaGCAGctaTATTTTTCTTCGAACCAGA CCT
HCS1 as N-tag with D overhang	oVS0026_fwd	aaaaGGTCTCaTCAGatgTACCCTTACGATGTACCGG ATTACGCAgaaGCAGTTCGTTCAACAACAA
HA-tag-C overhang	oVS0027_rev	aacaGGTCTCaAGCctgcGTAATCCGGTACATCGT
GEF3 without STOP with D overhang	oVS0028_rev	aacaGGTCTCaCTGATTCACTACCTCTCATGGTTTTG T
ROP2 d81-160 rev primer for part 1 use with oVS34_fwd	oVS0029_rev	aacaGGTCTCaGTGTgaaAACATCAGCACCACGGT
ROP2 d81-160 fwd primer for part 2 use with oVS34_rev	oVS0029_fwd	aaaaGGTCTCaACACagcAGAACGTGAAGGCAGTG
ROP2 d81-120 rev primer for part 1 use with oVS34_fwd	oVS0030_rev	aacaGGTCTCaGAAGgaaAACATCAGCACCACGGT
ROP2 d81-120 fwd primer for part 2 use with oVS34_rev	oVS0030_fwd	aaaaGGTCTCaCTTCgagATGACAAGCAATTCTTT
ROP2 d121-160 rev primer for part 1 use with oVS34_fwd	oVS0031_rev	aacaGGTCTCaGTGTatcGAGTTTTGTCCCAACAA
ROP2 d124-137 rev primer for part1 use with oVS34_fwd	oVS0032_rev	aacaGGTCTCaTAGTgtcATCTCGAAGATCGAGTT
ROP2 d124-137 fwd primer for part2 use with oVS34_rev	oVS0032_fwd	aaaaGGTCTCaACTAcaaACCAGGGAGAGGAACTG
ROP2 d124-148 rev primer for part 1 use with oVS34_fwd	oVS0033_rev	aacaGGTCTCaCAATgtcATCTCGAAGATCGAGTT
ROP2 d124-148 fwd primer for part 2 use with oVS34_rev	oVS0033_fwd	aaaaGGTCTCaATTGgatCTGCTGTCTACATTGAA
ROP2 CDS rev with STOP	oVS0034_rev	aacaGGTCTCaCTGACTAcaaGAACGCGCAACGGTT CT
ROP2 CDS fwd	oVS0034_fwd	aaaGGTCTCaGGCTatgGCGTCAAGGTTTATAAAGT G
pGEF3 with rev C overhang_for EstIInd system	oVS0035_fwd	aacaGGTCTCtAGCCctttaaactctaaacactccttaaag gtctg
pGEF3 with rev E overhang_for EstIInd system	oVS0035_rev	aacaGGTCTCaGCAGctcgatcaaccctttcacgg

Materials and Methods

pROP2 with rev C overhang_for EstInd system	oVS0036_fwd	aacaGGTCTCtAGCCctctgccgcaagatcg
pROP2 with rev E overhang_for EstInd system	oVS0036_rev	aacaGGTCTCaGCAGgacaaataattataagaagctaccgtctg
pGEf4 with rev C overhang_for EstInd system	oVS0037_fwd	aacaGGTCTCtAGCCcacgattgtgtataatgatcaatgtttttggtg
pGEf4 with rev E overhang_for EstInd system	oVS0037_rev	aacaGGTCTCaGCAGctcaatgtgcataagctgctctc
pGEF14 with rev C overhang_for EstInd system	oVS0038_fwd	aacaGGTCTCtAGCCcctttctctcttttgaattcttttgttgaa cca
pGEF14 with rev E overhang_for EstInd system	oVS0038_rev	aacaGGTCTCaGCAGgatGCATTGGTTGCTCACTTCA TG
TurboID with HA-tag for C tag with D overhang	oVS0040_fwd	aaaaGGTCTCaCGCAatgAAAGACAATACTGTGCCT CTGAAGCTGAT
TurboID for N tag, GAGA-linker, C overhang	oVS0041_rev	aacaGGTCTCaCTCCcttTTCGGCAGACCCGAGACT
Primer1 for GAGA for pVS141 pVS142	oVS0041_a	GGAGCAGGGGCGGGTgcc
Primer2 for GAGA for pVS141 pVS142	oVS0041_b	AGCCggcACCCGCCCTG
Primer1 for HA for pVS142	oVS0042_a	AACAatgTACCCTTACGATGTACCGGATTA
Primer2 for HA for pVS142	oVS0042_b	TGCGTAATCCGGTACATCGTAAGGGTAcac
miniTurbo for C tag, D overhang	oVS0044_fwd	aaaaGGTCTCaCGCAatgATCccgctgctgaacgctaaaca
Primer 1 for GAGA and HA for pVS144	oVS0044_a-NEW	TCAGcgatggGAGCAGGGGCGGGTGCctacCCTTAC GATGTACCGGATTA
Primer 2 for GAGA and HA for pVS144	oVS0044_b_NEW	TGCGTAATCCGGTACATCGTAAGGgtaGGCACCCG CCCCTGCTCccatcg
Primer1 for HA for pVS146	oVS0046_a	AACAatgTACCCTTACGATGTACCGGATTA
Primer2 for HA for pVS146	oVS0046_b	TGCGTAATCCGGTACATCGTAAGGGTAcac
TurboID for fusion with mCit, C overhang	oVS0047_fwd	aaaaGGTCTCaGGCTtaATGAAAGACAATACTGTGC CTCTGAAGCTGAT
TurboID for C tag, E overhang	oVS0047_rev	aacaGGTCTCaGCAGttaCTTTTCGGCAGACCCGAG ACT
Primer 1 for GAGA and HA for pVS140	oVS0040_a-NEW	TCAGcgatggGAGCAGGGGCGGGTGCctacCCTTAC GATGTACCGGATTA
Primer 2 for GAGA and HA for pVS140	oVS0040_b_NEW	TGCGTAATCCGGTACATCGTAAGGgtaGGCACCCG CCCCTGCTCccatcg
TurboID for C tag with E overhang	oVS0048_rev	aacaGGTCTCaGCAGctacttTTCGGCAGACCCGAGACT

Materials and Methods

miniTurbo for fusion with mCit, C overhang	oVS0049_fwd	aaaaGGTCTCaGGCTtaATGATCccgctgctgaacgctaa aca
miniTurbo for fusion with mCit, D overhang	oVS0050_fwd	aaaaGGTCTCaTCAGtaATGAAAGACAATACTGTGC CTCTGAAGCTGAT
	oVS0050_a	CAGGGGCGGGTgccggGGCT
	oVS0050_b	ccggcACCCGCCCTGCTCC
	oVS0051_fwd	aaaaGGTCTCaTCAGtaATGATCccgctgctgaacgctaa aca
TurboID for N tag, HA tag, B overhang	oVS0052_fwd	aaaaGGTCTCaAACAatgAAAGACAATACTGTGCCT CTGAAGCTGAT
miniTurbo for N tag, B overhang	oVS0053_fwd	aaaaGGTCTCaAACAatgATCccgctgctgaacgctaaaca

Bibliography

- Adams, A.E.M., Johnson, D.I., Longnecker, R.M., Sloat, B.F., and Pringle, J.R.** (1990). CDC42 and CDC43, two additional genes involved in budding and the establishment of cell polarity in the yeast *Saccharomyces cerevisiae*. *J. Cell Biol.* **111**: 131–142.
- Alban, C., Job, D., and Douce, R.** (2000). Biotin Metabolism in Plants. *Annu. Rev. Plant Physiol. Plant Mol. Biol.* **51**: 17–47.
- Allwood, E.G., Anthony, R.G., Smertenko, A.P., Reichelt, S., Drobak, B.K., Doonan, J.H., Weeds, A.G., and Hussey, P.J.** (2002). Regulation of the pollen-specific actin-depolymerizing factor LIADF1. *Plant Cell* **14**: 2915–2927.
- Allwood, E.G., Smertenko, A.P., and Hussey, P.J.** (2001). Phosphorylation of plant actin-depolymerising factor by calmodulin-like domain protein kinase. *FEBS Lett.* **499**: 97–100.
- Arnold, J.B.** (2019). ggthemes: Extra Themes, Scales and Geoms for “ggplot2.”
- Augustine, R.C., Vidali, L., Kleinman, K.P., and Bezanilla, M.** (2008). Actin depolymerizing factor is essential for viability in plants, and its phosphoregulation is important for tip growth. *Plant J.* **54**: 863–875.
- Bagci, H. et al.** (2020). Mapping the proximity interaction network of the Rho-family GTPases reveals signalling pathways and regulatory mechanisms. *Nat. Cell Biol.* **22**: 120–134.
- Basu, D., El-Assal, S.E.D., Le, J., Mallery, E.L., and Szymanski, D.B.** (2004). Interchangeable functions of Arabidopsis PIGORI and the human WAVE complex subunit SRA1 during leaf epidermal development. *Development* **131**: 4345–4355.
- Batsios, P., Ren, X., Baumann, O., Larochele, D., and Gräf, R.** (2016). Src1 is a Protein of the Inner Nuclear Membrane Interacting with the Dictyostelium Lamin NE81. *Cells* **5**: 13.
- Baxter-Burrell, A., Yang, Z., Springer, P.S., and Bailey-Serres, J.** (2002). RopGAP4-dependent Rop GTPase rheostat control of Arabidopsis oxygen deprivation tolerance. *Science* (80-.). **296**: 2026–2028.
- Bender, A. and Pringle, J.R.** (1989). Multicopy suppression of the *cdc24* budding defect in yeast by CDC42 and three newly identified genes including the ras-related gene RSR1. *Proc. Natl. Acad. Sci. U. S. A.* **86**: 9976–9980.
- Bendezú, F.O., Vincenzetti, V., Vavylonis, D., Wyss, R., Vogel, H., and Martin, S.G.** (2015). Spontaneous Cdc42 Polarization Independent of GDI-Mediated Extraction and Actin-Based Trafficking. *PLoS Biol.* **13**.
- Berken, A., Thomas, C., and Wittinghofer, A.** (2005). A new family of RhoGEFs activates the Rop molecular switch in plants. *Nature* **436**: 1176–1180.
- Berken, A. and Wittinghofer, A.** (2008). Structure and function of Rho-type molecular switches in plants. *Plant Physiol. Biochem.* **46**: 380–393.
- Bhat, R.A., Lahaye, T., and Panstruga, R.** (2006). The visible touch: In planta visualization of protein-protein interactions by fluorophore-based methods. *Plant Methods* **2**: 12.
- Bi, E. and Park, H.O.** (2012). Cell polarization and cytokinesis in budding yeast. *Genetics* **191**: 347–387.
- Bibikova, T. and Gilroy, S.** (2002). Root hair development. *J. Plant Growth Regul.* **21**: 383–415.
- Bierwagen, J., Testa, I., Fölling, J., Wenzel, D., Jakobs, S., Eggeling, C., and Hell, S.W.** (2010). Far-Field Autofluorescence Nanoscopy. *Nano Lett.* **10**: 4249–4252.
- Bischoff, F., Vahlkamp, L., Molendijk, A., and Palme, K.** (2000). Localization of AtROP4 and AtROP6 and interaction with the guanine nucleotide dissociation inhibitor AtRhoGDI1 from Arabidopsis. *Plant Mol. Biol.* **42**: 515–530.
- Bishop, A.L. and Hall, A.** (2000). Rho GTPases and their effector proteins. *Biochem. J.* **348**: 241–255.
- Böhme, K., Li, Y., Charlot, F., Grierson, C., Marrocco, K., Okada, K., Laloue, M., and Nogué, F.** (2004). The Arabidopsis COW1 gene encodes a phosphatidylinositol transfer protein essential for root hair tip growth. *Plant J.* **40**: 686–698.

Bibliography

- Bourne, H.R., Sanders, D.A., and McCormick, F.** (1991). The GTPase superfamily: conserved structure and molecular mechanism. *Nature* **349**: 117–127.
- Branon, T.C., Bosch, J.A., Sanchez, A.D., Udeshi, N.D., Svinkina, T., Carr, S.A., Feldman, J.L., Perrimon, N., and Ting, A.Y.** (2017). Directed evolution of TurboID for efficient proximity labeling in living cells and organisms. *bioRxiv*: 196980.
- Branon, T.C., Bosch, J.A., Sanchez, A.D., Udeshi, N.D., Svinkina, T., Carr, S.A., Feldman, J.L., Perrimon, N., and Ting, A.Y.** (2018). Efficient proximity labeling in living cells and organisms with TurboID. *Nat. Biotechnol.* **36**: 880–887.
- Cárdenas, L., Lovy-Wheeler, A., Kunkel, J.G., and Hepler, P.K.** (2008). Pollen tube growth oscillations and intracellular calcium levels are reversibly modulated by actin polymerization. *Plant Physiol.* **146**: 1611–1621.
- Carneseccchi, J., Sigismondo, G., Domsch, K., Baader, C.E.P., Rafiee, M.R., Krijgsveld, J., and Lohmann, I.** (2020). Multi-level and lineage-specific interactomes of the Hox transcription factor Ubx contribute to its functional specificity. *Nat. Commun.* **11**: 1–17.
- Carol, R.J. and Dolan, L.** (2002). Building a hair: tip growth in *Arabidopsis thaliana* root hairs. *Philos. Trans. R. Soc. London. Ser. B Biol. Sci.* **357**: 815–821.
- Carol, R.J., Takeda, S., Linstead, P., Durrant, M.C., Kakesova, H., Derbyshire, P., Drea, S., Zarsky, V., and Dolan, L.** (2005). A RhoGDP dissociation inhibitor spatially regulates growth in root hair cells. *Nature* **438**: 1013–1016.
- Chai, S., Ge, F.R., Feng, Q.N., Li, S., and Zhang, Y.** (2016). PLURIPETALA mediates ROP2 localization and stability in parallel to SCN1 but synergistically with TIP1 in root hairs. *Plant J.* **86**: 413–425.
- Chamberlain, L.H. and Shipston, M.J.** (2015). The physiology of protein s-acylation. *Physiol. Rev.* **95**: 341–376.
- Chang, F., Gu, Y., Ma, H., and Yang, Z.** (2013). AtPRK2 promotes ROP1 activation via RopGEFs in the control of polarized pollen tube growth. *Mol. Plant* **6**: 1187–1201.
- Chant, J., Corrado, K., Pringle, J.R., and Herskowitz, I.** (1991). Yeast BUD5, encoding a putative GDP-GTP exchange factor, is necessary for bud site selection and interacts with bud formation gene BEM1. *Cell* **65**: 1213–1224.
- Chant, J. and Stowers, L.** (1995). GTPase Cascades Choreographing Cellular Behavior: Movement, Morphogenesis, and More Minireview.
- Cherfils, J. et al.** (2013). Regulation of small GTPases by GEFs, GAPs, and GDIs. *Physiol. Rev.* **93**: 269–309.
- Cho, H.T. and Cosgrove, D.J.** (2002). Regulation of root hair initiation and expansin gene expression in *Arabidopsis*. *Plant Cell* **14**: 3237–3253.
- Cho, W. and Stahelin, R. V.** (2005). Membrane-protein interactions in cell signaling and membrane trafficking. *Annu. Rev. Biophys. Biomol. Struct.* **34**: 119–151.
- Choi-Rhee, E., Schulman, H., and Cronan, J.E.** (2008). Promiscuous protein biotinylation by *Escherichia coli* biotin protein ligase. *Protein Sci.* **13**: 3043–3050.
- Clough, S.J. and Bent, A.F.** (1998). Floral dip: a simplified method for *Agrobacterium*-mediated transformation of *Arabidopsis thaliana*. *Plant J.* **16**: 735–743.
- Cole, R.A. and Fowler, J.E.** (2006). Polarized growth: maintaining focus on the tip. *Curr. Opin. Plant Biol.* **9**: 579–588.
- Colicelli, J.** (2004). Human RAS superfamily proteins and related GTPases. *Sci. STKE* **2004**: RE13.
- Conlan, B., Stoll, T., Gorman, J.J., Saur, I., and Rathjen, J.P.** (2018). Development of a Rapid in planta BioID System as a Probe for Plasma Membrane-Associated Immunity Proteins. *Front. Plant Sci.* **9**: 1882.
- Crowell, D.N.** (2000). Functional implications of protein isoprenylation in plants. *Prog. Lipid Res.* **39**: 393–408.
- Crowell, D.N. and Huizinga, D.H.** (2009). Protein isoprenylation: the fat of the matter. *Trends Plant Sci.* **14**: 163–170.

Bibliography

- Cutler, S.R., Ehrhardt, D.W., Griffiths, J.S., and Somerville, C.R.** (2000). Random GFP::cDNA fusions enable visualization of subcellular structures in cells of *Arabidopsis* at a high frequency. *Proc. Natl. Acad. Sci.* **97**: 3718–3723.
- Das, P.P., Macharia, M.W., Lin, Q., and Wong, S.M.** (2019). In planta proximity-dependent biotin identification (BioID) identifies a TMV replication co-chaperone NbSGT1 in the vicinity of 126 kDa replicase. *J. Proteomics* **204**: 103402.
- Denninger, P.** (2018). PhD-Thesis: Timing of polar protein accumulation and signaling in *Arabidopsis thaliana*.
- Denninger, P., Reichelt, A., Schmidt, V.A.F., Mehlhorn, D.G., Asseck, L.Y., Stanley, C.E., Keinath, N.F., Evers, J.-F., Grefen, C., and Grossmann, G.** (2019). Distinct RopGEFs Successively Drive Polarization and Outgrowth of Root Hairs. *Curr. Biol.* **0**.
- Denyer, T., Ma, X., Klesen, S., Scacchi, E., Nieselt, K., and Timmermans, M.C.P.** (2019). Spatiotemporal Developmental Trajectories in the *Arabidopsis* Root Revealed Using High-Throughput Single-Cell RNA Sequencing. *Dev. Cell* **48**: 840-852.e5.
- DerMardirossian, C. and Bokoch, G.M.** (2005). GDIs: central regulatory molecules in Rho GTPase activation. *Trends Cell Biol.* **15**: 356–363.
- Dickson, R.M., Cubitt, A.B., Tsien, R.Y., and Moerner, W.E.** (1997). On/off blinking and switching behaviour of single molecules of green fluorescent protein. *Nature* **388**: 355–358.
- Djakovic, S., Dyachok, J., Burke, M., Frank, M.J., and Smith, L.G.** (2006). BRICK 1/HSPC300 functions with SCAR and the ARP2/3 complex to regulate epidermal cell shape in *Arabidopsis*. *Development* **133**: 1091–1100.
- Dong, C.H., Xia, G.X., Hong, Y., Ramachandran, S., Kost, B., and Chua, N.H.** (2001). ADF proteins are involved in the control of flowering and regulate f-actin organization, cell expansion, and organ growth in *Arabidopsis*. *Plant Cell* **13**: 1333–1346.
- Doumane, M., Colin, L., Lebecq, A., Fangain, A., Bareille, J., Hamant, O., Belkhadir, Y., Jaillais, Y., and Caillaud, M.-C.** (2020). iDePP: a genetically encoded system for the inducible depletion of PI(4,5)P2 in *Arabidopsis thaliana*. *bioRxiv*: 2020.05.13.091470.
- Dovas, A. and Couchman, J.R.** (2005). RhoGDI: Multiple functions in the regulation of Rho family GTPase activities. *Biochem. J.* **390**: 1–9.
- Dowd, P.E., Coursol, S., Skirpan, A.L., Kao, T.H., and Gilroy, S.** (2006). *Petunia* phospholipase C1 is involved in pollen tube growth. *Plant Cell* **18**: 1438–1453.
- Dresselhaus, T. and Franklin-Tong, N.** (2013). Male-female crosstalk during pollen germination, tube growth and guidance, and double fertilization. *Mol. Plant* **6**: 1018–1036.
- Drubin, D.G. and Nelson, W.J.** (1996). Origins of cell polarity. *Cell* **84**: 335–344.
- Etienne-Manneville, S.** (2004). Cdc42 - The centre of polarity. *J. Cell Sci.* **117**: 1291–1300.
- Etienne-Manneville, S. and Hall, A.** (2002). Rho GTPases in cell biology. *Nature* **420**: 629–635.
- Feiguelman, G., Fu, Y., and Yalovsky, S.** (2018). ROP GTPases structure-function and signaling pathways. *Plant Physiol.* **176**: 57–79.
- Feng, Q.N., Kang, H., Song, S.J., Ge, F.R., Zhang, Y.L., Li, E., Li, S., and Zhang, Y.** (2016). *Arabidopsis* RhoGDIs are critical for cellular homeostasis of pollen tubes. *Plant Physiol.* **170**: 841–856.
- Fields, S. and Song, O.K.** (1989). A novel genetic system to detect protein-protein interactions. *Nature* **340**: 245–246.
- Firat-Karalar, E.N. and Stearns, T.** (2015). Probing mammalian centrosome structure using BioID proximity dependent biotinylation. *Methods Cell Biol.* **129**: 153–170.
- Fölling, J., Bossi, M., Bock, H., Medda, R., Wurm, C.A., Hein, B., Jakobs, S., Eggeling, C., and Hell, S.W.** (2008). Fluorescence nanoscopy by ground-state depletion and single-molecule return. *Nat. Methods* **5**: 943–945.
- Foreman, J., Demidchik, V., Bothwell, J.H.F., Mylona, P., Miedema, H., Torres, M.A., Linstead, P., Costa, S.,**

Bibliography

- Brownlee, C., Jones, J.D.G., Davies, J.M., and Dolan, L.** (2003). Reactive oxygen species produced by NADPH oxidase regulate plant cell growth. *Nature* **422**: 442–446.
- Fox, J. and Weisberg, S.** (2019). *An {R} Companion to Applied Regression third*. (Sage: Thousand Oaks {CA}).
- Fu, Y., Wu, G., and Yang, Z.** (2001). Rop GTPase-dependent dynamics of tip-localized F-actin controls tip growth in pollen tubes. *J. Cell Biol.* **152**: 1019–1032.
- Galway, M.E., Heckman, J.W., and Schiefelbein, J.W.** (1997). Growth and ultrastructure of Arabidopsis root hairs: The *rh3* mutation alters vacuole enlargement and tip growth. *Planta* **201**: 209–218.
- Van Gestel, K., Slegers, H., Von Witsch, M., Šamaj, J., Baluška, F., and Verbelen, J.P.** (2003). Immunological evidence for the presence of plant homologues of the actin-related protein Arp3 in tobacco and maize: Subcellular localization to actin-enriched pit fields and emerging root hairs. *Protoplasma* **222**: 45–52.
- Gingras, A.C., Abe, K.T., and Raught, B.** (2019). Getting to know the neighborhood: using proximity-dependent biotinylation to characterize protein complexes and map organelles. *Curr. Opin. Chem. Biol.* **48**: 44–54.
- Glotzer, M. and Hyman, A.A.** (1995). Cell Polarity: The importance of being polar. *Curr. Biol.* **5**: 1102–1105.
- Goitre, L., Trapani, E., Trabalzini, L., and Retta, S.F.** (2013). The Ras Superfamily of Small GTPases: The Unlocked Secrets. *Methods Mol. Biol.* **1120**: 33–41.
- Graves, S., Piepho, H.-P., Selzer, L., and Dorai-Raj, S.** (2019). *multcompView: Visualizations of Paired Comparisons*.
- Grefen, C. and Blatt, M.** (2012). A 2in1 cloning system enables ratiometric bimolecular fluorescence complementation (rBiFC). *Biotechniques* **53**: 311–314.
- Grierson, C., Nielsen, E., Ketelaarc, T., and Schiefelbein, J.** (2014). Root Hairs. *Arab. B.* **12**: e0172.
- Gronnier, J., Franck, C.M., Stegmann, M., DeFalco, T.A., Cifuentes, A.A., Dünser, K., Lin, W., Yang, Z., Kleine-Vehn, J., Ringli, C., and Zipfel, C.** (2020). FERONIA regulates FLS2 plasma membrane nanoscale dynamics to modulate plant immune signaling. *bioRxiv*: 2020.07.20.212233.
- Gu, Y., Fu, Y., Dowd, P., Li, S., Vernoud, V., Gilroy, S., and Yang, Z.** (2005). A Rho family GTPase controls actin dynamics and tip growth via two counteracting downstream pathways in pollen tubes. *J. Cell Biol.* **169**: 127–38.
- Gu, Y., Li, S., Lord, E.M., and Yang, Z.** (2006). Members of a novel class of Arabidopsis Rho guanine nucleotide exchange factors control Rho GTPase-dependent polar growth. *Plant Cell* **18**: 366–381.
- Gungabissoon, R.A., Jiang, C.-J., Drøbak, B.K., Maciver, S.K., and Hussey, P.J.** (1998). Interaction of maize actin-depolymerising factor with actin and phosphoinositides and its inhibition of plant phospholipase C. *Plant J.* **16**: 689–696.
- Gupta, G.D. et al.** (2015). A Dynamic Protein Interaction Landscape of the Human Centrosome-Cilium Interface. *Cell* **163**: 1484–1499.
- Gustafsson, N., Culley, S., Ashdown, G., Owen, D.M., Pereira, P.M., and Henriques, R.** (2016). Fast live-cell conventional fluorophore nanoscopy with ImageJ through super-resolution radial fluctuations. *Nat. Commun.* **7**: 12471.
- Hall, A.** (1998). Rho GTPases and the actin cytoskeleton. *Science* (80-.). **279**: 509–514.
- Halme, A., Michelitch, M., Mitchell, E.L., and Chant, J.** (1996). Bud10p directs axial cell polarization in budding yeast and resembles a transmembrane receptor. *Curr. Biol.* **6**: 570–579.
- Han, S., Li, J., and Ting, A.Y.** (2018). Proximity labeling: spatially resolved proteomic mapping for neurobiology. *Curr. Opin. Neurobiol.*
- Harkins, H.A., Pagé, N., Schenkman, L.R., De Virgilio, C., Shaw, S., Bussey, H., and Pringle, J.R.** (2001). Bud8p and Bud9p, proteins that may mark the sites for bipolar budding in yeast. *Mol. Biol. Cell* **12**: 2497–2518.
- Hartwell, L.H., Culotti, J., Pringle, J.R., and Reid, B.J.** (1974). Genetic control of the cell division cycle in yeast. *Science* (80-.). **183**: 46–51.

Bibliography

- Haruta, M., Gray, W.M., and Sussman, M.R.** (2015). Regulation of the plasma membrane proton pump (H⁺-ATPase) by phosphorylation. *Curr. Opin. Plant Biol.* **28**: 68–75.
- Heilmann, I. et al.** (2016). Phosphoinositide signaling in plant development. *Development* **143**: 2044–55.
- Heilmann, I.** (2016). Phosphoinositide signaling in plant development. *Dev.* **143**: 2044–2055.
- Hell, S.W. and Kroug, M.** (1995). Ground-state-depletion fluorescence microscopy: a concept for breaking the diffraction resolution limit.
- Hellens, R.P., Edwards, E.A., Leyland, N.R., Bean, S., and Mullineaux, P.M.** (2000). pGreen: a versatile and flexible binary Ti vector for *Agrobacterium*-mediated plant transformation. *Plant Mol. Biol.* **42**: 819–832.
- Helling, D., Possart, A., Cottier, S., Klahre, U., and Kost, B.** (2006). Pollen tube tip growth depends on plasma membrane polarization mediated by tobacco PLC3 activity and endocytic membrane recycling. *Plant Cell* **18**: 3519–34.
- Hemsley, P.A., Kemp, A.C., and Grierson, C.S.** (2005). The TIP GROWTH DEFECTIVE1 S-acyl transferase regulates plant cell growth in *Arabidopsis*. *Plant Cell* **17**: 2554–2563.
- Do Heo, W., Inoue, T., Wei, S.P., Man, L.K., Byung, O.P., Wandless, T.J., and Meyer, T.** (2006). PI(3,4,5)P₃ and PI(4,5)P₂ lipids target proteins with polybasic clusters to the plasma membrane. *Science* (80-.). **314**: 1458–1461.
- Higashiyama, T. and Takeuchi, H.** (2015). The Mechanism and Key Molecules Involved in Pollen Tube Guidance. *Annu. Rev. Plant Biol.* **66**: 393–413.
- Higgs, H.N. and Pollard, T.D.** (2001). Regulation of Actin Filament Network Formation Through ARP2/3 Complex: Activation by a Diverse Array of Proteins. *Annu. Rev. Biochem.* **70**: 649–676.
- Himschoot, E., Beeckman, T., Friml, J., and Vanneste, S.** (2015). Calcium is an organizer of cell polarity in plants. *Biochim. Biophys. Acta - Mol. Cell Res.* **1853**: 2168–2172.
- Hoffman, G.R., Nassar, N., and Cerione, R.A.** (2000). Structure of the Rho family GTP-binding protein Cdc42 in complex with the multifunctional regulator RhoGDI. *Cell* **100**: 345–356.
- Honke, K. and Kotani, N.** (2011). The enzyme-mediated activation of radical source reaction: A new approach to identify partners of a given molecule in membrane microdomains. *J. Neurochem.* **116**: 690–695.
- Hu, C.D., Chinenov, Y., and Kerppola, T.K.** (2002). Visualization of interactions among bZIP and Rel family proteins in living cells using bimolecular fluorescence complementation. *Mol. Cell* **9**: 789–798.
- Huang, G.-Q., Li, E., Ge, F.-R., Li, S., Wang, Q., Zhang, C.-Q., and Zhang, Y.** (2013). *Arabidopsis* RopGEF4 and RopGEF10 are important for FERONIA-mediated developmental but not environmental regulation of root hair growth. *New Phytol.* **200**: 1089–1101.
- Huang, S., Gao, L., Blanchoin, L., and Staiger, C.J.** (2006). Heterodimeric capping protein from *Arabidopsis* is regulated by phosphatidic acid. *Mol. Biol. Cell* **17**: 1946–1958.
- Hwang, J.-U., Gu, Y., Lee, Y.-J., and Yang, Z.** (2005). Oscillatory ROP GTPase activation leads the oscillatory polarized growth of pollen tubes. *Mol. Biol. Cell* **16**: 5385–99.
- Hwang, J.U., Vernoud, V., Szumlanski, A., Nielsen, E., and Yang, Z.** (2008). A Tip-Localized RhoGAP Controls Cell Polarity by Globally Inhibiting Rho GTPase at the Cell Apex. *Curr. Biol.* **18**: 1907–1916.
- Hwang, J.U., Wu, G., Yan, A., Lee, Y.J., Grierson, C.S., and Yang, Z.** (2010). Pollen-tube tip growth requires a balance of lateral propagation and global inhibition of Rho-family GTPase activity. *J. Cell Sci.* **123**: 340–350.
- Irazoqui, J.E., Gladfelter, A.S., and Lew, D.J.** (2003). Scaffold-mediated symmetry breaking by Cdc42p. *Nat. Cell Biol.* **5**: 1062–1070.
- Ischebeck, T., Stenzel, I., and Heilmann, I.** (2008). Type B phosphatidylinositol-4-phosphate 5-kinases mediate *Arabidopsis* and *Nicotiana tabacum* pollen tube growth by regulating apical pectin secretion. *Plant Cell* **20**: 3312–3330.

Bibliography

- Ischebeck, T., Stenzel, I., Hempel, F., Jin, X., Mosblech, A., and Heilmann, I.** (2011). Phosphatidylinositol-4,5-bisphosphate influences Nt-Rac5-mediated cell expansion in pollen tubes of *Nicotiana tabacum*. *Plant J.* **65**: 453–468.
- Jaffe, A.B. and Hall, A.** (2005). RHO GTPASES: Biochemistry and Biology. *Annu. Rev. Cell Dev. Biol.* **21**: 247–269.
- Johnson, D.I. and Pringle, J.R.** (1990). Molecular characterization of CDC42, a *Saccharomyces cerevisiae* gene involved in the development of cell polarity. *J. Cell Biol.* **111**: 143–152.
- Johnson, J.M., Jin, M., and Lew, D.J.** (2011). Symmetry breaking and the establishment of cell polarity in budding yeast. *Curr. Opin. Genet. Dev.* **21**: 740–746.
- Jones, M.A., Raymond, M.J., and Smirnov, N.** (2006). Analysis of the root-hair morphogenesis transcriptome reveals the molecular identity of six genes with roles in root-hair development in *Arabidopsis*. *Plant J.* **45**: 83–100.
- Jones, M.A., Shen, J.-J., Fu, Y., Li, H., Yang, Z., and Grierson, C.S.** (2002). The *Arabidopsis* Rop2 GTPase is a positive regulator of both root hair initiation and tip growth. *Plant Cell* **14**: 763–76.
- Kang, P.J., Lee, B., and Park, H.O.** (2004). Specific residues of the GDP/GTP exchange factor Bud5p are involved in establishment of the cell type-specific budding pattern in yeast. *J. Biol. Chem.* **279**: 27980–27985.
- Kang, P.J., Sanson, A., Lee, B., and Park, H.O.** (2001). A GDP/GTP exchange factor involved in linking a spatial landmark to cell polarity. *Science* (80-.). **292**: 1376–1378.
- Kato, M., Nagasaki-Takeuchi, N., Ide, Y., and Maeshima, M.** (2010). An *Arabidopsis* Hydrophilic Ca²⁺-Binding Protein with a PEVK-Rich Domain, PCaP2, is Associated with the Plasma Membrane and Interacts with Calmodulin and Phosphatidylinositol Phosphates. *Plant Cell Physiol.* **51**: 366–379.
- Ketelaar, T.** (2013). The actin cytoskeleton in root hairs: All is fine at the tip. *Curr. Opin. Plant Biol.* **16**: 749–756.
- Ketelaar, T., Galway, M.E., Mulder, B.M., and Emons, A.M.C.** (2008). Rates of exocytosis and endocytosis in *Arabidopsis* root hairs and pollen tubes. *J. Microsc.* **231**: 265–273.
- Ketelaar, T., De Ruijter, N.C.A., and Emons, A.M.C.** (2003). Unstable F-actin specifies the area and microtubule direction of cell expansion in *Arabidopsis* root hairs. *Plant Cell* **15**: 285–292.
- Khan, M., Youn, J.-Y., Gingras, A.-C., Subramaniam, R., and Desveaux, D.** (2018). In planta proximity dependent biotin identification (BioID). *Sci. Rep.* **8**: 9212.
- Kiefer, C.S., Claes, A.R., Nzayisenga, J.C., Pietra, S., Stanislas, T., Hüser, A., Ikeda, Y., and Grebe, M.** (2015). *Arabidopsis* AIP1-2 restricted by WER-mediated patterning modulates planar polarity. *Dev.* **142**: 151–161.
- Kim, D.I., Birendra, K.C., Zhu, W., Motamedchaboki, K., Doye, V., and Roux, K.J.** (2014). Probing nuclear pore complex architecture with proximity-dependent biotinylation. *Proc. Natl. Acad. Sci. U. S. A.* **111**: E2453–E2461.
- Kim, D.I., Jensen, S.C., Noble, K.A., KC, B., Roux, K.H., Motamedchaboki, K., and Roux, K.J.** (2016). An improved smaller biotin ligase for BioID proximity labeling. *Mol. Biol. Cell* **27**: 1188–1196.
- Kim, D.I. and Roux, K.J.** (2016). Filling the Void: Proximity-Based Labeling of Proteins in Living Cells. *Trends Cell Biol.* **26**: 804–817.
- Kimura, S., Kaya, H., Kawarazaki, T., Hiraoka, G., Senzaki, E., Michikawa, M., and Kuchitsu, K.** (2012). Protein phosphorylation is a prerequisite for the Ca²⁺-dependent activation of *Arabidopsis* NADPH oxidases and may function as a trigger for the positive feedback regulation of Ca²⁺ and reactive oxygen species. *Biochim. Biophys. Acta - Mol. Cell Res.* **1823**: 398–405.
- Klahre, U. and Kost, B.** (2006). Tobacco RhoGTPase activating protein1 spatially restricts signaling of RAC/Rop to the apex of pollen tubes. *Plant Cell* **18**: 3033–3046.

Bibliography

- Koncz, C. and Schell, J.** (1986). The promoter of TL-DNA gene 5 controls the tissue-specific expression of chimaeric genes carried by a novel type of *Agrobacterium* binary vector. *MGG Mol. Gen. Genet.* **204**: 383–396.
- Konopka, C.A. and Bednarek, S.Y.** (2008). Variable-angle epifluorescence microscopy: a new way to look at protein dynamics in the plant cell cortex. *Plant J.* **53**: 186–196.
- Kosami, K., Ohki, I., Nagano, M., Furuita, K., Sugiki, T., Kawano, Y., Kawasaki, T., Fujiwara, T., Nakagawa, A., Shimamoto, K., and Kojima, C.** (2014). The crystal structure of the plant small GTPase OsRac1 reveals its mode of binding to NADPH oxidase. *J. Biol. Chem.* **289**: 28569–78.
- Kost, B., Lemichez, E., Spielhofer, P., Hong, Y., Tolia, K., Carpenter, C., and Chua, N.-H.** (1999). Rac Homologues and Compartmentalized Phosphatidylinositol 4, 5-Bisphosphate Act in a Common Pathway to Regulate Polar Pollen Tube Growth. *J. Cell Biol.* **145**: 317–330.
- Kotani, N., Gu, J., Isaji, T., Udaka, K., Taniguchi, N., and Honke, K.** (2008). Biochemical visualization of cell surface molecular clustering in living cells. *Proc. Natl. Acad. Sci. U. S. A.* **105**: 7405–7409.
- Koulouras, G., Panagopoulos, A., Rapsomaniki, M.A., Giakoumakis, N.N., Taraviras, S., and Lygerou, Z.** (2018). EasyFRAP-web: a web-based tool for the analysis of fluorescence recovery after photobleaching data. *Nucleic Acids Res.* **46**: W467–W472.
- Kozubowski, L., Saito, K., Johnson, J.M., Howell, A.S., Zyla, T.R., and Lew, D.J.** (2008). Symmetry-Breaking Polarization Driven by a Cdc42p GEF-PAK Complex. *Curr. Biol.* **18**: 1719–1726.
- Krappmann, A.B., Taheri, N., Heinrich, M., and Möscher, H.U.** (2007). Distinct domains of yeast cortical tag proteins Bud8p and Bud9p confer polar localization and functionality. *Mol. Biol. Cell* **18**: 3323–3339.
- Kusano, H., Testerink, C., Vermeer, J.E.M., Tsuge, T., Shimada, H., Oka, A., Munnik, T., and Aoyama, T.** (2008). The Arabidopsis Phosphatidylinositol Phosphate 5-Kinase PIP5K3 is a key regulator of root hair tip growth. *Plant Cell* **20**: 367–380.
- Lalonde, S., Ehrhardt, D.W., Loqué, D., Chen, J., Rhee, S.Y., and Frommer, W.B.** (2008). Molecular and cellular approaches for the detection of protein-protein interactions: latest techniques and current limitations. *Plant J.* **53**: 610–635.
- Lam, S.S., Martell, J.D., Kamer, K.J., Deerinck, T.J., Ellisman, M.H., Mootha, V.K., and Ting, A.Y.** (2014). Directed evolution of APEX2 for electron microscopy and proximity labeling. *Nat. Methods* **12**: 51–54.
- Lampropoulos, A., Sutikovic, Z., Wenzl, C., Maegeler, I., Lohmann, J.U., and Forner, J.** (2013). GreenGate - A Novel, Versatile, and Efficient Cloning System for Plant Transgenesis. *PLoS One* **8**: e83043.
- Lavy, M., Bracha-Drori, K., Sternberg, H., and Yalovsky, S.** (2002). A cell-specific, prenylation-independent mechanism regulates targeting of type II RACs. *Plant Cell* **14**: 2431–2450.
- Lavy, M. and Yalovsky, S.** (2006). Association of Arabidopsis type-II ROPs with the plasma membrane requires a conserved C-terminal sequence motif and a proximal polybasic domain. *Plant J.* **46**: 934–947.
- Lee, S.Y., Kang, M.G., Shin, S., Kwak, C., Kwon, T., Seo, J.K., Kim, J.S., and Rhee, H.W.** (2017). Architecture Mapping of the Inner Mitochondrial Membrane Proteome by Chemical Tools in Live Cells. *J. Am. Chem. Soc.* **139**: 3651–3662.
- Leonard, D., Hart, M.J., Platko, J. V., Eva, A., Henzel, W., Evans, T., and Cerione, R.A.** (1992). The identification and characterization of a GDP-dissociation inhibitor (GDI) for the CDC42Hs protein. *J. Biol. Chem.* **267**: 22860–22868.
- Lew, R.R.** (2004). Osmotic Effects on the Electrical Properties of Arabidopsis Root Hair Vacuoles in Situ. *Plant Physiol.* **134**: 352–360.
- Li, H., Lin, Y., Heath, R.M., Zhu, M.X., and Yang, Z.** (1999). Control of pollen tube tip growth by a Rop GTPase-dependent pathway that leads to tip-localized calcium influx. *Plant Cell* **11**: 1731–1742.
- Li, H., Wu, G., Ware, D., Davis, K.R., and Yang, Z.** (1998). Arabidopsis rho-related GTPases: Differential gene expression in pollen and polar localization in fission yeast. *Plant Physiol.* **118**: 407–417.
- Lin, Q., Zhou, Z., Luo, W., Fang, M., Li, M., and Li, H.** (2017). Screening of Proximal and Interacting Proteins in Rice Protoplasts by Proximity-Dependent Biotinylation. *Front. Plant Sci.* **8**: 749.

Bibliography

- Liu, D.S., Loh, K.H., Lam, S.S., White, K.A., and Ting, A.Y.** (2013). Imaging Trans-Cellular Neurexin-Neurologin Interactions by Enzymatic Probe Ligation. *PLoS One* **8**: e52823.
- Loh, K.H., Stawski, P.S., Draycott, A.S., Udeshi, N.D., Lehrman, E.K., Wilton, D.K., Svinkina, T., Deerinck, T.J., Ellisman, M.H., Stevens, B., Carr, S.A., and Ting, A.Y.** (2016). Proteomic Analysis of Unbounded Cellular Compartments: Synaptic Clefts. *Cell* **166**: 1295-1307.e21.
- Lord, M., Inose, F., Hiroko, T., Hata, T., Fujita, A., and Chant, J.** (2002). Subcellular localization of Axl1, the cell type-specific regulator of polarity. *Curr. Biol.* **12**: 1347–1352.
- Mair, A., Xu, S.L., Branon, T.C., Ting, A.Y., and Bergmann, D.C.** (2019). Proximity labeling of protein complexes and cell type specific organellar proteomes in Arabidopsis enabled by TurboID. *Elife* **8**.
- Manley, S., Gillette, J.M., Patterson, G.H., Shroff, H., Hess, H.F., Betzig, E., and Lippincott-Schwartz, J.** (2008). High-density mapping of single-molecule trajectories with photoactivated localization microscopy. *Nat. Methods* **5**: 155–157.
- Marston, A.L., Chen, T., Yang, M.C., Belhumeur, P., and Chant, J.** (2001). A localized gtpase exchange factor, bud5, determines the orientation of division axes in yeast. *Curr. Biol.* **11**: 803–807.
- Martell, J.D., Deerinck, T.J., Sancak, Y., Poulos, T.L., Mootha, V.K., Sosinsky, G.E., Ellisman, M.H., and Ting, A.Y.** (2012). Engineered ascorbate peroxidase as a genetically encoded reporter for electron microscopy. *Nat. Biotechnol.* **30**: 1143–8.
- Martiniere, A., Fiche, J.B., Smokvarska, M., Mari, S., Alcon, C., Dumont, X., Hematy, K., Jaillais, Y., Nollmann, M., and Maurel, C.** (2019). Osmotic stress activates two reactive oxygen species pathways with distinct effects on protein nanodomains and diffusion. *Plant Physiol.*: pp.01065.2018.
- Masucci, J.D. and Schiefelbein, J.W.** (1994). The *rhd6* mutation of *Arabidopsis thaliana* alters root-hair initiation through an auxin- and ethylene-associated process. *Plant Physiol.* **106**: 1335–1346.
- Meca, J., Massoni-Laporte, A., Martinez, D., Sartorel, E., Loquet, A., Habenstein, B., and McCusker, D.** (2019). Avidity-driven polarity establishment via multivalent lipid–GTPase module interactions. *EMBO J.* **38**: e99652.
- Meyer, I., Peter, T., Batsios, P., Kuhnert, O., Krüger-Genge, A., Camurça, C., and Gräf, R.** (2017). CP39, CP75 and CP91 are major structural components of the Dictyostelium centrosome’s core structure. *Eur. J. Cell Biol.* **96**: 119–130.
- Miernyk, J.A. and Thelen, J.J.** (2008). Biochemical approaches for discovering protein-protein interactions. *Plant J.* **53**: 597–609.
- Miller, D.D., De Ruijter, N.C.A., Bisseling, T., and Emons, A.M.C.** (1999). The role of actin in root hair morphogenesis: Studies with lipochito-oligosaccharide as a growth stimulator and cytochalasin as an actin perturbing drug. *Plant J.* **17**: 141–154.
- Molendijk, A.J., Bischoff, F., Rajendrakumar, C.S., Friml, J., Braun, M., Gilroy, S., and Palme, K.** (2001). *Arabidopsis thaliana* Rop GTPases are localized to tips of root hairs and control polar growth. *EMBO J.* **20**: 2779–88.
- Monshausen, G.B., Bibikova, T.N., Messerli, M.A., Shi, C., and Gilroy, S.** (2007). Oscillations in extracellular pH and reactive oxygen species modulate tip growth of *Arabidopsis* root hairs. *Proc. Natl. Acad. Sci. U. S. A.* **104**: 20996–21001.
- Monshausen, G.B., Bibikova, T.N., Weisenseel, M.H., and Gilroy, S.** (2009). Ca²⁺ regulates reactive oxygen species production and pH during mechanosensing in *Arabidopsis* roots. *Plant Cell* **21**: 2341–2356.
- Monshausen, G.B., Messerli, M.A., and Gilroy, S.** (2008). Imaging of the Yellow Cameleon 3.6 indicator reveals that elevations in cytosolic Ca²⁺ follow oscillating increases in growth in root hairs of *Arabidopsis*. *Plant Physiol.* **147**: 1690–1698.
- Mortensen, A. and Skibsted, L.H.** (1997). Importance of Carotenoid Structure in Radical-Scavenging Reactions. *J. Agric. Food Chem.* **45**: 2970–2977.
- Munnik, T. and Nielsen, E.** (2011). Green light for polyphosphoinositide signals in plants. *Curr. Opin. Plant Biol.* **14**: 489–497.

Bibliography

- Opitz, N., Schmitt, K., Hofer-Pretz, V., Neumann, B., Krebber, H., Braus, G.H., and Valerius, O.** (2017). Capturing the Asc1p/Receptor for Activated C Kinase 1 (RACK1) Microenvironment at the head region of the 40s ribosome with quantitative BioID in Yeast. *Mol. Cell. Proteomics* **16**: 2199–2218.
- Pan, X., Fang, L., Liu, J., Senay-Aras, B., Lin, W., Zheng, S., Zhang, T., Manor, U., Chen, W., and Yang, Z.** (2019). Auxin-induced nanoclustering of membrane signaling complexes underlies cell polarity establishment in Arabidopsis. *bioRxiv*: 734665.
- Park, H.-O. and Bi, E.** (2007). Central Roles of Small GTPases in the Development of Cell Polarity in Yeast and Beyond. *Microbiol. Mol. Biol. Rev.* **71**: 48–96.
- Park, H., Chant, J., and Herskowitz, I.** (1993). BUD2 encodes a GTPase-activating protein for Bud1/Rsr1 necessary for proper bud-site selection in yeast. *Nature* **365**: 269–274.
- Park, H.O., Kang, P.J., and Rachfal, A.W.** (2002). Localization of the Rsr1/Bud1 GTPase involved in selection of a proper growth site in yeast. *J. Biol. Chem.* **277**: 26721–26724.
- Payne, R.J.H. and Grierson, C.S.** (2009). A Theoretical Model for ROP Localisation by Auxin in Arabidopsis Root Hair Cells. *PLoS One* **4**: e8337.
- Platre, M.P. et al.** (2018). A Combinatorial Lipid Code Shapes the Electrostatic Landscape of Plant Endomembranes. *Dev. Cell* **45**: 465-480.e11.
- Platre, M.P. et al.** (2019). Developmental control of plant Rho GTPase nano-organization by the lipid phosphatidylserine. *Science* **364**: 57–62.
- Postma, M. and Goedhart, J.** (2019). PlotsOfData—A web app for visualizing data together with their summaries. *PLoS Biol.* **17**: e3000202.
- R Core Team** (2019). R: A language and environment for statistical computing.
- Repasky, G.A., Chenette, E.J., and Der, C.J.** (2004). Renewing the conspiracy theory debate: Does Raf function alone to mediate Ras oncogenesis? *Trends Cell Biol.* **14**: 639–647.
- Rhee, H.-W., Zou, P., Udeshi, N.D., Martell, J.D., Mootha, V.K., Carr, S.A., and Ting, A.Y.** (2013). Proteomic Mapping of Mitochondria in Living Cells via Spatially Restricted Enzymatic Tagging. *Science* (80-.). **339**.
- Richman, T.J., Sawyer, M.M., and Johnson, D.I.** (2002). *Saccharomyces cerevisiae* Cdc42p localizes to cellular membranes and clusters at sites of polarized growth. *Eukaryot. Cell* **1**: 458–468.
- Richman, T.J., Toenjes, K.A., Morales, S.E., Cole, K.C., Wasserman, B.T., Taylor, C.M., Koster, J.A., Whelihan, M.F., and Johnson, D.I.** (2004). Analysis of cell-cycle specific localization of the Rdi1p RhoGDI and the structural determinants required for Cdc42p membrane localization and clustering at sites of polarized growth. *Curr. Genet.* **45**: 339–349.
- Roemer, T., Madden, K., Chang, J., and Snyder, M.** (1996). Selection of axial growth sites in yeast requires Axl2p, a novel plasma membrane glycoprotein. *Genes Dev.* **10**: 777–793.
- Roth, R. et al.** (2018). A rice Serine/Threonine receptor-like kinase regulates arbuscular mycorrhizal symbiosis at the peri-arbuscular membrane. *Nat. Commun.* **9**.
- Rounds, C.M., Lubeck, E., Hepler, P.K., and Winship, L.J.** (2011). Propidium iodide competes with Ca(2+) to label pectin in pollen tubes and Arabidopsis root hairs. *Plant Physiol.* **157**: 175–87.
- Roux, K.J., Kim, D.I., Raida, M., and Burke, B.** (2012). A promiscuous biotin ligase fusion protein identifies proximal and interacting proteins in mammalian cells. *J. Cell Biol.* **196**: 801–810.
- Running, M.P.** (2014). The role of lipid post-translational modification in plant developmental processes. *Front. Plant Sci.* **5**.
- Ryu, K.H., Huang, L., Kang, H.M., and Schiefelbein, J.** (2019). Single-cell RNA sequencing resolves molecular relationships among individual plant cells. *Plant Physiol.* **179**: 1444–1456.
- Schaefer, A., Höhner, K., Berken, A., and Wittinghofer, A.** (2011). The unique plant RhoGAPs are dimeric and contain a CRIB motif required for affinity and specificity towards cognate small G proteins. *Biopolymers* **95**: 420–433.

Bibliography

- Schiefelbein, J.W. and Somerville, C.** (1990). Genetic Control of Root Hair Development in *Arabidopsis thaliana*. *Plant Cell* **2**: 235–243.
- Schindelin, J. et al.** (2012). Fiji: an open-source platform for biological-image analysis. *Nat. Methods* **9**: 676–82.
- Schmidt, A. and Hall, A.** (2002). Guanine nucleotide exchange factors for Rho GTPases: Turning on the switch. *Genes Dev.* **16**: 1587–1609.
- Schwille, P., Meyer-Almes, F.J., and Rigler, R.** (1997). Dual-color fluorescence cross-correlation spectroscopy for multicomponent diffusional analysis in solution. *Biophys. J.* **72**: 1878–1886.
- Sherrier, D.J. and VandenBosch, K.A.** (1994). Secretion of cell wall polysaccharides in *Vicia* root hairs. *Plant J.* **5**: 185–195.
- Shimada, Y., Wiget, P., Gulli, M.P., Bi, E., and Peter, M.** (2004). The nucleotide exchange factor Cdc24p may be regulated by auto-inhibition. *EMBO J.* **23**: 1051–1062.
- Shrivastava, J.** (2018). PhD-Thesis: *Arabidopsis* root hair development in asymmetric environments and the role of the receptor-like kinase PRK7.
- Simon, M.L.A., Platre, M.P., Assil, S., van Wijk, R., Chen, W.Y., Chory, J., Dreux, M., Munnik, T., and Jaillais, Y.** (2014). A multi-colour/multi-affinity marker set to visualize phosphoinositide dynamics in *Arabidopsis*. *Plant J.* **77**: 322–37.
- Simon, M.L.A., Platre, M.P., Marquès-Bueno, M.M., Armengot, L., Stanislas, T., Bayle, V., Caillaud, M.-C., and Jaillais, Y.** (2016). A PtdIns(4)P-driven electrostatic field controls cell membrane identity and signalling in plants. *Nat. Plants* **2**: 16089.
- Slaughter, B.D., Unruh, J.R., Das, A., Smith, S.E., Rubinstein, B., and Li, R.** (2013). Non-uniform membrane diffusion enables steady-state cell polarization via vesicular trafficking. *Nat. Commun.* **4**: 1–10.
- Smertenko, A.P., Jiang, C.-J., Simmons, N.J., Weeds, A.G., Davies, D.R., and Hussey, P.J.** (1998). Ser6 in the maize actin-depolymerizing factor, ZmADF3, is phosphorylated by a calcium-stimulated protein kinase and is essential for the control of functional activity. *Plant J.* **14**: 187–193.
- Smokvarska, M., Francis, C., Platre, M.P., Fiche, J.B., Alcon, C., Dumont, X., Nacry, P., Bayle, V., Nollmann, M., Maurel, C., Jaillais, Y., and Martiniere, A.** (2020). A plasma membrane nanoplatform ensures signal specificity during osmotic signaling in plants. *bioRxiv*: 2020.06.14.145961.
- Sorek, N., Gutman, O., Bar, E., Abu-Abied, M., Feng, X., Running, M.P., Lewinsohn, E., Ori, N., Sadot, E., Henis, Y.I., and Yalovsky, S.** (2011). Differential effects of prenylation and S-acylation on type I and II ROPS membrane interaction and function. *Plant Physiol.* **155**: 706–720.
- Sorek, N., Poraty, L., Sternberg, H., Bar, E., Lewinsohn, E., and Yalovsky, S.** (2007). Activation status-coupled transient S acylation determines membrane partitioning of a plant Rho-related GTPase. *Mol. Cell. Biol.* **27**: 2144–54.
- Sorek, N., Poraty, L., Sternberg, H., Buriakovsky, E., Bar, E., Lewinsohn, E., and Yalovsky, S.** (2017). Activation Status-Coupled Transient S-Acylation Determines Membrane Partitioning of a Plant Rho-Related GTPase. *Mol. Cell. Biol.* **37**: 1–19.
- Spira, F., Mueller, N.S., Beck, G., Von Olshausen, P., Beig, J., and Wedlich-Söldner, R.** (2012). Patchwork organization of the yeast plasma membrane into numerous coexisting domains. *Nat. Cell Biol.* **14**: 640–648.
- Staiger, C.J., Poulter, N.S., Henty, J.L., Franklin-Tong, V.E., and Blanchoin, L.** (2010). Regulation of actin dynamics by actin-binding proteins in pollen. *J. Exp. Bot.* **61**: 1969–1986.
- Stanislas, T., Hüser, A., Barbosa, I.C.R., Kiefer, C.S., Brackmann, K., Pietra, S., Gustavsson, A., Zourelidou, M., Schwechheimer, C., and Grebe, M.** (2015). *Arabidopsis* D6PK is a lipid domain-dependent mediator of root epidermal planar polarity. *Nat. Plants* **1**: 15162.
- Stanley, C.E., Shrivastava, J., Brugman, R., Heinzemann, E., van Swaay, D., and Grossmann, G.** (2018). Dual-flow-RootChip reveals local adaptations of roots towards environmental asymmetry at the physiological and genetic levels. *New Phytol.* **217**: 1357–1369.

Bibliography

- Szymanski, D.B.** (2005). Breaking the WAVE complex: The point of Arabidopsis trichomes. *Curr. Opin. Plant Biol.* **8**: 103–112.
- Takeda, S., Gapper, C., Kaya, H., Bell, E., Kuchitsu, K., and Dolan, L.** (2008). Local positive feedback regulation determines cell shape in root hair cells. *Science* (80-.). **319**: 1241–1244.
- Takeuchi, H. and Higashiyama, T.** (2016). Tip-localized receptors control pollen tube growth and LURE sensing in Arabidopsis. *Nature* **531**: 245–8.
- Thomas, C., Fricke, I., Scrima, A., Berken, A., and Wittinghofer, A.** (2007). Structural Evidence for a Common Intermediate in Small G Protein-GEF Reactions. *Mol. Cell* **25**: 141–149.
- Tinevez, J.-Y., Perry, N., Schindelin, J., Hoopes, G.M., Reynolds, G.D., Laplantine, E., Bednarek, S.Y., Shorte, S.L., and Eliceiri, K.W.** (2017). TrackMate: An open and extensible platform for single-particle tracking. *Methods* **115**: 80–90.
- Turing, A.M.** (1952). The chemical basis of morphogenesis. *Philos. Trans. R. Soc. Lond. B. Biol. Sci.* **237**: 37–72.
- Ueda, T., Kikuchi, A., Ohga, N., Yamamoto, J., and Takai, Y.** (1990). Purification and characterization from bovine brain cytosol of a novel regulatory protein inhibiting the dissociation of GDP from and the subsequent binding of GTP to rhoB p20, a ras p21-like GTP-binding protein. *J. Biol. Chem.* **265**: 9373–9380.
- Uezu, A., Kanak, D.J., Bradshaw, T.W.A., Soderblom, E.J., Catavero, C.M., Burette, A.C., Weinberg, R.J., and Soderling, S.H.** (2016). Identification of an elaborate complex mediating postsynaptic inhibition. *Science* (80-.). **353**: 1123–1129.
- Vernoud, V., Horton, A.C., Yang, Z., and Nielsen, E.** (2003). Analysis of the small GTPase gene superfamily of arabidopsis. *Plant Physiol.* **131**: 1191–1208.
- Vetter, I.R. and Wittinghofer, A.** (2001). The guanine nucleotide-binding switch in three dimensions. *Science* (80-.). **294**: 1299–1304.
- Vincent, P., Chua, M., Nogue, F., Fairbrother, A., Mekeel, H., Xu, Y., Allen, N., Bibikova, T.N., Gilroy, S., and Bankaitis, V.A.** (2005). A Sec14p-nodulin domain phosphatidylinositol transfer protein polarizes membrane growth of Arabidopsis thaliana root hairs. *J. Cell Biol.* **168**: 801–812.
- Volgger, M., Lang, I., Ovečka, M., and Lichtscheidl, I.** (2010). Plasmolysis and cell wall deposition in wheat root hairs under osmotic stress. *Protoplasma* **243**: 51–62.
- Wang, M. and Casey, P.J.** (2016). Protein prenylation: Unique fats make their mark on biology. *Nat. Rev. Mol. Cell Biol.* **17**: 110–122.
- Wang, T., Liang, L., Xue, Y., Jia, P.F., Chen, W., Zhang, M.X., Wang, Y.C., Li, H.J., and Yang, W.C.** (2016). A receptor heteromer mediates the male perception of female attractants in plants. *Nature* **531**: 241–244.
- Wedlich-Soldner, R., Altschuter, S., Wu, L., and Li, R.** (2003). Spontaneous cell polarization through actomyosin-based delivery of the Cdc42 GTPase. *Science* (80-.). **299**: 1231–1235.
- Wedlich-Soldner, R. and Li, R.** (2003). Spontaneous cell polarization: undermining determinism. *Nat. Cell Biol.* **5**: 267–70.
- Wennerberg, K., Rossman, K.L., and Der, C.J.** (2005). The Ras superfamily at a glance. *J. Cell Sci.* **118**: 843–846.
- Wickham, H.** (2016). *ggplot2: Elegant Graphics for Data Analysis* (Springer-Verlag New York).
- Williams, M.E., Torabinejad, J., Cohick, E., Parker, K., Drake, E.J., Thompson, J.E., Hortter, M., and Dewald, D.B.** (2005). Mutations in the Arabidopsis phosphoinositide phosphatase gene SAC9 lead to overaccumulation of PtdIns(4,5)P2 and constitutive expression of the stress-response pathway. *Plant Physiol.* **138**: 686–700.
- Won, D.H., Inoue, T., Wei, S.P., Man, L.K., Byung, O.P., Wandless, T.J., and Meyer, T.** (2006). PI(3,4,5)P3 and PI(4,5)P2 lipids target proteins with polybasic clusters to the plasma membrane. *Science* (80-.). **314**: 1458–1461.

Bibliography

- Wu, G., Gu, Y., Li, S., and Yang, Z.** (2001). A Genome-Wide Analysis of Arabidopsis Rop-Interactive CRIB Motif-Containing Proteins That Act as Rop GTPase Targets. *Plant Cell* **13**: 2841–2856.
- Wu, G., Li, H., and Yang, Z.** (2000). Arabidopsis RopGAPs are a novel family of Rho GTPase-activating proteins that require the Cdc42/Rac-interactive binding motif for Rop-specific GTPase stimulation. *Plant Physiol.* **124**: 1625–1636.
- Wu, Y., Zhao, S., Tian, H., He, Y., Xiong, W., Guo, L., and Wu, Y.** (2013). CPK3-phosphorylated RhoGDI1 is essential in the development of Arabidopsis seedlings and leaf epidermal cells. *J. Exp. Bot.* **64**: 3327–3338.
- Wymer, C.L., Bibikova, T.N., and Gilroy, S.** (1997). Cytoplasmic free calcium distributions during the development of root hairs of Arabidopsis thaliana. *Plant J.* **12**: 427–439.
- Xing, S., Mehlhorn, D.G., Wallmeroth, N., Asseck, L.Y., Kar, R., Voss, A., Denninger, P., Schmidt, V.A.F., Schwarzländer, M., Stierhof, Y.-D., Grossmann, G., and Grefen, C.** (2017). Loss of GET pathway orthologs in Arabidopsis thaliana causes root hair growth defects and affects SNARE abundance. *Proc. Natl. Acad. Sci. U. S. A.*: 201619525.
- Xing, S., Wallmeroth, N., Berendzen, K.W., and Grefen, C.** (2016). Techniques for the analysis of protein-protein interactions in vivo. *Plant Physiol.* **171**: 727–758.
- Xu, Y. and Beckett, D.** (1994). Kinetics of Biotinyl-5'-adenylate Synthesis Catalyzed by the Escherichia coli Repressor of Biotin Biosynthesis and the Stability of the Enzyme-Product Complex. *Biochemistry* **33**: 7354–7360.
- Yanagisawa, M., Zhang, C., and Szymanski, D.B.** (2013). ARP2/3-dependent growth in the plant kingdom: SCARs for life. *Front. Plant Sci.* **4**: 166.
- Zahner, J.E., Harkins, H.A., and Pringle, J.R.** (1996). Genetic analysis of the bipolar pattern of bud site selection in the yeast Saccharomyces cerevisiae. *Mol. Cell. Biol.* **16**: 1857–1870.
- Zhang, Y. and McCormick, S.** (2007). A distinct mechanism regulating a pollen-specific guanine nucleotide exchange factor for the small GTPase Rop in Arabidopsis thaliana. *Proc. Natl. Acad. Sci. U. S. A.* **104**: 18830–18835.
- Zhang, Y., Song, G., Lal, N.K., Nagalakshmi, U., Li, Y., Zheng, W., Huang, P. jui, Branon, T.C., Ting, A.Y., Walley, J.W., and Dinesh-Kumar, S.P.** (2019). TurboID-based proximity labeling reveals that UBR7 is a regulator of N NLR immune receptor-mediated immunity. *Nat. Commun.* **10**: 1–17.
- Zhao, Y., Yan, A., Feijó, J. a, Furutani, M., Takenawa, T., Hwang, I., Fu, Y., and Yang, Z.** (2010). Phosphoinositides regulate clathrin-dependent endocytosis at the tip of pollen tubes in Arabidopsis and tobacco. *Plant Cell* **22**: 4031–4044.
- Zheng, Y., Cerione, R., and Bender, A.** (1994). Control of the yeast bud-site assembly GTPase Cdc42. *J. Biol. Chem.* **269**: 2369–2372.
- Zheng, Z.L. and Yang, Z.** (2000). The Rop GTPase: An emerging signaling switch in plants. *Plant Mol. Biol.* **44**: 1–9.
- Zhu, L., Zhang, Y., Kang, E., Xu, Q., Wang, M., Rui, Y., Liu, B., Yuan, M., and Fu, Y.** (2013). MAP18 regulates the direction of pollen tube growth in Arabidopsis by modulating F-actin organization. *Plant Cell* **25**: 851–867.
- Zhu, S., Estévez, J.M., Liao, H., Zhu, Y., Yang, T., Li, C., Wang, Y., Li, L., Liu, X., Pacheco, J.M., Guo, H., and Yu, F.** (2020). The RALF1-FERONIA Complex Phosphorylates eIF4E1 to Promote Protein Synthesis and Polar Root Hair Growth. *Mol. Plant* **13**: 698–716.
- Zuo, J., Niu, Q.-W., and Chua, N.-H.** (2000). An estrogen receptor-based transactivator XVE mediates highly inducible gene expression in transgenic plants. *Plant J.* **24**: 265–273.

Appendix

List of figures

Figure 1: The activity cycle of small GTPases, at the example of a GTPase with a lipid anchor. In the active form, the GTPase is associated with the plasma membrane and binds GTP, which is hydrolyzed via a GTPase ACTIVATING PROTEIN (GAP). The GDP-bound GTPase in its inactive state is sequestered in the cytosol by GUANINE DISSOCIATION INHIBITORS (GDIs), that bind to the lipid anchor. GDP is replaced by GTP via GUANINE NUCLEOTIDE EXCHANGE FACTORS (GEFs), leading to the activation and association of the small GTPase with the plasma membrane. **19**

Figure 2: The Arabidopsis root hair system is a suitable model system to study the initiation of tip growth. (A) From left to right: Micrograph of an *Arabidopsis thaliana* seedling (scale bar = 1 mm), micrograph of the primary root tip of an Arabidopsis seedling (scale bar = 100 μ m), magnified view of the previous micrograph depicting a trichoblast cell file including cell stages +1 to +3 (scale bar = 50 μ m), schematic representation of a trichoblast cell file depicting the developmental time line and the nomenclature for cell stage determination: the first cell from the root tip that shows a bulge is named +1, younger cell are termed with increasing negative numbers. (B) Micrographs from a time lapse movie of a root grown in a microfluidic chamber showing the root hair growth response to the stop of flow (scale bar = 300 μ m). **22**

Chapter I - Polarization of the small Rho-type GTPase ROP2 at the root hair initiation domain

Figure I- 1: Schematic representation of the secondary protein structure of ROP2. ROP2 = full length ROP2, 195AA; G14V mutation leads to constitutively active ROP2 (*rop2CA*), D120A mutation leads to dominant negative ROP2 (*rop2DN*); amino acid abbreviations: G = glycine, V = valine, D = aspartic acid, A = alanine, C = cysteine. **35**

Figure I- 2: Schematic representation of the secondary protein structure of ROP2 and the ROP2 deletion variants investigated in this chapter. ROP2 = full length ROP2, G14V mutation leads to constitutively active (CA) ROP2, D120A mutation leads to dominant negative (DN) ROP2; *rop2 Δ N79* = deletion of the first 79 AA of the N-terminus of ROP2; *rop2 Δ N121* = deletion of the first 120 AA of the N-terminus of ROP2; *rop2 Δ N160* = deletion of the first 160 AA of the N-terminus of ROP2; *rop2 Δ C161* = deletion of the last 35 AA of the C-terminus of ROP2; *rop2 7K-A* = full length ROP2 in which the 7 lysines of the poly-lysine tail are substituted by alanines. **38**

Figure I- 3: Schematic showing the calculations for the polarity index and membrane association. On the left side, a schematic trichoblast cell illustrates the relation of individual ROIs for each of which the mean fluorescent intensity was measured. On the right side an example image of a fluorescent marker line is shown: Close-up views of indicated regions including ROIs with the original scaling of 15x3 px. Scale bar represents 10 μ m. **38**

Figure I- 4: The anionic lipids PS and PI(4)P do not polarize at the RHID. Polarity index of ROP2, a sensor for phosphatidylserine (PS), a sensor for phosphatidylinositol 4-phosphate (PI(4)P), LTI6B and mCitrine (mCit) at cell stage - 1 (A) and + 1 (C). Membrane association of ROP2, PS, PI(4)P, LTI6B and mCit inside (in) and outside (out) of the RHID at cell stage - 1 (B) and + 1 (D). Cell stage is indicated by the cartoon. Center lines represent median values, gray boxes represent the data range, n indicates the number of cells measured and letters represent the result of an ANOVA-Tukey test (significance value = 0.01; same letters indicate no significant difference). (E) representative images of PS and PI(4)P at the indicated cell stages. The scale bar represents 10 μ m, the root tip is located to the left side of the cells shown. Cartoons indicate the respective cell stage. **40**

Figure I- 5: The C-terminus of ROP2 is required, but not sufficient for its polarization at the RHID. (A) Polarity index of ROP2, *rop2 7K-A* (7K-A), *rop2 Δ C161* (Δ C161), *rop2 Δ N160* (Δ N160), a Farnesyl-Anchor with 8 lysines (8K-Farn), LTI6B and mCitrine (mCit). (B) Membrane association of ROP2, 7K-A, Δ C161, Δ N160, 8K-Farn, LTI6B and mCit inside (in) and outside (out) of the RHID. Center lines represent median values, gray boxes represent the data range, n indicates the number of cells measured and letters represent the result of an ANOVA-Tukey test (significance value = 0.01; same letters indicate no significant difference). All measurements were performed in cells of the developmental stage -1. Measurements for ROP2, LTI6B and mCit are shown for comparability, but

are the same as already presented in Figure I- 4. (C) Representative images of 7K-A, Δ C161, Δ N160 and 8K-Farn. The root tip is located to the left side of the cells shown. The scale bar represents 10 μ m. Cartoon indicates the respective cell stage and orientation (D) Micrographs of potential *rop2/4* rescue lines, either expressing full length ROP2 (middle panel) or the *rop2* 7-K-A (lower panel). Arrows indicate the first detectable bulge. The scale bar represents 300 μ m. **42**

Figure I- 6: The N-terminus of ROP2 is involved in its polarization at the RHID. (A) Polarity index of ROP2, *rop2* Δ N79 (Δ N79), *rop2* Δ N121 (Δ N121), *rop2* Δ N160 (Δ N160), LTI6B and mCitrine (mCit). (B) Membrane association of ROP2, Δ N79, Δ N121, Δ N160, LTI6B and mCit inside (in) and outside (out) of the RHID. Center lines represent median values, gray boxes represent the data range, n indicates the number of cells measured and letters represent the result of an ANOVA-Tukey test (significance value = 0.01; same letters indicate no significant difference). All measurements were performed in cells of the developmental stage -1. Cartoon indicates the respective cell stage. Measurements of ROP2, Δ N160, LTI6B and mCit are shown for comparability, but are the same as already presented in Figure I- 4 and -5. **43**

Figure I- 7: The activity status of ROP2 influences its polarization and association with the plasma membrane. (A) Polarity index of ROP2, constitutively active *rop2* (CA), dominant negative *rop2* (DN), LTI6B and mCitrine (mCit). (B) Representative images of ROP2, *rop2*CA and *rop2*DN. The root tip is located to the left side of the cells shown. Cartoon indicates the respective cell stage The scale bar represents 10 μ m. (C) Membrane association of ROP2, CA, DN, LTI6B and mCit inside (in) and outside (out) of the RHID. Center lines represent median values, gray boxes represent the data range, n indicates the number of cells measured and letters represent the result of an ANOVA-Tukey test (significance value = 0.01; same letters indicate no significant difference). All measurements were performed in cells of the developmental stage -1. Measurements of ROP2, LTI6B and mCit are shown for comparability, but are the same as already presented in Figure I- 4. **45**

Figure I- 8: The N-terminal interaction domain is involved in GEF3-dependent ROP2 polarization at the RHID. Polarity index of ROP2, *rop2* Δ N79 (Δ N79), ROP2 in the *gef3-1* mutant background (*gef3-1* ROP2), *rop2* Δ C161 (Δ C161), LTI6B and mCitrine (mCit) at cell stage - 1 (A) and + 1 (C). Membrane association of ROP2, Δ N79, *gef3-1* ROP2, Δ C161, LTI6B and mCit inside (in) and outside (out) of the RHID at cell stage - 1 (B) and + 1 (D). Center lines represent median values, gray boxes represent the data range, n indicates the number of cells measured and letters represent the result of an ANOVA-Tukey test (significance value = 0.01; same letters indicate no significant difference). Cartoons indicate the respective cell stages. Measurements of ROP2, Δ N79, Δ C161 LTI6B and mCit are shown for comparability, but are the same as already presented in Figure I- 4, -5 and -6. **47**

Chapter II - Local immobilization of ROP2 in membrane nanodomains by GEF3

Figure II- 1: ROP2 activation caused protein immobilization at the RHID. Fluorescent Recovery After Photobleaching (FRAP) measurements of ROP2 inside (A) and outside the RHID (B) and the corresponding mean recovery-curves (C). FRAP measurements for ROP2CA (D) and *rop2*DN (E) inside the RHID and the corresponding mean recovery-curves (F). Images of single time points before bleaching (-5 sec), directly after bleaching (0 sec) and at the middle of the recorded time (65 sec) are shown for each protein as well as kymographs drawn along a line spanning the bleached region. All measurements were performed at cell stage -1. Scale bars represent 10 μ m. **60**

Figure II- 2: GEF3 caused ROP2 immobilization at the RHID. (A, B) FRAP measurements for ROP2 in the *gef3-1* mutant background (A) and GEF3 (B), both inside the RHID. All measurements were performed at cell stage -1. Images for single time points before bleaching (-5 sec), directly after bleaching (0 sec) and at the middle of the recorded recovery time (65 sec) are shown for each protein, as well as a kymograph drawn along a line spanning the bleached region. Scale bars represent 10 μ m. (C) Corresponding mean recovery-curves for ROP2 in the *gef3-1* mutant background and GEF3. For comparison, the recovery-curve of ROP2 from Figure II- 1 is shown again. (D) Half time of recovery ($t^{1/2}$) for ROP2, GEF3 and ROP2 in the *gef3-1* mutant background inside (in) and outside (out) the RHID. Center lines represent median values, gray boxes show the data range, n indicates the number of measured cells. Asterisk indicate statistically significant difference; p-value determined by Student's t-test: n.s. = p-value >0.05; * = p-value < 0.05. **61**

Figure II- 3: VAEM reveals that ROP2 and GEF3 localize in diffraction limited, mobile puncta in the PM of trichoblasts of cell stage -1. (A) Schematic representation of the excitation illumination in Variable

Angle Epifluorescence Microscopy (VAEM) compared to epifluorescence (Epi). (B) kymograph of a mCitrine-GEF3 VAME time-lapse movie, drawn along the red line of the VAEM micrographs represented in (C, upper panel). VAEM micrographs of GEF3 (C), ROP2 (D) and ROP2 in the *gef3-1* mutant background (E). Single slices of time lapse stacks (upper panel) and kymographs drawn along the red, dashed line (lower panel). Note that the kymographs in (C-E) were created from time lapse stacks with enhanced contrast. The kymographs in (B) and (C, lower panel) are derived from the same time-lapse. Scale bars represent 5 μm . 64

Figure II- 4: mCitrine, but not mNeonGreen shows fluorophore blinking behavior in tobacco leaves.

VAEM-micrographs of the actin probe LifeAct tagged with mCitrine (A-C) and mNeonGreen (D-F). Single images from a time lapse stack acquired with the indicated imaging settings are shown (laser power in % and exposure time in ms). Kymographs drawn along the red, dashed lines are depicted next to the corresponding image. Panel (C) and (F) show sum projections of the time lapse stacks of (B) and (E), respectively. Scale bars represent 5 μm . 65

Figure II- 5: SRRF reconstruction can increase image resolution and signal to background ratio (A)

Schematic representation of the reconstruction of a super resolved image by integrating distinct blinking events (B) Sum intensity projection (upper panel) and a SRRF reconstruction (lower panel) of a time-lapse VAEM movie of an *Arabidopsis* trichoblast stably expressing LifeAct-mCitrine under the control of the *Ubiquitin10* promoter. The scale bar represents 5 μm ; colored lines within the micrographs represent the lines, along which the relative intensity profiles (C) were measured. 66

Figure II- 6: Sub-compartmentation of the RHID visualized by live-cell, laser scanning confocal microscopy.

Micrographs of GEF3 (A) and ROP2 (B) in trichoblasts of cell stage -1. Scale bar represents 5 μm . 67

Figure II- 7: ROP2 is recruited into stable nanoclusters in the RHID in a GEF3-dependent manner. (A-C)

Super Resolution Radial Fluctuation (SRRF) reconstructions of VAEM micrographs of GEF3 (A), ROP2 (B) and ROP2 in the *gef3-1* mutant background (C) in different developmental cell stages (-4 to +1). For each protein, the images were taken from different trichoblast cell stages but from the same root (exception: GEF3 +1 is derived from a different root than the other GEF3 cell stages). The root tip is always located to the left side of the cells. Stability of the structures is false-colored as indicated; scale bars represent 5 μm . (D, E) Quantification of the nanocluster density and area of the RHID for GEF3 (D) and ROP2 (E) over the course of root hair development. Center lines represent median values; gray boxes show the data range; n indicates the number of cells measured; note that for each graph an ANOVA-Tukey test (significance value = 0.01; same letters indicate no significant difference) revealed no significant difference between data for each developmental stage. 68

Figure II- 8: ROP2 polarization depends on and follows GEF3 polarization. Spot density determined by particle tracking inside (in) and outside (out) the RHID for GEF3 (A), ROP2 (B) and ROP2 in the *gef3-1* mutant background (C). Center lines represent median values; gray boxes show the data range.

Asterisks indicate statistically significant differences; p-value determined by Student's t-test: n.s. = p-value > 0.05; * = p-value < 0.05; ** = p-value < 0.01; *** = p-value < 0.001. 71

Figure II- 9: ROP2 shows a subtle reduction in mobility at the RHID prior to its polarization. Normalized distribution of track velocities for mCitrine-ROP2 puncta inside and outside the RHID over the course of root hair development. P-values indicate the statistical difference between the distribution of velocities inside and outside the RHID and were determined by two-way ANOVA. Curves represent polynomial fits (6th degree) of the data set, vertical lines indicate local maxima of the fitted curves. R² values for the fits can be found in Table II- 2. The y-axis shows the normalized frequency; the x-axis shows the track velocity; n (in; out) indicates the number of cells measured. 74

Figure II- 10: GEF3 mobility is not altered during RHID establishment. Normalized distribution of track velocities for mCitrine-GEF3 puncta inside and outside the RHID over the course of root hair development. p-values indicate the statistical difference between the distribution of velocities inside and outside the RHID and were determined by two-way ANOVA. Curves represent polynomial fits (6th degree) of the data set, vertical lines indicate local maxima of the fitted curves. R² values for the fits can be found in Table II- 4. The y-axis shows the normalized frequency; the x-axis shows the track velocity; n (in; out) indicates the number of cells measured. 76

Figure II- 11: ROP2 immobilization during root hair development depends on GEF3. Normalized distribution of track velocities for mCitrine-ROP2 puncta in the *gef3-1* mutant background, inside and outside the RHID over the course of root hair development. p-values indicate the statistical difference between the distribution of velocities inside and outside the RHID and were determined by two-way ANOVA. Curves represent polynomial fits (6th degree) of the data set, vertical lines indicate local maxima of the fitted curves. R² values for the fits can be found in Table II- 7. The y-axis shows the

normalized frequency; the x-axis shows the track velocity; n (in; out) indicates the number of cells measured.

78

Figure II- 12: The displacement of ROP2 is influenced by its activation as well as by GEF3. (A) Median displacement of mCitrine tagged GEF3, ROP2 and *rop2CA* dots inside (in) and outside (out) of the RHID. Center lines represent median values; gray boxes represent the data range; n indicates the number of cells measured and letters represent the result of an ANOVA-Tukey test (significance value = 0.01; same letters indicate no significant difference). All measurements were performed in cells of the developmental stage -1. (B) Single slice of a VAEM time-lapse movie of ROP2 Δ N79 and a kymograph drawn along the indicated line. (C) SRRF reconstruction of the same VAEM time-lapse movie shown in panel (B). (D) SRRF reconstruction of a VAEM time-lapse movie of a trichoblast from a plant stably expressing LTI6B-GFP under the control of the 35S promoter. The scale bar represents 5 μ m.

79

Figure II- 13: Activation of ROP2 caused a reduction in protein mobility as well as its accumulation in nanoclusters. (A) Normalized distribution of track velocities for mCitrine- *rop2CA* puncta, inside and outside of the RHID in trichoblast cells of stage -1 and stage +1. P-values indicate the statistical difference between the distribution of velocities inside and outside the RHID and were determined by two-way ANOVA. Curves represent polynomial fits (6th degree) of the data set; vertical lines indicate local maxima of the fitted curves. R² values for the fits can be found in Table II- 9. The y-axis shows the normalized frequency; the x-axis shows the track velocity; n (in; out) indicates the number of cells measured. (B) Single slices of a VAEM time lapse stacks (left panel) and a kymograph (right panel) drawn along the red, dashed line. Note that the kymograph was created from a time lapse stack with enhanced contrast. (C) SRRF reconstruction of a trichoblast cell expressing *rop2CA*. The scale bar represents 10 μ m in (C) and 5 μ m in (B).

81

Figure II- 14: GDP-locked ROP2 showed a reduced mobility in the plasmamembrane of root hair cells. (A) Normalized distribution of track velocities for mCitrine- *rop2DN* puncta, inside and outside of the RHID in trichoblast cells of stage -1. P-values indicate the statistical difference between the velocity distribution inside and outside the RHID and were determined by two-way ANOVA. (B) Normalized distribution of track velocities for autofluorescent puncta in atrichoblasts of wild type plants. Curves represent polynomial fits (6th degree) of the data set; vertical lines indicate local maxima of the fitted curves. R² values for the fits can be found in Table II- 10. The y-axis shows the normalized frequency; the x-axis shows the track velocity; n indicates the number of cells measured.

82

Figure II- 15: S-acylation of ROP2 does not reduce protein mobility, polarization or membrane association. (A) Normalized distribution of track velocities for mCitrine-*rop2 Δ C* puncta (left panel) and mCitrine-ROP2 puncta (right panel), inside and outside the RHID at cell stages -1. p-values indicate the statistical difference between the velocity distribution inside and outside the RHID and were determined by two-way ANOVA. Curves represent polynomial fits (6th degree) of the data set, vertical lines indicate local maxima of the fitted curves. R² values for the fits can be found in Table II- 11. The y-axis shows the normalized frequency; the x-axis shows the track velocity; n (in; out) indicates the number of cells measured. (B) Single slices of a *rop2*^{C8, 20, 157A} VAEM time lapse stack and a kymograph drawn along the red, dashed line. Note that the kymograph was created from a time lapse stack with enhanced contrast. (C-F) Polarity index of ROP2, *rop2*^{C8, 20, 157A}, LTI6B and mCitrine (mCit) at cell stage -1 (C) and +1 (E). Membrane association of ROP2, *rop2*^{C8, 20, 157A}, LTI6B and mCit inside (in) and outside (out) of the RHID at cell stage -1 (D) and +1 (F). Center lines represent median values; gray boxes represent the data range; n indicates the number of cells measured and letters represent the result of an ANOVA-Tukey test (significance value = 0.01; same letters indicate no significant difference). Measurements of ROP2, LTI6B and mCit are shown for comparability, but are the same as already presented in Figure I- 3. (G) Representative images of *rop2*^{C8, 20, 157A} at the indicated cell stages; the rightmost image shows a trichoblast exhibiting a ROP2-overexpression phenotype. The scale bars represent 10 μ m.

85

Figure II- 16: The mobility of ROP2 proteins was independent of the fluorophore-tag. Figure legend on the following page.

89

Figure II- 17: Test for co-localization of mCitrine-ROP2 and mRuby2-ROP2 in SRRF reconstructions. Single channel SRRF images of mCitrine-ROP2 (left), mRuby2-ROP2 (middle) and their merge (right), in a region within the RHID (upper panel) and in the background outside the sample (lower panel). The scale bar represents 2 μ m. Correlation maps of the images from the respective panel including the correlation coefficient R². Images were taken at a root hair of cell stage +1 from an unfixed

Arabidopsis root stably co-expressing mRuby2-ROP2 and mCitrine-ROP2, both under the control of the endogenous *ROP2* promoter in wild type background. 91

Figure II- 18: GEF3 is necessary but not sufficient to polarize Brk1 into nanoclusters at the RHID. (A-B) Representative confocal images of BRK1-YFP (BRK1) in wild type (A) and the *gef3* mutant (B) background over the course of root hair development. (C) Polarity index of BRK1, *gef3-1*BRK1 and LTI6B at cell stages -1 and +1. Measurements for LTI6B are shown for comparability, but are the same as already presented in Figure I- 3. Asterisks indicate statistically significant difference (p-value determined by Student's t-test: n.s. = p-value >0.05; * = p-value < 0.05); n represents the number of cells measured. (D) SRRF reconstructions of a VAEM time-lapse stack of BRK1-YFP in the wild type (left side) and in the *gef3-1-1* mutant background (right side) in trichoblasts of the cell stage -1 and +1. (E) Maximum intensity projection of an *Arabidopsis* root expressing BRK1-mTurquoise2 under its native promoter and mCitrine-GEF3 under the control of the estradiol inducible *Ubiquitin10* promoter. Box1 shows a trichoblast cell with co-localization; box2 shows an atrichoblast cell with no co-localization. The scale bars represent 10 μ m in (A) and (B), 5 μ m in (D) and 20 μ m in (E). 94

Figure II- 19: Other proteins of the tip growth machinery also localize into nanoclusters within the RHID. SRRF reconstructions of: mCitrine-ROP4 at cell stage -1; PIP5K3-mCitrine at cell stage +1; mCitrine-GEF4 at cell stage +1; PRK7-mCitrine at cell stage -1; Fer-GFP at cell stage +1;. The scale bars represent 5 μ m. 95

Chapter III - Establishment of proximity labeling to aid the identification of protein-protein interactions in trichoblasts

Figure III- 1: Schematic overview of proximity labelling using a biotin ligase based system: All transient and stable interaction partners of the biotin ligase-fusion protein are marked by covalent attachment of a biotin residue. 108

Figure III- 2: Schematic overview of the estradiol inducible promoter system. A promoter of choice is driving the expression of the chimeric transcription factor XVE. XVE binds to the oLexA-minimal 35S promoter only in the presence of estradiol and activates the transcription of the gene of interest (Gol). 112

Figure III- 3: Characterization of estradiol inducible, root hair-specific promoters. Cross-sections (A, B, C) and a maximum intensity projection (D) of the estradiol-inducible ROP2 (A), GEF3 (B) and ExpA7 (C and D) promoters driving mCitrine expression. Fluorescent images of mCitrine expression (left panel), propidium iodide (PI) staining (middle panel) and merge (right panel) are shown for each promoter. Asterisks indicate trichoblasts. Scale bars represent 10 μ m for A-C and 50 μ m for D. The arrows indicates the youngest cell in which signal for mCitrine was visible. Note that the two images belong to the same root, but their brightness was scaled differently. (E) Quantification of trichoblast-specificity of the fluorescent signal. Center lines represent median values, gray boxes represent the data range, n indicates the number of roots measured and letters represent the result of an ANOVA-Tukey test (significance value = 0.01, same letters indicate no significant difference). To obtain these values, 4 cross-sections per root were measured. 114

Figure III- 4: Proof-of-concept: Auto-biotinylation of TurboID in *N. benthamiana* leaves. Western Blots of protein extract from *N. benthamiana*, transiently expressing the GEF3-TurboID-HA construct under the control of an estradiol inducible promoter. (A) Western Blot membrane showing signal for the anti-HA antibody. (B) Western Blot membrane showing signal for Streptavidin, which binds to biotin. Asterisks indicates GEF3-TurboID-HA, dots indicate the break-down product TurboID-HA. The most left lane was loaded with proteins from not induced *N. benthamiana* leaves, but supplied with 100 μ M biotin; the middle lane was loaded with proteins from induced *N. benthamiana* leaves, not supplemented with biotin; rightmost lane was loaded with induced *N. benthamiana* leaves supplemented with 100 μ M biotin. As molecular weight standard, the protein ladder #p7719 from NEB was used. 116

List of tables

(excluding tables from Materials and Methods)

Table II- 1: Half time recovery ($t^{1/2}$) and mobile fraction calculated for ROP2, <i>rop2CA</i> , <i>rop2DN</i> , GEF3 and ROP2 in <i>gef3-1</i> , both at the inside of the RHID (RHID) or outside (out) of the RHID.	62
Table II- 2: R ² values for the polynomial fitted curves for ROP2 inside and outside the RHID (see Figure II- 9).	74
Table II- 3: p-values for the velocity distributions of ROP2, tested by two way ANOVA.	75
Table II- 4: R ² values for the polynomial fitted curves for GEF3 inside and outside the RHID (see Figure II- 10).	76
Table II- 5: p-values for the mobility distributions of GEF3, tested by two way ANOVA.	77
Table II- 6: p-values for the velocity distributions of ROP2 in <i>gef3-1</i> , tested by two-way ANOVA.	77
Table II- 7: R ² values for the polynomial fitted curves for <i>gef3-1</i> ROP2 inside and outside the RHID (see Figure II- 11).	78
Table II- 8: p-values for the velocity distributions of <i>rop2CA</i> in comparison to ROP2 at the RHID of the cell stages -1 and +1, tested by two-way ANOVA.	80
Table II- 9: R ² values for the polynomial fitted curves for <i>rop2CA</i> inside and outside the RHID (see Figure II- 13).	81
Table II- 10: R ² values for the polynomial fitted curves for <i>rop2DN</i> inside and outside the RHID, as well as for autofluorescent particles of atrichoblasts from wild type plants (see Figure II- 14).	83
Table II- 11: R ² values for the polynomial fitted curves for ROP2 and <i>rop2ΔC</i> inside and outside the RHID (see Figure II- 15).	84
Table II- 12: R ² values for the polynomial fitted curves for mCitrine-ROP2 in the <i>gef3</i> mutant background and mRuby2-ROP2 in the wild type background inside and outside the RHID (see Figure II- 16). R ² values for mCitrine-ROP2 fitting can be found in Table II- 11.	90

Appendix

List of abbreviations

%	percent	min	minute
°C	degree Celsius	min.	minimum
µg	microgram	mL	milliliter
µL	microliter	mM	millimolar
µM	micromolar	ms	millisecond
APS	ammonium persulfate	MS	Microsoft
AU	Airy unit	N.A.	numerical aperture
AXL	AXIAL-GROWTH	nm	nanometer
bit	binary digit	PAT	PROTEIN S-ACYLTRANSFERASE
BSA	bovine serum albumin	PBS	phosphate buffer saline
BUD	BUD SITE SELECTION	PFA	paraformaldehyde
CA	constitutively active	PGGT	PROTEIN GERANYLGERANYLTRANSFERASE
CDC	CELL DIVISION CYCLE	PH	pleckstrin homology domain
CDS	coding sequence	PI	propidium iodide
CFP	cyan fluorescent protein	PI(4)P	phosphatidylinositol 4-phosphate
CRIB	CDC42-RAC-INTERACTING-BINDING	PIP	phosphatidylinositol 4-phosphate
dag	days after germination	PIP2	phosphatidylinositol 4,5-bisphosphate
DN	dominant negative	PLP	PLURIPETALA
DNA	deoxyribonucleic acid	PS	phosphatidylserine
dNTPs	deoxynucleotides	PVDF	polyvinylidene difluoride
dSTORM	direct stochastic optical reconstruction microscopy	px	pixel
E. coli	Escherichia coli	r	radius
ECL	enhanced chemiluminescence	rcf	relative centrifugal force
ER	endoplasmic reticulum	RFP	red fluorescent protein
FER	FERONIA	RHID	root hair initiation domain
FLIM	fluorescent lifetime imaging	RLK	RECEPTOR LIKE KINASE
FRAP	fluorescence recovery after photobleaching	ROI	region of interest
FRET	Förster resonance energy transfer	ROP	Rho of plants
Fx	xth filial generation	RSR	RAS-RELATED GTPase
g	gram	SCN	SUPERCENTIPIDE
GAP	GTPase activating protein	SDS	sodium dodecyl sulfate
GDI	GUANINE DISSOCIATION INHIBITOR	SDS-PAGE	SDS-Polyacrylamide gel electrophoresis
gDNA	genomic deoxyribonucleic acid	sec	second
GDP	guanosine-5'-diphosphate	SRRF	super-resolution radial fluctuations
GEF	guanine nucleotide exchange factor	TBS	Tris buffered saline
GTP	guanosine-5'-triphosphate	TBST	Tris buffered saline with Tween20
HRP	horseradish peroxidase	T-DNA	transfer desoxyribonucleic acid
Hz	Hertz	TEMED	N,N,N',N'-Tetramethylethyldiamin
i.a.	inter alia (latin)	TiBA	2,3,5-triiodobenzoic acid
IAA	indole-3-acetic acid	v/v	volume per volume
LTI6B	Low temperature induced protein 6B	VAEM	variable angle epifluorescence microscopy
M	molar	VE	de-ionised (german: voll entsalzt)
max.	maximum	w/v	weight per volume
mCit	mCitrine	YFP	yellow fluorescent protein
mg	milligram		